TURBULENT FLOWS IN EQUILATERAL TRIANGULAR DUCTS AND ROD BUNDLE SUB-CHANNELS

by

Aly Mohamed Mortada Aly

A THESIS

SUBMITTED TO THE FACULTY OF GRADUATE STUDIES

IN PARTIAL FULFILLMENT OF THE REQUIREMENTS FOR THE DEGREE

OF DOCTOR OF PHILOSOPHY

DEPARTMENT OF MECHANICAL ENGINEERING

WINNIPEG, MANITOBA

OCTOBER 1977

TURBULENT FLOWS IN EQUILATERAL TRIANGULAR DUCTS AND ROD BUNDLE SUB-CHANNELS

BY

ALY MOHAMED MORTADA ALY

A dissertation submitted to the Faculty of Graduate Studies of the University of Manitoba in partial fulfillment of the requirements of the degree of

DOCTOR OF PHILOSOPHY

ABSTRACT

Fully developed air flows through an equilateral triangular duct of 12.7cm sides were investigated experimentally for a Reynolds number of 53,000. The measurements included all Reynolds stresses (except $\rho \overline{vw}$) and the secondary velocities. As expected, the secondary flow pattern was found to consist of six counter-rotating cells bounded by the corner bisectors. Maximum secondary velocities of about 1 1/2% of the bulk velocity were observed. Two models for flow prediction allowing for the secondary flow are presented. The first model is based on an assumed effective viscosity profile and an experimentally measured input for the vorticity equation. In the second model, the vorticity production terms are expressed by modelling the turbostresses in the plane of the cross-section in terms of gradients in the mean axial velocity and a geometrically calculated turbulence length scale. The predicted characteristics of the flow are shown to be in good agreement with the present experimental data and the measurements of Gerrard[1] who used the same experimental facility. The effects of secondary currents were evident in the cross-sectional distributions of mean axial velocity, wall shear stress and Reynolds stresses, and very prominent in the turbulent kinetic energy distributions. The second model performed particularly well and was subsequently applied to additional Reynolds numbers and extended to include heat transfer.

The second model was also applied to the case of an infinite equilateral triangular array of rods. Three rod spacings having pitch-to-diameter ratios of 1.123, 1.2 and 1.35 were examined over a Reynolds number range of 27,000 to 250,000. In a primary flow cell of a subchannel, the secondary flow is shown to be a single cell of circulation

bounded by the rod surface, the radial boundaries at $\theta = 30°$ and $0°$ and the maximum velocity line. For a Reynolds number of 27,000, the predicted maximum secondary velocity was about 1.4% of the average bulk velocity for $P'/D = 1.123$. The secondary velocities are shown to decrease with increasing P'/D and may be neglected for $P'/D > 1.5$ Comparison of the predicted parameters of the flow are shown to be in reasonable agreement with the experimental results of several investigators.

ACKNOWLEDGEMENTS

The author wishes to express his gratitude and appreciation to Dr. A.C. Trupp (thesis supervisor), Mechanical Engineering Department, for his valuable guidance and sincere help. The author also acknowledges the comments and encouragement of Dr. R.S. Azad, Mechanical Engineering Department.

Thanks are also due to Mrs. B. Glowasky and Mrs. M. Tyler who typed the thesis, and to Mr. P. Mitra for drafting most of the figures.

Special thanks and appreciation are also due to my wife Mona for her patience, encouragement and interest during this research.

The author held a University of Manitoba Post Graduate Fellowship during the course of this research and this support is acknowledged.

Finally, the funding provided by the National Research Council through a Grant to Dr. A.C. Trupp is gratefully acknowledged.

TABLE OF CONTENTS

PAGE

LIST OF TABLES

LIST OF FIGURES

NOMENCLATURE

A	Law of the wall constant
A^+	Wall damping constant
C, C_1, C_2, C_ν, C_D	Turbulence model constants
D	Rod diameter
D_h	Equivalent hydraulic diameter
E	Law of the wall constant
f	Friction factor defined by equation (6.30)
H	Height of a primary flow cell in the triangular duct
$\bar{H}$	Time average of specific enthalpy
k	Mean turbulent kinetic energy
k'	Fluctuating component of turbulent kinetic energy
L	Half side length of the triangular duct (Part I)
L	Grid Parameter (Part II)
ℓ	Turbulence length scale
ℓn	Natural Logarithm
M, N	Grid Parameters
P	Instantaneous static pressure
$\bar{P}$	Mean static pressure
P'	Pitch (distance between rod centers)
P*	Jayatilleke "P-function"
$\dot{q}''$	Wall heat flux

R_{ij} Reynolds stress tensor $(\overline{u_i u_j})$

R Rod radius

r Radial distance from center of rod

R_e Reynolds number based on U_b and D_h

S_{ij} Mean strain rate tensor

S Distance from certain node to the wall

T Local Temperature

t Time

T_W Duct wall temperature

U Instantaneous axial velocity

$\bar{U}$ Axial mean velocity

U^+ Dimensionless mean velocity

U* Average friction velocity

U_b Average mean velocity over primary flow cell cross-section (bulk velocity)

u,v,w Fluctuating components of the velocities in the axial, lateral and binormal directions respectively

u, v_θ, v_r Fluctuating components of the velocities in the axial, peripheral and radial directions respectively

V,W Instantaneous velocities in the lateral and binormal directions respectively

$\bar{V},\bar{W}$ Lateral and bi-normal mean velocities (secondary velocities)

V_r, V_θ Instantaneous velocities in the radial and peripheral directions respectively

$\bar{V}_r, \bar{V}_\theta$ Radial and peripheral mean velocities (secondary velocities)

v_r', v_θ' Root mean square values of the fluctuating components of the velocities in the radial and peripheral directions respectively

x	Axial coordinate
x'	Length of test section from inlet to measuring station
y	Lateral coordinate
Y	Radial distance from rod surface (= r - R)
$\hat{Y}$	Radial distance from rod surface to maximum velocity line (rod bundle subchannels)
Z	Binormal coordinate
$\hat{Z}$	Normal distance from the wall to the corner bisector (Triangular duct)
Z^+	Dimensionless normal distance from wall
ε	Dissipation rate of turbulent kinetic energy
θ	Angular coordinate
λ	Convergence criterion
μ	Laminar dynamic viscosity
μ_e	Effective viscosity
μ_t	Eddy viscosity
ν	Kinematic viscosity
ρ	Fluid density
σ_k	Effective Prandtl number for turbulent kinetic energy
σ_h	Prandtl number of the fluid
$\sigma_{h,t}$	Turbulent Prandtl number
τ	Local wall shear stress
τ_W	Average wall shear stress
ϕ	Parameter in the general elliptic equation (7.1 or 11.1)
Ψ	Stream function defined by equation (3.9 or 9.10)
ω	Axial vorticity defined by equation (3.8 or 9.9)
∇^2	Laplacian operator

TURBULENT FLOWS IN EQUILATERAL TRIANGULAR DUCTS AND ROD BUNDLES SUB-CHANNELS

1. INTRODUCTION

1.1 Motivation

Most nuclear power reactors have fuel bundles which consist of a parallel matrix of rods arranged mainly in triangular and/or square arrays. The space between the rods forms interconnected sub-channels through which the coolant flows axially. Accurate calculations of pressure drop and rod surface temperatures require detailed knowledge of local mean velocities and enthalpy distributions in the sub-channels. However, current design methods are usually based on a sub-channel mixing technology which involves sub-channel average quantities and does not explicitly recognize secondary flows. Hence, these methods may lead to serious discrepancies, particularly for closely spaced rods for which the variation around the circumference of a rod is significant for certain parameters since secondary flows are very active. In order to improve design procedures, rod bundles have recently received increased attention through a number of fundamental studies. Experimental data is now available for several finite arrays, but the measurements have been limited to pressure drop, wall shear stress and the distributions of mean axial velocity, turbulent kinetic energy and Reynolds stresses. There are still no reliable measurements of secondary velocities which play a major role in momentum and heat transfer.

The present research evolved from a desire to test an equilateral triangular array of rods having unity pitch-to-diameter ratio (i.e., rods

touching). This limiting aspect ratio is the only one that can be practically constructed to truly constitute a member of the infinite array series where secondary flows are confined to within each symmetric part of the sub-channel. But a tricuspid channel is difficult to build accurately, hence, the equilateral triangular duct was chosen for its similarity and simplicity and the fact that triangular ducts have received little previous attention. Studying this flow experimentally, added to the present state of knowledge on the structure of turbulent flows in non-circular ducts. It also allowed the development of secondary flow instrumentation and measuring techniques, and provided experimental data for use in verifying the mathematical models of turbulence that have been developed for predicting these flows. These mathematical models can be applied to predict turbulent flows in rod bundle arrays, based entirely on numerical solutions of the appropriate equations. Once experience and expertise is gained on homogeneous cases, heterogeneous (and hence real) geometries may be tackled, leading ultimately to completely numerical designs to replace the current expensive methods. This could be translated to better design concepts and hence higher cycle efficiency in a nuclear power plant.

1.2 Scope and Objectives

The experimental study described herein, concerns the fully developed flow structure in an equilateral triangular duct. The first phase of this study was performed by Gerrard[1] who proved the flow symmetry at the measuring station, and measured mean axial velocity distributions, pressure drops, wall shear stress and axial power spectra with reasonable accuracy. However, his secondary flow measurements were confined to the $\bar{V}$ component. In the present work, both secondary velocity components ($\bar{V}$ and $\bar{W}$) were measured, and more refined data on Reynolds

stresses (except $\rho \overline{vw}$) were obtained using an advanced hot wire system (DISA 55M); this provided better trend accuracies than the measurements of Gerrard[1]. The two sets of data are qualitatively similar, but there is slight quantitative difference due to the coarse adjustment of the DISA 55D05 anemometer that was used by Gerrard[1], who was not able to measure with the optimum overheat ratio.

For fully developed flow at the measuring station (133 equivalent hydraulic diameters from the entry station), the duct cross-section consists of six symmetric primary flow cells. Secondary flows are confined by symmetry to individual flow cells. This permitted detailed measurements in only one primary flow cell. Reynolds stresses (except $\rho \overline{vw}$) were obtained using a miniature X-probe, while secondary velocity components were measured with two different techniques involving X-probe and 45° slanting single wire probe.

The analytical work consisted of two models for prediction of fully developed turbulent flows in equilateral triangular ducts; the second model was also applied to study the fully developed turbulent flows in rod bundles sub-channels. The first prediction technique is based on the refined measurements of Reynolds stresses to provide source terms for the vorticity equation, and on an assumed spatial distribution for the eddy viscosity. The second prediction model adopted the fully modelling procedure outlined by Launder and Ying[2] to avoid any empirical input to the equations; but the model constants required some adjustment to yield the best comparison with the experimental data. The second model was also applied to predict the fully developed turbulent flow characteristics for equilateral triangular arrays of rod bundles with pitch-to-diameter ratios of 1.123, 1.2 and 1.35. The results were in fairly

reasonable agreement with the experimental measurements of several investigators. The main emphasis of the work (both experimental and numerical) is on secondary flows; their detail and variation with Reynolds numbers and pitch-to-diameter ratios and their influence on the mean axial velocity, turbulent kinetic energy and wall shear stress distributions.

CHAPTER 2

LITERATURE REVIEW

2.1 Review of Experimental Work

Fully developed turbulent flows in straight non-circular ducts are helical in nature. The spiral motion is due to secondary currents which act in the plane normal to the channel walls and generate mean shear stresses to maintain equilibrium between Reynolds stresses and pressure gradients in the asymmetric cross-section. Secondary flows of this type are encountered in many turbulent flow geometries including triangular and rectangular ducts, eccentric annulli and parallel flow rod bundles. The following is a brief presentation of the experimental work available in the literature for different secondary flow geometries.

2.1.1 Square and Rectangular Ducts

The square duct has been studied the most extensively. Nikuradse[3] was the first to notice the differences between turbulent flow in circular pipes and square ducts. He noted that lines of constant mean axial velocity (isovels) tended to bulge towards the corners and were displaced away from the mid-point of the walls compared to the isovels for laminar flow. Prandtl[4] suggested that these were the result of secondary flows which are directed from the center of the duct toward the corners and which, to satisfy continuity, required a return flow at the mid-point of the walls. He also suggested that these secondary flows occur as a result of the turbulent fluctuations along the isovels giving a net flow normal to the isovel whereever a variation in curvature occured. It was not possible at that time to measure the magnitude of the secondary

velocities due to the error introduced by the yaw-meter especially in regions possessing mean velocity gradients. Maslen[5] showed that these secondary flows do not appear in fully developed laminar duct flow but are confined to the turbulent case. Hoagland[6] measured mean axial velocities with both hot wire anemometer and pitot tube instrumentation, for rectangular ducts of aspect ratios 1:1, 2:1 and 3:1. Secondary velocities were determined from observations of flow direction, using a sensitive hot wire system. He showed that these secondary flows behave in the same manner originally suggested by Prandtl.[4] The magnitudes of the maximum secondary velocities for all the ducts were approximately 1 to 1 1/2 percent of the axial centerline velocity and occured near the wall in the corner region. Leutheusser[7] found that in both square and rectangular ducts, the inner law of the wall provides a good description of the flow in regions near the wall, but in the center of the duct, the velocity distribution does not follow the outer law formulation. Turbulent flows in square ducts were extensively studied by Brundrett and Baines[8] using a hot wire anemometer. They measured the six components of the Reynolds stress tensor as well as the three mean velocity components. They suggested that secondary velocities were generated by gradients of Reynolds stresses in the plane of the duct cross-section, and that the main contribution to the generation term is from the normal stress gradients. Gessner[9] using hot wire anemometer showed that a transverse flow is initiated and directed towards the corner as a direct result of turbulent shear stress gradients normal to the bisector. The results further indicated that anisotropy of the turbulent normal stresses did not play a major role in the generation of secondary flow. These conclusions do not necessarily contradict the explanations of Brundrett and Baines[8]

since the co-ordinate systems are different for both investigations. In earlier work, Gessner and Jones[10] found that secondary velocities, when non-dimensionalized by either the bulk velocity or the axial center-line velocity, decreased with increasing Reynolds number. However, Launder and Ying[11] established that secondary velocities normalized with friction velocity are effectively independent of Reynolds number. Kokorev at al[12] measured one component of the secondary velocities for a turbulent flow of air in a square channel using a five-tap tube with four taps oriented at about $45°$ angle to the probe axis. Recently, a detailed experimental study of developing turbulent flow in a rectangular duct was made using a laser Doppler anemometer by Melling and Whitelaw.[13] Contours of axial mean velocity and turbulence intensity were measured in the developing flow, and all three mean velocity components and five of the six - Reynolds stresses were obtained in the nearly fully developed flow. Their results confirm those qualitative features of turbulent flow through a rectangular duct previously indicated by results obtained using hot wire anemometry, but they indicate quantitative differences. For example, their results indicated that $|\overline{uv}|/U^{*2}$ increases towards the wall, approaching the value of 1.0, whereas Brundrett and Bains[8] reported values in excess of 1.5 near the wall, and Gessner[9] reported values of -1.5 and -1.21 (his octant is not the same as the above) near the bottom wall at two different Reynolds numbers. One should be careful in comparing the results of Melling and Whitlaw[13] to those of fully developed turbulent flows, since their measuring station was only at 36.8 equivalent hydraulic diameters (x/D_h) from the test section entry; this is considered still far from fully developed turbulent flow. Measurements of developing turbulent flow in a square duct was made also

by Gessner, Po and Emery[14] at x/D_h of 8, 16, 24, 40 and 84.

2.1.2 Rod Bundles

Experimental measurements of turbulent flows in rod bundles are few in number and limited to pressure drop, wall shear stress, mean axial velocity, mean turbulent kinetic energy and Reynolds stresses. There are no reliable measurements of secondary velocities neither with hot wire anemometers nor with laser Doppler anemometers. Mean axial velocity distributions of water flowing through the test section of cross-section shown in figure (2.1) were measured with a pitot tube by Eifler and Nijsing[15] for P'/D of 1.05, 1.10 and 1.15, and for Reynolds numbers in the range (15 - 50) x 10^3. Eifler[16] used the same facility but measured for P'/D = 1.08. The above investigators suggested that the secondary flow pattern consists of single circulation confined in each primary flow cell. A similar cross-section was used by Subbotin et al[17] to measure the velocity field and wall shear stress distribution in air for P'/D ratios of 1.05, 1.10 and 1.20, for Reynolds number in the range (18.8 - 81) x 10^3; pitot tube was also used in these measurements and local values of the wall shear stress were measured by Preston's method. Velocity distributions were distorted in both the above investigations due to the proximity of the wall; these walls were blocking the gap of the sub-channel adjoining the one where measurements were being performed. An experimental study of turbulent flow in a rod bundle of triangular array with P'/D of 1.217 was presented by Kjellstrom,[18] with the test section of cross-section shown in figure (2.2). The experiment included measurements of pressure drop and local distributions of axial and secondary velocities, turbulence intensities, Reynolds stresses and the wall shear stress. The measured data for secondary velocities

were too scattered to allow definite conclusions to be drawn and he indicated that the measurements probably were affected by large systematic error. Hall and Svenningsson[19] used the triangular array facility of Kjellstrom and Stenback,[20] but their secondary flow measurements using a rotatable hot wire were not conclusive and they recommended further investigation. Rowe,[21] was also unable to measure the secondary velocities in a square array of rods with a laser Doppler anemometer. His estimates and suggestions concerning the shape and number of swirls in his test section, were entirely based on the distortions in the maps of the axial turbulence and velocity. It is not possible to generalize his conclusions due to the corner effects. Similarly although Trupp and Azad[22] could infer the direction and approximate magnitude of secondary flows from momentum and energy balances, they were unable to measure the tiny secondary velocities via conventional X-probes and a three-wire probe in a simulated infinite triangular array with cross-section given in figure (2.3); however, their measurements of axial velocity, turbulent intensities, Reynolds stresses as well as power spectra of the axial turbulence and wall shear stress distribution for P'/D of 1.2, 1.35 and 1.50 are considered the most complete experimental work on rod bundles using hot wire anemometers. Carajilescov and Todreas[23] measured the distributions of axial velocity, turbulent kinetic energy and Reynolds stresses using a laser Doppler anemometer operating in a "fringe mode" with forward scattering, in a simulated interior sub-channel of a triangular rod array with $P'/D = 1.123$ as shown in figure (2.4), and $x/D_h = 77$. They proposed a new mixing length distribution from their experimental results, however, they were unable to measure the secondary velocities due to the error associated with the analog voltage produced

by the frequency tracker.

2.1.3 Triangular Ducts

Nikuradse[24] was the first to deal with turbulent flow in triangular ducts. He noted that the isovels in these ducts tended to bulge towards the corners, and confirmed the existence of secondary flows by flow visualization. Cremers and Eckert[25] published measurements of mean axial velocity and five Reynolds stresses in an isosceles triangular with a vertex angle of about 12°. They reported that there was no experimental evidence of secondary flows at a Reynolds number of 10,900, although contour plots of axial velocity fluctuations strongly suggest the presence of secondary flows near the base. In a similar channel (vertex angle of 20°), at double the Reynolds number, Kokorev et al[12] detected three cells of secondary flow in each symmetric half of the channel, but their results were qualitative. Other experimental investigations involving triangular ducts have mainly concerned the transitional flow regime (i.e., Cope and Hanks,[26] and Bandopadhayay and Hinwood[27]).

Other duct configurations which have been explored include, for example, an open triangular duct (Liggett, Chiu and Miao[28]), two interconnected sub-channels (Layall[29]) and a circular pipe with one or two eccentric rods (Kacker[30]).

2.2 Review of the Analytical Work

2.2.1 Computations of Turbulent Flows

Complete coverage of developments in the computation of turbulent flows is beyond the scope of this work. However, in this section the various schemes for computing flow are classified (according to closure) and discussed briefly with reference made to the more important relevant publications. For more complete details on turbulent flow closures, the

author recommends references 31 to 36 inclusive.

Computation methods of turbulent flows may be classified in different ways according to the equations to be solved and the relevant closure assumptions. They may be broadly classified as phenomenological turbulence models, eddy diffusivity models or statistical turbulence models. Another classification is related to the number of additional transport equations necessary to solve the basic equations. With this method, the different models are classified as zero-,one-,two-, or many-equation turbulence models. Another approach to classifying the turbulence models was proposed by Reynolds[31] as mean velocity field closure, mean turbulent kinetic energy closure or Reynolds stresses equations closure. The latter will be adopted here for purpose of reviewing the different computation schemes. Included in the discussion are recent developments, particularly as concerns the two-equation models.

a) Mean Velocity Field Closure (MVF, MVFN)

MVF closure is considered to be the simplest method. For the equations of the mean velocity field and pressure in an incompressible and constant property fluid given by:

$$\frac{\partial \bar{U}_i}{\partial x_i} = 0, \tag{2.1}$$

$$\frac{\partial \bar{U}_i}{\partial t} + \bar{U}_j \frac{\partial \bar{U}_i}{\partial x_j} = -\frac{1}{\rho}\frac{\partial \bar{P}}{\partial x_i} + \nu \frac{\partial^2 \bar{U}_i}{\partial x_j \partial x_j} - \frac{\partial \overline{u_i u_j}}{\partial x_j}, \tag{2.2}$$

the Reynolds stresses $\overline{u_i u_j}$ are to be related to the properties of the mean velocity field by using a constitutive equation involving an assumed spatial distribution for turbulence length scale. A general form of this constitutive equation is:

$$\overline{u_i u_j} = \frac{q^2}{3} \delta_{ij} - 2 \sqrt{2 S_{mn} S_{mn}}\, \ell^2 S_{ij}, \tag{2.3}$$

where the strain-rate tensor S_{ij} is given by:

$$S_{ij} = \frac{1}{2} \left(\frac{\partial \bar{U}_i}{\partial x_j} + \frac{\partial \bar{U}_j}{\partial x_i} \right), \tag{2.4}$$

$$q^2 = \overline{u_i u_j}, \tag{2.5}$$

and ℓ is a turbulence length scale.

Another closure may be achieved by assuming an eddy viscosity spatial distribution (ν_T). It is noted that an assumption for ℓ gives ν_T and vice versa. Prediction of turbulent boundary layer separation by MVF methods are not very successful.[31] Assuming a Newtonian behaviour, for MVFN closure, the principal axes of stress and strain rate are assumed to be aligned and the mixing length is assumed in terms of the flow geometry. Although this assumption is based on fallacy, MVFN works well in three-dimensional boundary layer to predict the mean velocity field.[37] It is much better in predicting integral properties of the flow than in predicting local details. MVFN methods have also been used with some success in compressible flows[38] and in contained and recirculating flows.[39] MVFN equations have not been tested in very many time dependent flows for there are practically no comparison data.

b) Mean Turbulent Kinetic Energy Closure (MTE)

A single equation for the turbulent kinetic energy is used in this closure in conjunction with some constitutive or structural equations relating the turbulent stresses to the turbulent kinetic energy. A more advanced approach which has been used recently by some investigators is to solve two transport equations for the turbulent kinetic energy and its

dissipation ($k - \varepsilon$ model). The turbulent kinetic energy equation is given by:

$$\frac{\partial k}{\partial t} + \bar{U}_K \frac{\partial k}{\partial x_K} = \underbrace{- \overline{u_i u_K} \frac{\partial \bar{U}_i}{\partial x_K}}_{\text{Production}} \underbrace{- \frac{\partial}{\partial x_K} (\overline{u_K u_i u_i}/2)}_{\text{Triple Correlation}}$$

$$\underbrace{- \frac{1}{\rho} \frac{\partial}{\partial x_K} (\overline{u_K P})}_{\substack{\text{Pressure} \\ \text{Velocity} \\ \text{Correlation}}} + \underbrace{\upsilon_{ii}/2}_{\text{Dissipation}}, \qquad (2.6)$$

as may be derived from the Navier Stokes equations.[40] A modelled form[36] may be written as:

$$\frac{Dk}{Dt} = \frac{1}{\rho} \frac{\partial}{\partial x_k} [\frac{\mu_t}{\sigma_k} \frac{\partial k}{\partial x_k}] + \frac{\mu_t}{\rho} (\frac{\partial \bar{U}_i}{\partial x_k} + \frac{\partial \bar{U}_k}{\partial x_i}) \frac{\partial \bar{U}_i}{\partial x_k} - \varepsilon, \qquad (2.6.a)$$

where σ_k is constant. In this closure, it is evident that modelling is required for the dissipation term, pressure-velocity correlation term and triple velocity correlation term. The dissipation may be obtained from the equation:

$$\frac{D\varepsilon}{Dt} = \frac{1}{\rho} \frac{\partial}{\partial x_k} [\frac{\mu_t}{\sigma_\varepsilon} \frac{\partial \varepsilon}{\partial x_k}] + \frac{C_{\varepsilon 1} \mu_t}{\rho} \frac{\varepsilon}{k} (\frac{\partial \bar{U}_i}{\partial x_k} + \frac{\partial \bar{U}_k}{\partial x_i}) - C_{\varepsilon 2} \frac{\varepsilon^2}{k}, \qquad (2.6.b)$$

where $C_{\varepsilon 1}$, $C_{\varepsilon 2}$ and σ_ε are constants related to the $(k - \varepsilon)$ model. Different methods of modelling the dissipation terms are reported.[31] The pressure-velocity term and triple correlation term may be modelled in two ways. The first is the gradient diffusion model which leads to elliptic type of equation, but it is thought by some that this model ignores the dominance of transport processes by large scale eddy motions.[31] The second approach is a generalization of a large eddy transport model, which leads to hyperbolic equations. The mathematical difference is due

to the physical differences in the models, however, both models were reported to provide successful predictions.[31] For complete closure of the system of equations, the turbulent kinetic energy in (2.6) must be related to Reynolds stresses. A MTEN procedure is most commonly used. In equation (2.3), $\ell^2(2\ S_{mn}\ S_{mn})^{\frac{1}{2}}$ is replaced by ν_T. The new equation is used with another constitutive equation of Newtonian behaviour which relates the turbulent viscosity to the turbulent kinetic energy via specified length scale (or the dissipation ε). The length scale may be calculated either algebraically[2,23], or through a differential equation.[41] An alternative approach (MTES procedure) is based on the idea that strained flows apparently develop an equilibrium structure. Reynolds stresses are directly related to the turbulent kinetic energy by assuming a turbulence structure.[42,43] However, it was argued by Lumley[44] that the homogeneous flows upon which MTES are based do not really reach equilibrium, and that the turbulence time and length scales continually increase. This expectation was confirmed experimentally by Champagne et al[43], hence a structural model cannot be fully correct in homogeneous flows.

The two approaches do not hold in the viscous region near the wall. The equations must either be modified to include viscous effects or employ special solutions (i.e., Mellor and Herring[45]) which contain terms to calculate for the inner region directly. For flows not too rapidly shocked by changes in free stream or wall conditions, consistent MVF and MTE treatments may be expected to give nearly the same results for the mean velocity and integral parameters.[31] In addition, MTE gives also the turbulence energy distribution directly. MTE can be also used to study the effects of variable free stream turbulence[46] and are able to handle sudden changes in boundary conditions.[47] As will be discussed in

Chapter 3, forms of the turbulent kinetic energy equation other than (2.6) have been used for turbulent flow predictions in non-circular ducts.

c) Reynolds Stresses Equations Closures (MRS)

The dynamical equations for Reynolds stresses $\overline{u_i u_j}$ are given by:

$$\frac{\partial \overline{u_i u_j}}{\partial t} + U_K \frac{\partial \overline{u_i u_j}}{\partial x_K} = - \overline{u_i u_K} \frac{\partial \bar{U}_j}{\partial x_K} - \overline{u_j u_K} \frac{\partial \bar{U}_i}{\partial x_K} - \frac{\partial}{\partial x_K} (\overline{u_i u_j u_K})$$

$$- \frac{1}{\rho} [\frac{\partial}{\partial x_j} (\overline{u_i P}) + \frac{\partial}{\partial x_i} (\overline{u_j P})]$$

$$+ \overline{\frac{P}{\rho} (\frac{\partial u_i}{\partial x_j} + \frac{\partial u_j}{\partial x_i})} + \upsilon_{ij} \qquad (2.7)$$

In MRS closure, the following type of assumptions are invoked to handle certain terms in the above equation:

i) Pressure-strain rate correlation

Many of MRS closures have used a model proposed by Rotta[48], and supported by Champagne et al[43] of the form:

$$P_{ij} = \overline{\frac{P}{\rho} (\frac{\partial u_i}{\partial x_j} + \frac{\partial u_j}{\partial x_i})} = \frac{C\sqrt{k}}{\ell} (\frac{2k}{3} \delta_{ij} - \overline{u_i u_j}). \qquad (2.8)$$

The objection to this model arises from the observation that the fluctuating pressure field given by Poisson equation suggests that P_{ij} model should contain terms arising from interaction between the mean and fluctuating velocities, and should reflect the dependence of the pressure fluctuations on distant velocity fluctuations.

ii) The pressure-velocity terms

This term may be represented by extensions of the gradient diffusion model[45,49,50] or may be neglected for high Reynolds numbers.[51,52]

iii) The triple velocity term

For this term, various forms of the gradient diffusion models have been used.[45,50,51,52] An alternative procedure included a large eddy transport model.[31]

iv) Viscous terms

Different models were proposed for these terms[45,49,50], or they were ignored for high Reynolds number flows.[51,52]

The prediction of the mean velocity profile by MRS method is good but not better than a good MVF or MTE calculation.[31] Turbulent stress distributions can also be predicted and are generally in good agreement with experiments. The MRS was used with moderate success in studying the distortion of isotropic turbulences.[53]

A Reynolds stress model of turbulence and its application to thin shear flows was presented by Hanjalic and Launder[51], and modified to include the wall region by Launder et al.[52] A simple derivative of that model was proposed by Launder and Ying.[2] It retains the essential vorticity generating features and requires the solution of only one turbulence property to be found from a differential equation. This simpler version was used to predict fully developed turbulent flows in square ducts[2,54], an equilateral triangular duct (this work) and rod bundle sub-channels[23] (and this work).

2.2.2 Prediction of Turbulent Flows In Triangular Ducts and Rod Bundle Sub-channels

a) Triangular Ducts

Unlike the square duct, there has been essentially no previous work done on triangular ducts since the pioneering efforts of Deissler

and Taylor[55] which did not allow for secondary flows. They proposed that the well known semi-logarithmic law should apply in an arbitrary duct along velocity gradient lines which are orthogonal to the axial isovels. They used a very tedious graphical iterative technique. The predicted isovels were substantially different from the experimental isovels as a result of ignoring the secondary velocities. The prediction of Kokorev et al[12] is limited to wall shear stress distributions, but includes an approximate estimate of the effect of secondary flow on the velocity distribution. Gerard[56] was unable to apply his finite element technique to the triangular duct geometry due to lack of experimental data as input in the vorticity equation.

b) Rod Bundles

A graphical iterative technique was also used by Diessler and Taylor[55] for rod bundle geometries, but it has the same deficiencies discussed above due to ignoring the secondary velocities. Bender and Switick[57] presented a method to determine the two-dimensional velocity distribution for turbulent, constant property single phase flow through an infinite triangular array rod bundle. In this method, turbulent momentum transport is directly calculated via a mixing length theory based on actual flow geometry. The velocity solution vector is determined by iteration between the momentum equation and the definition of turbulent momentum diffusivity. This method does not allow for secondary flows and hence predicts the local wall shear stress to monotonically increase from the gap to the position facing the sub-channel axial centerline. One of the disadvantages of this method is the fact that eddy diffusivities are forced to zero wherever the respective velocity gradients go to zero. Ibragimov and Co-workers[58] proposed a semi-empirical relation for the wall shear stress distribution determined only by geometric considerations.

With this distribution and the friction factor given by Blasius equation, they assumed the universal velocity distribution to hold normal to the channel walls. In a later work[59], they proposed a general method for any geometry based on an expression for the ratio between the friction factor for the specific geometry and that for circular tubes. Among the limitations of this method are neglect of secondary velocities and the assumption that the wall shear stress distribution is only a function of geometric parameters and independent of the Reynolds number.

Eifler and Nijsing[60] proposed that the lateral variation of the wall shear stress must be considered the prime cause for the existence of secondary flow. They concluded that a circular motion that transports high momentum fluid through the main flow in the direction of decreasing wall shear stress is induced by the lateral wall shear stress gradients. As a result, they proposed an expression for the peripheral secondary flow component and for the eddy diffusivities. These proposals are not realistic, since the experimental measurements of the wall shear stress showed that the maximum value does not always occur at the symmetry line of the sub-channel connecting the center of the channel to the rod center. An actual wall shear stress distribution in such a case, with their reasoning, produces secondary currents in disagreement with their proposed secondary flow pattern shown in figure (2.5).

Buleev[61] developed a theoretical model for turbulent transfer in three-dimensional fluid flow which can be applied to calculate the velocity and temperature distributions for turbulent flows in channels of arbitrary shape including rod bundles and rectangular ducts. This method was slightly modified and used by Ramm and Johannsen.[62] Neither the original nor modified models specifically involve secondary flows.

The simple Reynolds stress model outlined by Launder and Ying[2] and discussed earlier in this review, was used by Carajilescov and Todreas[23] to predict fully developed turbulent flows in an interior subchannel of a bare rod bundle. They used their proposed length scale distribution instead of the geometrically calculated one in the original model. Carajilescov and Todreas[23] work is considered to be the first successful prediction of secondary velocities in rod bundle geometries in spite of the disagreement with this investigation on the secondary velocity levels and the number of secondary flow cells in a primary flow cell as will be discussed later.

PART I: EQUILATERAL TRIANGULAR DUCTS

CHAPTER 3

THEORETICAL CONSIDERATIONS

3.1 Continuity and Reynolds Equations

In the equilateral triangular duct, symmetry permits the flow cross-section to be subdivided into six primary flow cells. Each of these cells is identical when viewed with respect to rotated coordinate systems (except for handedness of secondary flow circulation), and no net mass, momentum or energy is transferred across any boundary. A knowledge of the flow properties in any one cells is, therefore, sufficient to describe the entire flow field. The primary flow cells and Cartesian coordinate system used in the present investigation is shown in figure (3.1). The conservation equations pertinent to flow prediction are outlined below for fully developed, steady and incompressible turbulent flow of a constant property fluid.

The simplest forms of the continuity equations which can be applied within a flow cell are:

$$\frac{\partial \bar{V}}{\partial y} + \frac{\partial \bar{W}}{\partial z} = 0, \tag{3.1}$$

$$\frac{\partial u}{\partial x} + \frac{\partial v}{\partial y} + \frac{\partial w}{\partial z} = 0. \tag{3.2}$$

The Reynolds equations are:

y-direction;

$$\rho\left(\bar{V}\frac{\partial \bar{V}}{\partial y} + \bar{W}\frac{\partial \bar{V}}{\partial z}\right) = -\frac{\partial \bar{P}}{\partial y} + \mu\left(\frac{\partial^2 \bar{V}}{\partial y^2} + \frac{\partial^2 \bar{V}}{\partial z^2}\right) - \rho\left(\frac{\partial \overline{v^2}}{\partial y} + \frac{\partial \overline{vw}}{\partial z}\right), \tag{3.3}$$

z-direction;

$$\rho(\bar{V}\frac{\partial\bar{W}}{\partial y} + \bar{W}\frac{\partial\bar{W}}{\partial z}) = -\frac{\partial\bar{P}}{\partial z} + \mu\left(\frac{\partial^2\bar{W}}{\partial y^2} + \frac{\partial^2\bar{W}}{\partial z^2}\right) - \rho\left(\frac{\partial\overline{vw}}{\partial y} + \frac{\partial\overline{w^2}}{\partial z}\right), \tag{3.4}$$

x-direction;

$$\rho(\bar{V}\frac{\partial\bar{U}}{\partial y} + \bar{W}\frac{\partial\bar{U}}{\partial z}) = -\frac{\partial\bar{P}}{\partial x} + \mu\left(\frac{\partial^2\bar{U}}{\partial y^2} + \frac{\partial^2\bar{U}}{\partial z^2}\right) - \rho\left(\frac{\partial\overline{uv}}{\partial y} + \frac{\partial\overline{uw}}{\partial z}\right), \tag{3.5}$$

where the over-bar designates time-averaging.

The Reynolds equation for the x-direction can be regarded as an expression for the change in axial momentum of a small element of fluid. The roles of the various terms are more easily understood if the equation is rearranged in the following form:

$$-\frac{1}{\rho}\frac{\partial\bar{P}}{\partial x} = \bar{V}\frac{\partial\bar{U}}{\partial y} + \bar{W}\frac{\partial\bar{U}}{\partial z} - \nu\left[\frac{\partial^2\bar{U}}{\partial y^2} + \frac{\partial^2\bar{U}}{\partial z^2}\right] + \left[\frac{\partial\overline{uv}}{\partial y} + \frac{\partial\overline{uw}}{\partial z}\right]. \tag{3.6}$$

The term $-\frac{1}{\rho}\frac{\partial\bar{P}}{\partial x}$ represents the change in axial momentum due to the axial pressure gradient. Its magnitude is constant over the cross-section as can be verified by differentiating equations (3.3), (3.4), (3.5) with respect to x.

On the right hand side of equation (3.6), the two bracketed terms represent the change in momentum due to viscous and Reynolds shear stresses. The two remaining terms indicate that changes in the axial momentum of a small fluid particle that occur as a result of convection by secondary flows. These terms represent the difference between flow in circular and noncircular ducts.

Along the y-axis (wall boundary), the convective terms and y-direction gradients terms vanish from the Reynolds equations due to the no slip condition. Along the corner bisector,

$$\bar{V} = -\sqrt{3}\,\bar{W},$$

since no net flow crosses the boundary. Along the z-axis (normal to midwall),

equation (3.3) must vanish since there can be no net momemtum transfer in the y-direction across this boundary. In fact here,

$$\bar{V} = o \quad \text{everywhere so,}$$

$$\frac{\partial \bar{V}}{\partial z} = o = \frac{\partial^2 \bar{V}}{\partial z^2},$$

$$\frac{\partial^2 \bar{V}}{\partial y^2} = o,$$

since $\bar{V}$ has opposite signs on each side of the Z-axis,

$$\frac{\partial \bar{P}}{\partial y} = o = \frac{\partial \overline{v^2}}{\partial y},$$

due to symmetry, hence it can be readily shown that

$$\overline{vw} = o, \quad \text{along this boundary.}$$

On the other hand, on this same boundary, $\frac{\partial \overline{uv}}{\partial y}$ (like $\frac{\partial \bar{V}}{\partial y}$) may have finite values since $\overline{uv}$ (like $\bar{V}$) has an antisymmetric distribution about the z-axis. For this reason and the fact that $\bar{W}$ may have finite values along the z-axis except at the wall and duct centerline, it is not possible to obtain a simple theoretical distribution for $\overline{uw}$ at this boundary from (3.5).

3.2 Axial Vorticity and Stream Function Equations

The equation governing conservation of axial vorticity may be written in the form[8]:

$$\bar{V}\frac{\partial \omega}{\partial y} + \bar{W}\frac{\partial \omega}{\partial z} = \frac{\partial^2}{\partial y \partial z}(\overline{v^2} - \overline{w^2}) - \left(\frac{\partial^2 \overline{vw}}{\partial y^2} - \frac{\partial^2 \overline{vw}}{\partial z^2}\right) + \nu\left(\frac{\partial^2 \omega}{\partial y^2} + \frac{\partial^2 \omega}{\partial z^2}\right). \qquad (3.7)$$

Because this equation includes only velocities and gradients in the y and z directions, the axial vorticity ω given by:

$$\omega = \frac{\partial \bar{W}}{\partial y} - \frac{\partial \bar{V}}{\partial z}, \qquad (3.8)$$

exists only if the lateral velocities exist and vice versa. Terms on the left of equation (3.7) represent the convection of vorticity by the

secondary flow itself. The tendency of this process is to make the vorticity constant along the secondary flow streamlines. A similar effect is produced by the last terms on the right which represent the diffusion of vorticity by viscous effects and tend to make the vorticity uniform over the duct cross-section by diffusing it from regions of high intensity to regions of low intensity. Depending on the local turbulence field, the remaining terms may represent either production or dissipation of axial vorticity.

The stream function (Ψ) is defined by

$$\rho\bar{V} = \frac{\partial\Psi}{\partial z}, \qquad (3.9.a)$$

and

$$\rho\bar{W} = -\frac{\partial\Psi}{\partial y}. \qquad (3.9.b)$$

Substituting (3.9) into (3.8) yields:

$$-\frac{\partial}{\partial y}\left(\frac{1}{\rho}\frac{\partial\Psi}{\partial y}\right) - \frac{\partial}{\partial z}\left(\frac{1}{\rho}\frac{\partial\Psi}{\partial z}\right) - \omega = o, \qquad (3.10)$$

which is the stream function equation; ω represents the source term in this equation.

3.3 Turbulent Kinetic Energy Equation

A simulated transport equation for turbulent kinetic energy may be written in the form[2]:

$$\left[\frac{\partial}{\partial y}\left(k\frac{\partial\Psi}{\partial z}\right) - \frac{\partial}{\partial z}\left(k\frac{\partial\Psi}{\partial y}\right)\right] - \frac{\partial}{\partial y}\left[\left(\mu + \frac{\mu_t}{\sigma_k}\right)\frac{\partial k}{\partial y}\right] - \frac{\partial}{\partial z}\left[\left(\mu + \frac{\mu_t}{\sigma_k}\right)\frac{\partial k}{\partial z}\right]$$

$$- \mu_t\left[\left(\frac{\partial\bar{U}}{\partial y}\right)^2 + \left(\frac{\partial\bar{U}}{\partial z}\right)^2\right] + \frac{\rho C_D (k)^{3/2}}{\ell} = o. \qquad (3.11)$$

Equivalent forms were used by Emmons[71], Wolfshtein[72], Launder and Ying[2] and several others.

The same equation for k may be rewritten as:

$$I + II + III + IV = o,$$

where,

(a) Term I $= \frac{\partial}{\partial y}\left(k \frac{\partial \Psi}{\partial z}\right) - \frac{\partial}{\partial z}\left(k \frac{\partial \Psi}{\partial y}\right)$,

represents convection of the mean turbulent kinetic energy by secondary velocities.

(b) Term II $= \frac{\partial}{\partial y}\left[\left(\mu + \frac{\mu_t}{\sigma_K}\right) \frac{\partial k}{\partial y}\right] - \frac{\partial}{\partial z}\left[\left(\mu + \frac{\mu_t}{\sigma_K}\right] \frac{\partial k}{\partial z}\right]$,

represents energy diffusion by viscous and turbulence effects.

(c) Term III $= - \mu_t \left[\left(\frac{\partial \bar{U}}{\partial y}\right)^2 + \left(\frac{\partial \bar{U}}{\partial z}\right)^2\right]$,

represents the rate of production of turbulent energy.

(d) Term IV $= \rho C_D (k)^{3/2}/\ell$,

represents the rate of dissipation of turbulent energy by molecular viscosity, as suggested by Prandtl based on dimensional analysis to replace the actual terms.

3.4 Enthalpy Equation

The enthalpy conservation equation may be written as:[2]

$$\frac{\partial}{\partial y}\left(\bar{H} \frac{\partial \Psi}{\partial z}\right) - \frac{\partial}{\partial z}\left(\bar{H} \frac{\partial \Psi}{\partial y}\right) = \frac{\mu}{\sigma_h}\left\{\frac{\partial^2 \bar{H}}{\partial y^2} + \frac{\partial^2 \bar{H}}{\partial z^2}\right\} - \rho \frac{\partial}{\partial y} \overline{hv} - \frac{\partial}{\partial z} \overline{hw}. \tag{3.12}$$

The terms on the left side represent mean specific enthalpy convection by secondary velocities. The first term on the right side represents the mean enthalpy diffusion by viscous effect, while the last two terms represent the convection of the mean enthalpy by turbulence.

3.5 Turbulence Length Scale

In simple forms, turbulence length scale may be assumed as function of the normal distance from the point under consideration to the walls nearby. To improve the calculations in the viscous region, an expression containing an exponential term was used by some investigators.[31] Many workers used simply zonal models with the appropriate form in each of the

inner, further from the wall (buffer region) and the outer regions of the flow. Buleev[61] proposed a semi-empirical expression which gives ℓ from geometrical considerations and proved to provide reasonable predictions.[2] All the above expressions are algebraically assumed in terms of flow geometry.

Spalding[73] proposed a differential equation for $k\ell$ based on a spectral transport equation by Rotta,[48] but near solid walls it requires adjustments to one of the coefficients for each specific application. Using the mean velocity field in the region of the local point under consideration, Gawain and Pritchard[74] obtained ℓ from an integrodifferential equation.

CHAPTER 4

EXPERIMENTAL FACILITY AND EQUIPMENT

The present work was conducted using an existing facility. The measurements entailed the distributions of five Reynolds stresses (except $\rho\overline{vw}$) and both secondary velocity components in a primary flow cell of an equilateral triangular duct test section. A more advanced measuring system than the one used by Gerrard[1] in previous work was used. Figure (4.1) shows a schematic of the wind tunnel and test section. A brief description of the components is given below.

4.1 Wind Tunnel

The wind tunnel portion of the present facility was that used previously by Trupp and Azad[22] in their investigation of rod bundle flow, and was modified by Gerrard[1] to operate in the open circuit mode. Atmospheric air was drawn through a contracting inlet by four counter-rotating axial aerofoil fans. Each of these fans was powered by a two speed motor which could be used for air flow control. A damper was located just upstream of the fans for finer flow adjustments, and fan vibrations were isolated by a canvas coupling and silencer at the exit of the fan section. Following the silencer, air passed through a diffuser, two sets of turning vanes, a screen section, and a circular contraction cone before entering a transition section. In this section, the flow area was gradually reduced and transformed to match the cross-section of the triangular test section. Air discharged through the open end of the triangular duct.

4.2 Test-section

The triangular test section consisted of a wooden entrance length followed by a precision acrylic section. The entrance length totalled 7.32m in length and was fabricated in 3 lengths from 2cm thick mahogany plywood. A 2.44m sheet of 2cm thick clear acrylic plastic was used for the remaining section. The overall length of the duct was 9.76m and the length of the interior sidewalls was 12.70cm. An interlocking construction is illustrated in figure (3.1) was used for both sections. It is estimated[1] that variations in the sidewall lengths were less than ±0.25mm and 0.1mm for the acrylic and wooden sections respectively.

In order to provide the longest possible entrance length and easy access, the test plane for mean velocity and turbulence measurements was located 2.5cm inside the open end of the duct. This location corresponded to a distance of about 133 equivalent hydraulic diameters from the test section inlet.

Provision for axial pressure gradient measurements was made by locating static taps at 15.24cm intervals along the duct length. Taps in the wooden section consisted of 0.8mm holes drilled midway across the base. In the plastic section, piezometric rings were formed by joining 0.6mm square edge holes located in the middle of each wall. Connectors for the manometer tubing were epoxied in 8mm holes drilled behind the small diameter holes.

4.3 Traversing Mechanism

Accurate positioning of either a pitot tube or hot wire probe in the test plane was achieved by using a traversing mechanism (Fig. 4.2) having three orthogonal directions of motion. Vertical motion (z-direction) was achieved by means of a DISA 55H01 traversing mechanism.

This mechanism was mounted on two vernier calipers which allowed up to 15cm of horizontal travel in the test plane. The vernier scales gave an accurate indication of the horizontal position. Motion in the axial direction was provided by two concentric tubes. The latter was used initially to explore end effects, but more routinely simply to locate the probe in the test plane. It is also noted that a hot wire probe could also be rotated concentrically by turning the probe support. The angular rotation was gauged using a small acrylic protractor fixed to the support.

The absolute position of a probe in the y-direction was made by visual alignment of the probe with a scriber mark on the test-section base which located the midwall bisector. Probes were located in the z-direction by observing their images as they were brought into contact with the shiny acrylic wall. The distance between the active section of a hot wire probe and the wall was measured with travelling microscope. It was estimated that absolute probe positions could be determined to within ± 0.05mm and ± 0.1mm in the vertical and horizontal directions respectively. The relative positional accuracy was of course much better since resolutions were 0.01mm in the z-direction and 0.02mm in the y-direction.

4.4 Instrumentation

A pitot tube with outside diameter of 1.067mm and having inside to outside diameter ratio of 0.6 was used to calibrate the hot wire system. Pressure readings were taken using either a Betz Projection Manometer or a R. Fuess Manometer (DISA 134B). The first had a range of 0-400 mm H_2O and an accuracy of ± 0.05mm H_2O, while the second had five ranges varying from 0-16mm H_2O to 0-160mm H_2O and an accuracy of ± 0.5% of full scale.

Turbulence measurements were made using constant temperature linearized hot wire anemometry. The anemometry systems were manufactured by DISA and consisted of two sets of 55M10 anemometers with 55D10 linearizers and 55D25 auxiliary units. These systems were operated in conjunction with DISA probes having 1.25mm sensing lengths of 5μm diameter platinum plated tungsten wire. The ancillary equipment consisted of two 55D31 digital d.c. voltmeter, three 55D35 rms voltmeters, a 55D71 dual summing unit, and a 55D70 correlator.

The data presented in this investigation on Reynolds stresses and secondary velocities were obtained using a miniature 55P61 X-array probe. Values for $\bar{V}$ were checked using a rotatable 55P12 miniature 45° slanting probe. Measurements of axial velocity fluctuations were also made with a 55P01 single wire probe with the sensing wire normal to the main flow and parallel to the test section base. All hot wire probes were calibrated insitu against the pitot tube with the probe located at the duct centerline. A static calibration for the DISA 55M system with the 55D10 linearizers consisted of multipoints over a narrow range. For example, 14 points over the range of about 8m/sec to 18m/sec provided a straight line least squares fit with a correlation coefficient of 0.9993. A typical calibration curve is presented in figure (4.3) for the 55P12 wire.

During calibration and measurements, the probes were operated at an overheat ratio of 0.8. Simultaneous measurements of the normal and shear (except $\rho\,\overline{vw}$) stresses were made using two matched channels (DISA 55M10 anemometers and 55D10 linearizers). Addition and subtraction of the signals was performed via the dual summing unit (55D71), and the final processing that gives normalized values of the shear stresses was done by

the correlator (55D70). Simultaneous measurements of the RMS values of the signals were achieved via the three rms voltmeters (55D35). After reasonable intervals of time (usually one hour), the calibration of each channel was checked by measuring mean axial velocities at a fan setting in the narrow range of calibration and at the same location in which the original calibration was made (duct centerline). Adjustments were made at the linearizer gain as necessary to correct for any channel drift or wire sensitivity reduction due to contamination. The miniature 55P61 probe[75] was chosen in the above measurements since its shaft could be placed in contact with the wall, even when the X-wires were aligned in the X-Z plane, which permitted measurements close to the solid wall.

4.5 Secondary Velocities Measurements

Concerning secondary velocities, several investigators have used different techniques, ranging from flow visualization with smoke to laser Doppler anemometers. Nikuradse[24] was the first one to observe the helical motion of the total velocity-vector using flow visualization. The same technique was used also by Hoagland[6] at very low speed turbulent flow (Re $\tilde{\sim}$ 9000) so that the smoke would not be diffused too rapidly by the turbulence. Weak secondary flows were observed with a sequence of photographs taken of the smoke trace at various positions in the duct. In the same investigation, in order to obtain quantitative data, Hoagland[6] developed a technique for secondary velocities measurements using a hot wire system. His first trial with two different hot wire probes in a V-array (Gooseneck probe) was not satisfactory, however, he succeeded in his second technique. He measured the flow direction with a standard probe inserted through the duct wall, with the probe stem normal to the duct axis. It was only necessary to make two angle observations to obtain

the flow direction at a single point. This was done with the aid of a wheatstone bridge circuit of which the wire constituted one leg. Angular positions of the probe were determined from a protractor disc. This method of measuring flow direction indicated only the component in the plane normal to the probe stem axis. To obtain the complete three-dimensional flow direction, it was necessary to measure components in two mutually perpendicular planes.

The same basic technique was used by several investigators[8,10,30,76,77] for different duct geometries, but with more advanced hot wire systems and traversing mechanisms.

Kokorev et al[12] used a tube with five pressure taps to measure one secondary velocity component of the secondary flow in one quarter of the cross-section of a square duct. The probe was a 40mm long bar, 1.8mm diameter, soldered from five 0.5 x 0.3mm capillaries, each of the latter serving as a pressure tap. The nose part of each of the taps was tapered with a vertex angle of about 90°, which as reported by them, should provide for maximum probe sensitivity. The probe axis was aligned to the axis of the channel and calibrated at the duct centerline where there was no secondary flow. Secondary velocity components were then calculated using the different measured pressure drops. It should be noted that all flow direction instruments employing pressure sensing elements have a velocity gradient error that would have been equal to or greater than the flow angles measured.[6]

Attempts at measuring the secondary velocities in rod bundle geometry via X-probe and three wire probe, were unsuccessful as reported by Trupp and Azad.[22] The measuring systems lacked the required sensitivity to properly extract the very small secondary velocities. Difficulties

were encountered due to imperfect matching of anemometer channels, relative drift and signal processing. The three wire probe was useless near the wall because of high errors due to axial velocity gradients.

Secondary velocities measurements were not successful also with laser Doppler anemometers for both square and triangular array rod bundles as reported by Rowe[21] and Carajilescov and Todreas[23] due to the errors introduced in the system; e.g., the tracker[23] was operated in the range of 500KHz, with analog voltage error of 1% of the range of operation. This error (5KHz) was of the order of secondary velocities, hence no frequency shift was detected. However, for a square duct, Melling and Whitelaw[13] were able to measure the three mean velocity componenets with a laser Doppler anemometer (large secondary velocity magnitudes and less geometrical difficulties). This method has the same uncertainties concerning the absolute accuracy as all hot wire systems.

An ideal technique for secondary velocities measurement should not disturb the flow at the measuring station; at the same time, any end effects should be prevented. In the present work, the probe axis was parallel to the flow at the measuring station, which minimized the flow disturbance. Two techniques were employed namely an X-probe and a rotatable slanting 45° probe. In the first technique, rapid measurements along horizontal (for $\bar{W}$) and vertical (for $\bar{V}$) lines were performed, with the wires normal and parallel to the wall respectively. Rapid measurements were necessary to avoid any errors resulting from channel drift of the X-probe. The differences (for $\bar{V}$ and $\bar{W}$) and summations (for $\bar{U}$) of the D.C. signals from the two channels were observed simultaneously via two pre-calibrated and matched DISA 55D31 digital voltmeters. Measurements near the corner and the solid wall were not expected to be

as accurate due to the large velocity gradients in these regions, particularly for $\bar{V}$, for which the wires were parallel to the solid wall.

To avoid the problem of velocity gradients, and to estimate the trend accuracy of measurements, a second technique was developed. Four readings at each location, with rotations of 90 degrees each of the slanting wire were observed, via one channel ending with a DISA 55D31 digital voltmeter. The rotations were determined via a small protractor mounted on the probe support. The differences between the two readings when the wire was in the horizontal direction provided $\bar{V}$, whereas $\bar{W}$ was calculated from the differences between the two readings when the wire was normal to the wall. It was possible with the second technique to measure at points close to the wall and near the corner. Although, the quantitative agreement of the two methods was reasonable (Section 5.3), the author recommends the second scheme; the channel drift is minimized, single D.C. voltmeter is used to observe the readings and velocity gradients are not a major source of error, particularly near the wall and the corner. It was also found that an error of $\pm$ 0.5 degrees in the 90 degrees rotation, in any direction, does not affect the readings of the voltmeters, which provides a good relative accuracy of measurements. In such a technique, if the whole field is to be scanned, a more accurate rotating mechanism must be used.

CHAPTER 5

EXPERIMENTAL RESULTS AND DISCUSSION

5.1 General

As mentioned previously, the test station was located about 133 equivalent hydraulic diameters downstream of the test-section entrance, and 2.5cm from the end of the triangular duct. Pitot tube measurements by Gerrard[1] indicated that end effects on the mean axial velocity field penetrated only about 1cm. To prevent any blockage effect due to the probe holder and the traversing mechanism, the probe holder was entirely outside the duct for the position chosen. Hot wire measurements in the present work confirmed the above conclusions. Flow symmetry was also tested by Gerrard[1] at both mean velocity and turbulence levels. His measurements and discussion indicated that the flow at the test station was, for all practical purposes, symmetric. The importance of having achieved this condition is obvious. It in turn also meant that comprehensive measurements could be confined to one primary flow cell.

Detailed measurements were conducted at a Reynolds number of 53000. Hot wire measurements of Reynolds stresses were made at 150 locations constituting the nodes of a grid covering the test flow cell and is presented in figure (5.1). This grid was regular except for additional points near the wall, and included points on the symmetry line boundaries. For secondary velocity components, measurements were made only along certain vertical (for $\bar{V}$) and horizontal (for $\bar{W}$) lines rather than at all points in the grid. Detailed measurements of mean axial velocities, local wall shear stress distribution and axial pressure distribution at different

Reynolds numbers were available through Gerrard.[1]

5.2 Reynolds Stresses

Measurements of $\sqrt{\overline{v^2}}$, $\sqrt{\overline{w^2}}$, $\overline{uv}$ and $\overline{uw}$ were corrected for tangential cooling effects as suggested by Lawn.[78] The absolute accuracy of the experimental data is not known, due to the complexity of the hot wire anemometry system, however, based on repeatability (of the same probe or different probes or combination thereof), it is estimated that trend line accuracies are within about 3% for the normal stresses and about 10% for $\overline{uw}$. No figure is offered for $\overline{uv}$ as its values were very small over much of the flow cell, and its measurement was found to be very sensitive to probe alignment, channel match and wire cleanliness.

Contour plots of constant normal stresses and mean turbulent kinetic energy are presented in figures (5.2 to 5.5) inclusive where the results have been normalized by the average friction velocity. These plots clearly indicate the effects of convection of turbulent kinetic energy by secondary flows. In general, as is usual, turbulence levels are highest near the wall where the turbulence is produced and lowest near the duct centerline. But distortions similar to the bulges observed[1] in the mean velocity field, are evident. The low turbulence region extends far into the corner while the high turbulence region bulges outwards from the midpoint of the wall, thereby, indicating a clockwise circulation of secondary flow. In figure (5.6), a comparison of the distributions of $\sqrt{\overline{u^2}}/u^*$, $\sqrt{\overline{v^2}}/u^*$ and $\sqrt{\overline{w^2}}/u^*$ along the midwall bisector is given. It is clear that velocity fluctuations parallel to the wall generally exceed those normal to the wall, although the two components have equal magnitudes in the central region of the duct. The latter considered in conjunction

with the circular shape of the contours of constant $\sqrt{\overline{v^2}}/U^*$ and $\sqrt{\overline{w^2}}/U^*$ near the duct axis indicates that there is a small core region in which the transverse velocity fluctuations are essentially independent of orientation. This feature is consistent with the results of Laufer[79] for pipe flow and the measurements of Brundrett and Baines[8] for a square duct. The anisotropy of the distributions of $\sqrt{\overline{v^2}}$ and $\sqrt{\overline{w^2}}$ was reported by the latter investigators to be responsible for the generation of secondary flows in the plane of the cross-section of the duct. The distributions of turbulence intensities along normals to the wall are compared further with pipe and square duct flows in figures (5.7 - 5.10) inclusive. In the central region, the normalized values are generally somewhat higher than for pipe flow (mainly for $\sqrt{\overline{u^2}}/U^*$ and $\sqrt{\overline{w^2}}/U^*$) but lower than for a square duct.

Near the wall, the intensities of $\sqrt{\overline{v^2}}/U^*$ and $\sqrt{\overline{w^2}}/U^*$ deviate further from the pipe flow distribution, but approach the distribution for a square duct. Very close to the wall, the distributions for the triangular duct tend to peak closer to the wall than the peaks in pipe flow. Cremers and Eckert[25] found that similar peaks occur for the corresponding velocity fluctuations to $\sqrt{\overline{v^2}}/U^*$ in a narrow isosceles triangle.

Qualitative findings similar to the above discussion were reported by Gerrard[1], but the levels of his turbulence measurements were slightly different from this work as shown in figures (5.11) for the normalized turbulent kinetic energy along the midwall bisector. Further differences are discussed in conjunction with shear stresses measurements.

The contours of constant $(\overline{v^2} - \overline{w^2})/(U^*)^2$ are presented in figure (5.12). They are qualitatively similar to the contours given by Brundrett

and Baines[8] for a square duct. The steep gradients in the corner region indicate high vorticity production in this region. Vorticity production contours based on the normal stresses are presented in figure (5.13). It should be mentioned here that the results of differentiation after subtraction were smoothed to provide a monotonic decrease from the maximum value near the corner to the necessarily zero value on the boundaries. This necessitated ignoring some small positive values which were obtained in the central region of the flow cell. The numerical error introduced in this process affected the accuracy of the first prediction model.

Concerning the two measured shear stresses, the contours of $\overline{uv}$ presented in figure (5.14) show that $\overline{uv}$ was generally smallest in the midwall region and largest in the corner region and along the corner bisector. An unusual feature of the distribution is the region of small negative $\overline{uv}$ near the midwall bisector. Although these negative values are conceded to be comparable in magnitude to the precision limit, repeated measurements consistently indicated a distinct sign change when the probe entered this region. Brundrett and Baines[8] observed that the corresponding stress in the square duct flow also changes sign within a primary flow cell. It is also noted that measurements showed that $\overline{uv}$ (like $\bar{V}$) has an antisymmetric* distribution about the z-axis. It is, therefore logical that $\overline{uv}$ be zero on the midwall bisector, and this was basically substantiated by the measurements. This conclusion is contrary to that of Gerrard[1] who reported that the $\overline{uv}$ contours straddle the midwall bisector.

---

*Of course, if the X-probe is rotated $180°$ upon passing through the boundary into the adjoining flow cell, then $\overline{uv}$ appears symmetric (as would $\bar{V}$) since the y-direction is effectively reversed.

Contour plots of $\overline{uw}$ are shown in figure (5.15). The distribution is basically as expected. It may be noted that z-direction gradients in $\overline{uw}$ are much larger in the corner region than in the midwall region. Gerrard[1] has examined the x-momentum balance (equation 3.5) along the midwall bisector. The $\overline{uw}$ gradient was found to be dominant in the central region of the duct. The pertinent $\overline{uv}$ gradient also contributed significantly to the balance here. However, nearer the wall, the predominate term was indicated to be convection of axial momentum by $\bar{W}$.

5.3 Secondary Velocities

As discussed earlier (Section 4.5), measurements of the transverse components of velocity were made only for certain points rather than at all points in the grid. This technique eliminated errors due to relative channel drift of the X-probe and maintained repeatability to within about 15%. The results for $\bar{V}$ are shown in figure (5.16). The two probes differed most near the corner bisector. This was probably due to the influence of the two near walls. The results for $\bar{W}$ are shown in figure (5.17). From this distribution and figure (5.16), it is evident that the actual secondary flow is a single cell of clockwise rotation. Fluid is directed from the center of the duct to the corner via a path parallel and adjacent to the corner bisector. The results indicate that the maximum secondary velocity occurs in the return flow along the wall where $\bar{V}$ attains a value of about 1 1/2% of the bulk velocity. Secondary velocities are discussed further in conjunction with predicted results. Concerning comparison between experimental and predicted results for $\bar{V}$, the X-probe results were used as the basis for comparison, except for the station nearest to the corner.

CHAPTER 6

THE ANALYTICAL MODELS

6.1. General

Assuming a steady state, incompressible, constant properties and fully developed turbulent flow, and neglecting body forces, the momentum and continuity equations given in Chapter 3 can be reduced to a set of three transport equations for axial momentum, vorticity and stream function. In the first model, the vorticity production term based on the normal stresses is calculated from empirical correlations of the experimental data. In the second model, the vorticity production is calculated from algebraic approximations of the transport equations for the turbulent intensities by expressing the turbostresses in the plane of the cross section by gradients in the axial velocity field.

The pressure gradients in equations (3.1) and (3.2) may be eliminated by differentiating (3.1) with respect to z and (3.2) with respect to y, and subtracting one from the other. Using the definitions of ψ and ω given from (3.8) and (3.9), the resulting equation is

$$\frac{\partial}{\partial y}\left(\omega \frac{\partial \psi}{\partial z}\right) - \frac{\partial}{\partial z}\left(\omega \frac{\partial \psi}{\partial y}\right) - \frac{\partial}{\partial y}\left[\frac{\partial(\mu\omega)}{\partial y}\right] - \frac{\partial}{\partial z}\left[\frac{\partial(\mu\omega)}{\partial z}\right]$$

$$- \rho \frac{\partial^2(\overline{v^2} - \overline{w^2})}{\partial y\, \partial z} + \rho\left(\frac{\partial^2 \overline{vw}}{\partial y^2} - \frac{\partial^2 \overline{vw}}{\partial z^2}\right) = 0 \qquad (6.1)$$

The vorticity and stream function (hence secondary velocities) fields for the triangular duct geometry may now be obtained by solving (3.10) and (6.1) providing the distributions of $\overline{v^2}$, $\overline{w^2}$ and $\overline{vw}$ are known.

6.2. Model I: Eddy Viscosity Model

This model depends on an experimental input to the vorticity production terms in equation (6.1), and an eddy viscosity model. Since $\overline{vw}$ was not measured, only the vorticity production term involving normal stresses could be quantized. However, for the square duct case, Brundrett and Baines[8] reported that the contribution of the $\overline{vw}$ term was negligible since $\overline{vw}$ was much smaller than $(\overline{v^2} - \overline{w^2})$ and its second order derivatives tended to be self-cancelling. The first prediction model assumed this situation also applied to the triangular duct, but as shown later, this assumption leads to certain discrepancies in predicting secondary velocities.

For the axial velocity prediction, assuming the eddy viscosity (μt) to be locally isotropic, equation (3.3) may be written as:

$$\rho(\bar{V}\frac{\partial \bar{U}}{\partial y} + \bar{W}\frac{\partial \bar{U}}{\partial z}) = -\frac{\partial \bar{P}}{\partial x} + \frac{\partial}{\partial y}(\mu_e \frac{\partial \bar{U}}{\partial y}) + \frac{\partial}{\partial z}(\mu_e \frac{\partial \bar{U}}{\partial z}) \qquad (6.2)$$

where the effective viscosity μ_e is define by:

$$\mu_e = \mu + \mu_t \qquad (6.2a)$$

and the eddy viscosity is defined by:

$$\rho\,\overline{uv} = -\mu_t \frac{\partial \bar{U}}{\partial y} \quad ,$$

$$\rho\,\overline{uw} = -\mu_t \frac{\partial \bar{U}}{\partial z} \quad . \qquad (6.2b)$$

An interpretation of μ_t may be given by:

$$\frac{\mu_t}{\mu} = -\frac{R_{ij}\,S_{ij}}{2\nu S_{mn}S_{mn}} \quad ,$$

the numerator $\equiv$ rate of production of turbulent energy,

the denominator ≡ rate of dissipation of mechanical energy by the mean flow field.

Substituting (3.9) into (6.2) yields:

$$\frac{\partial}{\partial y}(\bar{U}\frac{\partial \psi}{\partial z}) - \frac{\partial}{\partial z}(\bar{U}\frac{\partial \psi}{\partial y}) - \frac{\partial}{\partial y}(\mu_e \frac{\partial \bar{U}}{\partial y}) - \frac{\partial}{\partial z}(\mu_e \frac{\partial \bar{U}}{\partial z}) + \frac{\partial \bar{P}}{\partial x} = 0 \qquad (6.3)$$

This equation was used to obtain the mean axial velocity distribution based on the converged solution for stream function, the appropriate value (constant) of $\partial\bar{P}/\partial x$[1] and the Van Driest[80] eddy viscosity. The latter, written in terms of effective viscosity, is:

$$\mu_e = \mu[0.5 + 0.5\sqrt{1 + 4K^2(z^+)^2\{1 - \exp(-z^+/A^+)\}^2} \qquad (6.4)$$

where K is a mixing length constant, $z+$ is given by:

$$z^+ = \frac{z\sqrt{\tau/\rho}}{\nu} \qquad (6.4a)$$

Values of $K = 0.4$ and $A^+ = 26$ were used in (6.4). The difficulty associated with this model was a result of the large error in calculating the vorticity production term, since it represents a small quantity obtained by the differences of large quantities, each containing certain experimental error. Obviously, the resulting gradients will also be uncertain and need smoothing to have the shape of figure (5.13).

6.3. Model II: One Equation Statistical Model

Ideally, a numerical prediction scheme should require only basic specifications of the flow, i.e., duct geometry, flow medium, and bulk velocity or Reynolds number. The principal aim of the second prediction model was therefore to eliminate empirical input. For the vorticity production terms in equation (6.1), Launder and Ying[2] have rationalized employing the following simple equations for the Reynolds stresses:

$$\overline{v^2} - \overline{w^2} = - C\ell^2 [(\frac{\partial \bar{U}}{\partial y})^2 - (\frac{\partial \bar{U}}{\partial z})^2] \, , \tag{6.5}$$

$$\overline{vw} = -C\ell^2 \, (\frac{\partial \bar{U}}{\partial y})(\frac{\partial \bar{U}}{\partial z}) \, , \tag{6.6}$$

where,

$$C = \frac{C_\nu}{C_D} \cdot \frac{2[6C_2 - 2]}{11[C_1 - 2C_2]} \, ,$$

with C_1 and C_2 as constants, ℓ is a geometrically calculated turbulence length scale. The latter was calculated from the geometric formula suggested by Buleev[62] and given by:

$$\frac{1}{\ell} = \frac{1}{2} \int_o^{2\pi} \frac{d\theta}{S} \, , \tag{6.7}$$

where S is the distance from point P to the wall and the angle θ is defined in figure (6.1). Integrating (6.7) yielded:

$$\frac{1}{\ell} = \frac{1}{2z_1} (\sin \alpha + \sin \eta) + \frac{1}{2z_2} (\sin \beta + \sin \gamma)$$

$$+ \frac{1}{2z_3} (\sin \delta + \sin \xi) \, , \tag{6.8}$$

where the notation is explained in figure (6.1). (See Appendix A for details). The closed form (6.8) was used to calculate the turbulence length scale for each node.

By modelling the Reynolds stresses in (6.1) via (6.5) and (6.6), it was possible in principle to solve (3.10), (6.1) and (6.3) to obtain the flow characteristics. However, an eddy viscosity model was still required, and although this presented no substantial handicap, it was fundamentally preferable to employ the Prandtl-Kolmogorov formula:

$$\mu_t = \rho \, C_\nu (k)^{\frac{1}{2}} \, \ell \tag{6.9}$$

which interrelates local values of eddy viscosity and turbulence length scale through the local mean turbulent kinetic energy k given by $k = (\overline{u^2} + \overline{v^2} + \overline{w^2})/2$, and the proportionality constant C_ν. Similar to (6.2b), assuming that:

$$\rho \overline{vk'} = - \Gamma_k \frac{\partial k}{\partial y}$$

$$\rho \overline{wk'} = - \Gamma_k \frac{\partial k}{\partial z}$$

the rather widely used form:

$$\frac{\partial}{\partial y}(k \frac{\partial \psi}{\partial z}) - \frac{\partial}{\partial z}(k \frac{\partial \psi}{\partial y}) - \frac{\partial}{\partial y}[(\mu + \frac{\mu_t}{\sigma_k})\frac{\partial k}{\partial y}] - \frac{\partial}{\partial z}[(\mu + \frac{\mu_t}{\sigma_k})\frac{\partial k}{\partial z}]$$

$$- \mu_t [(\frac{\partial \bar{U}}{\partial y})^2 + (\frac{\partial \bar{U}}{\partial z})^2] + \frac{\rho C_D (k)^{3/2}}{\ell} = 0 \qquad (6.10)$$

was then used for the additional auxiliary equation for k. In the above equation the exchange coefficient of the kinetic energy of the fluctuating motion Γ_k is replaced by (μ_t/σ_K). This approximation is a result of assuming that the diffusion of turbulent kinetic energy is produced by eddies with approximately the same scales of motion of those which promote momentum transfer.

The final computation scheme required solutions to equations (3.10), (6.1) (with 6.5, 6.6, 6.8), (6.10) (with 6.8 and 6.9), and (6.3) (with 6.8 and 6.9). Values used for the various constants were the following:

$C_1 = 2.93$

$C_2 = 0.355$

$C_\nu = 0.22$

$C_D = 0.39$

$\sigma_K = 1.5$

With the exception of C_1 and C_2 these values were the same as those used by Launder and Ying[2] for the square duct. The values of C_1 and C_2 were chosen to give $C = 0.006$, which was found to give the best fit to the experimental measurements of $\bar{U}$, $\bar{V}$ and $\bar{W}$.

The heat transfer characteristics of the flow were obtained by solving the enthalpy conservation equation which may be written as:

$$\frac{\partial}{\partial y}(\bar{H}\frac{\partial \psi}{\partial z}) - \frac{\partial}{\partial z}(\bar{H}\frac{\partial \psi}{\partial y}) = \frac{\mu}{\sigma_h}\{\frac{\partial^2 \bar{H}}{\partial y^2} + \frac{\partial^2 \bar{H}}{\partial z^2}\} - \rho\frac{\partial}{\partial y}\overline{hv} - \rho\frac{\partial}{\partial z}\overline{hw} \qquad (6.11)$$

The turbulent enthalpy flux terms were approximated by:

$$-\overline{hv} = \frac{\mu_t}{\rho\,\sigma_{h,t}}\frac{\partial \bar{H}}{\partial y} \qquad (6.11a)$$

$$-\overline{hw} = \frac{\mu_t}{\rho\,\sigma_{h,t}}\frac{\partial \bar{H}}{\partial z} \qquad (6.11b)$$

where $\sigma_{h,t}$ is the turbulent Prandtl number whose value was assumed equal to 0.9.

6.4. Boundary Conditions

Regarding boundary conditions, the stream function is constant along all three boundaries; this constant was conveniently taken to be zero. The vorticity is zero at the two symmetry line boundaries. Near the solid wall, the vorticity was assumed to vary linearly with normal distance from the wall. Along the corner and midwall bisectors, the normal-to-boundary gradients of the mean axial velocity (also k and $\bar{H}$ for model II) were set to zero as is demanded by symmetry. These conditions may be written as:

a) Midwall bisector:

$$\frac{\partial \bar{U}}{\partial y} = 0 \,, \qquad (6.12a)$$

$$\frac{\partial k}{\partial y} = 0 \ , \tag{6.12b}$$

$$\frac{\partial \bar{H}}{\partial y} = 0 \ . \tag{6.12c}$$

b) Corner bisector:

$$\frac{\partial \bar{U}}{\partial n} = 0 \ , \tag{6.13a}$$

$$\frac{\partial k}{\partial n} = 0 \ , \tag{6.13b}$$

$$\frac{\partial \bar{H}}{\partial n} = 0 \ . \tag{6.13c}$$

where n is the normal distance to the corner bisector. Near a solid wall, the mesh of the numerical procedure should be very fine to account for the large gradients of the velocity and turbulent kinetic energy in the z-direction. On the other hand, the coefficients of the analytical model are assigned certain values, and assumed to be constants based on the assumption that the corresponding nodes are outside the wall sublayer and in the fully turbulent region. Since inside the wall sublayer, convection of momentum is small, it is convenient to assume that the velocity profile in the region close to the wall could be represented accurately by a law of the wall. This assumption will allow a large mesh to give good prediction and also less expensive solution in terms of computer time. Gerrard[1] proved experimentally that the law of the wall holds for the equilateral triangular duct for z^+ up to 1000, if the local wall shear stress was used in the equation.

For both models, a boundary condition for mean axial velocity was imposed on the first string of nodes in the fluid immediately adjacent to the wall. The grid was designed to have these nodes located beyond the

wall sublayer for the Reynolds number range involved. The $\bar{U}$ boundary condition was the familiar form:

$$\bar{U} = \sqrt{\tau/\rho}\ [A\ \ell n\ (Ez^{+})] \tag{6.14}$$

with values of A and E of 2.5 and 7.69 respectively. For model II, a boundary condition for turbulent kinetic energy was also imposed at these same nodes. This was of the form:

$$k = \tau/(\rho^{2}\ C_{\nu}\ C_{D})^{\frac{1}{2}} \tag{6.15}$$

This boundary condition is obtained from the limiting form of the kinetic energy equation with convection and diffusion neglected compared to generation and dissipation near the wall[2].

The heat transfer field of the flow was solved at different Reynolds numbers for the case of a uniform average circumferential heat flux along the duct, and a uniform circumferential temperature distribution at any station. A semi logarithmic boundary condition law for the enthalpy was imposed on the first string of nodes in the fluid. This was of the form:

$$\bar{H} - \bar{H}_{w} = \frac{\dot{q}''\ \sigma_{h,t}}{\sqrt{\rho\tau}}\ [\bar{U}/\sqrt{\frac{\tau}{\rho}} + P^{*}] \tag{6.16}$$

where P^{*} is the Jayatilleke[81] "P-function" which accounts for the enhanced resistance to heat or mass transfer offered by the viscous sublayer and is given by:

$$P^{*} = 9.24[(\sigma_{h}/\sigma_{h,t})^{3/4} - 1] \tag{6.17}$$

6.5. Summary of the Equations to be Solved

The equations relevant to Model II only are presented here.

6.5.1. Transport Equations

a) Axial momentum equation

$$\frac{\partial}{\partial y}(\bar{U}\frac{\partial \psi}{\partial z}) - \frac{\partial}{\partial z}(\bar{U}\frac{\partial \psi}{\partial y}) - \frac{\partial}{\partial y}(\mu_e \frac{\partial \bar{U}}{\partial y}) - \frac{\partial}{\partial z}(\mu_e \frac{\partial \bar{U}}{\partial z}) + \frac{\partial P}{\partial x} = 0 \qquad (6.18)$$

b) Stream function equation

$$-\frac{\partial}{\partial y}(\frac{1}{\rho}\frac{\partial \psi}{\partial y}) - \frac{\partial}{\partial z}(\frac{1}{\rho}\frac{\partial \psi}{\partial z}) - \omega = 0 \qquad (6.19)$$

c) Vorticity equation

$$\frac{\partial}{\partial y}(\omega\frac{\partial \psi}{\partial z}) - \frac{\partial}{\partial z}(\omega\frac{\partial \psi}{\partial y}) - \frac{\partial}{\partial y}[\frac{\partial(\mu\omega)}{\partial y}] - \frac{\partial}{\partial z}[\frac{\partial(\mu\omega)}{\partial z}] - \rho\frac{\partial^2(\overline{v^2} - \overline{w^2})}{\partial y\,\partial z}$$

$$+ \rho(\frac{\partial^2 \overline{vw}}{\partial y^2} - \frac{\partial^2 \overline{vw}}{\partial z^2}) = 0 \qquad (6.20)$$

d) Turbulent kinetic energy equation

$$\frac{\partial}{\partial y}(k\frac{\partial \psi}{\partial z}) - \frac{\partial}{\partial z}(k\frac{\partial \psi}{\partial y}) - \frac{\partial}{\partial y}[(\mu + \frac{\mu_t}{\sigma_k})\frac{\partial k}{\partial y}] - \frac{\partial}{\partial z}[(\mu + \frac{\mu_t}{\sigma_k})\frac{\partial k}{\partial z}]$$

$$- \mu_t[(\frac{\partial \bar{U}}{\partial y})^2 + (\frac{\partial \bar{U}}{\partial z})^2] + \frac{\rho\, C_D (k)^{3/2}}{\ell} = 0 \qquad (6.21)$$

e) Enthalpy equation

$$\frac{\partial}{\partial y}(\bar{H}\frac{\partial \psi}{\partial z}) - \frac{\partial}{\partial z}(\bar{H}\frac{\partial \psi}{\partial y}) - \frac{\mu}{\sigma_h}\{\frac{\partial^2 \bar{H}}{\partial y^2} + \frac{\partial^2 \bar{H}}{\partial y^2}\} - \rho\frac{\partial}{\partial y}\overline{hv} - \rho\frac{\partial}{\partial z}\overline{hw} = 0 \qquad (6.22)$$

with

$$-\overline{hv} = \frac{\mu_t}{\rho\,\sigma_{h,t}}\frac{\partial \bar{H}}{\partial y}\ ;\ -\overline{hw} = \frac{\mu_t}{\rho\,\sigma_{h,t}}\frac{\partial \bar{H}}{\partial z} \qquad (6.23)$$

6.5.2. Algebraic Equations

a) Turbulent viscosity

$$\mu_t = \rho\, C_\nu (k)^{\frac{1}{2}}\, \ell \tag{6.24}$$

b) Turbulence Length Scale Distribution

$$\frac{1}{\ell} = \frac{1}{2z_1}(\sin\alpha + \sin\eta) + \frac{1}{2z_2}(\sin\beta + \sin\gamma) + \frac{1}{2z_3}(\sin\delta + \sin\xi) \tag{6.25}$$

c) Reynolds stresses

$$\overline{v^2} - \overline{w^2} = -C\ell^2\left[\left(\frac{\partial\bar{U}}{\partial y}\right)^2 - \left(\frac{\partial\bar{U}}{\partial z}\right)^2\right],$$

$$\overline{vw} = -C\ell^2\left(\frac{\partial\bar{U}}{\partial y}\right)\left(\frac{\partial\bar{U}}{\partial z}\right) \tag{6.26}$$

where

$$C = \frac{C_\nu}{C_D} \cdot \frac{2(6C_2 - 2)}{11(C_1 - 2C_2)} \tag{6.27}$$

d) Source term for axial momentum equation

$$\partial P/\partial X = 4\tau_W/D_h \tag{6.28}$$

where

$$D_h = 2H \tag{6.29}$$

e) Friction factor

$$f = 8\tau_W/(\rho\, U_b^{\,2}) \tag{6.30}$$

f) Average wall shear stress

$$\tau_W = \frac{1}{L}\int_o^L \tau\, dy \tag{6.31}$$

6.5.3. Boundary Conditions

a) Wall boundary conditions

$$\psi = 0 \tag{6.32a}$$

$$\omega_p = \omega_n + \frac{(X_p - X_n)(\omega_m - \omega_n)}{X_m - X_n} \tag{6.32b}$$

where P is the wall node, n is the node next to the wall, and m is the node twice removed from the wall in the z-direction.

$$\bar{U} = \sqrt{\tau/\rho}\ [A\ \ell n(EZ^+)] \tag{6.33}$$

$$k = \tau/(\rho^2\ C_\nu\ C_D)^{\frac{1}{2}} \tag{6.34}$$

$$\bar{H} - \bar{H}_W = (\dot{q}''\ \sigma_{h,t}/\sqrt{\rho\tau})\ [\bar{U}/\sqrt{\tau/\rho} + P^*] \tag{6.35}$$

where τ is calculated from equation (7.28) as shown in the numerical procedure.

b) Mid-wall bisector

$$\psi = \omega = 0 \tag{6.36}$$

$$\frac{\partial \bar{U}}{\partial y} = \frac{\partial k}{\partial y} = \frac{\partial \bar{H}}{\partial y} = 0 \tag{6.37}$$

c) Corner bisector

$$\psi = \omega = 0 \tag{6.38}$$

$$\frac{\partial \bar{U}}{\partial n} = \frac{\partial k}{\partial n} = \frac{\partial \bar{H}}{\partial n} = 0 \tag{6.39}$$

4.5.4. Constants of the model

$C_\nu = 0.22$, $C_D = 0.39$, $C_1 = 2.93$, $C_2 = 0.355$, $C = 0.006$, $\sigma_K = 1.5$, $A = 2.5$ and $E = 7.69$

CHAPTER 7

THE NUMERICAL PROCEDURE

7.1. Introduction

The general form of equations (6.18 - 6.22) may be written in the form:

$$A \frac{\partial}{\partial y}(\phi \frac{\partial \psi}{\partial z}) - A \frac{\partial}{\partial z}(\phi \frac{\partial \psi}{\partial y}) - \frac{\partial}{\partial y}[B \frac{\partial}{\partial y}(C \phi)]$$

$$- \frac{\partial}{\partial z}[B \frac{\partial}{\partial z}(C \phi)] + D = 0 . \qquad (7.1)$$

The new symbols in this standard elliptic form are identified for each equation in Table 1. In order to solve these equations numerically, the equations must be integrated over finite areas in the primary flow cell. Assumptions for the distributions of the variables between the nodes of the grid are required. The procedure must obey continuity requirements within the accuracy of the assumptions made. For both models, an upwind finite difference technique based on the general elliptic procedure of Gosman et al[39] was used with a Cartesian grid covering the same primary flow cell in which measurements were made (figure 3.1). This grid constituting of an irregular 31 x 31 mesh, is described in Table 2, and presented in figure (7.1). The nodes are closely spaced near the wall and corner region where the variables have steep gradients. Nodes on the corner bisector were achieved by maintaining the spacing of nodes in the two directions in the ratios of $\sqrt{3}$: 1. This grid is a modification of the experimental one presented in figure (5.1). It included extra nodes close to the walls and in the internal flow field. This was necessary for accurate numerical differentiation of the vorticity source term. The

31 x 31 grid is considered more than adequate in regard to accuracy of the numerical solution. Much coarser grids have been satisfactorilly employed by others; e.g. 11 x 11 by Launder and Ying[2] and 15 x 15 by Gerard [56] for a quadrant of a square duct. The fine grid used in this work also reduces false diffusion which results from the truncation error associated with the finite difference scheme. Part of the finite difference grid is shown in figure (7.2) with the dashed lines enclosing the domain in which the equations will be integrated.

To integrate equation (7.1), multiplying by dy dz, using the coefficients of Table 1, and integrating over the domain shown in figure (7.2) yields:

$$a_\phi \int_{z,s}^{z,n} \int_{y,w}^{y,e} \{\frac{\partial}{\partial y}(\phi \frac{\partial \psi}{\partial z}) - \frac{\partial}{\partial z}(\phi \frac{\partial \psi}{\partial y})\, dy\, dz$$

convection terms = I_c

$$- \int_{z,s}^{z,n} \int_{y,w}^{y,e} \{\frac{\partial}{\partial y}(\frac{\partial \mu\phi}{\partial y}) + \frac{\partial}{\partial z}(\frac{\partial \mu\phi}{\partial z})\} dy\, dz$$

diffusion terms = I_d

$$= \int_{z,s}^{z,n} \int_{y,w}^{y,e} D\ dy\, dz \ . \qquad (7.2)$$

source term = I_s

Equation (7.2) may be written in the simple form:

$$a_\phi I_c - I_d = I_s \ . \qquad (7.2a)$$

The integrals appearing in (7.2) are evaluated in the following sub-sections.

7.2. Convection Terms

Before integrating the convection terms, the following assumptions are considered to hold:

a) The function ϕ is uniform within each rectangle and has the value of node P.

b) The value of the stream function at a particular corner of the rectangle is equal to the average of the values on the four neighbouring nodes.

c) The average value of the function must take the value possessed by the fluid upstream of the specific face under consideration (upwind technique).

The convection terms of equation (7.2) can be integrated to give:

$$I_c = \int_{z,s}^{z,n} \{\phi_e (\frac{\partial \psi}{\partial z})_e - \phi_w (\frac{\partial \psi}{\partial z})_w\} dz$$

$$- \int_{y,w}^{y,e} \{\phi_n (\frac{\partial \psi}{\partial y})_n - \phi_s (\frac{\partial \psi}{\partial y})_s\} dy \quad , \qquad (7.3)$$

which in turn may be broken to four separate integrals. The first only will be considered since the others are exactly similar.

$$I_{c_1} = \int_{z,s}^{z,n} \phi_e (\frac{\partial \psi}{\partial z})_e \, dz \quad . \qquad (7.4)$$

For well-behaved functions for ϕ and ψ there exists an average value of ϕ_e which is $\bar{\phi}_e$ such that:

$$\bar{\phi}_e = \frac{\int_{z,s}^{z,n} \phi_e (\frac{\partial \psi}{\partial z})_e \, dz}{\int_{z,s}^{z,n} (\frac{\partial \psi}{\partial z})_e \, dz} \approx \frac{I_{c_1}}{(\psi_{ne} - \psi_{se})} \quad . \qquad (7.5)$$

Hence I_{c_1} can be written in the form:

$$I_{c_1} = \bar{\phi}_e \, (\psi_{ne} - \psi_{se}) \quad . \tag{7.6}$$

Regarding the above stated assumptions, $\bar{\phi}_e$, ψ_{ne} and ψ_{se} can be expressed in terms of values of the variables at the nodes of the grid.

Applying the upwind difference concept into equation (7.6) means that if the difference $(\psi_{ne} - \psi_{se})$ is positive, the direction of the flow will be from the point (P) to the point (E) and so the property ϕ_p has predominance at point e, and $\bar{\phi}_e$ is assumed to be equal to ϕ_p. On the other hand, if the difference is negative the flow will be from (E) to (P) and $\bar{\phi}_e$ will take the value at point E. Hence, I_c will take the form:

$$I_c \approx \phi_E \left\{\frac{(\psi_{ne} - \psi_{se}) - |\psi_{ne} - \psi_{se}|}{2}\right\} + \phi_p \left\{\frac{(\psi_{ne} - \psi_{se}) + |\psi_{ne} - \psi_{se}|}{2}\right\} . \tag{7.7}$$

Making use of assumption (b) one can write

$$\psi_{se} \approx \frac{\psi_{SE} + \psi_E + \psi_P + \psi_S}{4} \quad . \tag{7.8}$$

The other terms can be obtained by a similar treatment for each one. Assembling and rearranging the results gives:

$$I_c = A_E(\phi_P - \phi_E) + A_W(\phi_P - \phi_W) + A_N(\phi_P - \phi_N) + A_S(\phi_P - \phi_S), \tag{7.9}$$

where the coefficients A, using (7.8), are:

$$\begin{aligned}
A_E &= \tfrac{1}{8}\{(\psi_{SE} + \psi_S - \psi_{NE} - \psi_N) + |\psi_{SE} + \psi_S - \psi_{NE} - \psi_N|\} \, , \\
A_W &= \tfrac{1}{8}\{(\psi_{NW} + \psi_N - \psi_{SW} - \psi_S) + |\psi_{NW} + \psi_N - \psi_{SW} - \psi_S|\} \, , \\
A_N &= \tfrac{1}{8}\{(\psi_{NE} + \psi_E - \psi_{NW} - \psi_W) + |\psi_{NE} + \psi_E - \psi_{NW} - \psi_W|\} \, , \\
\text{and} \quad A_S &= \tfrac{1}{8}\{\psi_{SW} + \psi_W - \psi_{SE} - \psi_E + |\psi_{SW} + \psi_W - \psi_{SE} - \psi_E|\} \, ,
\end{aligned} \tag{7.10}$$

Special provision is made in the computer program to deal with points near the corner bisector.

7.3. Diffusion Terms

The diffusion terms of equation (7.2) can be integrated to give:

$$I_d = -\left[\int_{z,s}^{z,n} \{(\frac{\partial \mu\phi}{\partial y})_e - (\frac{\partial \mu\phi}{\partial y})_w\} dz - \int_{y,w}^{y,e} \{(\frac{\partial \mu\phi}{\partial z})_n - (\frac{\partial \mu\phi}{\partial z})_s\} dy\right] . \tag{7.11}$$

Since this term can be broken to four similar terms, integration of only the first one will be performed which is:

$$I_{d_1} = \int_{z,s}^{z,n} \frac{\partial}{\partial y} (\mu\phi)_e \, dz \, .$$

Assuming that $(\mu\phi)$ varies linearly with y in the domain, the integration will be:

$$I_{d_1} = \frac{\mu_E \phi_E - \mu_P \phi_P}{y_E - y_P} \cdot \frac{z_N - z_S}{2} \, . \tag{7.12}$$

Integrating the other terms, assembling and arranging yields:

$$I_d = B_E(\mu_E \phi_E - \mu_P \phi_P) + B_W(\mu_W \phi_W - \mu_P \phi_P)$$

$$+ B_N(\mu_N \phi_N - \mu_P \phi_P) + B_S(\mu_S \phi_S - \mu_P \phi_P) \, .$$

where

$$B_E = \frac{1}{2} \frac{z_N - z_S}{y_E - y_P} \, ,$$

$$B_W = \frac{1}{2} \frac{z_N - z_S}{y_P - y_W} \, ,$$

$$B_N = \frac{1}{2} \frac{y_E - y_W}{z_N - z_P} \, , \tag{7.13}$$

$$B_S = \frac{1}{2} \frac{y_E - y_W}{z_P - z_S} \, .$$

7.4. Source Terms

To obtain source terms for the different transport equations, the different parameters inside the integrals for each equation will be considered constant within the domain of integration, and assumed to have the value at the specific node under consideration. The validity of this assumption depends mainly on grid size; the finer the better.

a) Source term for vorticity equation

For the vorticity equation, the source term given by equation (7.2) at the node P is:

$$I_{SW}|_P = \int_{z,s}^{z,n} \int_{y,w}^{y,e} d\phi \, dy \, dz \quad , \tag{7.14}$$

where,

$$d\phi = -\rho\{\frac{\partial^2(\overline{v^2} - \overline{w^2})}{\partial y \, \partial z} - (\frac{\partial^2 \overline{vw}}{\partial y^2} - \frac{\partial^2 \overline{vw}}{\partial z^2})\} \quad . \tag{7.15}$$

Integrating equation (7.14) yields:

$$I_{SW}|_P = d\phi_p (\frac{y_E - y_W}{2})(\frac{z_N - z_S}{2}),$$

which may be written in the form

$$I_{SW}|_P = d\phi_p \, V_P \quad , \tag{7.16}$$

where V_P is given by:

$$V_P = (\frac{y_E - y_W}{2})(\frac{z_N - z_S}{2}) \quad . \tag{7.17}$$

For Model I, the values of $(\overline{v^2} - \overline{w^2})$ were taken from the experimental data. In Model II (equation 7.15), the values of $(\overline{v^2} - \overline{w^2})$ and $\overline{vw}$ are given by (6.26).

Assuming that $\Delta = (\overline{v^2} - \overline{w^2})$ and $\Delta_1 = \overline{vw}$, differentiation in the y-direction was obtained by:

$$\frac{\partial \Delta}{\partial y}\Big|_p = \left[\frac{(\Delta_E - \Delta_P)\dfrac{y_P - y_W}{y_E - y_P} + (\Delta_P - \Delta_W)\dfrac{y_E - y_P}{y_P - y_W}}{y_E - y_W}\right], \qquad (7.18)$$

and similarly for $\frac{\partial \Delta_1}{\partial y}\Big|_p$ by replacing Δ with Δ_1. The second derivative in the z-direction was given by:

$$\frac{\partial^2 \Delta}{\partial y\, \partial z}\Big|_p = \frac{(\frac{\partial \Delta}{\partial y}\Big|_N - \frac{\partial \Delta}{\partial y}\Big|_p)\dfrac{z_P - z_S}{z_N - z_P} + (\frac{\partial \Delta}{\partial y}\Big|_p - \frac{\partial \Delta}{\partial y}\Big|_s)\dfrac{z_N - z_P}{z_P - z_S}}{y_E - y_W}. \qquad (7.19)$$

For Model II, shear stress terms were similarly calculated by:

$$\frac{\partial^2 \Delta_1}{\partial y^2}\Big|_p = \frac{(\frac{\partial \Delta_1}{\partial y}\Big|_E - \frac{\partial \Delta_1}{\partial y}\Big|_p)\dfrac{y_P - y_W}{y_E - y_P} + (\frac{\partial \Delta_1}{\partial y}\Big|_P - \frac{\partial \Delta_1}{\partial y}\Big|_W)\dfrac{y_E - y_P}{y_P - y_W}}{y_E - y_W}, \qquad (7.20)$$

$$\frac{\partial^2 \Delta_1}{\partial z^2}\Big|_p = \frac{(\frac{\partial \Delta_1}{\partial z}\Big|_N - \frac{\partial \Delta_1}{\partial z}\Big|_p)\dfrac{z_P - z_S}{z_N - z_P} + (\frac{\partial \Delta_1}{\partial z}\Big|_P - \frac{\partial \Delta_1}{\partial z}\Big|_S)\dfrac{z_N - z_P}{z_P - z_S}}{z_N - z_S}. \qquad (7.21)$$

b) Source term for stream function equation

From the stream function transport equation,

$$I_{SS}|_p = \int_{z,s}^{z,n} \int_{y,w}^{y,e} \omega \, dy \, dz$$

Integrating the equation yields:

$$I_{SS}|_p = \omega_p V_p \qquad (7.22)$$

where V_P is given by equation (7.17).

c) Source term for axial momentum equation

The source term for the axial momentum equation is given by:

$$I_{SU}|_P = - \int_{z,s}^{z,n} \int_{y,w}^{y,e} \frac{\partial P}{\partial x} \, dy \, dz \quad . \tag{7.23}$$

Integrating the equation yields:

$$I_{SU}|_P = - \frac{\partial P}{\partial x} \cdot V_P \quad . \tag{7.24}$$

In the above equation, $\frac{\partial P}{\partial x}$ was calculated from (6.28) for Model II. For Model I, the appropriate constant value were used based on Gerrard[1] experimental measurements.

d) Source term for turbulent kinetic energy equation

For Model II, the source term for the turbulent kinetic energy equation is given by:

$$I_{SK}|_P = \int_{z,s}^{z,n} \int_{y,w}^{y,e} [-\mu_t \{(\frac{\partial \bar{U}}{\partial y})^2 + (\frac{\partial \bar{U}}{\partial z})^2\} + \frac{\rho \, C_D (k)^{3/2}}{\ell}] dy \, dz \quad . \tag{7.25}$$

The integration results may be written as:

$$I_{SK}|_P = [-\mu_{t_P} \{(\frac{\partial \bar{U}}{\partial y})^2 + (\frac{\partial \bar{U}}{\partial z})^2\}|_P + \{\frac{\rho C_D}{\ell_P} (k_P)^{3/2}\}] \cdot V_P \quad . \tag{7.26}$$

where μ_t is given by equation (6.24); the velocity gradients are obtained at the node P by a similar treatment as equations (7.20) and (7.21).

Assembling the convection, diffusion and source terms through equation (7.2) gives for any parameter:

$$\{A_E(\phi_P - \phi_E) + A_W(\phi_P - \phi_W) + A_N(\phi_P - \phi_N) + A_S(\phi_P - \phi_S)\}$$

$$-\{B_E(\mu_E\phi_E - \mu_P\phi_P) + B_W(\mu_W\phi_W - \mu_P\phi_P) + B_N(\mu_N\phi_N - \mu_P\phi_P)$$

$$+ B_S(\mu_S\phi_S - \mu_P\phi_P)\} + I_S = 0 \qquad (7.A)$$

where I_S is given for each equation by the corresponding term from equations (7.15, 7.22, 7.24 and 7.26).

Equation (7.A) gives the value of a certain parameter at the node P as function of the values at the surrounding nodes. Thus, one can write an equation for each variable at every interior node; knowing the boundary conditions, equations as many as the number of unknowns can be written.

The substitution formula in the computer program can be written in the form:

$$\phi_P = (C_E\,\phi_E + C_W\,\phi_W + C_N\,\phi_N + C_S\,\phi_S) + I_S/\Sigma_{AB} \qquad (7.B)$$

where, for constant property fluid (μ = constant),

$$C_E = (A_E + \mu B_E)/\Sigma_{AB} \quad ,$$

$$C_W = (A_W + \mu B_W)/\Sigma_{AB} \quad , \qquad (7.C)$$

$$C_N = (A_N + \mu B_N)/\Sigma_{AB} \quad ,$$

$$C_S = (A_S + \mu B_S)/\Sigma_{AB} \quad ,$$

$$\Sigma_{AB} = A_E + A_W + A_N + A_S + \mu(B_E + B_W + B_N + B_S). \qquad (7.D)$$

The A's and B's are identified by equations (7.10) and (7.13).

7.5. Boundary Conditions

a) Solid wall

On the solid wall, the stream function was set to zero. The vorticity is imposed on the wall as a function of the values at the two subsequent strings of nodes in the flow medium. This expression at a certain node P on the wall can be written as a function of the values at nodes m and n as given by equation (6.32b). For the numerical grid discussed earlier in this chapter, it was found that setting ω to zero on the wall nodes accelerated convergence with nearly identical solutions.

For turbulent kinetic energy, the boundary condition was applied in the first string of nodes in the fluid immediately adjacent to the wall which may be represented by

$$k_B = (\tau)/(\rho^2 C_\nu C_D)^{\frac{1}{2}} \quad . \tag{7.27}$$

The local wall shear stress appearing in equation (7.27) was calculated from the turbulence field data at the second string of nodes in the fluid from:

$$\tau = \rho(C_\nu C_D)^{1/4}(k_2)^{\frac{1}{2}} \bar{U}_2/\left[2.5 \ell n\left\{\frac{7.69\ z_2(C_\nu C_D)^{\frac{1}{4}}(k_2)^{1/2}}{\nu}\right\}\right] , \tag{7.28}$$

where 2 denotes the second string of nodes, k_2 and $\bar{U}_2$ are the values obtained in the previous iteration and z_2 is the normal distance from the wall. The value of τ is then used to update the axial velocity boundary condition by:

$$\bar{U}_B = \sqrt{\tau/\rho}\ [2.5\ \ell n(7.69 z^+_B)] , \tag{7.29}$$

where B denotes the first string of nodes in the fluid. It is obvious

that τ could not be calculated directly from velocity gradients near the wall ($\tau = \mu\, \partial\bar{U}/\partial z$), since the first string of nodes in the fluid is far from the viscous sublayer.

For the enthalpy, equation (6.35) was used with $\bar{H}$ imposed on the first string of nodes in the fluid, $\bar{H}_W$ was given; the values of $\dot{q}''$ and $\bar{U}$ were taken at the same nodes. The appropriate equation is given by:

$$\bar{H} = \bar{H}_W + \frac{\dot{q}''_B\, \sigma_{h,t}}{\sqrt{\rho\tau}} \left[\bar{U}_B/\sqrt{\tau/\rho} + P^*\right] \qquad (7.30)$$

Assuming that ρ and C_P are constants, equations (6.22) and (6.23) may be solved directly for the temperature. In this case, the boundary condition for the temperature is given by:

$$T_B = \bar{T}_W + \frac{\dot{q}''_B\, \sigma_{h,t}}{C_P\, \rho^{3/2}\sqrt{\tau}} \left[\bar{U}_B/\sqrt{\tau/\rho} + P^*\right] \qquad (7.30a)$$

b) Mid-wall bisector

On this boundary, the vorticity and stream function were set to zero on all the nodes. For $\bar{U}$, k and $\bar{H}$, gradients along the normal-to-the midwall bisector were set to zero. This was made by simply assigning the values at nodes on the mid-wall bisector to take the values of adjacent nodes on the normal-to-the boundary direction. This approximation is fairly good only if the mesh is fine enough, otherwise expanding the parameters in Taylor series may be necessary to include the effect of subsequent nodes.

c) Corner bisector

On the corner bisector, the vorticity and steam function were set to zero on the boundary nodes. $\bar{U}$, k and $\bar{H}$ gradients along the normal to the corner bisector were set to zero. Interpolation is necessary in

this case because the $\sqrt{3}$: 1 ratio of the grid does not permit the existence of nodes on the direction normal to the corner bisector. The following figure illustrates the procedure performed.

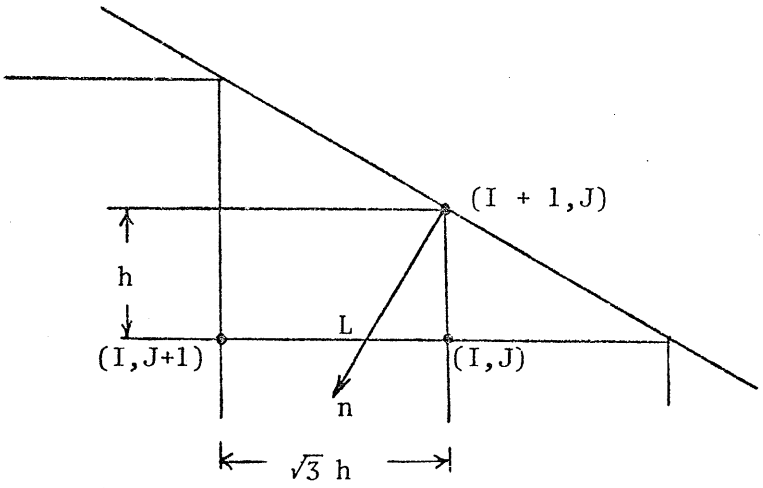

Boundary condition for the node (I + 1, J), can be described in terms of the two nodes (I,J) and (I, J + 1). Assuming linear variation of velocity between the last two nodes, the velocity at point L can be written in the form:

$$U_L = U_{i,j} + (U_{i,j+1} - U_{i,j})/3 \qquad (7.31)$$

To have zero gradient in the n-direction, the following condition was applied:

$$U_{i+1,j} = U_L \qquad (7.32)$$

The same treatment was applied for both k and $\tilde{H}$.

7.6. Iterative Technique

To solve the above transport equations, a point iterative method was used. In this method, the grid is systematically scanned node by node, and row after row in a destructive manner. The different updated para-

meters at a certain node are used immediately for the next node to accelerate the convergence. This method is known as the Gauss Seidel method. It was preferred to use a point iterative method rather than block methods (which require matrix inversion techniques) for its simplicity and ease of organizing the computer program. For the purpose of simplicity also, the coefficients of equation (7.B) and the source terms (except for ψ) were assumed to be given only the values of the parameters from the previous iteration cycle. A provision for over-or under-relaxation is included in the procedure only for the vorticity to compensate for variations in its value that can lead to divergence in some cases. This was taken as:

$$\omega^{n}_{i,j} = \alpha_R \, \omega^{n}_{i,j} + (1 - \alpha_R)\omega^{n-1}_{i,j}$$

where, $\omega^{n}_{i,j}$ is the value at a certain iteration, $\omega^{n-1}_{i,j}$ is the value at the same node in the previous iteration and α_R is the relaxation parameter, with $\alpha_R < 1$ or $\alpha_R > 1$ for under-or over-relaxation respectively. Actually, it was not necessary to use this feature in any of the calculations.

For Model I, solutions for mean axial velocity and local wall shear stress were obtained by stage iteration. The average wall shear stress (τ_W) was calculated from $\partial p/\partial x$ given by Gerrard[1]. The computation began by assigning $\tau = \tau_W$ in (6.4) and (6.31). Following convergence, local values of the wall shear stress were computed at the second string of nodes adjacent to the wall via (6.31) using the computed local $\bar{U}$ values. The revised local τ values were then used to update the $\bar{U}$ boundary condition for the second stage, and the procedure was repeated. Convergence in τ was well-behaved, and was typically achieved

after three or four stages. It was necessary to use this scheme to achieve convergence, since every trial to iterate τ failed because of the effective viscosity model.

For Model II, unlike the Model I calculation involving stage iteration, this time continuously updated values of τ were used immediately within the main iterative procedure. After each iteration step, local values of wall shear stress were computed at the second string of nodes from equation (7.28), using the current computed values of $\bar{U}$ and k. The new τ values were then used to revise the $\bar{U}$ and k boundary conditions via (7.27) and (7.29). It is noted that a similar boundary condition technique has been previously employed by Gosman and Pun[82]. After solving the flow field, the enthalpy equation was solved for the previously identified problem.

Concerning the vorticity source term, it was found that the simple stress model which was proposed by Launder and Ying[2] and used in Model II, produces vorticity production source terms with both positive and negative signs. From the literature review, it was found that the contours of Brundrett and Baines[8] for the same term have only negative signs in a corresponding primary flow cell in a square duct test section. Also, when Gerard[56] applied his finite element technique to the square duct case, he differentiated Brundrett and Baines[8] data using a fine grid, and obtained terms with different signs. To have a montonic change from the maximum value near the corner to the necessarily zero value at the boundaries, he had to smooth the data by replacing the negative sign terms with positive ones. The same procedure was used to smooth the contours presented in figure (5.12) as discussed earlier. Since the production terms in Model II are iterated and not experimentally determined,

smoothing was not possible. Since the secondary flows were found experimentally to be a clockwise swirl (in a primary flow cell with the orientation of figure 3.1), the vorticity production must be of negative sign everywhere. A condition was therefore imposed in the computer program through which a net positive vorticity source term at any node in this specific cell was set to zero in the iteration cycle under consideration in order to accelerate the solution. Convergence was achieved without any relaxation to the vorticity. Predictions were in good agreement with the experimental results right down to the secondary flow levels when the turbulence model constants C_1 and C_2 were optimized to the values presented earlier. These values are related to the above mentioned scheme and should not be used without it, since it became an integral part of the computation scheme. Further discussion and details concerning the vorticity production term are presented in Part II.

7.7. Convergence Criterion

The convergence criterion used was to impose that the maximum fractional change of the parameter ϕ in the field from one cycle of iteration to the next should not exceed a prescribed value. This was of the form:

$$\left| \frac{\phi_{i,j}^{(n)} - \phi_{i,j}^{(n-1)}}{\phi_{i,j}^{(n-1)}} \right|_{max} \leq \lambda \qquad (7.33)$$

where λ was taken as 0.001 for both the vorticity and steam function, and 0.0005 for the other parameters. Fundamentally, it was preferred to use (7.33) rather than a criterion that relates the change of the variable at certain node to the maximum value in the field as has been used by some investigators. The latter criterion given by:

$$\left| \frac{\phi_{i,j}^{(n)} - \phi_{i,j}^{(n-1)}}{\phi_{max}^{(n-1)}} \right|_{max} \leq \lambda \qquad (7.34)$$

may lead to a false convergence if the ratio between a certain parameter at a certain node in the field to its maximum value in the whole field is extremely small, while its relative change given by (7.33) is still large.

7.8. Initial Conditions

For the first run of the computer program, the values of ω and ψ were assumed to be zero everywhere. The axial velocity in the whole field was given the value of the average bulk velocity, while the value of the turbulent kinetic energy was given the value at the boundary. The temperature of the whole field was given the value of the average bulk temperature. Even with these unrealistic initial conditions, the fields converged well. After any successful run, the output was directly used as initial conditions for any subsequent cases. It was naturally found that using better initial conditions accelerated the convergence, but it is again emphasized that convergence was achieved regardless of the initial conditions.

CHAPTER 8

RESULTS AND DISCUSSION OF THE PREDICTION TECHNIQUES

8.1. General

Converged solutions were obtained using the two computation schemes described earlier. Model I is discussed only in conjunction with mean axial velocity, secondary velocity component $\bar{V}$ and wall shear stress predictions at a Reynolds number of 53,000. At the same Reynolds number, it is shown that Model II provided superior prediction compared to the experimental data. Hence Model II was used for all subsequent computations involving Reynolds numbers in the range 53,000 to 200,000.

Solutions were obtained with Model II using different vorticity production source terms. In one case (hereafter designated Model IIa), the normal stress term only was applied. In the second case (Model IIb), both normal and shear stress terms were retained.

8.2. Vorticity and Stream Function

The vorticity distribution for Reynolds numbers of 53,000, 107,300 and 150,000 are presented in figures (8.1 - 8.3) as derived from Model IIb. The predictions with Model IIa were qualitatively similar, but low in levels. The sign appearing on the contours indicates the secondary flow is clockwise in this particular flow cell. The contours are also qualitatively similar to those derived experimentally by Brundrett and Baines[8] for the square duct, with very close spacing near the wall, particularly in the corner region. The above figures show the tendency of the vorticity to increase with Reynolds number. The maximum vorticity

for each of the three cases was predicted in the corner region, close to the solid wall.

Comparisons of the contour plots of predicted stream function at the same Reynolds numbers mentioned earlier are afforded by figures (8.4 - 8.6). From figure (8.4), prediction with Model IIb suggests that the penetration of the contours into the corner is mainly due to the shear stress term. This in turn has a direct effect on secondary flow magnitudes in the corner region. As can be seen in figure (8.7), Model IIa predicts smaller $\bar{V}$ values in the corner region than both Model IIb and the experiment (discrepancies of Model I prediction are discussed in the next subsection). Since the agreement between Model IIa and IIb and the experimental data is generally good elsewhere, this suggests that normal stresses vorticity production predominates over most of the duct cross-section; the exception being the corner regions where the shear stress term contributes significantly. This differs from the square duct case where, according to the measurements of Brundrett and Baines[8], the normal stress term predominate everywhere. Further, they suggested that this should be the case for all ducts having parallel sides, which of course is not the case for the present geometry. From figures (8.4 - 8.6), it is evident that the maximum value of the stream function increases with Reynolds number, with more penetration of the contours towards the corner. This indicates that the absolute magnitude of the secondary velocities increases with Reynolds number. On the other hand, normalized secondary velocities with either the average bulk velocities or duct centerline velocities were found to decrease with Reynolds number in the range considered (over 53,000). Similar to the results of Launder and Ying[2], secondary velocities were found to scale with the average friction

velocity. Better scaling may be achieved by normalizing with the local friction velocities rather than the average.

8.3. Secondary Velocities

The secondary velocities predicted by Model IIb (full source) are compared to the experimental data in figure (8.7) ($\bar{V}$) and figure (5.17) ($\bar{W}$). The agreement is good except near the wall where in fact the measurement accuracy may have deteriorated due to wall effect on the probes. Figures (8.8 and 8.9) show the predicted results more fully.

The agreement between $\bar{V}$ predicted by Model I and the experimental data (figure 8.7) is not as good as for the Model IIb case. The predicted secondary flows are generally too strong, and this corresponds to excessive vorticity production. Since the trend accuracy of the turbulence data is thought to be reliable, errors in the vorticity source term are probably due to inaccuracies in numerical differentiation of the field of small $(\overline{v^2} - \overline{w^2})$ values (section 5.2). Errors in the vorticity source term are also suggested to some extent by the lack of agreement between the results of Model I and IIa. Both involve vorticity production due only to normal stresses, hence it would appear that the calculated (IIa) and experimentally derived (I) vorticity productions must be different, and the evidence indicates the former to be the more correct. At the same time, however, it must be recognized that similar $\bar{V}$ results should not necessarily have been expected in the first place because the methods are quite different in both the modelling and the number of coupled equations in each solution. In any event, it is interesting to note that if the levels of vorticity production were reduced for Model I, the agreement with the experimental data would improve away from the corner, but deteriorate in the corner region where good agreement now exists. This behaviour would then be

consistent with the earlier observation concerning differences between Models IIa and IIb.

8.4. Mean Axial Velocity Distributions

Mean axial velocity distribution is presented in figure (8.10) as predicted by Model I, using the Van Driest[80] effective viscosity model for a Reynolds number of 53,000. The effect of the secondary flows on the distribution is evident. The agreement with the experimental distributions of Gerrard[1] is fairly reasonable when viewed in terms of percentage differences. However, certain dificiencies are evident; for example, the predicted contours do not penetrate sufficiently towards the corner. In fact, the secondary flow appears too weak which is contrary to the earlier evidence. Since the converged stream function solution (which was used for calculating secondary velocities) was used to solve the mean axial velocity equation, the eddy viscosity model appears to be responsible for this inconsistency. Further examination, indicated that the deficiency may be largely attributed to the effective viscosity model since it is not completely suitable for this shape of flow cell due to the effect of the second wall on regions near the corner bisector. The Z-direction distribution of eddy viscosity predicted by the Van Driest equation is compared to the distribution of eddy viscosity values calculated at $y/L = 0$ from the experimental data in figure (8.11). It is evident that the Van Driest model predicted considerable higher values of eddy viscosity for $z/\hat{z} > 0.4$, where $\hat{z}$ is the normal distance from the wall to the corner bisector. This overestimate tends to overflatten the predicted axial velocity distribution for $z/\hat{z} > 0.4$, which in turn shifts the predicted isovels below the experimental ones over much of the duct cross section.

In figure (8.12), a comparison of the axial velocity contours predicted by Model IIb and the same experimental contours of figure (8.10) is presented. It is clear that Model II provides remarkable improvement. The contours are identical near the midwall bisector and over most of the duct, and close to each other near the duct centerline. The highest disagreement is shown to be near the corner bisector particularly near the duct center. This can be partially attributed to the length scale calculations. An attempt was made to determine the validity of using Buleev's formula for the case of an equilateral triangular duct. The turbulence length scale was calculated from the experimental data of shear stress, turbulent kinetic energy, and axial velocity gradients along the lines $y/L = 0$, and $y/L = 0.4$ from the formula,

$$\ell = -\frac{1}{c_\nu} \frac{\overline{uw}}{(k)^{\frac{1}{2}} \partial\bar{U}/\partial z} , \tag{8.1}$$

with the value c_ν the same as noted earlier. Comparison of these two distributions with the corresponding ones obtained from Buleev's formula (6.7) is provided by figure (8.13). It is clear that for the region $z/\hat{z} > 0.6$, equation (6.25) tends to overestimate the actual length scale. This means that by using this equation a more flattened axial velocity distribution will result. Nevertheless, despite this minor shortcoming, the author does not hesitate to recommend employing the Buleev length scale since it produces reasonable results while avoiding experimental input to the prediction technique. An expression to calculate the turbulence length scale based on the experimental measurements for each of two regions in the primary flow cell is proposed; the two expressions are:

$$\ell = mz/c_\nu , \quad 0 < y < 0.3 \tag{8.2}$$

$$\ell = \hat{z}/c_{\nu}\{A + B(z/\hat{z}) + C(z/\hat{z})^2\},\ 0.3 \leq y \leq 1.0 \qquad (8.3)$$

where the coefficient m is given the value 0.1667, and A, B and C are given the values:

a) A = -0.0734
   B = 0.477 $\qquad 0.6 \leq z/\hat{z} \leq 1$
   C = -0.375

b) A = -0.0245
   B = 0.326 $\qquad 0.3 \leq z/\hat{z} \leq 0.6$
   C = -0.258

These values provided the best fit to the estimated average distribution on most of the primary flow cell (from y/L = 0.0 to 0.4); for the remaining part, the formula (6.25) can be used. However, Buleev length scale was used for all predictions with Model IIb.

Mean axial velocity distributions for Reynolds numbers of 107,300 and 150,000 are given by figures (8.14 and 8.15). It is noted that the duct centerline velocity (normalized with the average bulk velocity U_b) decreases with Reynolds number. Also, the distortions of the contours increases slightly with Reynolds number as a result of secondary flows. These results are consistent with the experimental results of Gerrard[1]. Comparison of axial velocity contours as predicted with and without secondary flow is presented in figure (8.16). Distortions in the isovels are shown to be a direct effect of secondary flows.

8.5. Mean Turbulent Kinetic Energy Distributions

The mean turbulent kinetic energy predicted by Model IIb is compared to the experimental contours in figure (8.17) for Reynolds number of 53,000. It is evident that the distortion in these contours is much larger than that of the axial velocity contours. The corresponding

situation has also been noted for the square duct case (Brundrett and Baines[8]; Launder and Ying[2]). Predictions for Reynolds numbers of 107,300 and 150,000 are presented in figures (8.18 and 8.19). It is shown that the turbulent kinetic energy scales fairly reasonably with square of the average friction velocity. The same distortions are evident for the three cases because of the secondary flow effect..

8.6. Wall Shear Stress

The predicted wall shear stress for both models are compared to the experimental results of Gerrard[1] in figure (8.20). The distribution of wall shear stress as predicted with secondary flow supressed is superimposed on the above distributions. It is evident that the secondary flows tend to equalize the wall shear stress along the wall. The Model I prediction is in error due to the discrepancy mentioned earlier in the mean axial velocity field predicted by this model. It is interesting to note that in the case of the equilateral triangle duct, the peak value of the wall shear stress is not displaced as far towards the corner as for the square duct case. For the latter, several investigators have reported that the peak value is located at $y/L = 0.5$, while in the triangular duct it was found to be at $y/L \approx 1/3$.

8.7. Effect Of Reynolds Number

The effect of Reynolds number on the vorticity, stream function, mean axial velocity and turbulent kinetic energy have already been described. Friction factor dependence on Reynolds number was investigated by conducting a series of calculations with Model IIb; this model having proven to provide the best predictions. The predicted results are compared to the experimental data[1] in figure (8.21). On the same figure, comparison

with the prediction obtained by the Blasius correlation for friction factors in smooth circular tubes is shown. For equilateral triangular ducts, both experimental[1] and prediction results indicate that friction factors are from 5% to 6½% lower than the prediction by Blasius equation. Similar deviations have been reported for other noncircular ducts, e.g., Leutheusser[7] for square ducts, and Carlson and Irvine[83] for isosceles triangular ducts. This deviation is evident from figure (8.21) while also includes a correction for the inadequacies in the equivalent hydraulic diameter concept which has been suggested by Malak et al[84]. This correction which includes a geometrical factor in the correlation of friction factor and Reynolds number data gave also a good representation of the limited data of Gerrard[1]. It should be noted that the predicted friction factors are slightly below the experimental points. Launder and Ying[2] observed a similar difference for the square duct case which they attributed as being probably due to the Buleev method for calculating the length scale distribution in the duct. In any event, both Model IIb and the equation of Malak et al[84] provide better values of friction factors than the Blasius equation.

The distributions of predicted local wall shear stress for three Reynolds numbers are compared in figure (8.22) after normalization by their respective integrated average values. These distributions do not show any significant tendency towards greater uniformity with increasing Reynolds number (in the range from 53,000 to 150,000) as is the case for rectangular ducts[7]. This finding is consistent with the experimental results of Gerrard[1].

8.8. Heat Transfer Prediction

Although all the isotherms were predicted at three Reynolds numbers,

since the data were similar, only the isotherms for Reynolds number of 53,000 are presented in figure (8.23). These isotherms are qualitatively similar to the predicted pattern for mean axial velocity shown in figure (8.12). Normalization of the local fluid temperature was made with the uniform wall temperature T_W, and the bulk average temperature $\bar{T}$ at the station. The existence of secondary flow is evident by its effect on the temperature field. Figure (8.24) shows the predicted relationship between Stanton number and Reynolds number and includes, for comparison purposes, data for both square duct and pipe flow. For a given Reynolds number, the Stanton numbers for the equilateral triangular duct and the square duct are within 10% of each other over the indicated Reynolds number range. The heat flux distribution around the periphery of the duct is presented in figure (8.25), where the average heat flux $(\bar{\dot{q}}'')$ was obtained by integrating the local $(\dot{q}'')$ values. It is clear that the distribution is similar to that of the wall sheer stress with a maximum value of heat flux at $y/L = 1/3$. For square ducts, Launder and Ying[2] also predicted a maximum value of heat flux at $y/L = 1/2$, the same position where wall shear stress peaks.

PART II: EQUILATERAL TRIANGULAR ARRAY ROD BUNDLE

CHAPTER 9

THEORETICAL CONSIDERATIONS

9.1 General; Reynolds and Continuity Equations

In an equilateral triangular array of rods, each tricuspid subchannel is symmetric in six parts, each part constituting a 'primary flow cell' as indicated in figure (9.1). For an infinite array, there is no momentum transfer across the boundaries of the primary flow cell because of symmetry considerations. The cases to be investigated are steady, fully developed turbulent flows of an incompressible isothermal fluid. The primary flow cell and the cylindrical polar coordinate system (r, θ, x) used in the investigation are shown in figure (9.2). The primary flow is in the positive X-direction. Due to the fully developed flow condition,

$$\partial \bar{P}/\partial x = \text{constant and } \partial(\bar{\ })/\partial x = 0.$$

Due to the no slip condition at the wall:

a) $\bar{U} = \bar{V}_\theta = \bar{V}_r = o = u = v = w$, for all θ.

Due to symmetry with neighbouring cells, for the boundaries $\theta = o$ and $\theta = \pi/6$ the conditions are:

b) $\dfrac{\partial(\bar{\ })}{\partial\theta} = o$, for all Y.

For symmetry around maximum velocity line:

c) $\dfrac{\partial(\bar{\ })}{\partial r} = -\tan\theta \dfrac{\partial(\bar{\ })}{r\partial\theta}$ at $Y = \hat{Y}$, for all θ.

From the last condition, it can be shown that at the point $r = P'/2$,

d) $\dfrac{\partial(\bar{\ })}{\partial r} = o$, and at least $\dfrac{\partial \bar{U}}{\partial r} = o$ at $r = (P'/2)\cos(\pi/6)$

since here $\bar{U}$ is a maximum.

Since the secondary flow is bounded by lines of symmetry,

e) $\bar{V}_\theta = o$ at $\theta = 0$ and $30°$, for all Y; and

f) $\bar{V}_\theta = \bar{V}_r = o$ at the singular points defined by $r = P'/2$ and $r = (p'/2)\cos(\pi/6)$.

The secondary velocity component $\bar{V}_r$ may have finite values on both the radial boundaries $\theta = 0°$ and $30°$. Similar to the triangular duct analysis, it can be shown that along the above two boundaries, $\overline{v_r v_\theta} = 0$. On the other hand for the boundaries, $\frac{\partial \overline{uv_\theta}}{r\partial\theta}$ (like $\frac{\partial \overline{V_\theta}}{r\partial\theta}$) may have finite values since $\overline{uv_\theta}$ (like $\bar{V}_\theta$) has an antisymmetric distribution about those boundaries.

The continuity equations representing conservation of mass are:

$$\frac{1}{r}\frac{\partial r\bar{V}_r}{\partial r} + \frac{1}{r}\frac{\partial \bar{V}_\theta}{\partial \theta} = 0, \tag{9.1}$$

$$\frac{\partial u}{\partial x} + \frac{1}{r}\frac{\partial rv_r}{\partial r} + \frac{1}{r}\frac{\partial v_\theta}{\partial \theta} = 0. \tag{9.2}$$

The Reynolds equations representing conservation of momentum are given by:

For the axial direction:

$$\bar{V}_r\frac{\partial \bar{U}}{\partial r} + \frac{\bar{V}_\theta}{r}\frac{\partial \bar{U}}{\partial \theta} = -\frac{1}{\rho}\frac{\partial \bar{P}}{\partial x} - \left[\frac{1}{r}\frac{\partial r\,\overline{uv}_r}{\partial r} + \frac{1}{r}\frac{\partial \overline{uv}_\theta}{\partial \theta}\right] + \nu\left[\frac{\partial^2 \bar{U}}{\partial r^2} + \frac{1}{r}\frac{\partial \bar{U}}{\partial r} + \frac{1}{r^2}\frac{\partial^2 \bar{U}}{\partial \theta^2}\right]. \tag{9.3}$$

For the radial direction:

$$\bar{V}_r\frac{\partial \bar{V}_r}{\partial r} + \frac{\bar{V}_\theta}{r}\frac{\partial \bar{V}_r}{\partial \theta} - \frac{\bar{V}_\theta^2}{r} = -\frac{1}{\rho}\frac{\partial \bar{P}}{\partial r} - \left[\frac{1}{r}\frac{\partial}{\partial r}(r\,\overline{v_r^2}) + \frac{1}{r}\frac{\partial \overline{v_r v_\theta}}{\partial \theta} - \frac{\overline{v_\theta^2}}{r}\right] +$$

$$+ \nu\left[\frac{\partial^2 \bar{V}_r}{\partial r^2} + \frac{1}{r}\frac{\partial \bar{V}_r}{\partial r} + \frac{1}{r^2}\frac{\partial^2 \bar{V}_r}{\partial \theta^2} - \frac{\bar{V}_r}{r^2} - \frac{2}{r^2}\frac{\partial \bar{V}_\theta}{\partial \theta}\right]. \tag{9.4}$$

For the peripheral direction:

$$\bar{V}_r \frac{\partial \bar{V}_\theta}{\partial r} + \frac{\bar{V}_\theta}{r} \frac{\partial \bar{V}_\theta}{\partial \theta} + \frac{\bar{V}_r \bar{V}_\theta}{r} = -\frac{1}{\rho r} \frac{\partial \bar{P}}{\partial \theta} - \left[\frac{\partial}{\partial r} \overline{v_r v_\theta} + \frac{1}{r} \frac{\partial \overline{v_\theta^2}}{\partial \theta} + \frac{2\overline{v_r v_\theta}}{r}\right] +$$

$$+ \nu\left[\frac{\partial^2 \bar{V}_\theta}{\partial r^2} + \frac{1}{r} \frac{\partial \bar{V}_\theta}{\partial r} + \frac{1}{r^2} \frac{\partial^2 \bar{V}_\theta}{\partial^2 \theta} + \frac{2}{r^2} \frac{\partial \bar{V}_r}{\partial \theta} - \frac{\bar{V}_\theta}{r^2}\right]. \qquad (9.5)$$

The eddy viscosities in the radial and peripheral directions are defined by:

$$\overline{uv_r} = -\nu_r \frac{\partial \bar{U}}{\partial r}, \qquad (9.6)$$

and

$$\overline{uv_\theta} = \frac{\nu_\theta}{r} \frac{\partial \bar{U}}{\partial \theta}. \qquad (9.7)$$

Hence, equation (9.5) may be rewritten as:

$$\bar{V}_r \frac{\partial \bar{U}}{\partial r} + \frac{\bar{V}_\theta}{r} \frac{\partial \bar{U}}{\partial \theta} = -\frac{1}{\rho} \frac{\partial \bar{P}}{\partial x} + \frac{1}{r} \frac{\partial}{\partial r} r\left[(\nu_r + \nu) \frac{\partial \bar{U}}{\partial r}\right] + \frac{1}{r} \frac{\partial}{\partial \theta} \left[(\nu_\theta + \nu) \frac{1}{r} \frac{\partial \bar{U}}{\partial \theta}\right]. \qquad (9.8)$$

Using the locally isotropic eddy viscosity assumption, $\nu_\theta = \nu_r = \nu_T$. By applying boundary conditions to the Reynolds equations, it can be readily shown that $v'_r = v'_\theta$ at the singular point $r = P'/2$, and $\overline{v_r v_\theta} = 0$ over the radial boundaries given by $\theta = 0°$ and $30°$.

9.2 Axial Vorticity and Stream Function Equations

The mean axial vorticity component ω is defined by:

$$\omega = \frac{1}{r}\left[\frac{\partial r\bar{V}_\theta}{\partial r} - \frac{\partial \bar{V}_r}{\partial \theta}\right]. \qquad (9.9)$$

The equation for conservation of the axial vorticity component may be derived by multiplying equation (9.4) by ρ and differentiating with respect to $(rd\theta)$, multiplying equation (9.5) by ρr and differentiating with respect to r, and finally subtracting one from the other to eliminate the pressure term.

By defining the stream function ψ as:

$$\rho\bar{V}_r = \frac{1}{r}\frac{\partial\psi}{\partial\theta} \quad \text{and} \quad \rho\bar{V}_\theta = -\frac{\partial\psi}{\partial r}, \tag{9.10}$$

the velocity equation may be written in the form:

$$\frac{1}{r}\frac{\partial}{\partial r}\left[\omega\frac{\partial\psi}{\partial\theta}\right] - \frac{1}{r}\frac{\partial}{\partial\theta}\left[\omega\frac{\partial\psi}{\partial r}\right] + d\phi - \mu\nabla^2\omega = 0 \tag{9.11}$$

where,

$d\phi$ = the vorticity production term given by,

$$d\phi = \rho\left[\frac{1}{r}\frac{\partial^2}{\partial r\partial\theta}\left(\overline{v_\theta^2} - \overline{v_r^2}\right) + \left\{\frac{\partial^2}{\partial r^2} - \frac{1}{r^2}\frac{\partial^2}{\partial\theta^2}\right\}\left\{\overline{v_r v_\theta}\right\} + \right.$$

$$\left. + \frac{1}{r^2}\frac{\partial}{\partial\theta}\left(\overline{v_\theta^2} - \overline{v_r^2}\right) + \frac{3}{r}\frac{\partial}{}\frac{\overline{v_r v_\theta}}{\partial r}\right], \tag{9.12}$$

and,

$$\nabla^2 = \frac{1}{r}\frac{\partial}{\partial r}\left[r\frac{\partial(\ )}{\partial r}\right] + \frac{1}{r^2}\frac{\partial^2(\ )}{\partial\theta^2}, \tag{9.13}$$

for fully developed flow. The last term of equation (9.11) represents diffusion of vorticity by viscous effects, while the first two terms on the left side represents the convection of vorticity by the secondary velocities.

Substituting (9.10) into (9.9) yields the stream function equation as:

$$+\frac{1}{r}\frac{\partial}{\partial r}\left\{r\left(\frac{\partial\psi}{\partial r}\right)\right\} + \frac{\partial}{r\partial\theta}\left(\frac{\partial\psi}{r\partial\theta}\right) + \omega = 0. \tag{9.14}$$

9.3 Turbulent Kinetic Energy Equation

A simulated transport equation for turbulent kinetic energy may be written in the form:

$$\frac{1}{r}\frac{\partial}{\partial r}rk\left(\frac{\partial\psi}{r\partial\theta}\right) - \frac{\partial}{r\partial\theta}k\left(\frac{\partial\psi}{\partial r}\right) - \frac{1}{r}\frac{\partial}{\partial r}r\left\{\mu\frac{\partial k}{\partial r} - \overline{v_r k'}\right\} - \frac{\partial}{r\partial\theta}\left\{\mu\frac{\partial k}{r\partial\theta} - \overline{v\ k'}\right\} =$$

$$\frac{-C_D\ \rho(k)^{3/2}}{\ell} - \left\{\overline{v_r u}\left(\frac{\partial U}{\partial r}\right) + \overline{v_\theta u}\left(\frac{\partial U}{\partial r}\right)\right\}. \tag{9.15}$$

Similar to the assumption (6.2.b), one may write:

$$\rho \overline{v_r k'} = - \Gamma_k \frac{\partial k}{\partial r} , \tag{9.16}$$

$$\rho \overline{v\ k'} = - \Gamma_k \frac{\partial k}{r\partial \theta} , \tag{9.17}$$

where Γ_k has the same definition of Chapter (6), and can be approximated similarly by:

$$\Gamma_K = \frac{\mu_T}{\sigma_k} . \tag{9.18}$$

Equation (9.15) with (9.16, 9.17 and 9.18) may now be written as:

$$\frac{1}{r}\frac{\partial}{\partial r}\left(k \frac{\partial \psi}{\partial \theta}\right) - \frac{1}{r}\frac{\partial}{\partial \theta}\left(k \frac{\partial \psi}{\partial r}\right) - \frac{1}{r}\frac{\partial}{\partial r} r \left\{\left(\mu + \frac{\mu_t}{\sigma_k}\right) \frac{\partial k}{\partial r}\right\} - \frac{\partial}{r\partial \theta}\left\{\left(\mu + \frac{\mu_t}{\sigma_k}\right) \frac{\partial k}{r\partial \theta}\right\} -$$

$$\mu_t \left\{\left(\frac{\partial U}{\partial r}\right)^2 + \left(\frac{\partial U}{r\partial \theta}\right)^2\right\} + \frac{\rho\, C_{Dk}^{3/2}}{\ell} = 0, \tag{9.19}$$

or in the short form:

$$I + II + III + IV = 0, \tag{9.20}$$

where,

(a) Term I $= \frac{1}{r}\frac{\partial}{\partial r}\left(k \frac{\partial \psi}{\partial \theta}\right) - \frac{1}{r}\frac{\partial}{\partial \theta}\left(k \frac{\partial \psi}{\partial r}\right)$,

represents convection of the mean turbulent kinetic energy by the secondary velocities;

(b) Term II $= - \frac{1}{r}\frac{\partial}{\partial r} r \left\{\left(\mu + \frac{\mu_t}{\sigma_k}\right) \frac{\partial k}{\partial r}\right\} - \frac{\partial}{r\partial \theta}\left\{\left(+ \frac{\mu_t}{\sigma_k}\right) \frac{\partial k}{r\partial \theta}\right\}$,

represents diffusion of the mean turbulent kinetic energy by the turbulence and viscous effects.

(c) Term III $= -\mu_t \left\{\left(\frac{\partial U}{\partial r}\right)^2 + \left(\frac{\partial U}{r\partial \theta}\right)^2\right\}$,

represents the rate of production of the mean turbulent kinetic energy.

(d) Term IV $= \frac{\rho\, C_D k^{3/2}}{\ell}$,

represents the rate of dissipation of the mean turbulent kinetic energy by molecular viscosity.

9.4 Turbulence Length Scale

Regarding the mixing length distribution, the only available information about its distribution in rod arrays based on experimental data, is the work presented by Carajilescov and Todreas[23]. Based on analysis of rod bundles sub-channel experimental data obtained, they proposed the mixing length distribution be expressed as:

$$\frac{\ell}{\hat{Y}} = \frac{Y}{\hat{Y}} \quad , \quad \text{for} \quad 0 \leq \frac{Y}{\hat{Y}} \leq 0.44 \ ,$$

$$\frac{\ell}{\hat{Y}} = 0.44 + 0.066 \sin \left[\frac{\pi}{0.38} \left(\frac{Y}{\hat{Y}} - 0.44\right)\right] \ , \qquad (9.21)$$

$$\text{for} \quad 0.44 \leq \frac{Y}{\hat{Y}} \leq 1.0,$$

where $\hat{Y}$ is distance from the wall to the maximum velocity line along a radial line.

The semi-empirical expression of turbulence length scale proposed by Buleev[61] and given by equation (6.7) in Part I was used by Bender and Switick[57] for rod bundles analysis, but they neglected the secondary flows. Comparison of the distributions obtained from equations (9.21) and (6.7) at different angular positions showed that discrepancies between the two methods occur mainly for values of $Y/\hat{Y}$ larger than 0.5. These discrepancies exceeded those discussed earlier for the equilateral triangular duct. Although the use of Buleev's equation would not introduce appreciable error, since the discrepancies occur only over regions where axial velocity gradients are small, it is preferred to use equation (9.21) for its presumed accuracy over Buleev and for its simplicity in that the difficulty associated with the integration of equation (6.7) in this complicated geometry is avoided.

CHAPTER 10

THE ANALYTICAL MODEL

10.1 General

In developing the analytical model, the treatment is similar to Model II for the equilateral triangular ducts presented in Chapter 6. By assuming steady, incompressible, constant property, fully developed turbulent flow, and neglecting body forces, the momentum and continuity equations can be reduced to a set of three transport equations for axial momentum, vorticity and stream function using the prescribed cylindrical co-ordinate system. Vorticity production terms are then calculated in similar way by expressing the turbostresses in the plane of the cross-section by gradients in the axial mean velocity field.

10.2 The Model

Combining equations (9.11 - 9.13) inclusive yields the general vorticity equation given by:

$$- \frac{1}{r}\frac{\partial}{\partial r}\left[\omega \frac{\partial \psi}{\partial \theta}\right] + \frac{1}{r}\frac{\partial}{\partial \theta}\left[\omega \frac{\partial \psi}{\partial r}\right] - \frac{\mu}{r}\frac{\partial}{\partial r} r \left(\frac{\partial \omega}{\partial r}\right) - \frac{\mu}{r^2}\frac{\partial^2 \omega}{\partial \theta^2} + \rho\left[\frac{1}{r} \frac{\partial^2}{\partial r \partial \theta}\left(\overline{v_\theta{}^2} - \overline{v_r{}^2}\right) + \right.$$

$$\left. + \left(\frac{\partial^2}{\partial r^2} - \frac{1}{r^2}\frac{\partial^2}{\partial \theta^2}\right)\left(\overline{v_\theta v_r}\right) + \frac{1}{r^2}\frac{\partial}{\partial \theta}\left(\overline{v_\theta{}^2} - \overline{v_r{}^2}\right) + \frac{3}{r}\frac{\partial \overline{v_r v_\theta}}{\partial r}\right] = 0 \qquad (10.1)$$

The vorticity and stream function (hence secondary velocities) fields for the rod bundle array sub-channel may now be obtained by solving (9.14) and (10.1), with the vorticity production term calculated by the following algebraic equations. Using the same basic proposals of equations (6.5) and (6.6), with cylindrical co-ordinates, it can be shown that:

$$\overline{v_\theta^2} - \overline{v_r^2} = -C\ell^2 \left[\left(\frac{\partial \bar{U}}{r\partial\theta}\right)^2 - \left(\frac{\partial \bar{U}}{\partial r}\right)^2\right], \tag{10.2}$$

$$\overline{v_\theta v_r} = -C\ell^2 \left(\frac{\partial \bar{U}}{r\partial\theta}\right)\left(\frac{\partial \bar{U}}{\partial r}\right), \tag{10.3}$$

where C has the same definition as before. The turbulence length scale ℓ was calculated via (9.21) for each node. The mean axial velocity field was then obtained by solving (9.8). The Prandlt-Kolmogorov formula for eddy viscosity given by (6.9) was used to interrelate local values of eddy viscosity and turbulence length scale through the local mean turbulent kinetic energy k obtained by solving (9.19) with the constant C_ν.

The final computation scheme required solutions to equations (9.14), (10.1) (with 9.21, 10.2, 10.3), (9.19) (with 6.9, 9.21) and (9.8) (with 6.9, 9.21). Values used for the various constants were the same values used in Model II for the triangular duct, however, a study was made to determine the effect of changing some of them on the predicted results as will be discussed in Chapter 12. Since there is still no reliable measurements for secondary velocities in rod bundle geometries, the constants were optimized only to give reasonable agreement with the experimental data available for mean axial velocity, mean turbulent kinetic energy and local wall shear stress. Hence, although the predicted secondary velocities produce the approximately correct, mean velocity field in the cross-section of the flow, the absolute accuracy of these results cannot be evaluated. Following successful measurements of the components $\bar{V}_r$ and $\bar{V}_\theta$ in a sub-channel of a semi-infinite array, the constants may be changed if necessary in order to give good agreement at the secondary flow level.

10.3 Boundary Conditions

a) Solid wall

The analysis which was applied to the solid wall in section (6.4) was applied also here for the rod surface between $\theta = 0°$ and $30°$. The constant ψ was conveniently taken as zero, while ω was assumed to change linearly with radial distance from the wall. The velocity profile was also represented by the same law of the wall given by (6.14), while the boundary condition for k was represented by (6.15). The boundary conditions for both $\bar{U}$ and k were imposed at the first string of nodes in the fluid adjacent to the wall. The grid was designed to have these nodes located beyond the viscous sublayer for the Reynolds number range involved.

b) $\theta = 0°$ and $\theta = 30°$ boundaries

Since no net flow crosses these two boundaries, ψ and ω were set to zero. The normal-to-boundary gradients of the mean axial velocity and turbulent kinetic energy were set to zero as is demanded by symmetry.

c) Maximum velocity line (MVL)

Since no net flow crosses the MVL boundary, ψ and ω were set to zero. The normal-to-boundary gradients of the mean axial velocity and turbulent kinetic energy were set to zero as demanded by symmetry. that is,

$$\left(\frac{\partial \bar{U}}{\partial n}\right)_{MVL} = 0,$$

$$\left(\frac{\partial k}{\partial n}\right)_{MVL} = 0.$$

Regarding the position of nodes in the grid, the above two conditions may simply be represented by:

$$\left(\frac{\partial \bar{U}}{\partial r}\right)_{MVL} = \left(\frac{\partial \bar{U}}{r\partial\theta}\right)_{MVL} \tan\theta \,,$$

$$\left(\frac{\partial k}{\partial r}\right)_{MVL} = \left(\frac{\partial k}{r\partial\theta}\right)_{MVL} \tan\theta \,, \qquad (10.4)$$

10.4 Summary Of The Equations To be Solved

10.4.1 Transport Equations

a) Axial momentum equation

$$\overline{V_r}\frac{\partial \bar{U}}{\partial r} + \frac{\overline{V_\theta}}{r}\frac{\partial \bar{U}}{\partial \theta} = -\frac{1}{\rho}\frac{\partial \bar{P}}{\partial x} + \frac{1}{r}\frac{\partial}{\partial r}\, r[(\nu_T + \nu)\frac{\partial \bar{U}}{\partial r}] + \frac{1}{r}\frac{\partial}{\partial \theta}[(\nu_T + \nu)\frac{1}{r}\frac{\partial \bar{U}}{\partial \theta}] \qquad (10.5)$$

b) Stream function equation

$$\frac{1}{r}\frac{\partial}{\partial r}\{r\frac{\partial \psi}{\partial r}\} + \frac{\partial}{r\partial\theta}\{\frac{\partial \psi}{r\partial\theta}\} + \omega = 0 \qquad (10.6)$$

c) Vorticity equation

$$-\frac{1}{r}\frac{\partial}{\partial r}[\omega\frac{\partial \psi}{\partial \theta}] + \frac{1}{r}\frac{\partial}{\partial \theta}[\omega\frac{\partial \psi}{\partial r}] - \frac{\mu}{r}\frac{\partial}{\partial r}\, r(\frac{\partial \omega}{\partial r}) - \frac{\mu}{r^2}(\frac{\partial^2 \omega}{\partial \theta^2}) + \rho[\frac{1}{r}\frac{\partial^2}{\partial r \partial \theta}(\overline{v_\theta^2} - \overline{v_r^2}) +$$

$$+\{\frac{\partial^2}{\partial r^2} - \frac{1}{r^2}\frac{\partial^2}{\partial \theta^2}\}\overline{(v_\theta v_r)} + \frac{1}{r^2}\frac{\partial}{\partial \theta}(\overline{v_\theta^2} - \overline{v_r^2}) + \frac{3}{r}\frac{\partial \overline{v_r v_\theta}}{\partial r}] = 0 \qquad (10.7)$$

d) Turbulent kinetic energy

$$\frac{1}{r}\frac{\partial}{\partial r}(k\frac{\partial \psi}{\partial \theta}) - \frac{1}{r}\frac{\partial}{\partial \theta}(k\frac{\partial \psi}{\partial r}) - \frac{1}{r}\frac{\partial}{\partial r}\, r\{(\mu + \frac{\mu_t}{\sigma_k})\frac{\partial k}{\partial r}\} - \frac{\partial}{r\partial\theta}\{(\mu + \frac{\mu_t}{\sigma_k})\frac{\partial k}{r\partial\theta}\} -$$

$$-\mu_t\{(\frac{\partial \bar{U}}{\partial r})^2 + (\frac{\partial \bar{U}}{r\partial\theta})^2\} + \frac{\rho C_d k^{3/2}}{\ell} = 0 \qquad (10.8)$$

10.4.2 Algebraic Equations

a) Turbulent viscosity

$$\mu_t = \rho C_\nu (k)^{3/2} \ell \qquad (10.9)$$

b) Turbulence length scale distribution

$$\frac{\ell}{\hat{Y}} = \frac{Y}{\hat{Y}} \quad , \quad \text{for} \quad 0 \leq \frac{Y}{\hat{Y}} \leq 0.44,$$

$$\frac{\ell}{\hat{Y}} = 0.44 + 0.066 \sin \left[\frac{\pi}{0.38} \left(\frac{Y}{\hat{Y}} - 0.44\right)\right], \tag{10.10}$$

$$\text{for} \quad 0.44 \leq \frac{Y}{\hat{Y}} \leq 1.0.$$

c) For vorticity production source term

$$\overline{v_\theta^2} - \overline{v_r^2} = - C\ell^2 \left[\left(\frac{\partial \bar{U}}{r\partial\theta}\right)^2 - \left(\frac{\partial \bar{U}}{\partial r}\right)^2\right], \tag{10.11}$$

$$v_\theta v_r = - C\ell^2 \left[\left(\frac{\partial \bar{U}}{r\partial\theta}\right)\left(\frac{\partial \bar{U}}{\partial r}\right)\right].$$

where,

$$C = \frac{C_\nu}{C_D} \cdot \frac{2(6C_2 - 2)}{11(C_1 - 2C_2)} \tag{10.12}$$

d) Source term for axial momentum equation

$$\frac{\partial \bar{P}}{\partial x} = 4\tau_\omega / D_h \ , \tag{10.13}$$

where,

$$D_h = 2R \left[\frac{2\sqrt{3}}{\pi} \left(\frac{P'}{D}\right)^2 - 1\right]. \tag{10.14}$$

e) Friction factor

$$f = \frac{8\,\tau_\omega}{\rho U_b^2} \tag{10.15}$$

f) Average wall shear stress

$$\tau_\omega = \frac{1}{(\pi/6)} \int_0^{\pi/6} \tau d\theta \tag{10.16}$$

10.4.3 Boundary Conditions

a) Wall boundary conditions

$$\psi = 0$$

$$\omega_p = \omega_n + \frac{(X_p - X_n)(\omega_m - \omega_n)}{(X_m - X_n)} \quad , \tag{10.17}$$

where, p is the wall node, n is the node next to wall and m is the node twice removed from the wall in the radial direction.

$$\bar{U} = \sqrt{\tau/\rho}\ [A\ Ln(EY^+)] \quad , \tag{10.18}$$

where Y^+ is the dimensionless distance from the wall in the radial direction and given by:

$$Y^+ = \frac{(R_2 - R)\sqrt{\tau/\rho}}{\nu} \quad , \tag{10.19}$$

and

$$\tau = \rho(C_\nu C_D)^{1/4}(k)_2^{1/2}\ \bar{U}_2/[A\ Ln\{E\ Y_2(C_\nu C_D)^{1/4}(k)_2^{1/2}/\nu\}], \tag{10.19.a}$$

where 2 denotes the second string of nodes, and Y_2 is the normal distance from the wall to this string.

$$k = \tau/(\rho^2 C_\nu C_D)^{1/2} \tag{10.20}$$

b) Boundaries $\theta = 0°$ and $\theta = 30°$

$$\psi = 0 \tag{10.21}$$

$$\omega = 0 \tag{10.22}$$

$$\frac{\partial \bar{U}}{r\partial\theta} = 0 \tag{10.23}$$

$$\frac{\partial \bar{k}}{r\partial\theta} = 0 \tag{10.24}$$

c) MVL Boundary

$$\psi = 0 \tag{10.25}$$

$$\omega = 0 \tag{10.26}$$

$$\frac{\partial \bar{U}}{\partial r} = \frac{\partial \bar{U}}{r\partial\theta} \tan\theta \qquad (10.27)$$

$$\frac{\partial k}{\partial r} = \frac{\partial k}{r\partial\theta} \tan\theta \qquad (10.28)$$

10.4.4 Constants of the Model

These were the same as in (6.5.4) except as otherwise stated explicitly.

CHAPTER 11

THE NUMERICAL PROCEDURE

11.1. Introduction

Equations (10.5 - 10.8) may be written in the general form:

$$a_\phi \left[\frac{1}{r}\frac{\partial}{\partial r}\Phi\frac{\partial\psi}{\partial\theta} - \frac{\partial\Phi}{r\partial\theta}\frac{\partial\psi}{\partial r}\right] - \left[\frac{1}{r}\frac{\partial}{\partial r}rb_\phi\frac{\partial\Phi}{\partial r} + \frac{\partial}{r\partial\theta}b_\phi\frac{\partial\Phi}{\partial\theta}\right] + d\phi = 0 \tag{11.1}$$

The new symbols in this standard elliptic form are identified for each equation in Table 3. As for the triangular duct, in order to solve these equations numerically, the equations were integrated over finite areas in the primary flow cell. Again, an upwind finite difference technique based on the general elliptic procedure of Gosman et al[39] was used, but here with a cylindrical co-ordinate grid covering the primary flow cell. Assumptions for the distributions of the parameters between the nodes of the grid are basically the same as those discussed in details in Chapter 7. Fundamentally, there is no difference between the two integration schemes except for differences associated with using cylindrical co-ordinate system.

The integration steps for the different terms are not reported here, however the full system of equations resulting from the integration are presented below.

11.2. The Substitution Formula

Figure (11.1) shows part of the cylindrical co-ordinate grid which will be presented in more details later in this section. For the node P, the area of integration is bounded by the dashed lines. A certain parameter at this node (ϕ_P) can be calculated from the values at the

surrounding nodes from the formula:

$$\Phi_P = (C_E \phi_E + C_W \phi_W + C_N \phi_N + C_S \phi_S) + (I_S)/\Sigma_{AB} , \qquad (11.2)$$

where,

$$\begin{aligned} C_E &= [a_\phi A_E + (b_{\phi E} + b_{\phi P})B_E]/\Sigma_{AB} , \\ C_W &= [a_\phi A_W + (b_{\phi W} + b_{\phi P})B_W]/\Sigma_{AB} , \\ C_N &= [a_\phi A_N + (b_{\phi N} + b_{\phi P})B_N]/\Sigma_{AB} , \\ C_S &= [a_\phi A_S + (b_{\phi S} + b_{\phi P})B_S]/\Sigma_{AB} , \end{aligned} \qquad (11.3)$$

$$\Sigma_{AB} = a_\phi(A_E + A_W + A_N + A_S) + (b_{\phi E} + b_{\phi P})B_E + (b_{\phi W} + b_{\phi P})B_W + (b_{\phi N} + b_{\phi P})B_N + (b_{\phi S} + b_{\phi P})B_S . \qquad (11.4)$$

The A's are given by:

$$\begin{aligned} A_E &= \tfrac{1}{8}\{(\psi_{SE} - \psi_{NE} + \psi_S - \psi_N) + |\psi_{SE} - \psi_{NE} + \psi_S - \psi_N|\} , \\ A_W &= \tfrac{1}{8}\{(\psi_{NW} - \psi_{SE} + \psi_N - \psi_S) + |\psi_{NW} - \psi_{SE} + \psi_N - \psi_S|\} , \\ A_N &= \tfrac{1}{8}\{(\psi_{NE} - \psi_{NW} + \psi_E - \psi_W) + |\psi_{NE} - \psi_{NW} + \psi_E - \psi_W|\} , \\ A_S &= \tfrac{1}{8}\{(\psi_{SW} - \psi_{SE} + \psi_W - \psi_E) + |\psi_{SW} - \psi_{SE} + \psi_W - \psi_E|\} . \end{aligned} \qquad (11.5)$$

The B's are given by:

$$\begin{aligned} B_E &= \frac{1}{8}\,\frac{r_E + r_P}{r_E - r_P}(\theta_N - \theta_S) , \\ B_W &= \frac{1}{8}\,\frac{r_P + r_W}{r_P - r_W}(\theta_N - \theta_S) , \\ B_N &= \frac{1}{4}\cdot\frac{1}{r_P}\cdot\frac{r_E - r_W}{\theta_N - \theta_P} , \\ B_S &= \frac{1}{4}\cdot\frac{1}{r_P}\cdot\frac{r_E - r_W}{\theta_P - \theta_S} . \end{aligned} \qquad (11.6)$$

The appropriate integrated source term (I_S) for each equation is given by:

a) Source term for Vorticity Equation

$$I_{S\omega}|_P = \int_{r,w}^{r,e} \int_{\theta,s}^{\theta,n} (d\phi) r \, dr \, d\theta \quad ,$$

Integrating the equation yields:

$$I_{S\omega}|_P = -d\phi_P \cdot V_P \quad , \tag{11.7}$$

where,

$$V_P = \int_{r,w}^{r,e} \int_{\theta,s}^{\theta,n} r \cdot dr d\theta \quad ,$$

hence

$$V_P = \frac{1}{16}(\theta_N - \theta_S)[(r_E + r_P)^2 - (r_P + r_W)^2] \tag{11.8}$$

and $d\phi$ is defined in Table 3 for ω equation. In order to calculate the complicated term $d\phi_P$, the same differentiation scheme presented in section (7.4) was used. Normal stress terms were considered first for the sake of comparison with similar work in literature, but the recommended scheme includes both the normal and shear stresses source terms. Detailed analysis of the vorticity production term is given in the discussion of results since it plays a major role in achieving convergence.

b) Source term for stream function

From the stream function transport equation:

$$I_{SS}|_P = \int_{r,w}^{r,e} \int_{\theta,s}^{\theta,n} \omega r \, dr \, d\theta$$

Integrating the equation yields:

$$I_{SS}|_P = -\omega_P \cdot V_P \quad , \tag{11.9}$$

where V_P is given by (11.8).

c) Source term for axial momentum equation

The term is given by:

$$I_{SU}|_P = \int_{r,w}^{r,e} \int_{\theta,s}^{\theta,n} \frac{\partial P}{\partial x} \, r dr \, d\theta \quad ,$$

which yields:

$$I_{SU}|_P = \frac{\partial P}{\partial x} \cdot V_P \, , \tag{11.10}$$

where V_P is also given by (11.3), and $\frac{\partial P}{\partial x}$ is given by equations (10.13) and (10.14).

d) Source term for turbulent kinetic energy equation.

Similar analysis yields:

$$I_{SK}|_P = d\phi_{kP} \cdot V_P \tag{11.11}$$

where V_P is given by (11.8), and $d\phi_P$ is defined in Table 3 for k equation as:

$$d\phi_{kP} = (d\phi_1 - d\phi_2)_P,$$

where

$$d\phi_1|_P = -\mu_{tP}[(\frac{\partial \bar{U}}{\partial r})^2 + (\frac{\partial \bar{U}}{r\partial \theta})^2]_P \quad ,$$

$$d\phi_2|_P = -\frac{\rho C_D \, k_P^{3/2}}{\ell_P} \tag{11.12}$$

The term $d\phi_{2|_P}$ may vary so widely as to cause divergence due to the power 3/2 associated with k_P in it, which was true in the early stages of computations. Gosman et al[39] recommended some re-arrangement of the substitution formula for turbulence kinetic energy to reduce these variations. This approach was adopted here for its simplicity and effectiveness in achieving convergence. The term $d\phi_{2|_P}$ may be written as:

$$d\phi_{2|_P} = k_P \cdot (C_D \rho k^{1/2}/\ell)_P = k_P \cdot d\phi'_{2|_P} . \qquad (11.13)$$

The substitution formula of k then becomes:

$$k_P = C_E k_E + C_W k_W + C_N k_N + V_P(d\phi_1 - k_P\, d\phi'_2)_P/\Sigma_{AB} . \qquad (11.14)$$

Rearranging (11.14) yields:

$$k_P = \frac{C_E k_E + C_W k_W + C_N k_N + C_S k_S + V_P(d\phi_1)_P/\Sigma_{AB}}{1 + V_P(d\phi'_2)_P/\Sigma_{AB}} \qquad (11.15)$$

where in this new formula, the variations in the modified source term is much less than in the original one.

11.3. The Finite Difference Grid

A uniform grid was chosen for the peripheral direction with spacings determined by the radius of specific string of nodes, and the increment $\Delta\theta$ as 2°. This assumption is based on the absence of large gradients for any property in that direction. For MVL, the grid points were chosen on that boundary such that if at $P'/2$ the radius is r_L, then r_{L+1} is given by:

$$r_{L+1} = \frac{P'/2}{\cos\theta_1}$$

The general term will be:

$$r_{L+n} = \frac{P'/2}{\cos \theta_n} \quad ,$$

where n varies from 1 to 15 corresponding to values of θ from $2°$ to $30°$ respectively. The grid spacing in the radial direction was chosen such that the nodes are closely spaced near the wall where the variables have steep gradients, and then increases irregularly to fill the gap region. The number of strings of nodes varied from 26 to 33 for P'/D ratios of 1.123 to 1.35 respectively. The grid spacing near the wall was carefully designed for the range of Reynolds number involved in the computations since the friction velocity varies considerably with Reynolds number. For all the cases, the first string of nodes in the fluid was always beyond the viscous sublayer and varied with Reynolds number such that Y^+ was always in the range:

$$30 \leq Y^+ \leq 50$$

In the computer program, the peripheral direction is given the subscript J which varies from 1 at $\theta = 0°$ to 16 at $\theta = 30°$, while the radial direction is given the subscript I which varies from 1 at the wall to M at the center of the subchannel. The different notations are presented and defined in figure (11.2).

11.4. Boundary Conditions

a) Solid wall

For the solid wall extending from the radial boundaries $\theta = 0°$ to $\theta = 30°$, the analysis is exactly the same as section (7.5.4) except that z_2 and z^+_2 are replaced by Y_2 and Y^+_2, where Y is the radial distance from the surface of the rod to the first node in the fluid

at any angle θ, and Y^+ is the dimensionless distance defined by (10.19).

b) The boundaries $\theta = 0°$ and $30°$

On both boundaries, the vorticity and stream function were set to zero on all the nodes. For both $\bar{U}$ and k, the gradients given by (10.23) and (10.24) were set to zero by simply assigning the values at the nodes on a radial line adjacent to the boundary to the corresponding nodes on the boundary. This may be written for $\theta = 0$ as:

$$\bar{U}_{i,j} = \bar{U}_{i,j+1} \tag{11.16}$$

and for $\theta = 30$ as:

$$\bar{U}_{i,j} = \bar{U}_{i,j-1} \tag{11.17}$$

and similarly for k. This assumption is considered reasonable, since it is not expected to have large gradients in the peripheral direction for both $\bar{U}$ and k near both boundaries.

c) MVL boundary

On MVL boundary, the vorticity and stream function were set to zero on all the nodes. Equation (10.27) is expressed in finite difference form by:

$$\frac{\bar{U}_{i,j} - \bar{U}_{i-1,j}}{r_i - r_{i-1}} = \frac{\bar{U}_{i,j+1} - \bar{U}_{i,j}}{r_i(\theta_{j+1} - \theta_j)} \tan \theta_j \ ,$$

which yields after rearranging:

$$\bar{U}_{i,j} = \frac{C_j \bar{U}_{i,j+1} + \bar{U}_{i-1,j}}{C_{j+1}} \ , \tag{11.18}$$

where,

$$C_j = \frac{r_i - r_{i-1}}{r_i(\theta_{j+1} - \theta_i)} \tan \theta_j \tag{11.19}$$

Similarly, equation (10.28) may be expressed in the form:

$$k_{i,j} = \frac{C_j\, k_{i,j+1} + k_{i-1,j}}{C_{j+1}} \qquad (11.20)$$

where C_j is given by (11.19).

11.5. Interative Technique

The same technique presented in section (7.6) was also used here to solve the set of equations for rod bundle geometries. The grid was systematically scanned node by node in a destructive manner. Both radial and peripheral scanning was investigated. Scanning in the peripheral direction was from the radial line $j = 2$ to the radial line $j = n - 1$, where n corresponds to $\theta = 30°$. After scanning one string of nodes, consecutive strings were scanned similarly up to the string corresponding to $r = P'/2$. At this point, for the next string, scanning starts from j_3 to j_{n-1}, then from j_4 to j_{n-1} and so on. For radial scanning, the procedure was started from $i = 2$ up to a node on the same line just before the MVL boundary. The next radial line is then scanned and so on up to and including the radial line j_{n-1}. Both scanning methods gave identical solutions, but the radial scanning provided faster convergence, particularly for the lowest P'/D. Nonetheless, it should be noted that for large P'/D, the peripheral scanning may provide faster convergence, since the speed of convergence depends mainly on the speed of transfer of data between the boundaries. Nash and Patel[85] proposed an alternating scanning technique to speed convergence by repeatedly scanning the grid first circumfrencially then radially. This method accelerates the transfer of data between the four boundaries. However, it was not applied in the present scheme, although it may be recommended for cases in which convergence is very slow.

Convergence was achieved for the case of $P'/D = 1.123$, and water as a working medium. No condition was imposed on the vorticity production first, since there was no confidence in any data on secondary velocities. Convergence was achieved also for a similar case with air as a working medium. For both cases, one swirl of secondary flow was predicted with clockwise rotation. Similar results were obtained for different P'/D ratios. To accelerate the convergence, a condition similar to the one discussed in section (7.6) was imposed on the vorticity source term. Details of both predictions are discussed in Chapter XII. The initial conditions used are similar to those of section (7.8).

11.6. Convergence Criterion

Due to the very slow convergence, particularly for the cases that included the whole vorticity source term, a convergence criterion of the form,

$$\left| \frac{\phi^{(n)} - \phi^{(n-1)}}{\phi^{n-1}} \right|_{max} \leq \lambda ,$$

was used, with $\lambda = 0.001$ for both $\bar{U}$ and k. For economy reasons, $\lambda = 0.002$ was used for both ω and ψ. It is noted that Gosman et al[39] for a similar convergence criterion recommended values of λ in the range from 0.001 to 0.005. When the condition was imposed on the vorticity source term (chapter 12), it was possible to achieve smaller residuals for ω and ψ ($\lambda = 0.001$) without increasing computer time. Provision for over or under relaxation to the vorticity is provided in the same manner discussed in section (7.6). Similar observations to those of Gosman et al[39] indicated that over-relaxation of ω leads always to divergence, while under relaxation slightly increases the stability of the solution. The latter was used in conjunction with studying the effect of the vorticity production term on the convergence.

CHAPTER 12

NUMERICAL PREDICTION RESULTS AND DISCUSSION

12.1. General

The predicted results are compared where possible to the corresponding experimental and numerical results available in literature. For the mean velocity, turbulent kinetic energy and local wall shear stress distributions, comparisons are presented with the experimental results of Kjellstrom[18] for $P'/D = 1.217$ and Trupp and Azad[22] for $P'/D = 1.2$ and 1.35. For P'/D of 1.123, comparisons are presented with the experimental and predicted results of Carajilescov[86] and Carajilescov and Todreas[23]. Concerning secondary velocities, the only experimental data available in the literature were those of Kjellstrom[18] (very scattered) and Hall and Svenningsson[19] who recommended further investigation using a more advanced technique since their measurements showed that the flow crossed the primary flow cell boundaries. This was probably the result of either systematic error or finite array effects. However, their measurements of the radial distribution of the peripheral secondary velocity $\bar{V}_\theta$ in two primary flow cells at $\theta = 0°$, 15°, 30°, 45° and 60° indicated $\bar{V}_\theta$ to be about 1% of the bulk average axial velocity for $P'/D = 1.217$ at a Reynolds number of 270,000. In general, it was concluded that the experimental data on secondary velocities are very sparse and too unreliable to allow for any comparison with the model results. Experimental errors may occur from several sources; for example, from finite array effects, inaccuracies in constructing the different test sections, inaccuracies in the hot wire systems, signal processing instruments and traversing mechanisms, and blockage effects that might disturbed the

flow in the limited cross-section of a primary flow cell particularly for small P'/D ratios. It was therefore decided that any tuning of the constants of the model would be based on experimental data for mean axial velocity, mean turbulent kinetic energy and wall shear stress, since these distributions are available in the literature with reliable accuracies.

Numerically, Carajilescov and Todreas[23] were the only investigators to predict the secondary velocities in rod bundle arrays, but their results were not confirmed experimentally. Considerable differences exist between their prediction and this research particularly as regards the number of swirls in a primary flow cell.

Before undertaking any comparison, a study of the vorticity production term was made to inspect its effect on convergence. The case chosen was for P'/D = 1.123 and Reynolds number of 27,000 for which Carajilescov and Todreas[23] predicted two secondary flow cells. Only the terms containing normal stresses were allowed for in the vorticity production (the same as Carajilescov and Todreas[23]) with both positive and negative signs, as given by (11.7, 11.8, 10.2 and Table 3). Convergence was achieved after a large number of iterations (1800 iterations) with the criterion given in section (11.6). The residuals for $\bar{U}$ and k smoothly approached the prescribed value of λ, while the residuals for ω and ψ oscillated up to about the 900 th iteration and then started to converge with damped oscillations. Under-relaxation of ω helped to reduce these oscillations, but the final solution (obtained with more computer time) was the same. Convergence was impossible to achieve when shear terms were included in the vorticity production due to oscillations of the ω and ψ residuals. Carajilescov[86] did not comment on the convergence process itself or the effect of the vorticity production

terms on convergence, however the same difficulties may have been encountered.

The predicted secondary flow was only one swirl with a clockwise rotation (ω and ψ had negative signs relative to the prescribed coordinate system), which is contrary to the prediction of Carajilescov and Todreas[23]. The limiting case (P'/D = 1.0) is similar to the equilateral triangular duct case which indicated (experimentally) only one swirl in each primary flow cell. Predictions of large P'/D (this work and Carajilescov[86] by extrapolation) indicated also one swirl only. A conclusion was therefore drawn that there should be one swirl in a primary flow cell for all P'/D for infinite triangular arrays. These secondary flows transport the fluid from the center of the subchannel (high momentum region) via the MVL, with the return flow along the wall and the $\theta = 30°$ boundary. This conclusion confirms the proposal of Trupp and Azad[22] which was based on experimental evidence employing the momentum and mean energy equations. It is interesting to report that during the early stages of computations (typically before the 800th iteration for this specific case), the fields of ω and ψ indicated two swirls in a primary flow cell. Although the residuals of $\bar{U}$ and k were below λ at this stage, the residuals of ω and ψ were still above λ and oscillated far from a converged solution. The two fields (ω and ψ) then started to converge towards one cell. Several trials made with different initial conditions behaved similarly. This suggests that Carajilescov and Todreas[23] may have accepted an early solution which was not fully converged. According to the above investigators, they used a convergence criterion similar to (7.34) with $\lambda = 0.0001$, whereas for this specific criterion, Gosman et al[39] reported that λ should be

from 0.00001 to 0.00005. Other differences between the two prediction schemes mainly as related to boundary conditions are discussed in sections (10.4 and 12.2).

Prediction of a one clockwise swirl suggested that a condition similar to the one rationalized in section (7.6) is allowable for the vorticity production source term. This was tested by allowing only negative vorticity production terms (which produce clockwise swirl), with all positive terms set to zero. Convergence was faster (about half the number of iterations) and much more stable. The residuals of $\bar{U}$, k and ψ decreased smoothly, while the residual of ω oscillated with smaller amplitudes than the previous case (particularly early in the computations). Although the mean flow characteristics were in fair agreement with the first prediction results, the secondary flow levels were somewhat higher. It is interesting to note that changing the constants of the model C_1 and C_2 in such a way that $C = 0.01$ (the value suggested by Launder and Ying[2] for square duct) for the first case, resulted in secondary flow levels that compared well with the second case for which $C = 0.006$. This is shown in figure (12.1). The agreement between the two cases was fairly reasonable for the mean axial velocity and turbulent kinetic energy distributions as shown in figures (12.2 - 12.7) inclusive for $\theta = 0$, 15 and 30 degrees. In view of this outcome and since the secondary flow levels were not known experimentally, it was finally decided for economy reasons to use the second method for which a condition was imposed on the vorticity source term. Convergence was also achieved by this method when shear stress terms were included in the vorticity production. The last method (full vorticity production) was used for all subsequent predictions and provided reasonable agreement with the experimental

measurements as is shown in the following sections.

12.2. Prediction for P'/D = 1.123

12.2.1 Vorticity and Stream Function

The vorticity and stream function distributions are presented in figures (12.8) and (12.9) as derived using different vorticity production source terms. In one case, the normal stress term only was applied. In the second case, both normal and shear stress terms were retained. The vorticity distributions were qualitatively similar for both cases. Figure (12.8) shows the result for full source. The sign appearing on the contours indicates the secondary flow is clockwise in this particular primary flow cell. Due to the absence of a corner in such a geometry, it is interesting to note that the position of the maximum non-dimensional vorticity is shifted away from the wall and from the gap region. A comparison of the stream function distributions for both cases is afforded by figure (12.9). The two distributions are similar near the gap region, but differ significantly near the maximum value locations. Obviously, in both the triangular duct and rod bundle geometries, the maximum differences occur where the vorticity is maximum. This has the effect of under-estimating the secondary velocities magnitude in these regions if only the normal stress terms were used as shown in figure (12.10). This suggests that normal stress vorticity production terms predominate over most of the flow cell, except for the central region where the shear stress terms contribute significantly.

12.2.2. Secondary Velocities

The secondary velocity component $\bar{V}_\theta$ predicted at different θ values are given in figure (12.10). Both secondary velocity components

$\bar{V}_r$ and $\bar{V}_\theta$ contours are shown more fully in figures (12.11 and 12.12). These distributions show a maximum value of the secondary velocity component $\bar{V}_\theta$ in the return flow (close to the wall) of about 1.4% of the average bulk velocity U_b. This value is high as compared to the prediction of Carajilescov and Todreas[23] for the same P'/D, but they had predicted two secondary flow cells.

Due to lack of accurate secondary flow measurements, it is impossible to judge the accuracy of these levels. Once established by reliable measurements, the turbulence model constants could be easily optimized to predict the actual secondary flow levels. In such a case, it may be necessary to modify the model by assuming anisotropic eddy viscosity in order to balance the effect of reducing the secondary flow levels on the mean axial velocity distributions. As mentioned earlier, the turbulence model constants were optimized to predict reasonable mean axial velocities, assuming locally isotropic eddy viscosities. This simplified assumption was employed due to the uncertainties of both secondary flow levels and the peripheral eddy viscosity.

12.2.3. Mean Axial Velocity Distributions

Figures (12.13 - 12.15) show comparison of the predicted mean axial velocity distributions with previous measurement and predictions (58, 86), at $\theta = 0°$, $15°$ and $30°$ respectively. The present predictions compare well with the experimental data over most of the subchannel. A maximum difference of 4% occurs in the gap region. This may be attributed (as discussed by Carajilescov[86]) to an error of the measurements in this region. Descrepancies between the prediction and the distributions of Ibragimov[58] are mainly a result of neglecting secondary flows in his technique.

12.2.4. Turbulent Kinetic Energy Distributions

The predicted turbulent kinetic energy distributions are compared with the measurements and prediction of Carajilescov[86] in figures (12.16 - 12.18), for $\theta = 0°$, $15°$ and $30°$ respectively. It is evident from these comparisons that the measurements and predictions of Carajilescov[86] are lower in levels than the prediction of this research, particularly for $\theta = 30°$. As indicated in the figures, he had to adjust the turbulence model constants C_ν and C_D to have agreement with his measurements which presumably are low. This will be discussed further in conjunction with the work of Kjellstrom[18] in the next section. In general, all the distributions are qualitatively similar, with the turbulent kinetic energy peaking near the solid wall with a maximum value on the boundary at $\theta = 30°$.

12.2.5. Local Wall Shear Stress

A comparison between the predicted local wall shear stress distribution and the distribution predicted by Carajilescov and Todreas[23] is affored by figure (12.19). Their distribution is shown to be slightly flat compared to this work, although they have predicted lower secondary velocities levels. This inconsistency may be attributed to their method of applying the boundary conditions near a solid wall for the mean axial velocity. They have extrapolated the velocities at the first two strings of nodes in the fluid linearly to a fictitious set of nodes located at $Y^+ = 30$. In the present work, the universal law of the wall given by equation (10.18) was used, with the local wall shear stress calculated from the turbulence field by equation (10.19a). From figure (12.19), it is evident that the maximum wall shear stress does not occur on the wall at $\theta = 30°$ as the cases predicted without secondary flows,

but is shifted to a point between $\theta = 20°$ and $25°$ (depending on Reynolds number).

12.3. Prediction For P'/D = 1.2

Figures (12.20) and (12.21) show the vorticity and stream function contours for a Reynolds number of 49,100. The values of ψ are lower than the previous case of P'/D = 1.123 which confirms the proposals of several investigators that the secondary flow becomes weaker with increasing P'/D. The effect of the shear stress term on the distribution of ψ is less than the previous case. It is shown also that the penetration of the contours towards the gap is slightly more than for P'/D = 1.123; this will be discussed in details in section 12.5.

Comparison of the mean axial velocity contours with an experimental contour plot of Trupp and Azad[22] is made in figure (12.22). The agreement is very good except for regions close to the MVL boundary. A maximum difference of about 1% occurs near the center of a subchannel. It is very interesting to observe that although only one swirl was predicted in the primary flow cell with clockwise rotation, the deformation in the predicted contours are similar to the experimental ones near the gap. This indicates that these deformations are mainly a result of the weakness of the secondary flows in that region, and not due to an additional swirl with opposite direction to the first one[86]. This conclusion is consistent with the role of secondary flows which act in the plane of the cross-section and transport the fluid from the high momentum regions to the low momentum regions near the gap.

The mean axial velocity distributions predicted at different θ values are presented in figures (12.23 - 12.25) and compared to those of Carajilescov[86] and to the experimental data of Kjellstrom[18] for

P'/D = 1.217 and Reynolds number of 149,000. The present prediction provides slightly better agreement than that of Carajilescov[86] compared to the experiment, for the three θ positions of 0°, 15° and 30°. The same applies for the turbulent kinetic energy as shown in figures (12.26 - 12.28) at the positions θ = 0°, 18° and 30° respectively. Here, the agreement of this work with the measurements of Kjellstrom[18], particularly for θ = 0° and 18°, supports the observations made in section (12.2.4), and suggests that the levels of k in Carajilescov's[86] work were probably affected by a systematic error. The predicted distributions were compared also to the measurements of Trupp and Azad[22] for a Reynolds number of 49,100 in figure (12.29). Their turbulent kinetic energy are lower than both Kjellstrom's[18], measurements and this work; this may be attributed to either geometrical effects and probe interference or to the lower sensitivity of their DISA 55D05 hot wire anemometer. The first factor is thought to be the main reason, since the agreement between both distributions for P'/D = 1.35 (section 12.4) was found fairly reasonable.

Comparison of the predicted local wall shear stress distribution with those of Trupp and Azad[22] for a Reynolds number of 49,100 and Subbotin et al[17] for the range of 35,000 - 115,000 is given in figure (12.30). The predicted distribution is also compared to those of Kjellstrom[18] and Carajilescov and Todreas[23] for a Reynolds number of 250,000 in figure (12.31). From both figures, it is evident that there are no quantitative agreement between any two distributions, although qualitative similarity existed which indicates the effect of secondary flows. The best qualitative agreement with the present research was with the distribution of Subbotin et al[17] for P'/D = 1.2. More details on

the effect of Reynolds number on the wall shear stress distribution are presented in section (12.5).

The secondary velocity component $\bar{V}_\theta$ is given for Reynolds number of 149,000 as compared to the scattered data of Kjellstrom[18] and the prediction of Carajilescov and Todreas[23] in figure (12.32). As discussed before, the actual levels are not certain, however, the predicted distributions are in the range of the scattered points of Kjellstrom[18]. The maximum value of $\bar{V}_\theta$ was predicted along the MVL for this P'/D ratio.

12.4. Prediction For P'/D = 1.35

The vorticity and stream function contours predicted for P'/D = 1.35 and Reynolds number of 48,130 were qualitatively similar to the previous cases for the same Reynolds number, but the absolute values were lower here as expected. No figures are presented for these contours, however the secondary velocity component $\bar{V}_\theta$ is compared to the previous cases of P'/D = 1.123 and 1.2 in section (12.5). The maximum value of $\bar{V}_\theta$ was also found to occur along the MVL boundary similar to P'/D = 1.2.

Comparisons of the mean axial velocity distributions with those of Trupp and Azad[22] are presented in figures (12.33 - 12.35) and shown to be in good agreement. The maximum difference occurs (as for all previous comparisons) near the subchannel centerline however, this difference lies within the range of the experimental error.

The mean turbulent kinetic energy is compared to the results of the same investigators in figure (12.36). Since the comparison is fairly reasonable with both their work and that of Kjellstrom, it can be suspected that measurements for the lower P'/D were not as reliable as those for P/D = 1.35 because of geometrical effects and probe interference. Another

possibility as related to the turbulence model itself is that the locally isotropic eddy viscosity assumption is more suitable for large P'/D rather than small values.

Comparison of the wall shear stress distributions for both cases is given in figure (12.37). The qualitative agreement is not satisfactory, however, the experimental axial velocity contours presented by Trupp and Azad[22] for the same P'/D suggests that the wall shear stress must be close to a uniform distribution. In any event, the two distributions are quantitatively within ≈ 3% from each other. More details on this difference and the effect of Reynolds number and P'/D ratios on the wall shear stress are presented in the next section.

12.5. Effect of Reynolds Number And P'/D Ratio

Friction factor dependence on Reynolds number for the range of 27,000 to 250,000 is presented in figure (12.38) for P'/D = 1.2 as compared to the smooth tube given by Blasius equation and the prediction of Carajilescov[86]. In figure (12.39) comparisons are presented for P'/D = 1.123, 1.2 and 1.35 with the experimental points of Trupp and Azad[22] obtained for P'/D = 1.2, 1.35 and 1.5. It is evident that the agreement between the predictions and the experiments is reasonable if viewed in terms of percentage differences. Contrary to the square and triangular ducts (section 8.7), friction factors for the same Reynolds numbers for a triangular array of rods are larger than the corresponding ones for smooth tube in the range of P'/D considered. For the same Reynolds number, friction factors are shown to increase with P'/D. By reducing P'/D, friction factors approach the smooth tube line (apparently by about P'/D = 1.10) and then decrease close to the triangular duct values at the limiting aspect ratio of P'/D = 1.0. These conclusions are

consistent with the findings reported by several investigators[87, 88].

The effect of increasing Reynolds number on the secondary velocities and wall shear stress distributions are examined with figures (12.40) and (12.41) respectively. It is evident that the secondary velocity component $\bar{V}_\theta$ when normalized with the average bulk velocity, increases with Reynolds number for the two cases of Reynolds number of 27,000 and 200,000 presented in figure (12.40). This dependence tends towards a limit as the wall shear stress becomes more uniform, and further increase in Reynolds number may cause a reduction of the same normalized component. Increasing Reynolds number is shown in figure (12.41) to shift the position of the peak value of τ to lower θ values due to the increase of secondary velocities; these in addition act to flatten the τ distribution by increasing the wall shear stress in the gap region.

For a given Reynolds number, the wall shear stress was found to follow a certain trend with increasing P'/D ratio. From figure (12.42), for P'/D = 1.123, the local wall shear stress at $\theta = 0°$ is much smaller than the one at $\theta = 30°$ and the peak value. By increasing P'/D, the wall shear stress tends to become more uniform. This behaviour is linked to the secondary flow. The distributions of the velocity component $\bar{V}_\theta$ are given in figure (12.43) for the same Reynolds number for the three P'/D ratios. For P'/D = 1.123, the secondary flow is unable to penetrate significantly into the gap region. Increasing P'/D to 1.2 permits more secondary flow to penetrate into the gap which acts to equalize the wall shear stress along the wall. A further increase of P'/D to 1.35 may allow more penetration, but the levels are now much lower in magnitudes as indicated in figure (12.43). The reason for the slight overshoot of the wall shear stress at $\theta = 0°$ for P'/D = 1.35

as shown from figures (12.37) and (12.42) may be attributed to a slightly high secondary flow in the gap region. This probably is a result of using the same constants in the turbulence model for the three P'/D ratios. It should be noted that these constants may provide better predictions for small P'/D ratios, which are more close to the triangular duct case for which the constants were first optimized.

Generally, it is evident that the secondary flows become weaker with increasing P'/D, and presumably will vanish for sufficiently large P'/D values (Probably P'/D > $\tilde{}$ 1.5) as shown in figure (12.44). In this figure, the secondary velocity component $\bar{V}_\theta$ at a specific point is plotted as function of P'/D and extrapolated to obtain the value of P'/D at which $\bar{V}_\theta = 0$.

CHAPTER 13

CONCLUSIONS AND RECOMMENDATIONS FOR FUTURE WORK

A) Equilateral Triangular Ducts

The following conclusions are based on the results of Part I and are applicable to fully developed turbulent flows in equilateral triangular ducts for Reynolds numbers in the range of 5×10^4 to 2×10^5.

(i) The secondary flow pattern observed by Nikuradse[24] was confirmed by direct measurements of the $\bar{V}$ and $\bar{W}$ components. For each of the six counter-rotating flow cells, the pattern is such that the flow is directed from the center of the duct to the corner via the corner bisector. The return flow is along the wall and the wall bisector. The $\bar{V}$ component of the secondary velocity has a maximum strength of about $1\frac{1}{2}\%$ of U_b in the return flow along the wall.

(ii) The turbulence fields are clearly influenced by the presence of secondary flows. The effect on the turbulent kinetic energy field is more pronounced than on the axial velocity field.

(iii) Anisotropy of the normal Reynolds stresses produces negative vorticity production (in the cell identified in Chapter 4) which is mainly responsible for generation of the secondary flow. Model IIb results indicate that the shear stress $\rho\overline{vw}$ gradients contribute significantly to vorticity production in the corner region. Although the vorticity production contours are qualitatively similar to those of Brundrett and Baines[8] for a square duct flow, the magnitudes are considerably higher particularly

near the corner.

(iv) The shear stress $\rho\overline{uw}$ predominates over most of the duct cross-section; the exception is the corner region where $\rho\overline{uv}$ is comparable in magnitude.

(v) The negative region of $\overline{uv}$ near the mid-wall plane is consistent with the concept of a positive eddy viscosity since the mean velocity gradients in the Y-direction change their signs upon entering this region due to the secondary flow effect on the isovels. This conclusion is also consistent with the findings of Melling and Whitelaw [13] for square duct flows.

(vi) Predictions with an experimental vorticity production term are not practical, since such schemes require a different input for each case. Errors usually are introduced from the numerical differentiation of the small values obtained from the difference of two large values each containing experimental error. The resultant distribution usually requires smoothing.

(vii) Successful flow predictions without experimental input to the vorticity equation can be achieved by expressing the turbostresses in the plane of the cross-section by gradients in the mean axial velocity (Launder-Ying Model). Both normal and shear stress terms must be included in the vorticity production source term in order to provide accurate prediction in the corner region.

(viii) Accurate predictions of mean axial velocity and local wall shear stress distributions require the use of local friction velocities in the law of the wall as a boundary condition.

(ix) The Buleev formula for turbulence length scale is adequate for the equilateral triangular duct providing (for negative vorticity

production only) the value of 0.006 is assigned to C in (6.26) by adjusting C_1 and C_2 in (6.27) in their allowable ranges.

(x) Due to momentum transport by secondary flows, the predicted wall shear stress over the central half of each wall is constant to within a few percent. The effect of Reynolds number on the normalized wall shear stress distribution is not significant in the range considered.

(xi) The predicted friction factors agree with the measurements of Gerrard[1]. They are 5% to 6 1/2% lower than those predicted by Blasius equation and similar to the prediction by the "Universal Criterion Relationship" proposed by Malak et al[84].

(xii) For the heat transfer prediction, the isotherms are qualitatively similar to the isovels and are affected by the secondary flow. The local heat flux distribution along the wall is similar to the local wall shear stress distribution with a peak value at $Y/L \tilde{\simeq} 1/3$. The predicted results also indicate that equilateral triangular ducts and square ducts have a similar $St - R_e$ relationship.

Generally, for the fully developed situation, the one-equation model is fairly reasonable in predicting the flow characteristics as compared to the experimental results down to the secondary flow levels.

As a further application of the recent model (IIb), the author recommends studying fully developed flows in a series of isosceles triangles with different aspect ratios. In such cases, a cross-section is treated as only two symmetrical primary flow cells. This study will help to fully understand the flow characteristics in triangular ducts in

particular and non-circular conduits in general. Once fully developed flows are well established, studying the developing flow of an equilateral triangular duct may prove advantageous as a first step towards studying the developing flow in equilateral triangular array rod bundles sub-channels (the practical case). Since the last flow is three-dimensional, a two-equation model (e.g., the k-ε model) is more adequate than the present one-equation model.

B) Equilateral Triangular Array Rod Bundles

The following conclusions are based on the predicted results of Part II and are applicable to fully developed turbulent flows in equilateral triangular array rod bundles for Reynolds numbers in the range of 3×10^4 to 3×10^5.

(i) The predicted secondary flow pattern in a primary flow cell for any P'/D ratio consists of a single secondary flow cell (with a clockwise rotation for the cell considered). These secondary flows transport the fluid from the high momentum region near the sub-channel centerline to the low momentum region near the gap along the MVL boundary. The return flow is along the boundary $\theta = 0°$, the rod surface and the boundary $\theta = 30°$. Maximum values of the component $\bar{V}_\theta$ were predicted near the rod surface in the return flow for the smallest P'/D (1.123). For $P'/D = 1.2$ and 1.35, the maximum values were predicted near the MVL boundary.

(ii) The magnitudes of the secondary flows decrease dramatically with increasing P'/D ratio. For the same Reynolds number, the maximum predicted $\bar{V}_\theta$ decreased (for $Re = 27{,}000$) from about 1.4% of U_b for $P'/D = 1.123$ to about 0.5% for $P'/D = 1.35$, and

may vanish for $P'/D > \sim 1.5$. For P'/D less than 1.123, the maximum value of $\bar{V}_\theta$ probably continues to increase with decreasing P'/D and may approach a value in excess of that for an equilateral triangular duct (1.5%) at or near the limiting ratio $P'/D = 1$.

(iii) The secondary velocities normalized with the bulk average velocity U_b increase with Reynolds number for a given P'/D throughout the range of P'/D considered. The rate of increase decreases with Reynolds number.

(iv) The effect of the secondary flow is evident on the mean axial velocity, turbulent kinetic energy and wall shear stress distributions. It acts to homogenize the wall shear stress along the rod surface by (relative to no secondary flow) increasing the local values of τ near the gap and shifting the peak value away from $\theta = 30°$. For a given P'/D, the wall shear stress distribution becomes more uniform with increasing Reynolds number due to increase in secondary flows.

(v) For the same Reynolds number, the wall shear stress distribution becomes more uniform with increasing P'/D ratio due to increased penetration of the secondary flow into the gap region. However, for increasing P'/D beyond about 1.35, the magnitudes of the secondary flow become gradually smaller (item ii) and the uniformity of τ is mainly a result of the system approaching that of a free cylinder in an axial stream of fluid.

(vi) Friction factors are function of both P'/D ratio and Reynolds number. For a given P'/D, friction factors decrease with Reynolds number as is usual for channel flows. For the same

Reynolds number, friction factors increase with P'/D ratio. For $P'/D > \sim 1.1$[87] friction factors lie above the smooth tube values given by Blasius equation. For $P'/D < \sim 1.1$, friction factors lie below the smooth tube values and presumably are similar to the triangular duct values at the limiting case of $P'/D = 1.0$.

(vii) Comparison of the predicted parameters with corresponding experimental work of several investigators indicate that the one-equation model provides reasonable predictions for the fully developed flow situation.

The locally isotropic eddy viscosity assumption was employed in the present research due to the uncertainty of the peripheral eddy viscosity in rod bundle geometries. The constants used in the turbulence model were the same as those used for the triangular duct flow. This may imply that predictions for small P'/D ratios are more accurate than predictions for large P'/D ratios due to the similarity of the first with the triangular ducts. However, there are some uncertainties concerning the secondary flow magnitudes and the turbulence length scale (the distribution of ℓ was proposed[23] for $P'/D = 1.123$).

The author feels that more experimental data is urgently needed on secondary flows magnitudes and patterns for several P'/D ratios, which may require developing new secondary flow measurement techniques and instrumentation. Anisotropy of the eddy viscosity may be then included and optimized to yield accurate predictions on both mean axial and secondary velocities levels. The same success may be achieved if reliable measurements of the peripheral eddy viscosity can be made to allow for the perfect anisotropy factor.

The two-equation model appears very promising for any future work since it can predict the developing flow along the sub-channel. However, it should be tested first for the fully developed flow situation. It is clear that it still needs informations on the peripheral eddy viscosity to allow for the anisotropy factor in the model. The author suspects that overestimating this anisotropy factor may produce the same effect of secondary flow on the mean velocity-field (and hence wall shear stress distribution), although the mechanism is different. This leads to an erroneous secondary flow prediction with very low levels.

Once a model is established, heterogeneous sub-channels are the logical next step to investigate to predict the diversion cross flow between two adjacent sub-channels. Extension of the model to include heat transfer for prediction of local surface temperatures is a following practical application.

REFERENCES

1. A.D. Gerrard: "Turbulent Flow in an Equilateral Triangular Duct", M.Sc. Thesis, U. of Manitoba, 1976.

2. B.E. Launder and W.M. Ying: "Prediction of Flow and Heat Transfer in Ducts of Square Cross-Section", Proc. Inst. Mech. Engrs., Vol. 187, 37/73, 1973.

3. J. Nikuradse: "Untersuchungen uber die Geschwindikeitsverteitung in Turbulenten Stromungen", Ph.D. Thesis Gottingen, 1926, Also VDI-Forschungsheft 281, Berlin, 1926.

4. L. Prandtl: "Proc. Second Int. Congr. of Applied Mech., 1926, p. 71 et seq Zurich, 1927 (Also translated as NACA TM-435).

5. S.H. Maslen: "Transverse Velocities in Fully Developed Flows", Quarterly of Applied Mathematics, Vol. 16, p. 173, 1958.

6. L.C. Hoagland: "Fully Developed Turbulent Flow in Straight Rectangular Ducts - Secondary Flow, its Causes and Effect on the Primary Flow", Ph.D. Thesis, Massachusetts Institute of Technology, 1960.

7. H.J. Leutheusser: "Turbulent Flow in Rectangular Ducts", Amer. Soc. of Civil Engrs., J. of the Hydraulics Division, Vol. 89, No. HY3, pp. 1-19, May, 1963.

8. E. Brundrett and W.D. Baines: "The Production and Diffusion of Vorticity in Duct Flow", J. Fluid Mech., Vol. 19, pp. 375-394, 1964.

9. F.B. Gessner: "The Origin of Secondary Flow in Turbulent Flow Along a Corner", J. Fluid Mech., Vol. 58, Pt. 1, pp. 1-25, 1973.

10. F.B. Gessner and J.B. Jones: "On Some Aspects of Fully Developed Turbulent Flow in Rectangular Channels", J. Fluid Mech., Vol. 23,

Pt. 4, pp. 689-713, 1965.

11. B.E. Launder and W.M. Ying: "Secondary Flows in Ducts of Square Cross-Section", J. Fluid Mech., Vol. 54, Pt. 2, pp. 289-295, 1972.

12. L.S. Kokorev, A.S. Korsun, B.N. Kostyunin, V.I. Petrovichev and R.L. Struenze: "Effect of Secondary Flows on the Velocity Distribution and Hydraulic Drag in Turbulent Liquid Flows in Noncircular Channels", Heat Trans.-Soviet Res. 3, Vol. 1, p. 66, 1971.

13. A. Melling and J.H. Whitelaw: "Turbulent Flow in a Rectangular Duct", J. Fluid Mech., Vol. 78, Pt. 2, pp. 289-315, 1976.

14. F.B. Gessner, J.K. Po and A.F. Emery: "Measurements of Developing Turbulent Flow in a Square Duct", Symposium on Turbulent Shear Flows, Univ. Park, Pennsylvania, Vol. 1, p. 9.1, April 1977.

15. W. Eifler and R. Nijsing: "Experimental Investigation of Velocity Distribution and Flow Resistance in a Triangular Array of Parallel Rods", Nuc. Eng. and Design, Vol. 5, pp. 22-42, 1967.

16. W. Eifler: "Uber die Turbulente Geschwindigkeitsverteilung und Wandreibung in Stromungskanalen Verschiedener Querschnitte", Ph.D. Thesis, Technische Hochschule, Darmstadt, 1968.

17. V.I. Subbotin, P.A. Ushakov, Y.D. Levchenko and A.M. Alexandrov: "Velocity Field of Turbulent Fluid Flow in a Longitudinal Streamline of Clusters of Rods", USAEC Translation Rep. AEC-tr-7/89, issued Feb., 1971.

18. B. Kjellstrom: "Studies of Turbulent Flow Parallel to a Rod Bundle of Triangular Array", Rep. AE-RV-196, AB Atomenergi, Sweden, 1971.

19. C. Hall and P.J. Svenningsson: "Secondary Flow Velocities in a Rod-Bundle of Triangular Array", Rep. AE-RL-1326, AB Atomenergi, Sweden, 1971.

20. B. Kjellstrom and A. Stenback: "Pressure Drop, Velocity Distributions and Turbulence Distributions for Flow in Rod Bundles", Rep. AE-RV-145, (RL-1236), AB Atomenergi, Sweden, 1970.

21. D.S. Rowe: "Measurements of Turbulent Velocity Intensity and Scale in Rod Bundle Flow Channels", BNWL-1736, UC-80, Battelle, 1973.

22. A.C. Trupp and R.S. Azad: "The Structure of Turbulent Flow In Triangular Array Rod Bundles", Nucl. Eng. and Design, Vol. 32, No. 1, pp. 47-84, 1975.

23. P. Carajilescov and N.E. Todreas: "Experimental and Analytical Study of Axial Turbulent Flows in an Interior Subchannel of a Bare Rod Bundle", Trans. of the ASME, Journal of Heat Transfer, pp. 262-268, May 1976.

24. J. Nikuradse: "Turbulente Strömung in Nicht Kreisförmigen Rohren", Ing.-Arch., 1, 306, 1930.

25. C.J. Cremers and E.R.G. Eckert: "Hot-wire Measurements of Turbulence Correlations in a Triangular Duct", Trans. ASME, 84E, J. Appl. Mech., Vol. 4, pp. 609-614, 1962.

26. R.C. Cope and R.W. Hanks, Ind. Eng. Chem. Fundam., Vol. 11, No. 1, p. 106, 1972.

27. P.C. Bandopadhayoy and J.B. Hinwood: "On the Co-existence of Laminar and Turbulent Flow in a Narrow Triangular Duct", J. Fluid Mech., Vol. 59, Pt. 4, pp. 775-783, 1973.

28. J.A. Liggett, C. Chiu and L.S. Miao" "Secondary Currents in a Corner", Proc. ASCE, J. Hyd. Div., Vol. 91, No. HY6, p. 99, 1965.

29. H.G. Lyall: "Measurement of Flow Distribution and Secondary Flow in Ducts Composed of Two Square Interconnected Sub-Channels", Paper No. 33, Symposium on Internal Flows, Univ. of Salford, April 1971.

30. S.C. Kacker: "Some Aspects of Fully Developed Turbulent Flow in Non-Circular Ducts", J. Fluid Mech., Vol. 57, Pt. 3, pp. 583-602, 1973.

31. W.C. Reynolds: "Computation of Turbulent Flows-State-Of-The-Art", Report MD-27, Thermo-sciences Division, Department of Mechanical Engineering, Stanford University, 1970.

32. W.C. Reynolds: "Computation of Turbulent Flows", AIAA Paper 74-556, 1974.

33. B.E. Launder and D.B. Spalding: "Mathematical Models of Turbulence", Academic Press, New York, 1972.

34. B.E. Launder and D.B. Spalding: "The Numerical Computation of Turbulent Flow", Comp. Meth. in Appl. Mech. and Eng., Vol. 3, p. 269, 1974.

35. J.L. Lumley and B. Khajeh Nouri: "Computational Modelling of Turbulent Transport", Proc. 2nd. IUGG-IUTAM Symposium on Atmospheric Diffusion in Envirnomental Pollution, Academic Press, 1974.

36. B.E. Launder: "Progress in the Modelling of Turbulent Transport", Supplementary Notes of a course on Flow, Heat and Mass Transfer in Turbulent Recirculating Flows - Prediction and Measurements, Dept. of Chem. Eng., McGill Univ., August 4-6, 1976.

37. G.L. Mellor: "Incompressible Turbulent Boundary Layers with Arbitrary Pressure Gradients and Divergent or Convergent Cross Flows", AIAA Jour., Vol. 5, p. 1570, 1967.

38. H.J. Herring and G.L. Mellor: "A Method of Calculating Compressible Turbulent Boundary Layers", NASA CR-1444, 1968.

39. A.D. Gosman, W.M. Pun, A.K. Runchal, D.B. Spalding and M. Wolfshtein: "Heat and Mass Transfer in Recirculating Flows", Academic Press, London, 1969.

40. J.O. Hinze: "Turbulence-An Introduction to its Mechanism and Theory", McGraw-Hill, 1959.

41. K.G. Ng and D.B. Spalding: "Turbulence Model for Boundary Layer Near Walls", Phys. of Fluids, Vol. 15, No. 1, pp. 20-30, 1972.

42. A.A. Townsend: "The Structure of Turbulent Shear Flow", Cambridge Univ. Press, 1956.

43. F.H. Champagne, V.G. Harris and S. Corrsin: "Experiments on Nearly Homogeneous Turbulent Shear Flow", J. Fluid Mech., Vol. 41, p. 81, 1970.

44. J.L. Lumley: "Toward a Turbulent Constitutive Equation", J. Fluid Mech., Vol. 41, p. 413, 1970.

45. G.L. Mellor and H.J. Herring: "A Study of Turbulent Boundary Layer Models", Part I and Part I, Sandia Lab., Report SC-CR-70-6125, 1970.

46. D. Kearney et al: "The Effect of Free-Stream Turbulence on Heat Transfer to Strongly Accelerated Turbulent Boundary Layers", Proc. Heat Transfer and Fluid Mech. Institute, Stanford U. Press, 1970.

47. R.J. Loyd, R.J. Moffat and W.M. Kays: "The Turbulent Boundary Layer on a Porous Plate; an Experimental Study of the Fluid Dynamics with Strong Favorable Pressure Gradients and Blowing", Report HMT-13, Mech. Eng. Dept., Stanford Univ., 1970.

48. J.C. Rotta: "Statistische Theorie Nichthomogener Turbulenz", Z. Phys., Vol. 129, pp. 547-752, 1951.

49. C.D. Donaldson and H. Rosenbaum: "Calculation of Turbulent Shear Flows Through Closure of the Reynolds Equations by Invariant Modelling", Aero Res. Assoc. of Princeton, Report No. 127, 1968.

50. B.J. Daly and F.H. Harlow: "Transport Equations in Turbulence", Phys. of Fluids, Vol. 13, No. 11, pp. 2634-2649, 1970.

51. K. Hanjalic and B.E. Launder: "A Reynolds Stress Model of Turbulence and its Application to Thin Shear Flows", J. Fluid Mech., Vol. 52, pp. 609-638, 1972.

52. B.E. Launder, G.J. Reece, W. Rodi: "Progress in the Development of a Reynolds Stress Turbulence Closure", J. Fluid Mech., Vol. 68, Pt. 3, pp. 537-566, 1975.

53. F.H. Harlow and N.C. Romero: "Turbulence Distortion in a Nonuniform Tunnel", Los Alamos Lab. Report LA-4247, 1969.

54. D.G. Tatchell: "Convection Processes in Confined 3-dimensional boundary Layers", Ph.D. Thesis, University of London, 1975.

55. R.G. Deissler and M.F. Taylor: "Analysis of Turbulent Flow and Heat Transfer in Non-Circular Passages", NASA Tech. Rep. R-31, 1959.

56. R. Gerard: "Finite Element Solution for Flow in Non-Circular Conduits", Journal of the Hydraulics Division, ASCE, Vol. 100, No. HY3, pp. 425-441, 1974.

57. D.J. Bender and D.M. Switick: "Turbulent Velocity Distributions in a Rod Bundle", ASME 68-WA/HT-36, 1968.

58. M. Kh. Ibragimov et al: "Calculation of the Tangential Stresses at the Wall of a Channel and the Velocity Distribution in a Turbulent Flow of Liquid", Soviet Atomic Energy, Vol. 21, No. 2, pp. 731-739, 1966.

59. M. Kh. Ibragimov et al: "Calculation of Hydraulic Resistivity Coefficients for Turbulent Fluid Flow in Channels of Noncircular Cross-Sections," Soviet Atomic Energy, Vol. 23, No. 4, pp. 1042-47, 1967.

60. R. Nijsing et al: "Analysis of Fluid Flow and Heat Transfer in a Triangular Array of Parallel Heat Generating Rods", Nucl. Eng. Design, Vol. 4, pp. 375-398, 1966.

61. N.I. Buleev: "Theoretical Model for Turbulent Transfer in Three Dimensional Fluid Flow", Paper presented at the Third United Nations Conference on the Peaceful Uses of Atomic Energy, Paper A/CONF.28/p/329, May, 1964.

62. H. Ramm and K. Johannsen: "Hydrodynamics and Heat Transfer in Regular Arrays of Circular Tubes", Intern. Seminar on Recent Developments in Heat Exchangers of the International Center of Heat and Mass Transfer, Trogir, Yugoslavia, Aug. 30-Sept. 6, 1972.

63. F.H. Harlow and P.I. Nakayama: "Transport of Turbulence Energy Decay Rate", Report LA-3854, Los Alamos Sci. Lab. Rep., 1968.

64. D.B. Spalding: "The k-ω Model of Turbulence", Imperial College Report, HTs/72/12, 1972.

65. W.P. Jones and B.E. Launder: "The Prediction of Laminarization with a Two-Equation Model of Turbulence", Int. J. Heat and Mass Transfer, Vol. 15, p. 301, 1972.

66. W. Rodi: "The Prediction of Free Turbulent Boundary Layers by Use of a 2-Equation Model of Turbulence", Ph.D. Thesis, University of London, 1972.

67. W.P. Jones and B.E. Launder: "The Calculation of Low Reynolds Number Phenomena with a Two-Equation Model of Turbulence", Int. J. Heat and Mass Transfer, Vol. 16, p. 1189, 1973.

68. B.E. Launder and B.I. Sharma: "Application of the Energy-Dissipation Model of Turbulence to Flow Near a Spinning Disc", Letters in Heat and Mass Transfer, Vol. 2, 1974.

69. B.E. Launder and A. Morse: "Numerical Prediction of Axisymmetric Free Shear Flows with a Second-Order Reynolds Stress Closure", Symposium on Turbulent Shear Flows, Univ. Park, Pennsylvania, Vol. 1, P. 4.21, April 1977.

70. A.D. Gosman and A.P. Watkins: "A Computer Prediction Method For Turbulent Flow and Heat Transfer in Piston/Cylinder Assemblies", Symposium on Turbulent Shear Flows, Univ. Park, Pennsylvania, Vol. 1, p. 5.23, April 1977.

71. H. Emmons: "Shear Flow Turbulence", Proc. 2nd U.S. National Congress Appl. Mech., pp. 1-12, 1954.

72. M. Wolfshtein: "The Velocity and Temperature Distribution in One-Dimensional Flow with Turbulence Augmentation and Pressure Gradient", Int. J. Heat Mass Transfer, Vol. 12, pp. 301-18, 1969.

73. W. Rodi and D.B. Spalding: "A Two-Parameter Model of Turbulence and Its Application to Free Jets", Warme und Stoffubertragung, Vol. 3, p. 85, 1970.

74. T.H. Gawain and J.W. Pritchard: "A Unified Hueristic Model of Turbulence", J. Comp. Physics, Vol. 5, p. 385, 1970.

75. DISA Probe Manual, DISA Elektronik A/S, Herlev, Denmark.

76. P.D. Hollingsworth, Central Elec. Gen. Board, Rep. RD/B/N 892, 1967.

77. W.M. Ying, Ph.D. Thesis, Imperial College, London, 1971.

78. C.J. Lawn: "Turbulence Measurements with Hot Wires at B.N.L.", Central Elec. Gen. Board, Berkley Nuclear Labs. Rep. RD/B/M1277, 1969.

79. J. Laufer: "The Structure of Turbulence in Fully Developed Pipe Flow", NACA Rep. 1174, 1954.

80. E.R. Van Driest, Heat Trans. and Fluid Mech. Inst. Symposium (UCLA), Paper 12, 1955.

81. C.L.V. Jayatilleke: "The Influence of Prandtl Number and Surface Roughness on the Resistance of the Laminar Sublayer to Momentum and Heat Transfer", Progress in Heat and Mass Transfer, Pergamon Press Ltd., London, 1969.

82. A.D. Gosman and W.M. Pun: "KASE Problems for the TEACH Computer Programs", Imperial College, Mech. Eng. Dept., Rep HTS/74/3, 1974.

83. C.W. Carlson and T.F. Irvine: "Fully Developed Pressure Drop in Triangular Shaped Ducts", Trans. ASME, J. Heat Trans., Vol. 83, pp. 441-444, 1961.

84. J. Malak, J. Hejna and J. Schmid: "Pressure Losses and Heat Transfer in Non-Circular Channels with Hydraulically Smooth Walls", Int. J. Heat Mass Transfer, Vol. 18, pp. 139-149, 1975.

85. J.F. Nash and V.C. Patel: "Advances in Turbulent Boundary Layer Calculation Methodology", Symposium on Turbulent Shear Flows, Univ. Park, Pennsylvania, Vol. 1, p. 5.1, 1977.

86. P. Carajilescov: "Experimental And Analytical Study of Axial Turbulent Flows in an Interior Subchannel of a Bare Rod Bundle", Ph.D. Thesis, Nuclear Engineering Department, MIT, 1975.

87. L.S. Tong: "Pressure Drop Performance of a Rod Bundle", Symposium on Heat Transfer in Rod Bundles, ASME Winter Annual Meeting, New York, 1968.

88. W.A. Sutherland: "Experimental Heat Transfer in Rod Bundles", Symposium on Heat Transfer in Rod Bundles, ASME Winter Annual Meeting, New York, 1968.

APPENDIX A

INTEGRATION OF BULEEV'S LENGTH SCALE FORMULA IN AN EQUILATERAL TRIANGULAR DUCT

The geometric formula suggested by Buleev[61] for any arbitrary geometry is given by:

$$\frac{1}{\ell} = \frac{1}{2}\int_0^{2\pi} \frac{d\theta}{S} \tag{A.1}$$

where S is the distance from point P to the wall and the angle θ is defined in figure (6.1). To integrate (A.1) for the triangular duct geometry, three coordinate systems were assumed as shown on figure (6.1). On the same figure, the different notations that will be used here are also defined.

The integral in equation (A.1) may be divided into six parts given by:

$$\int_0^{2\pi} \frac{d\theta}{S} = \int_0^{\alpha} \frac{d\theta}{S} + \int_{\alpha}^{(\alpha+\beta)} \frac{d\theta}{S_1} + \int_{(\alpha+\beta)}^{(\alpha+\beta+\gamma)} \frac{d\theta}{S_2}$$
$$+ \int_{(\alpha+\beta+\gamma)}^{(\alpha+\beta+\gamma+\delta)} \frac{d\theta}{S_3} + \int_{(\alpha+\beta+\gamma+\delta)}^{(2\pi-\eta)} \frac{d\theta}{S_4} +$$
$$+ \int_{(2\pi-\eta)}^{2\pi} \frac{d\theta}{S_5} \tag{A.2}$$

where,

$$\begin{aligned}
\alpha &= \tan^{-1}(Y_1/Z_1) \quad , \\
\eta &= \tan^{-1}[(2L - Y_1)/Z_1] \quad , \\
\beta &= \tan^{-1}(Y_2/Z_2) \quad , \\
\gamma &= \tan^{-1}[(2L - Y_2)/Z_2] \quad , \\
\delta &= \tan^{-1}(Y_3/Z_3) \quad , \\
\xi &= \tan^{-1}[2L - Y_3)/Z_3] \quad .
\end{aligned} \tag{A.3}$$

The S's are given by:

$$
\begin{aligned}
S &= Z_1/\cos\theta \quad , \\
S_1 &= Z_2/\cos[(\alpha + \beta) - \theta] \quad , \\
S_2 &= Z_2/\cos[\theta - (\alpha + \beta)] \quad , \\
S_3 &= Z_3/\cos[(\alpha + \beta + \gamma + \delta) - \theta] \quad , \\
S_4 &= Z_3/\cos[\theta - (\alpha + \beta + \gamma + \delta)] \quad , \\
S_5 &= Z_1/\cos(2\pi - \theta) \quad .
\end{aligned}
\tag{A.4}
$$

Using the following simple relations given by:

$$
\begin{aligned}
r_1^2 &= Z_1^2 + (2L - Y_1)^2 \quad , \\
r^2 &= Z_1^2 + Y_1^2 \quad , \\
\chi_1 &= \alpha - \pi/6 \quad , \\
\chi &= \eta - \pi/6 \quad ,
\end{aligned}
\tag{A.5}
$$

and using (A.3) and (A.5), the coordinate systems (Y_2, Z_2) and (Y_3, Z_3) can be written as functions of (Y_1, Z_1) on the form:

$$
\begin{aligned}
Z_2 &= r_1 \sin \chi_1 \quad , \\
Y_2 &= r_1 \cos \chi_1 \quad , \\
Z_3 &= r \sin \chi \quad , \\
Y_2 &= r \cos \chi \quad .
\end{aligned}
\tag{A.6}
$$

Substituting (A.4) into (A.2) yields:

$$\int_o^{2\pi} \frac{d\theta}{S} = \frac{1}{Z_1}\left[\int_o^{\alpha} \cos\theta\, d\theta + \int_{(2\pi-\eta)}^{2\pi} \cos(2\pi - \theta)d\theta\right]$$

$$+ \frac{1}{Z_2}\left[\int_{\alpha}^{(\alpha+\beta)} \cos(\alpha + \beta - \theta)d\theta + \int_{(\alpha+\beta)}^{(\alpha+\beta+\gamma)} \cos(\theta - \alpha - \beta)d\theta\right] +$$

$$+ \frac{1}{Z_3}\left[\int_{(\alpha+\beta+\gamma)}^{(\alpha+\beta+\gamma+\delta)} \cos(\alpha + \beta + \gamma + \delta - \theta)d\theta\right.$$

$$\left. + \int_{(\alpha+\beta+\gamma+\delta)}^{(2\pi-\eta)} \mathrm{Cos}(\theta - \alpha - \beta - \gamma - \delta)d\theta\right]$$

The last equation may be rewritten in the form:

$$\int_o^{2\pi} \frac{d\theta}{S} = \frac{1}{Z_1}\left[\int_o^{\alpha} \cos\theta\, d\theta + \int_{(2\pi-\eta)}^{2\pi} \mathrm{Cos}\theta\, d\theta\right]$$

$$+ \frac{1}{Z_2}\left[\int_{\alpha}^{(\alpha+\beta+\gamma)} \mathrm{Cos}(\alpha + \beta - \theta)d\theta\right]$$

$$+ \frac{1}{Z_3}\left[\int_{(\alpha+\beta+\gamma)}^{(2\pi-\eta)} \mathrm{Cos}(\alpha + \beta + \gamma + \delta - \theta)d\theta\right]$$

which can be easily integrated to give after rearrangement:

$$\int_o^{2\pi} \frac{d\phi}{S} = \frac{1}{Z_1}[\sin\alpha + \sin\eta] + \frac{1}{Z_2}[\sin\beta + \sin\gamma] + \frac{1}{Z_3}[\sin\delta + \sin\xi] \qquad (A.7)$$

From (A.1) and (A.7), the turbulence length scale may be calculated for any internal point in the duct from the simple expression:

$$\frac{1}{\ell} = \frac{1}{2Z_1}[\sin\alpha + \sin\eta] + \frac{1}{2Z_2}[\sin\beta + \sin\gamma] + \frac{1}{2Z_3}[\sin\delta + \sin\xi]$$

where Z_2, Z_3, α, β, γ, δ, η and ξ are calculated by (A.3), (A.5) and (A.6).

APPENDIX B

COMPUTER CODE FOR EQUILATERAL TRIANGULAR DUCTS

In order to solve the set of equations summarized in section (6.5), the computer code "MODEL" was developed. The block diagram of the program is presented in figure (B.1), and the input data are defined in the following:

Card 1

FORTRAN SYMBOLS	MEANING
M	Numerical grid parameter (MXM)
DEQ	Equivalent Hydraulic Diameter
RE	Reynolds Number
ROW	Density of Fluid
AMU	Dynamic Viscosity of Fluid
TB1	Average bulk temperature
CPHT	Specific heat of fluid
THCON	Thermal conductivity of fluid
SEGHT	Turbulent Prandtl number of fluid
TWALL	Duct wall temperature

Card 2

C_1	
C_2	
CU	Turbulence model constants
CD	
SEGK	

IC	Control number; if initial conditions are available as input, IC = 1.
IMAX	Maximum number of iterations
ALAMD	Convergence criterion
ALPHAU	Relaxation factor

Card 3

(Y(J), J = 1,M)

Grid specifications

Card 4

(Z(I), I = 1,M)

The nomenclature of the computer program is presented in Table (B.1).

TABLE B.1

NOMENCLATURE OF THE COMPUTER PROGRAM

FORTRAN SYMBOLS	MEANING
Y(J),Z(I)	Grid specification
BE(I,J)	Coefficients of the numerical procedure (Chapter 7)
BW(I,J)	
BN(I,J)	
BS(I,J)	
AE(I,J)	
AW(I,J)	
AN(I,J)	
AS(I,J)	
VP(I,J)	$\iint_A dydz$ (eqn. 7.17)
U(I,J)	Axial velocity
V(I,J)	Secondary velocity components
W(I,J)	
AKE(I,J)	Turbulent kinetic energy
OMEG(I,J)	Vorticity
AMUT(I,J)	Eddy viscosity
S(I,J)	Turbulence length scale
T(I,J)	Temperature
ANDT(I,J)	Dimensionless temperature
Q11(J)	Heat flux
HTL(J)	Heat transfer coefficient
TOW(J)	Wall shear stress
TLOC(J)	Normalized wall shear stress

Table B.1. continued

UPLUS(J)	Dimensionless axial velocity at the secondary string of nodes in the fluid
UF(J)	Friction velocity
UBC(J)	Velocity at the first string of nodes in the fluid (boundary condition)
AkBC(J)	Turbulent kinetic energy at the first string of nodes in the fluid
DUY(I,J)	$[\partial(\ )/\partial y]_{i,j}$
DUZ(I,J)	$[\partial(\ )/\partial z]_{i,j}$
F1(I,J)	Temporary storage locations
F2(I,J)	
F3(I,J)	$d\phi$, defined by equation (7.15)
F4(I,J)	Production term in k equation
PF	P*, (eqn. 6.17)
UFI	Initial condition for average friction velocity
TAVI	Initial condition for average wall shear stress
FACTOR	Friction factor
DPDX	$\partial P/\partial X$
Z PLUS	Z^+
ITER	Iteration number
RESDW	Maximum residual of ω
RESDS	Maximum residual of ψ
RESDU	Maximum residual of U
RESD	Maximum residual of k

Table B.1. Continued

D	Vorticity production term
D1	Source term for ψ equation
TKS	Source term for k equation
D2	Source term for $\bar{U}$ equation

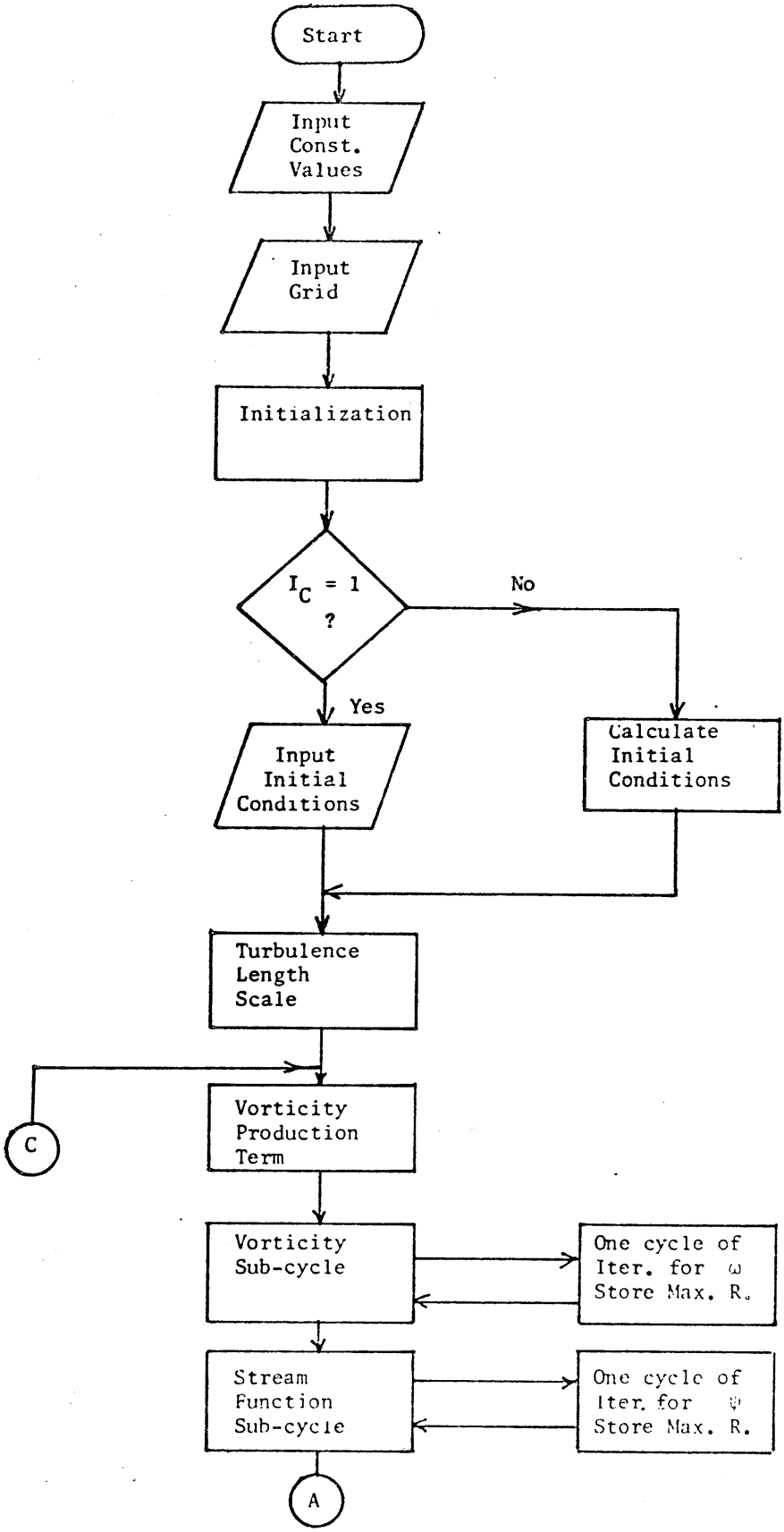

Fig.B.1.Block Diagram of the Computer Program " MODEL ".

continued, Fig.B.1.

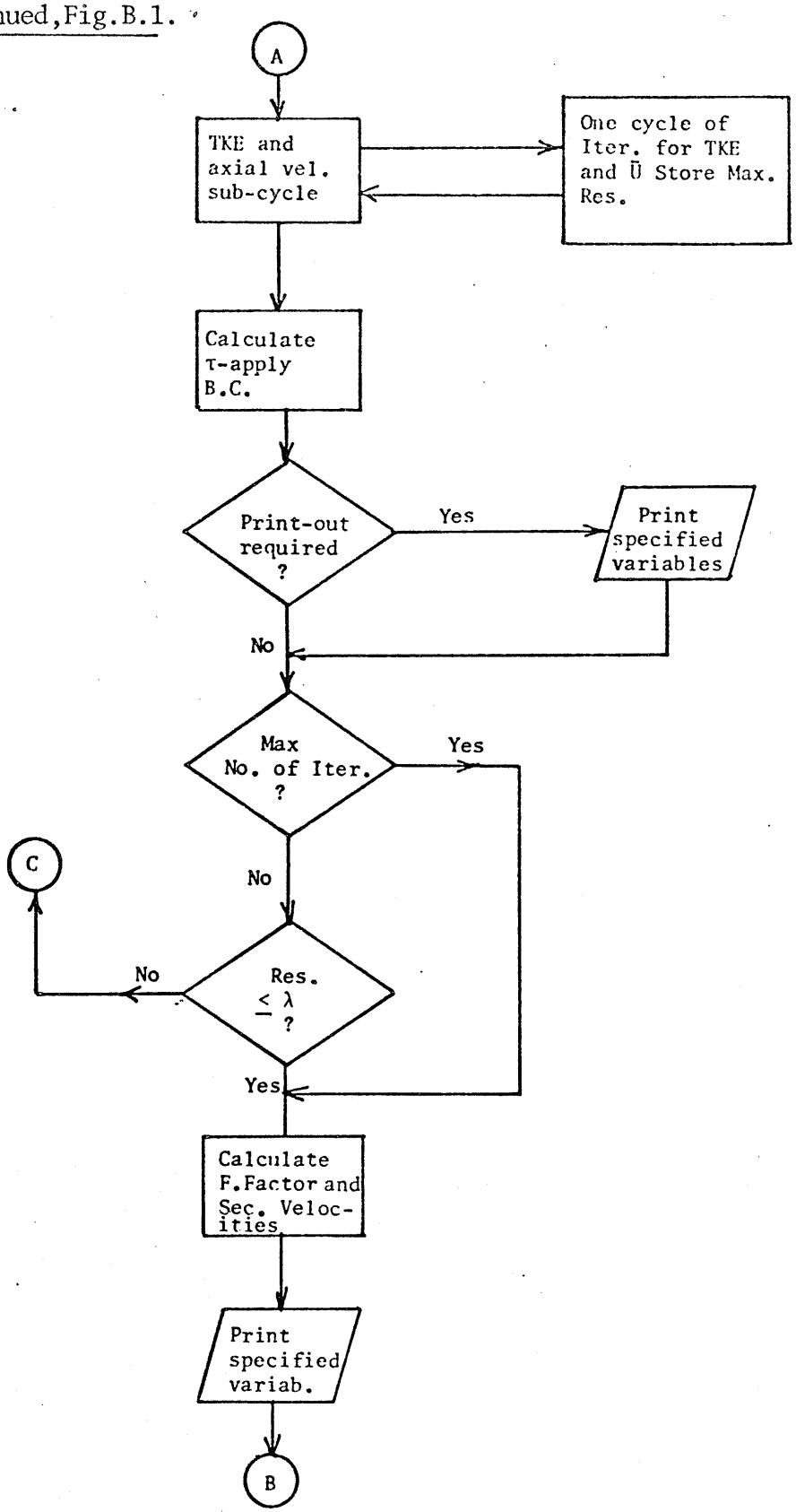

continued, Fig.B.1.

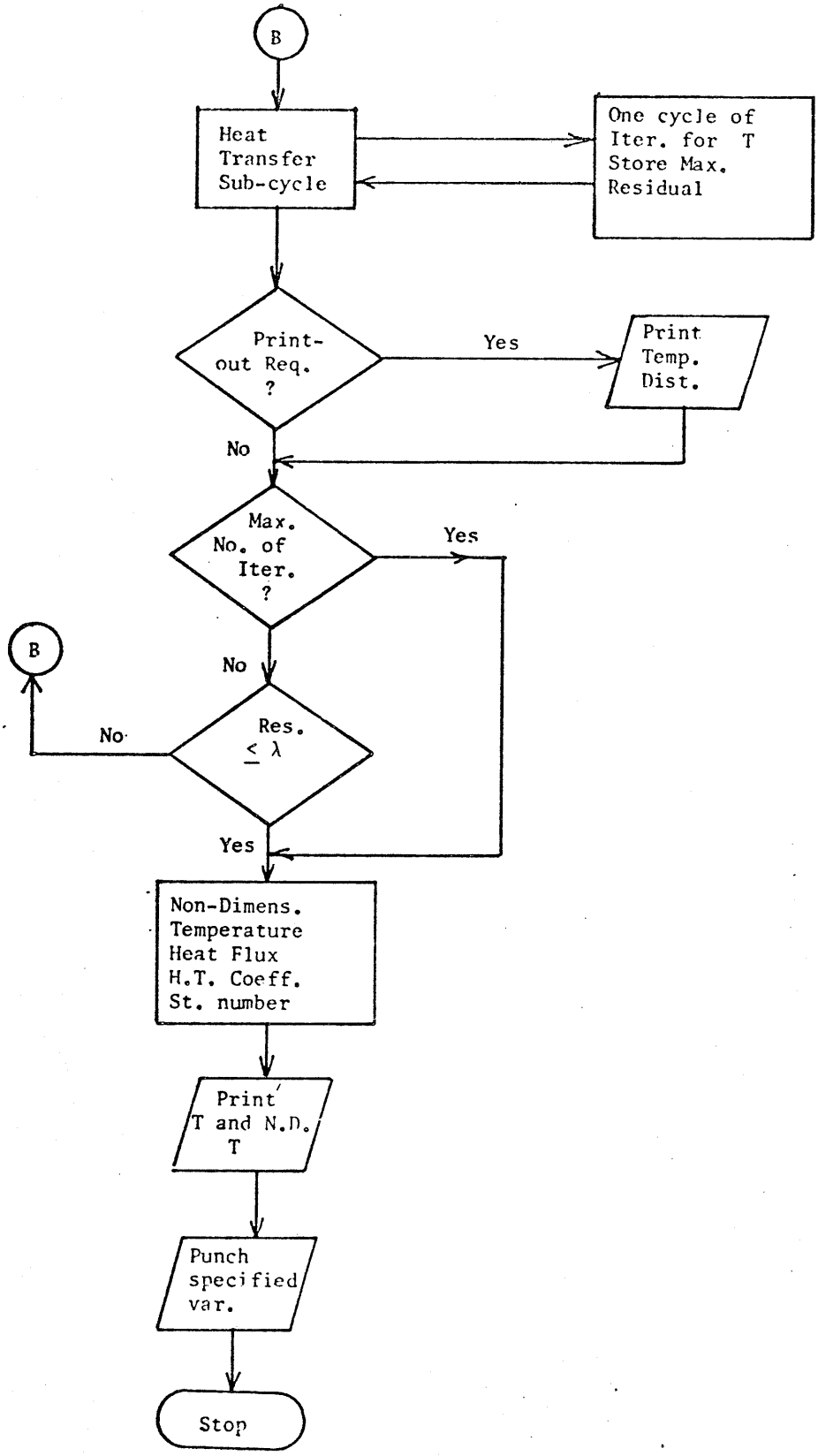

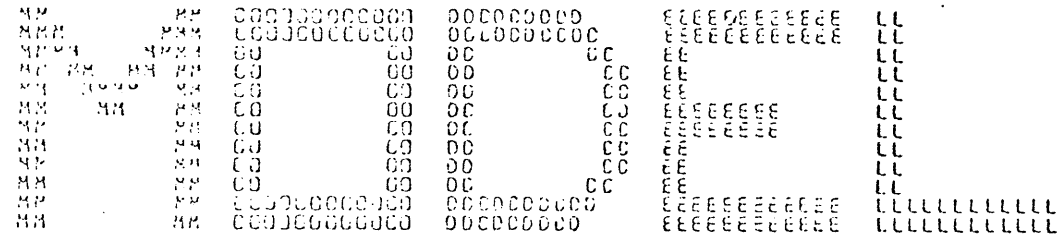

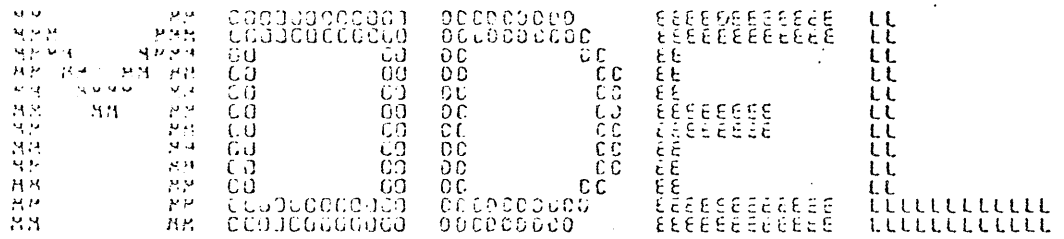

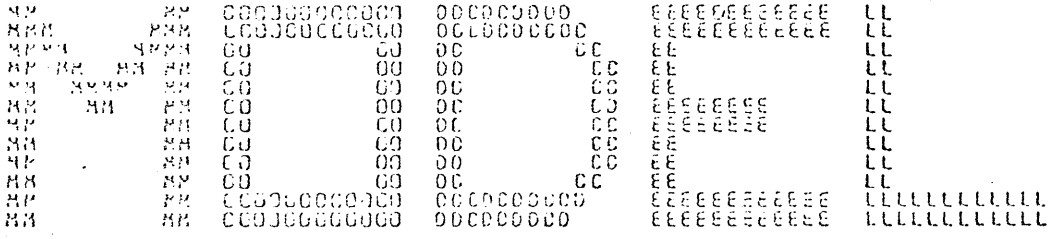

```
      $JOB  WATIV   ALY M. MORTADA ALY
    1       DIMENSION Y(31),Z(31),BE(31,31),BW(31,31),BN(31,31),BS(31,31),VP(
           *31,31),AP(31,31),AW(31,31),AN(31,31),AS(31,31),F1(31,31),F2(31,31)
           *,F3(31,31),F4(31,31),DUY(31,31),DUZ(31,31),AMUT(31,31),EP(31,31),
           *OMEG(31,31),AKE(31,31),U(31,31),T(31,31),ANDT(31,31),S(31,31),
           *UPLUS(31),UBC(31),AKBC(31),UF(31),TOW(31),TLOC(31),Q11(31),HTL(31)
           *,V(31,31),W(31,31)
      C
      C
      C    *****CONSTANT VALUES ********
      C
      C
    2       READ ,M,DEQ,RE,ROW,AMU,THCON,SEGHT,CPHT,TB1,TWALL
    3       READ ,C1,C2,CU,CD,SEGK,IC,ALAMD,IMAX,ALPHAU
    4       MM=M-1
    5       MMM=M-2
    6       MN=M-4
    7       MJ=M-5
    8       UBAV=RE*AMU/(ROW*DEQ)
    9       SEGH=CPHT*AMU/THCON
   10       PF=9.24*((SEGH/SEGHT)**0.75-1.0)
      C
      C***      GRID SPECIFICATIONS
      C
   11       READ ,(Y(J),J=1,M)
   12       READ ,(Z(I),I=1,M)
      C
      C  *****  INITIALIZATION BY ZERO  *************
      C
   13       DO 1111 I=1,M
   14       DO 1111 J=1,M
   15       S(I,J)=0.0
   16       F3(I,J)=0.0
   17       U(I,J)=0.0
   18       V(I,J)=0.0
   19       W(I,J)=0.0
   20       AKE(I,J)=0.0
   21       OMEG(I,J)=0.0
   22       EP(I,J)=0.0
   23       T(I,J)=0.0
   24       ANDT(I,J)=0.0
   25  1111 AMUT(I,J)=0.0
      C
      C ***  INITIAL CONDITIONS AVAILABLE ON CARDS ??  ********
      C
   26       IF(IC.EQ.1)GO TO 2222
      C
      C  ****   INITIAL CONDITIONS ARE NOT AVAILABLE  ********
      C
      C ***  ASSUME ANY INITIAL CONITIONS  AND BOUNDARY CONDITIONS  *******
      C  *********          FOR  U  AND   K         ***************
      C
   27       UF1=3.445
   28       TAV1=ROW*(UF1**2)
   29       DPDX=4.0*TAV1/DEQ
   30       ZPLUS=ROW*Z(2)*UF1/AMU
   31       DO 1 J=2,M
   32       UF(J)=UF1
   33       AKBC(J)=(UF(J)**2)/SQRT(CU*CD)
   34     1 UBC(J)=UF(J)*(2.5*ALOG(ZPLUS)+5.1)
   35       K=2
   36       DO 444 I=2,M
   37       DO 443 J=K,M
   38       U(I,J)=UBAV
   39       T(I,J)=TB1
   40   443 AKE(I,J)=AKBC(J)
```

```
41          K=K+1
42       444 CONTINUE
43          GO TO 3333
44       2222 CONTINUE
         C
         C  ******   INITIAL CONDITIONS ARE AVAILABLE ON CARDS !!!   **********
         C
         C
         C   ************ INPUT DATA **********
         C
45          DO 8080 I=1,M
46       8080 READ 505,(ANDT(I,J),J=2,M)
47          DO 1080 I=1,M
48       1080 READ 505,(AKE(I,J),J=2,M)
49          DO 1070 I=1,M
50       1070 READ 505,(U(I,J),J=2,M)
51          DO 7777 I=1,M
52       7777 READ 1002,(OMEG(I,J),J=2,M)
53          DO 1001 I=1,M
54       1001 READ 1002,(EP(I,J),J=2,M)
55       3333 CONTINUE
         C
         C   ********************************************************************
         C
         C
         C***   CASE OF ZERO WALL VORTICITY ASSUMPTION
         C***    BOUNDARY CONDITIONS
         C
56          DO 12 J=1,M
57          EP(1,J)=0.0
58       12 OMEG(1,J)=0.0
59          DO 13 I=2,M
60       13 OMEG(I,M)=0.0
61          DO 14 I=2,MM
62          EP(I,I)=0.0
63       14 OMEG(I,I)=0.0
         C
         C***   TURBULENT LENGTH SCALE FOR TRIANGULAR DUCT WITH BULEEV FORMULA ****
         C
64          XL=2.*Y(M)
65          K=2
66          DO 5 I=2,M
67          DO 4 J=K,M
68          A=Y(J)/Z(I)
69          FTA=ATAN(A)
70          B=(XL-Y(J))/Z(I)
71          ALPHA=ATAN(B)
72          R=SQRT(Z(I)**2+(XL-Y(J))**2)
73          R1=SQRT(Z(I)**2+Y(J)**2)
74          EXI=ALPHA-30.*3.1416/180.
75          EXI1=BETA-30.*3.1416/180.
76          Z1=R*SIN(EXI)
77          Z2=R1*SIN(EXI1)
78          Y1=R*COS(EXI)
79          Y2=XL-R1*COS(EXI1)
80          C=Y1/Z1
81          BETA=ATAN(C)
82          D=(XL-Y1)/Z1
83          GAMA=ATAN(D)
84          E=Y2/Z2
85          DELTA=ATAN(E)
86          F=(XL-Y2)/Z2
87          THETA=ATAN(F)
88          AL=(0.5)*((SIN(ALPHA)+SIN(FTA))/Z(I)+(SIN(BETA)+SIN(GAMA))/Z1+
           1(SIN(DELTA)+SIN(THETA))/Z2)
89        4 S(I,J)=(1.0/AL)
```

```
 90          K=K+1
 91        5 CONTINUE
 92          PRINT 1335
 93          DO 1336 I=2,M
 94     1336 PRINT 505,(S(I,J),J=4,M,3)
      C
      C******    MAIN LOOP OF ITERATIONS
      C
 95          C=(2.*CU/CD)*(6.*C2-2.)/(11.*(C1-2.*C2))
 96          PRINT 2000
 97          ITER=0.0
 98       69 ITER=ITER+1
      C
      C ***  INITIALIZATION OF RESIDUALS  *******
      C
 99          RESDW=0.0
100          RESDS=0.0
101          RESDU=0.0
102          RESD=0.0
      C
      C **** COEFFICIENTS CALCULATIONS FOR VORTICITY AND STREAM FUNCTION EQUATIONS
      C
103          K=3
104          DO 926 I=2,MMM
105          DO 925 J=K,MM
106          BE(I,J)=0.5*(Z(I+1)-Z(I-1))/(Y(J+1)-Y(J))
107          BW(I,J)=0.5*(Z(I+1)-Z(I-1))/(Y(J)-Y(J-1))
108          BN(I,J)=0.5*(Y(J+1)-Y(J-1))/(Z(I)-Z(I-1))
109          BS(I,J)=0.5*(Y(J+1)-Y(J-1))/(Z(I+1)-Z(I))
110          VP(I,J)=0.25*(Y(J+1)-Y(J-1))*(Z(I+1)-Z(I-1))
111          AE(I,J)=(ABS(EP(I+1,J)+EP(I+1,J+1)-EP(I-1,J)-EP(I-1,J+1))+(EP(I+1,
            1J)+EP(I+1,J+1)-EP(I-1,J)-EP(I-1,J+1)))/8.0
112          AW(I,J)=(ABS(EP(I-1,J-1)+EP(I-1,J)-EP(I+1,J-1)-EP(I+1,J))+(EP(I-1,
            1J-1)+EP(I-1,J)-EP(I+1,J-1)-EP(I+1,J)))/8.0
113          AN(I,J)=(ABS(EP(I-1,J+1)+EP(I,J+1)-EP(I-1,J-1)-EP(I,J-1))+(EP(I-1,
            1J+1)+EP(I,J+1)-EP(I-1,J-1)-EP(I,J-1)))/8.0
114        925 AS(I,J)=(ABS(EP(I+1,J-1)+EP(I,J-1)-EP(I+1,J+1)-EP(I,J+1))+(EP(I+1,
            1J-1)+EP(I,J-1)-EP(I+1,J+1)-EP(I,J+1)))/8.0
115          K=K+1
116        926 CONTINUE
      C
      C
      C ***    VORTICITY SOURCE TERM
      C
      C
117          K=3
118          DO 332 I=2,MMM
119          DO 331 J=K,M
120        331 DUZ(I,J)=((U(I+1,J)-U(I,J))*(Z(I)-Z(I-1))/(Z(I+1)-Z(I))+(U(I,J)-U(
            1I-1,J))*(Z(I+1)-Z(I))/(Z(I)-Z(I-1)))/(Z(I+1)-Z(I-1))
121          K=K+1
122        332 CONTINUE
123          K=3
124          DO 334 I=2,MMM
125          DO 333 J=K,MM
126        333 DUY(I,J)=((U(I,J+1)-U(I,J))*(Y(J)-Y(J-1))/(Y(J+1)-Y(J))+(U(I,J)-U(
            1I,J-1))*(Y(J+1)-Y(J))/(Y(J)-Y(J-1)))/(Y(J+1)-Y(J-1))
127          K=K+1
128        334 CONTINUE
      C    ***  BOUNDARY VALUES
129          DO 336 J=2,M
130        336 DUZ(1,J)=U(2,J)/(Z(2)-Z(1))
131          J=2
132          DO 338 I=2,MM
133          DUZ(I,J)=(U(I,J)-U(I-1,J))/(Z(I)-Z(I-1))
134          J=J+1
```

```
135      338 CONTINUE
136          DUZ(MM,M)=(U(MM,M)-U(MMM,M))/(Z(MM)-Z(MMM))
137          DO 339 J=1,M
138      339 DUY(1,J)=0.0
139          DO 351 I=2,M
140      351 DUY(I,M)=(U(I,M)-U(I,M-1))/(Y(M)-Y(M-1))
141          J=2
142          DO 352 I=2,MM
143          DUY(I,J)=(U(I,J+1)-U(I,J))/(Y(J+1)-Y(J))
144          J=J+1
145      352 CONTINUE
146          K=1
147          DUZ(1,1)=0.0
         C
         C  *****  LAUNDER - YING APPROXIMATION   **********
         C
148          DO 354 I=1,MM
149          DO 353 J=K,M
150          F1(I,J)=-C*(S(I,J)**2)*((DUY(I,J)**2)-(DUZ(I,J)**2))
151          F2(I,J)=-C*(S(I,J)**2)*DUY(I,J)*DUZ(I,J)
152      353 F4(I,J)=DUY(I,J)**2+DUZ(I,J)**2
153          K=K+1
154      354 CONTINUE
         C
         C***  NORMAL STRESSES SOURCE TERM FOR VORTICITY EQUATION  ******
         C
155          K=3
156          DO 357 I=2,MMM
157          DO 356 J=K,M
158      356 DUZ(I,J)=((F1(I+1,J)-F1(I,J))*(Z(I)-Z(I-1))/(Z(I+1)-Z(I))+(F1(I,J)
            1-F1(I-1,J))*(Z(I+1)-Z(I))/(Z(I)-Z(I-1)))/(Z(I+1)-Z(I-1))
159          K=K+1
160      357 CONTINUE
         C***   BOUNDARY VALUES
161          J=2
162          DO 358 I=2,MM
163          DUZ(I,J)=(F1(I,J)-F1(I-1,J))/(Z(I)-Z(I-1))
164          J=J+1
165      358 CONTINUE
         C
         C  *****  FINAL EXPRESSION OF NORMAL STRESS SOURCE TERM *****
         C
166          K=3
167          DO 362 I=2,MMM
168          DO 361 J=K,MM
169      361 F3(I,J)= ((DUZ(I,J+1)-DUZ(I,J))*(Y(J)-Y(J-1))/(Y(J+1)-Y(J))+(DUZ(I
            1,J)-DUZ(I,J-1))*(Y(J+1)-Y(J))/(Y(J)-Y(J-1)))/(Y(J+1)-Y(J-1))
170          K=K+1
171      362 CONTINUE
         C
         C   ****** SHEAR STRESSES SOURCE TERM ********
         C
172          K=3
173          DO 457 I=2,MMM
174          DO 456 J=K,M
175      456 DUZ(I,J)=((F2(I+1,J)-F2(I,J))*(Z(I)-Z(I-1))/(Z(I+1)-Z(I))+(F2(I,J)
            1)*(Z(I+1)-Z(I))/(Z(I)-Z(I-1)))/(Z(I+1)-Z(I-1))
176          K=K+1
177      457 CONTINUE
         C***   BOUNDARY VALUES
178          J=2
179          DO 458 I=2,MM
180          DUZ(I,J)=(F2(I,J)-F2(I-1,J))/(Z(I)-Z(I-1))
181          J=J+1
182      458 CONTINUE
183          DO 459 J=2,M
```

```
184      459 DUZ(1,J)=F2(2,J)/(Z(2)-Z(1))
      C  ****  F1(I,J) IS NOW A NEW VARIABLE  *****
185           K=3
186           DO 556 I=2,MMM
187           DO 555 J=K,MM
188      555 F1(I,J)=((DUZ(I+1,J)-DUZ(I,J))*(Z(I)-Z(I-1))/(Z(I+1)-Z(I))+(DUZ(I,
            1J)-DUZ(I-1,J))*(Z(I+1)-Z(I))/(Z(I)-Z(I-1)))/(Z(I+1)-Z(I-1))
189           K=K+1
190      556 CONTINUE
191           K=3
192           DO 634 I=2,MMM
193           DO 633 J=K,MM
194      633 DUY(I,J)=((F2(I,J+1)-F2(I,J))*(Y(J)-Y(J-1))/(Y(J+1)-Y(J))+(F2(I,J)
            1-F2(I,J-1))*(Y(J+1)-Y(J))/(Y(J)-Y(J-1)))/(Y(J+1)-Y(J-1))
195           K=K+1
196      634 CONTINUE
      C***   BOUNDARY VALUES
197           J=2
198           DO 635 I=2,MM
199           DUY(I,J)=(F2(I,J+1)-F2(I,J))/(Y(J+1)-Y(J))
200           J=J+1
201      635 CONTINUE
      C  ****  F2(I,J) IS NOW A NEW VARIABLE  *****
202           K=3
203           DO 638 I=2,MMM
204           DO 637 J=K,MM
205           F2(I,J)=((DUY(I,J+1)-DUY(I,J))*(Y(J)-Y(J-1))/(Y(J+1)-Y(J))+(DUY(I,
            1J)-DUY(I,J-1))*(Y(J+1)-Y(J))/(Y(J)-Y(J-1)))/(Y(J+1)-Y(J-1))
      C
      C  ***  FINAL EXPRESSION OF SHEAR STRESS SOURCE TERM  *****
      C
206           F2(I,J)=F1(I,J)-F2(I,J)
      C
      C  ****  TOTAL VORTICITY PRODUCTION  ***************
      C
207      637 F3(I,J)= (F2(I,J)+F3(I,J))
208           K=K+1
209      638 CONTINUE
      C
      C
      C**    VORTICITY SUBCYCLE
      C
      C
210           K=3
211           DO 26 I=2,MMM
212           DO 25 J=K,MM
213           SEGAB=AE(I,J)+AW(I,J)+AN(I,J)+AS(I,J)+(BE(I,J)+BW(I,J)+BN(I,J)+BS(
            1I,J))*AMU
214           CE=(AE(I,J)+AMU*BE(I,J))
215           CW=(AW(I,J)+AMU*BW(I,J))
216           CN=(AN(I,J)+AMU*BN(I,J))
217           CS=(AS(I,J)+AMU*BS(I,J))
218           D=-VP(I,J)*ROW*F3(I,J)
219           IF(D.GT.0.0)D=0.0
220           OMEG1=(CE*OMEG(I,J+1)+CW*OMEG(I,J-1)+CN*OMEG(I-1,J)+CS*OMEG
            1(I+1,J)+D)/SEGAB
221           IF(OMEG1.EQ.0.0) GO TO 25
      C***      CALCULATE RESIDUAL
222           RSW=1.0-OMEG(I,J)/OMEG1
      C***     STORE MAX. RESIDUAL
223           IF(ABS(RSW).GT.ABS(RESDW))RESDW=RSW
224        25 OMEG(I,J)=ALPHAU*OMEG1+(1.-ALPHAU)*OMEG(I,J)
225           K=K+1
226        26 CONTINUE
      C
      C
```

```
      C***   STREAM FUNCTION SUBCYCLE
      C
      C
227         K=3
228         DO 31 I=2,MMM
229         DO 30 J=K,MM
230         SEGB=BE(I,J)+BW(I,J)+BN(I,J)+BS(I,J)
      C ***  SOURCE TERM FOR STREAM FUNCTION EQUATION ********
231         D1= OMEG (I,J)*VP(I,J)*ROW
232         EPSI=(BE(I,J)*EP(I,J+1)+BW(I,J)*EP(I,J-1)+BN(I,J)*EP(I-1,J)+BS(I,J
           1)*EP(I+1,J)+D1)/SEGB
233         IF(EPSI.EQ.0.0) GO TO 30
      C ***      CALCULATE RESIDUAL
234         RSS=1.0-EP(I,J)/EPSI
      C***     STORE MAX. RESIDUAL
235         IF(ABS(RSS).GT.ABS(RESDS)) RESDS=RSS
236      30 EP(I,J)=EPSI
237         K=K+1
238      31 CONTINUE
      C **** FOR NUMERICAL TREATMENT OF NODES NEAR CORNER BI-SECTOR  *******
      C            NO PHYSICAL MEANING
239         N=2
240         DO 21 I=3,MM
241         EP(I,N)=-EP(I-1,N+1)
242         N=N+1
243      21 CONTINUE
      C
      C
      C    *****AXIAL VELOCITY AND T. K. E. SUBCYCLE ******
      C
      C
244         K=2
245         DO 65 I=2,M
246         DO 64 J=K,M
247         IF(AKE(I,J).LE.0.0) GO TO 64
248         AMUT(I,J)=CU*SQRT(AKE(I,J))*S(I,J)*ROW
249      64 CONTINUE
250         K=K+1
251      65 CONTINUE
      C
      C ****  COEFFICIENTS FOR  K  EQUATION    *******
      C
252         K=4
253         DO 71 I=3,MMM
254         DO 70 J=K,MM
255         BE(I,J)=BE(I,J)*(2.*AMU+(AMUT(I,J+1)+AMUT(I,J))/SEGK)/2.0
256         BW(I,J)=BW(I,J)*(2.*AMU+(AMUT(I,J-1)+AMUT(I,J))/SEGK)/2.0
257         BN(I,J)=BN(I,J)*(2.*AMU+(AMUT(I-1,J)+AMUT(I,J))/SEGK)/2.0
258         BS(I,J)=BS(I,J)*(2.*AMU+(AMUT(I+1,J)+AMUT(I,J))/SEGK)/2.0
259         SEGABK=AE(I,J)+AW(I,J)+AN(I,J)+AS(I,J)+BE(I,J)+BW(I,J)+BN(I,J
           1)+BS(I,J)
260         CE=AE(I,J)+BE(I,J)
261         CW=AW(I,J)+BW(I,J)
262         CN=AN(I,J)+BN(I,J)
263         CS=AS(I,J)+BS(I,J)
      C  ***  SOURCE TERM FOR  K  EQUATION    *****
264         TKS=VP(I,J)*(AMUT(I,J)*F4(I,J)-CD*ROW*(AKE(I,J)*SQRT(AKE(I,J)
           1)/S(I,J)))
265         AK1=(CE*AKE(I,J+1)+CW*AKE(I,J-1)+CN*AKE(I-1,J)+CS*AKE(I+1,J)
           1+TKS)/SEGABK
      C
      C  *****  COEFFICIENTS FOR  U  EQUATION    *************
      C
266         BE(I,J)=BE(I,J)*(2.*AMU+(AMUT(I,J+1)+AMUT(I,J)))/(2.*AMU+(AMUT(I,J
           1+1)+AMUT(I,J))/SEGK)
267         BW(I,J)=BW(I,J)*(2.*AMU+(AMUT(I,J-1)+AMUT(I,J)))/(2.*AMU+(AMUT(I,J
```

```
          1-1)+AMUT(I,J))/SEGK)
268       BN(I,J)=BN(I,J)*(2.*AMU+(AMUT(I-1,J)+AMUT(I,J)))/(2.*AMU+(AMUT(I-1
          1,J)+AMUT(I,J))/SEGK)
269       BS(I,J)=BS(I,J)*(2.*AMU+(AMUT(I+1,J)+AMUT(I,J)))/(2.*AMU+(AMUT(I+1
          1,J)+AMUT(I,J))/SEGK)
270       SEGABU=AE(I,J)+AW(I,J)+AN(I,J)+AS(I,J)+BE(I,J)+BW(I,J)+BN(I,J
          1)+BS(I,J)
271       CE=AE(I,J)+BE(I,J)
272       CW=AW(I,J)+BW(I,J)
273       CN=AN(I,J)+BN(I,J)
274       CS=AS(I,J)+BS(I,J)
      C  ****  SOURCE TERM FOR  U  EQUATION
275       D2=VP(I,J)*DPDX
276       U1=(CE*U(I,J+1)+CW*U(I,J-1)+CN*U(I-1,J)+CS*U(I+1,J)+D2)/SEGABU
277       IF(U1.EQ.0.0) GO TO 74
      C ***   CALCULATE RESIDUAL
278       RSU=1.0-U(I,J)/U1
      C  **  STORE MAX. RESIDUAL
279       IF(ABS(RSU).GT.ABS(RESDU))RESDU=RSU
280    74 U(I,J)=U1
281       IF(AK1.LE.0.0) GO TO 72
282       GO TO 774
283    72 AK1=AKBC(J)
284       GO TO 70
      C  **  CALCULATE RESIDUAL   ********
285   774 RSK=1.0-AKE(I,J)/AK1
      C ***   STORE MAX. RESIDUAL
286       IF(ABS(RSK).GT.ABS(RESD))RESD=RSK
287    70 AKE(I,J)=AK1
288       K=K+1
289    71 CONTINUE
      C
      C ***  U AND  K BOUNDARY CONDITIONS
      C
      C ***  SOLID WALL     *******
290       DO 20 J=2,M
291       U(2,J)=UBC(J)
292    20 AKE(2,J)=AKBC(J)
      C  **   MID-WALL BISECTOR
293       DO 73 I=2,MMM
294       U(I,M)=U(I,MM)
295    73 AKE(I,M)=AKE(I,MM)
      C** CORNER BI-SECTOR     ******
296       J=3
297       DO 75 I=2,MMM
298       AKL=AKE(I,J)+(AKE(I,J+1)-AKE(I,J))/3.0
299       AKE(I+1,J)=AKL
300       UL=U(I,J)+(U(I,J+1)-U(I,J))/3.0
301       U(I+1,J)=UL
302       J=J+1
303    75 CONTINUE
      C  ***  NODES NEAR DUCT CENTER    *******
304       AKE(MM,M)=(AKE(M-2,M)*(Z(M-1)-Z(M-3))-AKE(M-3,M)*(Z(M-1)-Z(M-2)))/
          1(Z(M-2)-Z(M-3))
305       AKE(MM,MM)=AKE(MM,M)
306       AKE(M,M)=(AKE(M-1,M)*(Z(M)-Z(M-2))-AKE(M-2,M)*(Z(M)-Z(M-1)))/
          1(Z(M-1)-Z(M-2))
307       U(MM,M)=U(M-3,M)+(U(M-2,M)-U(M-3,M))*(Z(M-1)-Z(M-3))/(Z(M-2)-Z(M-3
          1))
308       U(MM,MM)=U(MM,M)
309       U(M,M)=U(M-2,M)+(U(M-1,M)-U(M-2,M))*(Z(M)-Z(M-2))/(Z(M-1)-Z(M-2))
      C
      C***  AVERAGE BULK VEL. CALCULATION
      C
310       SUMDV=0.0
311       K=3
```

```
312           DO 605 I=2,MM
313           DO 604 J=K,M
314           UAV=(U(I,J)+U(I-1,J)+U(I-1,J-1)+U(I,J-1))/4.0
315           DV=(UAV)*(Z(I)-Z(I-1))*(Y(J)-Y(J-1))
316       604 SUMDV=SUMDV+DV
317           K=K+1
318       605 CONTINUE
          C***    SYMMETRY LINE TRIANGLES
319           J=2
320           DO 7 I=2,M
321           UL=(U(I,J)+U(I-1,J))/2.0
322           UAV=(2.0/3.0)*UL+1./3.*U(I-1,J-1)
323           DV=UAV*(Z(I)-Z(I-1))*(Y(J)-Y(J-1))/2.0
324           SUMDV=SUMDV+DV
325           J=J+1
326         7 CONTINUE
327           AREA=(Z(M)-Z(1))*(Y(M)-Y(1))/2.0
328           UB=SUMDV/AREA
329           DO 8000 I=2,M
330           DO 8000 J=2,M
331      8000 U(I,J)=U(I,J)*UBAV/UB
          C
          C    ******    WALL SHEAR STRESS AND BOUNDARY UPDATING  ********
          C
332           TOW(1)=0.0
333           DO 1116 J=3,M
334           UPLUS(J)=2.5*ALOG(ROW*((CU*CD)**0.25)*SQRT(AKE(3,J))*Z(3)/AMU)+5.1
335      1116 TOW(J)=ROW*((CU*CD)**0.25)*SQRT(AKE(3,J))*U(3,J)/UPLUS(J)
336           TOW(2)=TOW(3)*Y(2)/Y(3)
337           SEGT=0.0
338           DO 1117 J=2,M
339           TW=(TOW(J)+TOW(J-1))/2.0
340      1117 SEGT=SEGT+TW*(Y(J)-Y(J-1))
341           TAV=SEGT/(Y(M)-Y(1))
342           UFAVE=SQRT(TAV/ROW)
343           DPDX=4.0*TAV/DEQ
344           DO 1119 J=2,M
345           UF(J)=SQRT(TOW(J)/ROW)
346           AKBC(J)=(UF(J)**2)/SQRT(CU*CD)
347           ZPLUS=ROW*Z(2)*UFAVE/AMU
348           UBC(J)=UF(J)*(2.5*ALOG(ZPLUS)+5.1)
349           U(2,J)=UBC(J)
350      1119 AKE(2,J)=AKBC(J)
          C
          C
          C    ****    CONVERGENCE CHECKS OF MAIN FLOW CYCLE  ********
          C
          C
351           PRINT 1000,ITER,RESDS,RESDW,RESD,RESDT
352           IF(ABS(RESDS).GT.ALAMD) GO TO 41
353           IF(ABS(RESDW).GT.ALAMD) GO TO 41
354           IF(ABS(RESDU).GT.ALAMD) GO TO 41
355           IF(ABS(RESD).GT.ALAMD) GO TO 41
356         76 GO TO 30
357         41 CONTINUE
358            IF(ITER.EQ.10) GO TO 78
359            IF(ITER.EQ.100) GO TO 78
360            IF(ITER.EQ.200) GO TO 78
361            IF(ITER.EQ.300) GO TO 78
362            IF(ITER.EQ.400) GO TO 78
363            IF(ITER.EQ.IMAX) GO TO 80
364            GO TO 69
365         78 PRINT 2600
366            DO 79 I=2,M
          C
          C    *****    NON-CONVERGED VALUES DURING ITERATIONS  *****
```

```
      C
367      79 PRINT 501,(AKE(I,J),J=9,31,2)
368         PRINT 3100
369         DO 225 I=2,M
370     225 PRINT 501,(U(I,J),J=9,31,2)
371     240 PRINT 1100
372         DO 300 I=1,MJ
373     300 PRINT 500,(EP(I,J),J=9,31,2)
374         PRINT 1200
375         DO 250 I=1,MJ
376     250 PRINT 500,(OMEG(I,J),J=9,31,2)
      C
      C  ***  GO BACK FOR ANOTHER ITERATION CYCLE  *****
      C
377         GO TO 69
378      80 CONTINUE
      C
      C
      C   *****   CONVERGED VALUES OF MAIN FLOW CYCLE   ******
      C
      C
379         PRINT 2600
380         DO 81 I=1,M
381      81 PRINT 501,(AKE(I,J),J=9,31,2)
382         PRINT 3100
383         DO 226 I=1,M
384     226 PRINT 501,(U(I,J),J=9,31,2)
385         PRINT 1100
386         DO  49 I=1,MJ
387      49 PRINT 500,(EP(I,J),J=9,31,2)
388         PRINT 1200
389         DO  50 I=1,MJ
390      50 PRINT 500,(OMEG(I,J),J=9,31,2)
      C
      C *********    SECONDARY VELOCITIES  ******************
      C
391         K=3
392         DO 3032 I=2,MMM
393         DO 3031 J=K,M
394    3031 DUZ(I,J)=((EP(I+1,J)-EP(I,J))*(Z(I)-Z(I-1))/(Z(I+1)-Z(I))+(EP(I,J)
           1-EP(I-1,J))*(Z(I+1)-Z(I))/(Z(I)-Z(I-1)))/(Z(I+1)-Z(I-1))
395         K=K+1
396    3032 CONTINUE
397         K=3
398         DO 3034 I=2,MMM
399         DO 3033 J=K,MM
400    3033 DUY(I,J)=((EP(I,J+1)-EP(I,J))*(Y(J)-Y(J-1))/(Y(J+1)-Y(J))+(EP(I,J)
           1-EP(I,J-1))*(Y(J+1)-Y(J))/(Y(J)-Y(J-1)))/(Y(J+1)-Y(J-1))
401         K=K+1
402    3034 CONTINUE
      C ** BOUNDARY CONDITIONS ****
403         DO 3036 J=2,M
404    3036 DUZ(I,J)=EP(2,J)/(Z(2)-Z(1))
405         J=2
406         DO 3038 I=2,MM
407         DUZ(I,J)=(EP(I,J)-EP(I-1,J))/(Z(I)-Z(I-1))
408         J=J+1
409    3038 CONTINUE
410         DUZ(MM,M)=(EP(MM,M)-EP(MMM,M))/(Z(MM)-Z(MMM))
411         DO 3039 J=1,M
412    3039 DUY(1,J)=0.0
413         DO 3051 I=2,M
414    3051 DUY(I,M)=(EP(I,M)-EP(I,M-1))/(Y(M)-Y(M-1))
415         J=2
416         DO 3052 I=2,MM
417         DUY(I,J)=(EP(I,J+1)-EP(I,J))/(Y(J+1)-Y(J))
```

```
418          J=J+1
419       3052 CONTINUE
420          K=3
421          DO 3053 I=2,MMM
422          DO 3054 J=K,M
423          V(I,J)=(1.0/ROW)*DUZ(I,J)
424       3054 W(I,J)=-(1.0/ROW)*DUY(I,J)
425          K=K+1
426       3053 CONTINUE
427          PRINT 2200
428          DO 3055 I=1,MMM
429       3055 PRINT 500,(V(I,J),J=9,31,2)
430          PRINT 2300
431          DO 3056 I=1,MMM
432       3056 PRINT 500,(W(I,J),J=9,31,2)
433          PRINT 10,UB
          C ***   FRICTION FACTOR
434          FACTOR=(8./(ROW*(UB**2)))*TAV
435          TAV1=TAV
436          DO 1115 J=2,M
437       1115 TLOC(J)=TOW(J)/TAV1
438          PRINT 2700,(TOW(J),J=3,31,2)
439          PRINT 2800,TAV1
440          PRINT 5432,FACTOR
441          PRINT 2710,(TLOC(J),J=3,31,2)
442          PRINT 2750,(UF(J),J=3,31,2)
          C
          C
          C   *****              HEAT TRANSFER PART            **********
          C
          C
          C
          C***   CALCULATE INITIAL B.C. WITH Q11 PROPORTIONAL TO WALL SHEAR STRESS
          C
          C  *****   ASSUME ANY VALUE FOR INITIAL AVERAGE HEAT FLUX *********
          C
443          Q11AV=0.1
444          DO 6669 J=1,M
445       6669 T(1,J)=TWALL
446          DO 6001 J=2,M
447          Q11(J)=Q11AV*TLOC(J)
448       6001 T(2,J)=T(1,J)-Q11(J)*SEGHT*(UBC(J)/UF(J)+PF)/(ROW*CPHT*UF(J))
449          K=2
450          DO 8081 I=2,M
451          DO 8082 J=K,M
452       8082 T(I,J)=T(1,J)-ANDT(I,J)*(T(1,J)-TB1)
453          K=K+1
454       8081 CONTINUE
          C
          C***   TEMPRATURE LOOP
          C
455          PRINT 2400
456          ITER=0.0
457          AMU=AMU/SEGH
          C
          C***   B,S CALCULATIONS
          C
458          K=3
459          DO 9260 I=2,MMM
460          DO 9250 J=K,MM
461          BE(I,J)=0.5*(Z(I+1)-Z(I-1))/(Y(J+1)-Y(J))
462          BW(I,J)=0.5*(Z(I+1)-Z(I-1))/(Y(J)-Y(J-1))
463          BN(I,J)=0.5*(Y(J+1)-Y(J-1))/(Z(I)-Z(I-1))
464          BS(I,J)=0.5*(Y(J+1)-Y(J-1))/(Z(I+1)-Z(I))
465          BE(I,J)=BE(I,J)*(2.*AMU+(AMUT(I,J+1)+AMUT(I,J))/SEGHT)/2.0
466          BW(I,J)=BW(I,J)*(2.*AMU+(AMUT(I,J-1)+AMUT(I,J))/SEGHT)/2.0
```

```
467          BN(I,J)=BN(I,J)*(2.*AMU+(AMUT(I-1,J)+AMUT(I,J))/SEGHT)/2.0
468     9250 BS(I,J)=BS(I,J)*(2.*AMU+(AMUT(I+1,J)+AMUT(I,J))/SEGHT)/2.0
469          K=K+1
470     9260 CONTINUE
471     1010 ITER=ITER+1
     C  **    INITIALIZATION OF RESIDUALS  **********
472          RSTI=0.0
473          K=4
474          DO 9003 I=3,MMM
475          DO 9002 J=K,MM
476          CE=AE(I,J)+BE(I,J)
477          CW=AW(I,J)+BW(I,J)
478          CN=AN(I,J)+BN(I,J)
479     6002 CS=AS(I,J)+BS(I,J)
480          SEGABK=AE(I,J)+AW(I,J)+AN(I,J)+AS(I,J)+BE(I,J)+BW(I,J)+BN(I,J
            1)+BS(I,J)
481          T1=(CE*T(I,J+1)+CW*T(I,J-1)+CN*T(I-1,J)+CS*T(I+1,J))/SEGABK
     C
     C***     CALCULATE RESIDUAL
     C
482          IF(T1.EQ.0.0) GO TO 9002
483          RST=1.-T(I,J)/T1
     C
     C***    STORE MAXIMUM RESIDUAL
     C
484          IF(ABS(RST).GT.ABS(RSTI)) RSTI=RST
485     9002 T(I,J)=T1
486          K=K+1
487     9003 CONTINUE
     C
     C***     TEMPERATURE BOUNDARY CONDITIONS
     C
     C***   NEW Q11 DISTRIBUTION
     C
488          DO 9004 J=3,M
489     9004 Q11(J)=(T(1,J)-T(3,J))*ROW*CPHT*UF(J)/(SEGHT*(UPLUS(J)+PF))
490          Q11(2)=Q11(3)*Y(2)/Y(3)
     C
     C***    UPDATED BOUNDARY VALUES OF TEMP.
     C
491          DO 6005 J=2,M
492     6005 T(2,J)=T(1,J)-Q11(J)*SEGHT*(UBC(J)/UF(J)+PF)/(ROW*CPHT*UF(J))
     C  ***   MID-WALL BISECTOR    ****
493          DO 703 I=2,MMM
494       703 T(I,M)=T(I,MM)
     C  ***   CORNER BI-SECTOR   *******
495          J=3
496          DO 705 I=2,MMM
497          AKL=T(I,J)+(T(I,J+1)-T(I,J))/3.0
498          T(I+1,J)=AKL
499          J=J+1
500       705 CONTINUE
     C  *** NODES NEAR THE DUCT CENTER  *****
501          T(MM,M)=(T(M-2,M)*(Z(M-1)-Z(M-3))-T(M-3,M)*(Z(M-1)-Z(M-2)))/
            1(Z(M-2)-Z(M-3))
502          T(MM,MM)=T(MM,M)
503          T(M,M)=(T(M-1,M)*(Z(M)-Z(M-2))-T(M-2,M)*(Z(M)-Z(M-1)))/
            1(Z(M-1)-Z(M-2))
     C
     C***    AVERAGE BULK TEMPERATURE
     C
504          SUMT=0.0
505          K=3
506          DO 6008 I=2,MM
507          DO 6007 J=K,M
508          TAVER=(T(I,J)+T(I-1,J)+T(I-1,J-1)+T(I,J-1))/4.0
```

```
509           DV=(TAVER)*(Z(I)-Z(I-1))*(Y(J)-Y(J-1))
510      6007 SUMT=SUMT+DV
511           K=K+1
512      6008 CONTINUE
      C***    SYM. LINE TRIANGLES
513           J=2
514           DO 6009 I=2,M
515           TL=(T(I,J)+T(I-1,J))/2.0
516           TAVER=(2.0/3.0)*TL+1./3.*T(I-1,J-1)
517           DV=TAVER*(Z(I)-Z(I-1))*(Y(J)-Y(J-1))/2.0
518           SUMT=SUMT+DV
519           J=J+1
520      6009 CONTINUE
521           TB=SUMT/AREA
522           DO 8007 I=1,M
523           DO 8007 J=1,M
524      8007 T(I,J)=T(I,J)*TB1/TB
      C
      C***    CONVERGENCE CHECKS OF T
      C
525           PRINT 4444,ITER,RSTI
526           IF(ABS(RSTI).GT.ALAMD) GO TO 401
527           CONTINUE
528           GO TO 402
529       401 CONTINUE
530           IF(ITER.EQ.100) GO TO 403
531           IF(ITER.EQ.150) GO TO 403
532           IF(ITER.EQ.200) GO TO 403
533           IF(ITER.EQ.IMAX) GO TO 402
534           GO TO 1010
535       403 PRINT 5555
536           DO 5554 I=2,M
537      5554 PRINT 500,(T(I,J),J=9,31,2)
538           GO TO 1010
539       402 CONTINUE
      C
      C***      CONVERGED VALUES OUTPUT
      C
540           PRINT 5555
541           DO 5556 I=1,M
542      5556 PRINT 500,(T(I,J),J=9,31,2)
      C
      C***    NONDIMENSIONAL TEMPERATURE DISTRIBUTION
      C
543           K=1
544           DO 6011 I=1,M
545           DO 6010 J=K,M
546      6010 ANDT(I,J)=(T(1,J)-T(I,J))/(T(1,J)-TB)
547           K=K+1
548      6011 CONTINUE
549           PRINT 5559
550           DO 6012 I=2,M
551      6012 PRINT 500,(ANDT(I,J),J=9,31,2)
552           PRINT 6013,TB
      C  ****  AVERAGE : HEAT FLUX , HEAT TRANSFER COEFF. , AND NU NUMBER  ******
553           SEGQ=0.0
554           Q11(1)=0.0
555           DO 6004 J=2,M
556           QW=(Q11(J)+Q11(J-1))/2.0
557      6004 SEGQ=SEGQ+QW*(Y(J)-Y(J-1))
558           QAV=SEGQ/(Y(M)-Y(1))
559           HTCO=QAV/(T(1,1)-TB)
560           FNUS=HTCO/(DEQ*THCON)
      C **    LOCAL HEAT TRANSFER COEFFICIENT  *****
561           DO 6016 J=2,M
562      6016 HTL(J)=Q11(J)/(T(1,J)-TB)
```

```
563         PRINT 6666,QAV
564         PRINT 7778,(Q11(J),J=9,M,2)
565         PRINT 8888,HTCO
566         PRINT 9999,(HTL(J),J=9,M,2)
567         PRINT 5566,FNUS
      C
      C  *****   SPECIFIED OUTPUT ON PUNCHED CARDS  **********
      C
568         DO 6014 I=1,M
569       6014 PUNCH 505,(ANDT(I,J),J=2,M)
570         DO 82 I=1,M
571        82 PUNCH 505,(AKE(I,J),J=2,M)
572         DO 227 I=1,M
573       227 PUNCH 505,(U(I,J),J=2,M)
574         DO 228 I=1,M
575       228 PUNCH 1002,(OMEG(I,J),J=2,M)
576         DO 229 I=1,M
577       229 PUNCH 1002,(EP(I,J),J=2,M)
      C
      C
      C   ****   INPUT OUTPUT FORMATS    ***********
      C
      C
578        10 FORMAT('1','AVERAGEB BULK VELOCITY = ',F10.4////)
579       500 FORMAT(12E10.3)
580       501 FORMAT('0',12F8.2)
581       505 FORMAT(10F8.3)
582      1000 FORMAT(1X,I3,4E12.4//)
583      1002 FORMAT(6E12.5)
584      1100 FORMAT(1H1,1X,24HSTREAM FUN. DISTRIBUTION//)
585      1200 FORMAT(1H1,1X,22HVORTICITY DISTRIBUTION//)
586      1335 FORMAT('1','BULFEV LENGTH SCALE'//)
587      2000 FORMAT('1','ITER',2X,'R.STF',5X,'R.VOR.',7X,'R.TKE',5X,'R.AX.VEL.'
           1//)
588      2200 FORMAT('1','V  DISTRIBUTION'//)
589      2300 FORMAT('1','W  DISTRIBUTION'//)
590      2400 FORMAT('1','ITER1',4X,'MAX. RESIDUAL FOR TEMP. LOOP'////)
591      2600 FORMAT('1','TURBULENT K.E . DISTRIBUTION'//)
592      2700 FORMAT('0','WALL SHEAR STRESS',//2X,15F7.3////)
593      2710 FORMAT('0','LOCAL WALL SHEAR STRESS',//2X,15F7.3///)
594      2750 FORMAT('0','LOCAL FRICTION VELOCITY',//2X,15F7.3)
595      2800 FORMAT('0','AVERAGE WALL SHEAR STRESS = ',F8.3////)
596      3100 FORMAT('1','AXIAL VEL. DISTRIBUTION'//)
597      4444 FORMAT(1X,I3,E12.4//)
598      5432 FORMAT('0','FRICTION FACTOR = ',E12.4///)
599      5555 FORMAT('1','TEMPERATURE DISTRIBUTION'//)
600      5559 FORMAT('1','DIMENSIONLESS TEMPERATURE DISTRIBUTION'///)
601      5566 FORMAT('0','NU. NUMBER = ',E12.4//)
602      6013 FORMAT('1','AVERAGE BULK TEMPERATURE = ',F10.4///)
603      6665 FORMAT('0','AVERAGE HEAT FLUX= ',E12.5//)
604      7778 FORMAT('0','LOCAL HEAT FLUX DISTRIBUTION',//12E10.3///)
605      8888 FORMAT('0','AVERAGE HEAT TRANSFER CO-EFFICIENT= ',E12.5///)
606      9999 FORMAT('0','LOCAL HEAT TRANSFER CO-EFF. DISTRIBUTION',//12E10.3)
607           STOP
608           END

      $ENTRY
```

APPENDIX C

COMPUTER CODE FOR EQUILATERAL ROD BUNDLE SUB-CHANNELS

The computer code "MODEL" was modified in order to solve the system of equations summarized in section (10.4) for the new geometry of rod bundle sub-channels. The same logic of the block diagram presented in figure (B.1) was followed also in the second version of the code "MODELM". The modification was mainly associated with using cylindrical co-ordinate system and applying different boundary conditions. "MODELM" is limited to the flow characteristics and does not include heat transfer.

The nomenclature of the modified program is the same as in Table (B.1), except as shown in Table (C.1).

TABLE C.1

NOMENCLATURE DIFFERENCE OF "MODELM" AND "MODEL"

MODEL	MODELM
Y(J),Z(I)	TH(J), R(I) (Grid)
DUY(I,J), DUZ(I,J)	DUR(I,J), DUTH(I,J)
V(I,J), W(I,J)	VR(I,J), VTH(I,J)
ZPLUS	R PLUS
———	YHAT (For length scale)

Some geometrical parameters were also introduced in "MODELM" and defined in the following input data cards:

Card 1

FORTRAN SYMBOLS	MEANING
M, N, L	Numerical grid parameters (Fig. 11.2)
DEQ	Equivalent hydraulic diameter
RE	Reynolds number
ROW	Density of Fluid
AMU	Dynamic viscosity of fluid
D	Rod Diameter
P1	Pitch of the array
ALPHAU	Relaxation factor
DTH	Grid spacing in peripheral direction

Card 2

(Y(I), I = 1,L)	Grid division in the gap

Card 3

C_1, C_2, CU, CD, SEGK	Turbulence Model constants
IC	Control number; if initial conditions are available as input, IC = 1.
IMAX	Maximum number of iterations
ALAMD	Convergence criterion

```
MM          MM   OOOOOOOOOOOO   DDDDDDDDD      EEEEEEEEEEEEE   LL              MM          MM
MMM        MMM  OOOOOOOOOOOOOO  DDDDDDDDDD     EEEEEEEEEEEEE   LL              MMM        MMM
MMMM      MMMM  OO          OO  DD        DD   EE              LL              MMMM      MMMM
MM MM    MM MM  OO          OO  DD         DD  EE              LL              MM MM    MM MM
MM  MM  MM  MM  OO          OO  DD         DD  EEEEEEEEE       LL              MM  MM  MM  MM
MM   MMMM   MM  OO          OO  DD         DD  EEEEEEEEE       LL              MM   MMMM   MM
MM    MM    MM  OO          OO  DD         DD  EE              LL              MM    MM    MM
MM          MM  OO          OO  DD        DD   EE              LL              MM          MM
MM          MM  OO          OO  DD       DD    EE              LL              MM          MM
MM          MM  OOOOOOOOOOOOOO  DDDDDDDDDD     EEEEEEEEEEEEE   LLLLLLLLLLLLL   MM          MM
MM          MM   OOOOOOOOOOOO   DDDDDDDDD      EEEEEEEEEEEEE   LLLLLLLLLLLLL   MM          MM
```

```
      $JOB  WATIV   ALY %- MORTADA ALY
    1       DIMENSION TH(16),R(33),EP(33,16),OMEG(33,16),AKE(33,16)',U(33,16),
           1BE(33,16),BW(33,16),BN(33,16),BS(33,16),AE(33,16),AN(33,16),AS(33,
           216),AW(33,16),AMUT(33,16),S(33,16),P1(33,16),P2(33,16),UBC(16),
           3VP(33,16),AKBC(16),UPLUS(16),TOW(16),TLOC(16),Y(20),VTH(33,16)
           4,VR(33,16),P3(33,16),DUR(33,16),DUTH(33,16),UF(16),P3(33,16)
      C
      C ******* CONSTANT VALUES *****
      C
    2       READ ,M,N,L,DEQ,RE,ROW,AMU,D,P1,ALPHAU,DTH
    3       L1=L-1
    4       L2=L+1
    5       M1=M-1
    6       M2=M-2
    7       N1=N-1
    8       READ ,C1,C2,CU,CD,SEGK,IC,IMAX,ALAMD
    9       UBAV=RE*AMU/(ROW*DEQ)
   10       C=(2.*CU/CD)*(6.*C2-2.)/(11.*(C1-2.*C2))
      C
      C **** GRID SPECIFICATIONS ****
      C
   11       TH(1)=0.0
   12       DO 1 J=2,N
   13     1 TH(J)=TH(J-1)+DTH
      C
      C  ****    GAP DIVISION ONLY  *****
      C
   14       READ ,(Y(I),I=1,L)
   15       R(1)=D/2.
   16       DO 3 I=2,L
   17     3 R(I)=R(1)+Y(I)
   18       RL=P1/2.0
   19       J=1
   20       DO 4 I=L,M
   21       R(I)=RL/COS(TH(J))
   22       J=J+1
   23     4 CONTINUE
      C
      C  *****  INITIALIZATION BY ZERO  **************
      C
   24       DO 6 I=1,M
   25       DO 6 J=1,N
   26       S(I,J)=0.0
   27       P3(I,J)=0.0
   28       U(I,J)=0.0
   29       VR(I,J)=0.0
   30       VTH(I,J)=0.0
   31       AKE(I,J)=0.0
   32       OMEG(I,J)=0.0
   33       EP(I,J)=0.0
   34     6 AMUT(I,J)=0.0
      C
      C ***  INITIAL CONDITIONS AVAILABLE ON CARDS ??  ********
      C
   35       IF(IC.EQ.1)GO TO 2222
      C
      C  ****   INITIAL CONDITIONS ARE NOT AVAILABLE  ********
      C
      C ***  ASSUME ANY INITIAL CONITIONS  AND BOUNDARY CONDITIONS  *******
      C  *********          FOR  U  AND   K          ***************
   36       UP1=0.3
   37       TAV1=ROW*(UP1**2)
   38       DPDX=4.*TAV1/DEQ
   39       RPLUS=ROW*(R(2)-R(1))*UP1/AMU
   40       DO 7 J=1,N
   41       UF(J)=UP1
```

```
42          AKBC(J)=(UF(J)**2)/SQRT(CU*CD)
43        7 UBC(J)=UF(J)*(2.5*ALOG(RPLUS)+5.1)
44          K=1
45          DO 666 I=2,M
46          DO 665 J=K,N
47          U(I,J)=UBAV
48      665 AKE(I,J)=AKBC(J)
49          IF(I.GE.L) K=K+1
50      666 CONTINUE
51          GO TO 3333
52     2222 CONTINUE
       C
       C  ******   INITIAL CONDITIONS ARE AVAILABLE ON CARDS !!!    *********
       C
53          DO 108 I=1,M
54      108 READ 3200,(EP(I,J),J=1,N)
55          DO 102 I=1,M
56      102 READ 3200,(OMEG(I,J),J=1,N)
57          DO 103 I=1,M
58      103 READ 3300 ,(U(I,J),J=1,N)
59          DO 104 I=1,M
60      104 READ 3300,(AKE(I,J),J=1,N)
61          DO 1040 J=1,N
62          UPLUS(J)=2.5*ALOG(ROW*((CU*CD)**0.25)*SQRT(AKE(3,J))*(R(3)-R(1))
           1/AMU)+5.1
63     1040 TOW(J)=ROW*((CU*CD)**0.25)*SQRT(AKE(3,J))*U(3,J)/UPLUS(J)
64          SEGT=0.0
65          DO 1050 J=2,N
66          TW=(TOW(J)+TOW(J-1))/2.
67     1050 SEGT=SEGT+TW*(TH(J)-TH(J-1))
68          TAV=SEGT/(TH(N)-TH(1))
69          UFAVE=SQRT(TAV/ROW)
70          DPDX=4.*TAV/DEQ
71          DO 1060 J=1,N
72          UF(J)=SQRT(TOW(J)/ROW)
73          AKBC(J)=(UF(J)**2)/SQRT(CU*CD)
74          RPLUS=ROW*(R(2)-R(1))*UFAVE/AMU
75          UBC(J)=(2.5*ALOG(RPLUS)+5.1)*UF(J)
76          U(2,J)=UBC(J)
77     1060 AKE(2,J)=AKBC(J)
78     3333 CONTINUE
       C
       C  ****  TURBULENCE LENGTH SCALE BY CARAJILESCOV  AND TODREAS EXPRESSION  **
       C
79          K=1
80          DO 9 I=2,M
81          DO 8 J=K,N
82          YHAT=(RL/COS(TH(J))-R(1))
83          RATIO=(R(I)-R(1))/YHAT
84          IF(RATIO.LE.0.44) GO TO 101
85          S(I,J)=YHAT*(0.44+0.066*SIN(3.14159 /0.38*(RATIO-0.44)))
86          GO TO 8
87      101 S(I,J)=R(I)-R(1)
88        8 CONTINUE
89          IF(I.GE.L) K=K+1
90        9 CONTINUE
91          PRINT 3100
92          DO 310 I=1,M
93      310 PRINT 1200,(S(I,J),J=1,N1,2)
       C
       C
       C *****  MAIN LOOP OF ITERATIONS ***
       C
       C
94          PRINT 100
95          ITER =0.0
```

```
 96       10 ITER=ITER+1
          C
          C ***  INITIALIZATION OF RESIDUALS  *******
          C
 97             RESDW=0.0
 98             RESDS=0.0
 99             RESDU=0.0
100             RESD =0.0
          C
          C ***  COEFFICIENTS FOR VORTICITY AND STREAM FUNCTION EQUATIONS ****
          C
101             K=2
102             DO 12 I=2,M2
103             DO 11 J=K,N1
104             BE(I,J)=(R(I+1)+R(I))*(TH(J+1)-TH(J-1))/(8.*(R(I+1)-R(I)))
105             BW(I,J)=(R(I)+R(I-1))*(TH(J+1)-TH(J-1))/(8.*(R(I)-R(I-1)))
106             BN(I,J)=(R(I+1)-R(I-1))/(4.*R(I)*(TH(J+1)-TH(J)))
107             BS(I,J)=(R(I+1)-R(I-1))/(4.*R(I)*(TH(J)-TH(J-1)))
108             AE(I,J)=(EP(I+1,J-1)+EP(I,J-1)-EP(I+1,J+1)-EP(I,J+1)+ABS(EP(I+1,J-
                11)+EP(I,J-1)-EP(I+1,J+1)-EP(I,J+1)))/8.0
109             AW(I,J)=(EP(I-1,J+1)+EP(I,J+1)-EP(I-1,J-1)-EP(I,J-1)+ABS(EP(I-1,J+
                11)+EP(I,J+1)-EP(I-1,J-1)-EP(I,J-1)))/8.0
110             AN(I,J)=(EP(I+1,J+1)+EP(I+1,J)-EP(I-1,J+1)-EP(I-1,J)+ABS(EP(I+1,J+
                11)+EP(I+1,J)-EP(I-1,J+1)-EP(I-1,J)))/8.0
111             AS(I,J)=(EP(I-1,J-1)+EP(I-1,J)-EP(I+1,J-1)-EP(I+1,J)+ABS(EP(I-1,J-
                11)+EP(I-1,J)-EP(I+1,J-1)-EP(I+1,J)))/8.0
112          11 VP(I,J)=(TH(J+1)-TH(J-1))*((R(I+1)+R(I))**2-(R(I)+R(I-1))**2)/16.0
113             IF(I.GE.L) K=K+1
114          12 CONTINUE
          C
          C **** VORTICITY SOURCE TERM ******
          C
          C
          C  *****  LAUNDER - YING APPROXIMATION  **********
          C
115             K=1
116             DO 14 I=2,M2
117             DO 13 J=K,N
118          13 DUR(I,J)=((U(I+1,J)-U(I,J))*(R(I)-R(I-1))/(R(I+1)-R(I))+(U(I,J)-
                1U(I-1,J))*(R(I+1)-R(I))/(R(I)-R(I-1)))/(R(I+1)-R(I-1))
119             IF(I.GE.L1) K=K+1
120          14 CONTINUE
121             K=2
122             DO 16 I=2,M2
123             DO 15 J=K,N1
124          15 DUTH(I,J)=(1./R(I)*((U(I,J+1)-U(I,J))*(TH(J)-TH(J-1))/(TH(J+1)-TH(
                1J))+(U(I,J)-U(I,J-1))*(TH(J+1)-TH(J))/(TH(J)-TH(J-1)))/(TH(J+1)-
                2TH(J-1)))
125             IF(I.GE.L ) K=K+1
126          16 CONTINUE
          C
          C ***   BOUNDARY VALUES *****
          C
127             DO 17 J=1,N
128          17 DUR(1,J)=U(2,J)/(R(2)-R(1))
129             J=1
130             DO 18 I=L,M
131             DUR(I,J)=(U(I,J)-U(I-1,J))/(R(I)-R(I-1))
132             J=J+1
133          18 CONTINUE
134             DUR(M1,N)=(U(M1,N)-U(M2,N))/(R(M1)-R(M2))
135             DO 19 J=1,N
136          19 DUTH(1,J)=0.0
137             DO 20 I=2,M1
138          20 DUTH(I,N)=(U(I,N)-U(I,N1))/(R(I)*(TH(N)-TH(N1)))
139             J=1
```

```
140         DO 21 I=L,M1
141         DUTH(I,J)=(U(I,J+1)-U(I,J))/(R(I)*(TH(J+1)-TH(J)))
142         J=J+1
143      21 CONTINUE
144         J=1
145         DO 22 I=2,L1
146      22 DUTH(I,1)=(U(I,J+1)-U(I,J))/(R(I)*(TH(J+1)-TH(J)))
147         K=1
148         DO 24 I=1,M1
149         DO 23 J=K,N
150         F1(I,J)= C*(S(I,J)**2)*((DUTH(I,J)**2)-(DUR(I,J)**2))
151         F2(I,J)= C*(S(I,J)**2)*DUTH(I,J)*DUR(I,J)
152      23 F4(I,J)=DUTH(I,J)**2+DUR(I,J)**2
153         IF(I.GE.L) K=K+1
154      24 CONTINUE
       C
       C**********  NORMAL STRESSES SOURCE TERM ****
       C
155         K=1
156         DO 26 I=2,M2
157         DO 25 J=K,N
158      25 DUR(I,J)=((F1(I+1,J)-F1(I,J))*(R(I)-R(I-1))/(R(I+1)-R(I))+(F1(I,J)
          1-F1(I-1,J))*(R(I+1)-R(I))/(R(I)-R(I-1)))/(R(I+1)-R(I-1))
159         IF(I.GE.L1) K=K+1
160      26 CONTINUE
       C******  BOUNDARY VALUES *****
161         J=1
162         DO 27 I=L,M1
163         DUR(I,J)=(F1(I,J)-F1(I-1,J))/(R(I)-R(I-1))
164         J=J+1
165      27 CONTINUE
       C
       C *****  FIRST TERM OF NORMAL STRESS PRODUCTION TERM  *******
       C
166         K=2
167         DO 29 I=2,M2
168         DO 28 J=K,N1
169         F3(I,J)=+((DUR(I,J+1)-DUR(I,J))*(TH(J)-TH(J-1))/(TH(J+1)-TH(J))+(
          1DUR(I,J)-DUR(I,J-1))*(TH(J+1)-TH(J))/(TH(J)-TH(J-1)))/(R(I)*(TH(J+
          21)-TH(J-1)))
       C
       C  *****  FINAL EXPRESSION OF NORMAL STRESS SOURCE TERM *****
       C
170      28 F3(I,J)=F3(I,J)+1./(R(I)**2)*((F1(I,J+1)-F1(I,J))*(TH(J)-TH(J-1))/
          1(TH(J+1)-TH(J))+(F1(I,J)-F1(I,J-1))*(TH(J+1)-TH(J))/(TH(J)-TH(J-1)
          2))/(TH(J+1)-TH(J-1))
171         IF(I.GE.L ) K=K+1
172      29 CONTINUE
       C
       C ****      SHEAR STRESSES SOURCE TERM ********
       C
173         K=1
174         DO 202 I=2,M2
175         DO 201 J=K,N
176     201 DUR(I,J)=((F2(I+1,J)-F2(I,J))*(R(I)-R(I-1))/(R(I+1)-R(I))+(F2(I,J)
          1-F2(I-1,J))*(R(I+1)-R(I))/(R(I)-R(I-1)))/(R(I+1)-R(I-1))
177         IF(I.GE.L1) K=K+1
178     202 CONTINUE
       C  ***    BOUNDARY VALUES *****
179         J=1
180         DO 203 I=L,M1
181         DUR(I,J)=(F2(I,J)-F2(I-1,J))/(R(I)-R(I-1))
182         J=J+1
183     203 CONTINUE
184         DO 204 J=1,N
185     204 DUR(1,J)=F2(2,J)/(R(2)-R(1))
```

```
186          DUR(M1,N)=(F2(M1,N)-F2(M2,N))/(R(M1)-R(M2))
187          K=2
188          DO 206 I=2,M2
189          DO 205 J=K,N1
190       205 DUTH(I,J)=  (F2(I,J+1)-F2(I,J-1))/(TH(J+1)-TH(J-1))
191          IF(I.GE.L)  K=K+1
192       206 CONTINUE
193          DO 207 I=2,L1
194       207 DUTH(I,1)=(F2(I,J+1)-F2(I,J))/(TH(J+1)-TH(J))
195          DO 208 I=2,M1
196       208 DUTH(I,N)=(F2(I,N)-F2(I,N1))/(TH(N)-TH(N1))
197          J=1
198          DO 2090 I=L,M1
199          DUTH(I,J)=(F2(I,J+1)-F2(I,J))/(TH(J+1)-TH(J))
200          J=J+1
201       2090 CONTINUE
          C
          C  ****  F1(I,J) IS NOW A NEW VARIABLE  *****
          C
202          K=1
203          DO 210 I=2,M2
204          DO 209 J=K,N
205       209 F1(I,J)=((DUR(I+1,J)-DUR(I,J))*(R(I)-R(I-1))/(R(I+1)-R(I))+(DUR(I,
               1J)-DUR(I-1,J))*(R(I+1)-R(I))/(R(I)-R(I-1)))/(R(I+1)-R(I-1))
206          IF(I.GE.L1)  K=K+1
207       210 CONTINUE
          C
          C  ****  F2(I,J) IS NOW A NEW VARIABLE  *****
          C
208          K=2
209          DO 212 I=2,M2
210          DO 211 J=K,N1
211       211 F2(I,J)=(DUTH(I,J+1)-DUTH(I,J-1))/(TH(J+1)-TH(J-1))
212          IF(I.GE.L)  K=K+1
213       212 CONTINUE
          C
          C  ****  TOTAL VORTICITY PRODUCTION  ***************
          C
214          K=2
215          DO 214 I=2,M2
216          DO 213 J=K,N1
217       213 F3(I,J)=F3(I,J)+F1(I,J)+3.*DUR(I,J)/R(I)-F2(I,J)/(R(I)**2)
218          IF(I.GE.L)  K=K+1
219       214 CONTINUE
          C
          C   ******    VORTICITY SUBCYCLE ******
          C
220          K=L
221          DO 31 J=2,N1
222          DO 30 I=2,K
223          SEGAB=AE(I,J)+AW(I,J)+AN(I,J)+AS(I,J)+2.0*AMU*(BE(I,J)+BW(I,J)+BN
               1(I,J)+BS(I,J))
224          CE=AE(I,J)+2.0*AMU*BE(I,J)
225          CW=AW(I,J)+2.0*AMU*BW(I,J)
226          CN=AN(I,J)+2.0*AMU*BN(I,J)
227          CS=AS(I,J)+2.0*AMU*BS(I,J)
228          D=-VP(I,J)*ROW*F3(I,J)
          C
          C ***   CASE OF NEGATIVE VORTICITY PRODUCTION !!!  (CHAPTER 12)  ******
          C
229          IF(D.GT.0.0)  D=0.0
230          OMEG1=(CE*OMEG(I+1,J)+CW*OMEG(I-1,J)+CN*OMEG(I,J+1)+CS*OMEG(I,J-1)
               1+D)/SEGAB
231          IF(OMEG(I,J).EQ.0.0)  GO TO 30
          C  ****   CALCULATE RESIDUAL     **************
232          RSW=(OMEG1-OMEG(I,J))/OMEG(I,J)
```

```
      C  STORE MAX. RESIDUAL    ******
233         IF(ABS(RSW).GT.ABS(RESDW)) RESDW=RSW
234      30 OMEG(I,J)=ALPHAU*OMEG1+(1.-ALPHAU)*OMEG(I,J)
235         K=K+1
236      31 CONTINUE
         C
         C  *****   STREAM FUNCTION SUBCYCLE  *******
         C
237         K=L
238         DO 33 J=2,M1
239         DO 32 I=2,K
         C ***  SOURCE TERM FOR STREAM FUNCTION EQUATION ********
240         D1=ROW*VP(I,J)*OMEG(I,J)
241         SEGB=2.*(BE(I,J)+BW(I,J)+BN(I,J)+BS(I,J))
242         EPSI=(2.*(BE(I,J)*EP(I+1,J)+BW(I,J)*EP(I-1,J)+BN(I,J)*EP(I,J+1)+
           1BS(I,J)*EP(I,J-1))+D1)/SEGB
243         IF(EP(I,J).EQ.0.0) GO TO 32
         C  ****   CALCULATE RESIDUAL     ***************
244         RSS=(EPSI-EP(I,J))/FP(I,J)
         C  STORE MAX. RESIDUAL    ******
245         IF(ABS(RSS).GT.ABS(RESDS)) RESDS=RSS
246      32 EP(I,J)=EPSI
247         K=K+1
248      33 CONTINUE
         C **** FOR NUMERICAL TREATMENT OF NODES NEAR CORNER BI-SECTOR  *******
         C            NO PHYSICAL MEANING
         C
249         J=1
250         DO 34 I=L2,M1
251         EP(I,J)=-EP(I-1,J+1)
252         J=J+1
253      34 CONTINUE
         C
         C  ***** AXIAL VELOCITY AND TURBULENT K. E. SUBCYCLE ************
         C
         C   ******      EDDY VISCOSITY        *****************
         C
254         K=1
255         DO 36 I=2,M
256         DO 35 J=K,N
257         IF(AKE(I,J).LE.0.0) GO TO 335
258         AMUT(I,J)=CU*SQRT(AKE(I,J))*S(I,J)*ROW
259         GO TO 35
260       335 AMUT(I,J)=0.0
261      35 CONTINUE
262         IF(I.GE.L) K=K+1
263      36 CONTINUE
264         K=L
265         DO 42 J=2,M1
266         DO 41 I=3,K
         C
         C ****  COEFFICIENTS FOR  K  EQUATION    *******
         C
267         CE=AE(I,J)+BE(I,J)*(2.*AMU+(AMUT(I,J)+AMUT(I+1,J))/SEGK)
268         CW=AW(I,J)+BW(I,J)*(2.*AMU+(AMUT(I,J)+AMUT(I-1,J))/SEGK)
269         CN=AN(I,J)+BN(I,J)*(2.*AMU+(AMUT(I,J)+AMUT(I,J+1))/SEGK)
270         CS=AS(I,J)+BS(I,J)*(2.*AMU+(AMUT(I,J)+AMUT(I,J-1))/SEGK)
271         SEGABK=CE+CW+CN+CS
         C  ***  SOURCE TERM FOR  K  EQUATION    *****
272         TKS=VP(I,J)*(AMUT(I,J)*P4(I,J))
273         AK1=(CE*AKE(I+1,J)+CW*AKE(I-1,J)+CN*AKE(I,J+1)+CS*AKE(I,J-1)+TKS)
           1/SEGABK/(1.+VP(I,J)*CD*ROW*SQRT(AKE(I,J))/(S(I,J)*SEGABK))
         C
         C  *****  COEFFICIENTS FOR  U  EQUATION   *************
         C
274         CE=AE(I,J)+BE(I,J)*(2.*AMU+AMUT(I,J)+AMUT(I+1,J))
```

```
275         CW=AW(I,J)+BW(I,J)*(2.*AMU+AMUT(I,J)+AMUT(I-1,J))
276         CN=AN(I,J)+BN(I,J)*(2.*AMU+AMUT(I,J)+AMUT(I,J+1))
277         CS=AS(I,J)+BS(I,J)*(2.*AMU+AMUT(I,J)+AMUT(I,J-1))
278         SEGABU=CE+CW+CN+CS
      C  ****  SOURCE TERM FOR  U  EQUATION
279         D2=VP(I,J)*DPDX
280         U1=(CE*U(I+1,J)+CW*U(I-1,J)+CN*U(I,J+1)+CS*U(I,J-1)+D2)/SEGABU
281         IF(U(I,J).EQ.0.0) GO TO 37
      C  ****   CALCULATE RESIDUAL      **************
282         RSU=(U1-U(I,J))/U(I,J)
      C  STORE MAX. RESIDUAL    ******
283         IF(ABS(RSK).GT.ABS(RESD))RESD=RSK
284      37 U(I,J)=U1
285         IF(AKE(I,J).LE.0.0) GO TO 41
      C  ****   CALCULATE RESIDUAL      **************
286      39 RSK=(AK1-AKE(I,J))/AKE(I,J)
      C  STORE MAX. RESIDUAL    ******
287         IF(ABS(RSU).GT.ABS(RESDU)) RESDU=RSU
288      41 AKE(I,J)=AK1
289         K=K+1
290      42 CONTINUE
      C
      C  ****     U  AND  K   BOUNDARY CONDITIONS   ******
      C
      C ***     WALL   CONDITIONS *******
      C
291         DO 43 J=1,N
292         U(2,J)=UBC(J)
293      43 AKE(2,J)=AKBC(J)
      C
      C ****     THETA=0.0  CONDITIONS ********
      C
294         DO 44 I=2,L
295         U(I,1)=U(I,2)
296      44 AKE(I,1)=AKE(I,2)
      C
      C  *****  THETA=30   CONDITIONS  ******
      C
297         DO 45 I=2,M2
298         U(I,N)=U(I,N-1)
299      45 AKE(I,N)=AKE(I,N-1)
300         AKE(M1,N)=(AKE(M2,N)*(R(M1)-R(M-3))-AKE(M-3,N)*(R(M1)-R(M2)))/(R(M
           12)-R(M-3))
301         AKE(M,N)=(AKE(M1,N)*(R(M)-R(M2))-AKE(M2,N)*(R(M)-R(M1)))/(R(M1)-
           1R(M2))
302         U(M1,N)=U(M-3,N)+(U(M2,N)-U(M-3,N))*(R(M1)-R(M-3))/(R(M2)-R(M-3))
303         U(M,N)=U(M2,N)+(U(M1,N)-U(M2,N))*(R(M)-R(M2))/(R(M1)-R(M2))
      C  ****     MAX. VELCCITY LINE    **************
      C
304         I=L2
305         DO 46 J=2,N1
306         CJ=  (R(I)-R(I-1))*TAN(TH(J))/(R(I)*(TH(J+1)-TH(J)))
307         U(I,J)=  (CJ*U(I,J+1)+U(I-1,J))/(CJ+1.)
308         AKE(I,J)=  (CJ*AKE(I,J+1)+AKE(I-1,J))/(CJ+1.0)
309         I=I+1
310      46 CONTINUE
      C
      C **** AVERAGE BULK VELOCITY CALCULATION *****
      C
311         SUMDV=0.0
312         K=2
313         DO 48 I=2,M1
314         DO 47 J=K,N
315         UAV=(U(I,J)+U(I-1,J)+U(I-1,J-1)+U(I,J-1))/4.
316         DV=(UAV)*(R(I)-R(I-1))*((R(I)+R(I-1))/2.)*(TH(J)-TH(J-1))
317      47 SUMDV=SUMDV+DV
```

```
318         IF(I.GE.L) K=K+1
319      48 CONTINUE
      C *** MVL TRIANGLES ****
320         J=2
321         DO 49 I=L2,M
322         UL=(U(I,J)+U(I-1,J))/2.0
323         UAV=2./3.*UL+(1./3.)*U(I-1,J-1)
324         DV=UAV*(R(I)-R(I-1))*((R(I)+R(I-1))/2.)*(TH(J)-TH(J-1)) /2.
325         SUMDV=SUMDV+DV
326         J=J+1
327      49 CONTINUE
328         AREA=0.5*((RL**2)*TAN(3.14159/6.)-3.14159*(R(1)**2)/6.)
329         UB=SUMDV/AREA
330         DO 50 I=2,M
331         DO 50 J=1,N
332      50 U(I,J)=U(I,J)*UBAV/UB
      C
      C  ****  WALL SHEAR STRESS AND BOUNDARY UPDATING  **********
      C
333         DO 51 J=1,N
334         UPLUS(J)=2.5*ALOG(ROW*((CU*CD)**0.25)*SQRT(AKE(3,J))*(R(3)-R(1))
           1/AMU)+5.1
335      51 TOW(J)=ROW*((CU*CD)**0.25)*SQRT(AKE(3,J))*U(3,J)/UPLUS(J)
336         SEGT=0.0
337         DO 52 J=2,N
338         TW=(TOW(J)+TOW(J-1))/2.
339      52 SEGT=SEGT+TW*(TH(J)-TH(J-1))
340         TAV=SEGT/(TH(N)-TH(1))
341         UFAVE=SQRT(TAV/ROW)
342         DPDX=4.*TAV/DEQ
343         DO 53 J=1,N
344         UF(J)=SQRT(TOW(J)/ROW)
345         AKBC(J)=(UF(J)**2)/SQRT(CU*CD)
346         RPLUS=ROW*(R(2)-R(1))*UFAVE/AMU
347         UBC(J)=(2.5*ALOG(RPLUS)+5.1)*UF(J)
348         U(2,J)=UBC(J)
349      53 AKE(2,J)=AKBC(J)
      C
      C *****      CONVERGENCE CHECKS *****
      C
350         PRINT 1000,ITER,RESDS,RESDW,RESD,RESDU
351         IF(ABS(RESDS).GT.ALAMD) GO TO 60
352         IF(ABS(RESDW).GT.ALAMD) GO TO 60
353         IF(ABS(RESDU).GT.ALAMD) GO TO 60
354         IF(ABS(RESD).GT.ALAMD) GO TO 60
355      55 GO TO 80
356      60 CONTINUE
357         IF(ITER.EQ.200) GO TO 65
358         IF(ITER.EQ.400) GO TO 65
359         IF(ITER.EQ.600) GO TO 65
360         IF(ITER.EQ.800) GO TO 65
361         IF(ITER.EQ.IMAX) GO TO 80
      C  ***  GO BACK FOR ANOTHER ITERATION CYCLE  *****
362         GO TO 10
      C
      C ***   NON-CONVERGED VALUES  *******
      C
363      65 PRINT 2000
364         DO 70 I=1,M
365      70 PRINT 1100,(AKE(I,J),J=1,N)
366         PRINT 2100
367         DO 71 I=1,M
368      71 PRINT 1100,(U(I,J),J=1,N)
369         PRINT 2200
370         DO 72 I=1,M
371      72 PRINT 1200,(UP(I,J),J=1,N1,2)
```

```
372          PRINT 2300
373          DO 73 I=1,M
374       73 PRINT 1200,(OMEG(I,J),J=1,N1,2)
      C
      C  ***  GO BACK FOR ANOTHER ITERATION CYCLE  *****
      C
375          GO TO 10
376       80 CONTINUE
      C
      C  **** CONVERGED VALUES   ******
      C
377          PRINT 2000
378          DO 90 I=1,M
379       90 PRINT 1100,(AKE(I,J),J=1,N)
380          PRINT 2100
381          DO 91 I=1,M
382       91 PRINT 1100,(U(I,J),J=1,N)
383          PRINT 2200
384          DO 92 I=1,M
385       92 PRINT 1200,(EP(I,J),J=1,N1,2)
386          PRINT 2300
387          DO 93 I=1,M
388       93 PRINT 1200,(OMEG(I,J),J=1,N1,2)
389          PRINT 3000
390          DO 360 I=1,M
391      360 PRINT 1200,(AMUT(I,J),J=1,N1,2)
      C
      C  ****    SECONDARY VELOCITIES    *******
      C
392          K=1
393          DO 1041 I=2,M2
394          DO 1031 J=K,N
395     1031 DUR(I,J)=((EP(I+1,J)-EP(I,J))*(R(I)-R(I-1))/(R(I+1)-R(I))+(EP(I,J)
            1-EP(I-1,J))*(R(I+1)-R(I))/(R(I)-R(I-1)))/(R(I+1)-R(I-1))
396          IF(I.GE.L1)K=K+1
397     1041 CONTINUE
398          K=2
399          DO 1061 I=2,M2
400          DO 1051 J=K,N1
401     1051 DUTH(I,J)=(1./R(I)*((EP(I,J+1)-EP(I,J))*(TH(J)-TH(J-1))/(TH(J+1)-
            1TH(J))+(EP(I,J)-EP(I,J-1))*(TH(J+1)-TH(J))/(TH(J)-TH(J-1)))/(TH(J
            2+1)-TH(J-1)))
402          IF(I.GE.L)K=K+1
403     1061 CONTINUE
      C
      C  ******  BOUNDARY VALUES    *********
404          DO 1070 J=1,N
405     1070 DUR(1,J)=EP(2,J)/(R(2)-R(1))
406          J=1
407          DO 1080 I=L,M
408          DUR(I,J)=(EP(I,J)-EP(I-1,J))/(R(I)-R(I-1))
409          J=J+1
410     1080 CONTINUE
411          DUR(M1,N)=(EP(M1,N)-EP(M2,N))/(R(M1)-R(M2))
412          DO 1090 J=1,N
413     1090 DUTH(1,J)=0.0
414          DO 1091 I=2,M1
415     1091 DUTH(I,N)=(EP(I,N)-EP(I,N1))/(R(I)*(TH(N)-TH(N1)))
416          J=1
417          DO 2010 I=L,M1
418          DUTH(I,J)=(EP(I,J+1)-EP(I,J))/(R(I)*(TH(J+1)-TH(J)))
419          J=J+1
420     2010 CONTINUE
421          J=1
422          DO 2020 I=2,L1
423     2020 DUTH(I,1)=(EP(I,J+1)-EP(I,J))/(R(I)*(TH(J+1)-TH(J)))
```

```
424           K=1
425           DO 3003 I=2,M2
426           DO 3002 J=K,N
427           VTH(I,J)=(-1./ROW)*DUR(I,J)*100./UBAV
428        3002 VR(I,J)=1./(RCW)*DUTH(I,J)*100./UBAV
429           IF(I.GE.L) K=K+1
430        3003 CONTINUE
431           PRINT 2001
432           DO 405 I=2,M2
433         405 PRINT 1100,(VTH(I,J),J=1,N)
434           PRINT 3001
435           DO 505 I=2,M2
436         505 PRINT 1100,(VR(I,J),J=1,N)
437           PRINT 1300,UB
          C
          C ***    FRICTION FACTOR
          C
438           FACTOR=(8./(RCW*(UB**2)))*TAV
439           DO 94 J=1,N
440          94 TLOC(J)=TOW(J)/TAV
441           PRINT 2400,(TOW(J),J=1,16)
442           PRINT 2500,TAV
443           PRINT 2600,FACTOR
444           PRINT 2700,(TLOC(J),J=1,16)
445           PRINT 2800,(UF(J),J=1,16)
446           DO 95 I=1,M
447          95 PUNCH 3200,(EP(I,J),J=1,N)
448           DO 96 I=1,M
449          96 PUNCH 3200,(OMEG(I,J),J=1,N)
450           DO 97 I=1,M
451          97 PUNCH 3300,(U(I,J),J=1,N)
452           DO 98 I=1,M
453          98 PUNCH 3300,(AKE(I,J),J=1,N)
          C
          C ***  INPUT OUTPUT FORMATS   ********
          C
454         100 FORMAT('1','ITER',4X,'R.STF',5X,'R.VOR',5X,'R.TKE',5X,'R.AX.VEL.'/
                1//)
455        1000 FORMAT(1X,I4,4E12.4,E18.6//)
456        1100 FORMAT(1X,16F7.2)
457        1200 FORMAT(1X,8E14.5)
458        1300 FORMAT ('1','AVERAGE BULK VEL.= ',F10.4//// )
459        2000 FORMAT('1','TURBULENT K. E. DISTRIBUTION'//)
460        2001 FORMAT('1','VTH  DISTRIBUTION-PERCENT OF UB' ///)
461        2100 FORMAT('1','AXIAL VELOCITY DISTRIBUTION'//)
462        2200 FORMAT ('1','STREAM FUNCTION DISTRIBUTION'//)
463        2300 FORMAT('1','VORTICITY DISTRIBUTION'//)
464        2400 FORMAT('0','WALL SHEAR STRESS',//2X,16F7.3////)
465        2500 FORMAT('0','AVERAGE WALL SHEAR STRESS= ',F8.3////)
466        2600 FORMAT('0','FRICTION FACTOR= ',E12.4///)
467        2700 FORMAT('0','NORMALIZED WALL SHEAR STRESS',//2X,16F7.3)
468        2800 FORMAT('3','LOCAL FRICTION VELOCITY',//2X,16F7.3)
469        3000 FORMAT('1','EDDY VISCOSITY DISTRIBUTION'///)
470        3001 FORMAT('1','VR  DISTRIBUTION - PERCENT OF UB' ///)
471        3100 FORMAT('1','TURBULENCE LENGTH SCALE'///)
472        3200 FORMAT(8F10.3)
473        3300 FORMAT(8F10.4)
474           STOP
475           END
```

TABLE 1

EQUATIONS TO BE SOLVED IN THE GENERAL ELLIPTIC FORM FOR TRIANGULAR DUCTS

Model	Equation	ϕ	A	B	C	D
I, II	(6.19)	ψ	0	$1/\rho$	1	$-\omega$
I	(6.20)	ω	1	1	μ	$-\rho \frac{\partial^2(\overline{v^2} - \overline{w^2})}{\partial y \partial z} + \rho\left(\frac{\partial^2 \overline{vw}}{\partial y^2} - \frac{\partial^2 \overline{vw}}{\partial z^2}\right)$
I	(6.18)	$\overline{U}$	1	μ_e (6.4)	1	$\partial P/\partial x$
II	(6.20 and 6.26)	ω	1	1	μ	$\rho \frac{\partial^2}{\partial y \partial z}\left\{c\ell^2\left[\left(\frac{\partial \overline{U}}{\partial y}\right)^2 - \left(\frac{\partial \overline{U}}{\partial z}\right)^2\right]\right\}$ $- \rho \frac{\partial^2}{\partial y^2}\left[c\ell^2\left(\frac{\partial \overline{U}}{\partial y}\right)\left(\frac{\partial \overline{U}}{\partial z}\right)\right] + \rho \frac{\partial^2}{\partial z^2}\left[c\ell^2\left(\frac{\partial \overline{U}}{\partial y}\right)\left(\frac{\partial \overline{U}}{\partial z}\right)\right]$
II	(6.18)	$\overline{U}$	1	$\mu + \mu_t$ (6.9)	1	$\partial P/\partial x = 4\ \tau_w/D_h$
II	(6.21)	k	1	$\mu + \frac{\mu_t}{\sigma_k}$	1	$-\mu_t\left[\left(\frac{\partial \overline{U}}{\partial y}\right)^2 + \left(\frac{\partial \overline{U}}{\partial z}\right)^2\right] + \frac{\rho c_D (k)^{3/2}}{\ell}$
II	(6.22-6.23)	$\overline{H}$	1	$\frac{\mu}{\sigma_h} + \frac{\mu_t}{\sigma_{h,t}}$	1	0

TABLE 2

NUMERICAL GRID FOR THE EQUILATERAL TRIANGULAR DUCT

Index of Node (j)	Node Position* (z_j/H)
1	0 (wall)
2	.01091
3	.02182
4	.03082
5	.04528
6	.06165
7	.07938
8	.09711
9	.1135
10	.1408
11	.1817
12	.2158
13	.2499
14	.2840
15	.3181
16	.3522
17	.3863
18	.4203
19	.4544
20	.4885
21	.5226
22	.5567
23	.5908
24	.6249
25	.6590
26	.6931
27	.7272
28	.7954
29	.8636
30	.9318
31	1.0000 (duct centerline)

*For the y-direction, node locations were $\frac{y_i}{L} = 1 - \left[\frac{z_j}{H}\right]_{j = 32-i}$

TABLE 3

EQUATIONS TO BE SOLVED IN THE GENERAL ELLIPTIC FORM FOR ROD BUNDLES

Equation	Φ	a_ϕ	b_ϕ	$d\phi$
10.5	$\bar{U}$	1	$\mu+\mu_t$	$\partial\bar{P}/\partial x = 4\tau_W/D_h$
10.6	ψ	0	$1/\rho$	$-\omega$
10.7	ω	1	μ	$\rho[\{\frac{1}{r}\frac{\partial^2}{\partial r\partial\theta} + \frac{1}{r^2}\frac{\partial}{\partial\theta}\}\{C\ell^2[(\frac{\partial\bar{U}}{r\partial\theta})^2 - (\frac{\partial\bar{U}}{\partial r})^2]\}]$
				$+ \rho[\{\frac{\partial}{\partial r^2} - \frac{1}{r^2}\frac{\partial^2}{\partial\theta^2} + \frac{3}{r}\frac{\partial}{\partial r}\}\{C\ell^2(\frac{\partial\bar{U}}{r\partial\theta})(\frac{\partial\bar{U}}{\partial r})\}]$
10.8	k	1	$\mu + \frac{\mu_t}{\sigma_k}$	$-\mu_t[(\frac{\partial\bar{U}}{\partial r})^2 + (\frac{\partial\bar{U}}{r\partial\theta})^2] + \frac{\rho C_D k^{3/2}}{\ell}$

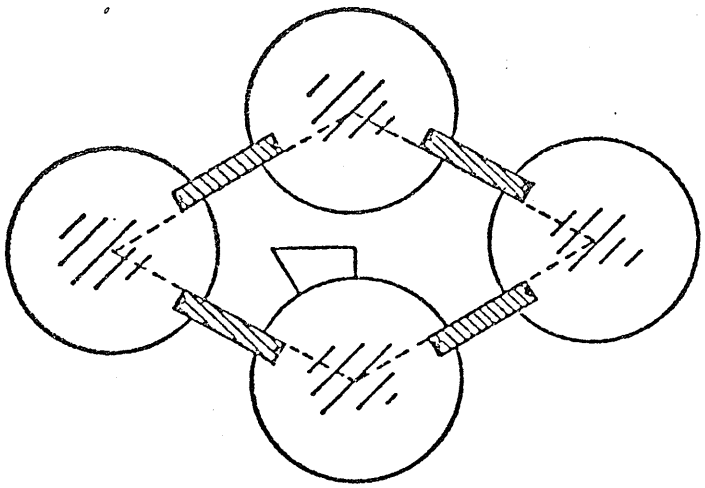

Fig. 2.1. Cross-section of Test-section Used By Eifler and Nijsing

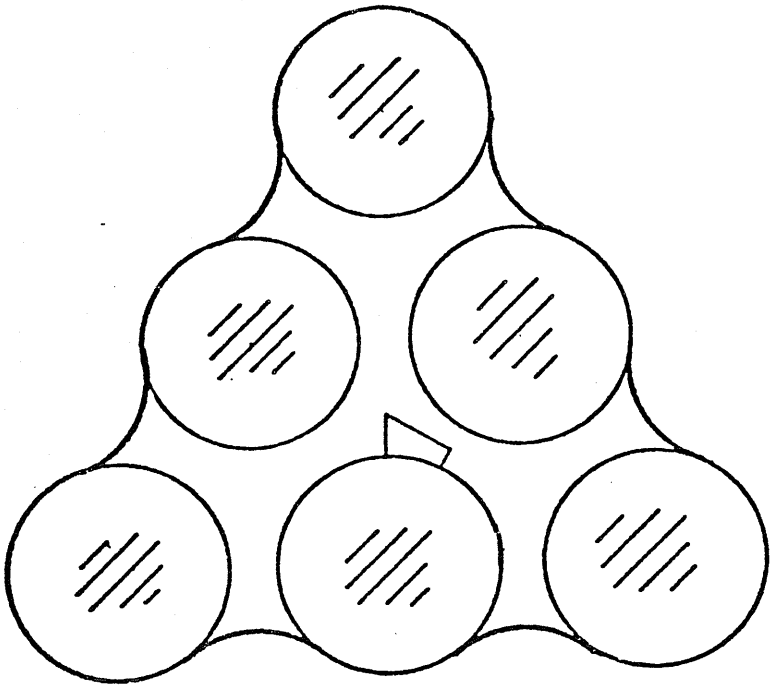

Fig. 2.2. Cross-Section of Test-Section Used By Kjellstrom.

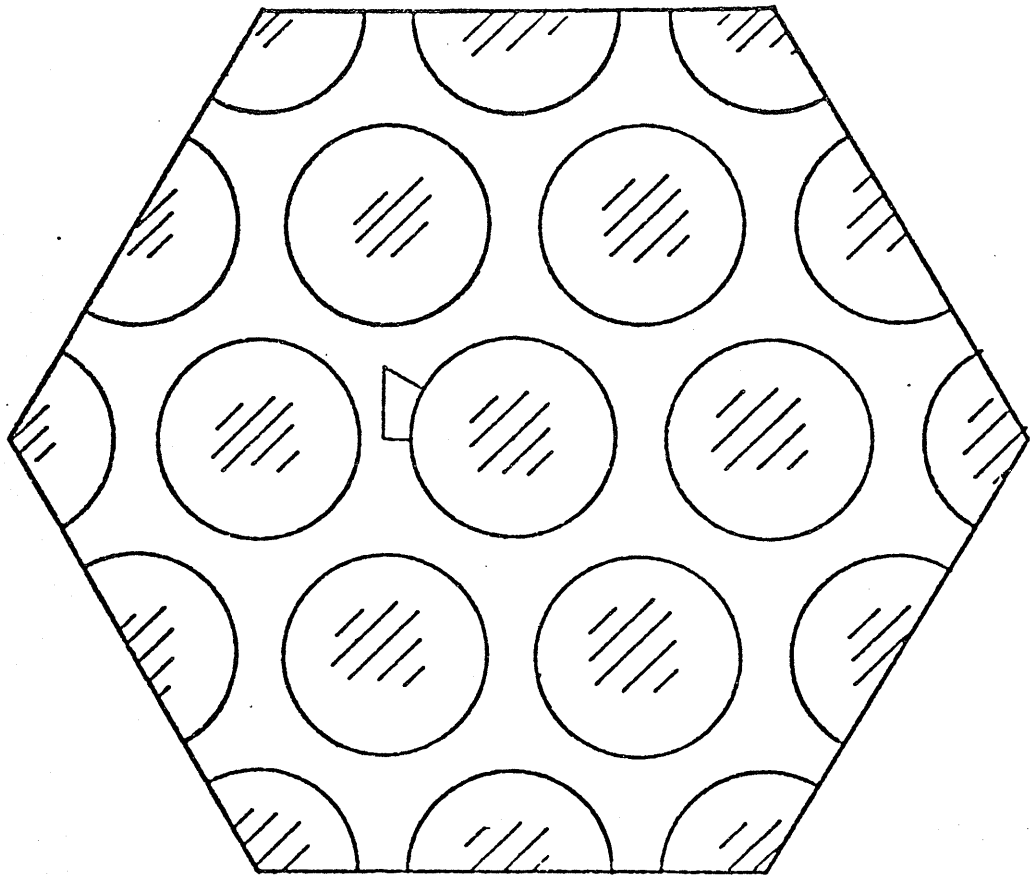

Fig. 2.3. Cross-Section of Test-Section Used By Trupp and Azad.

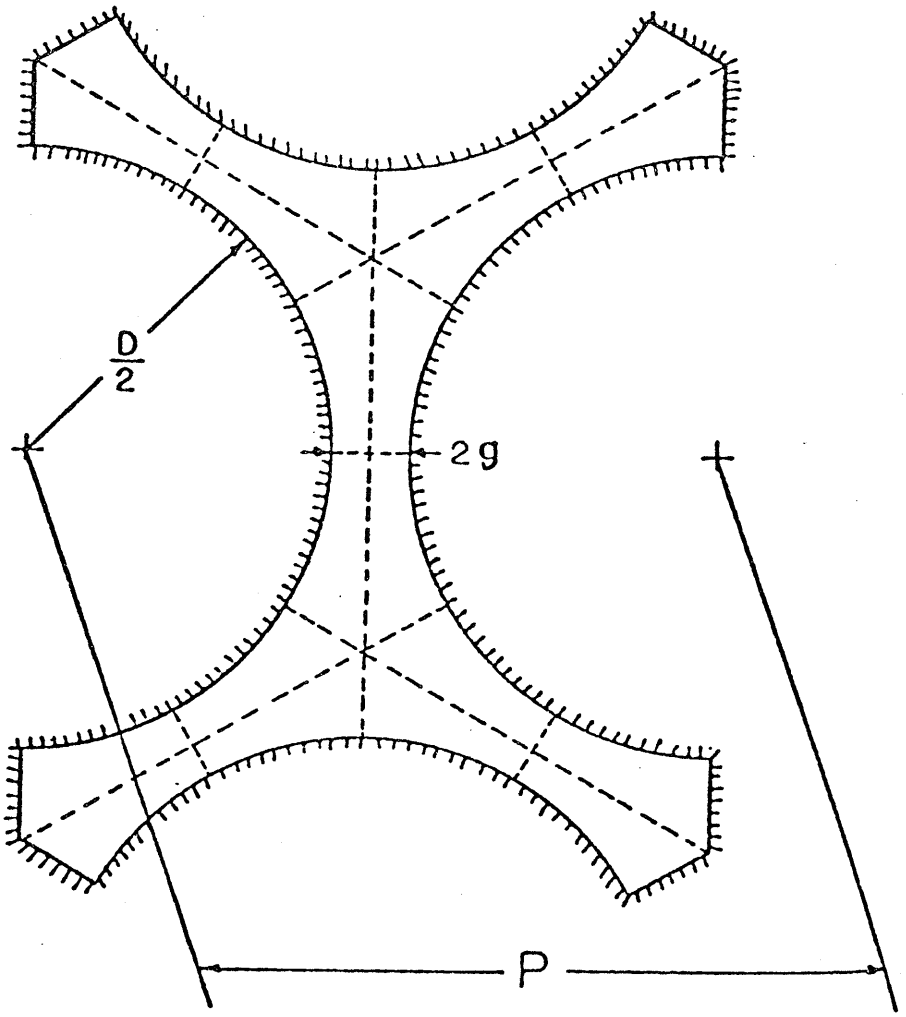

Fig. 2.4. Cross-section of Test-section Used by Carajilescov and Todreas

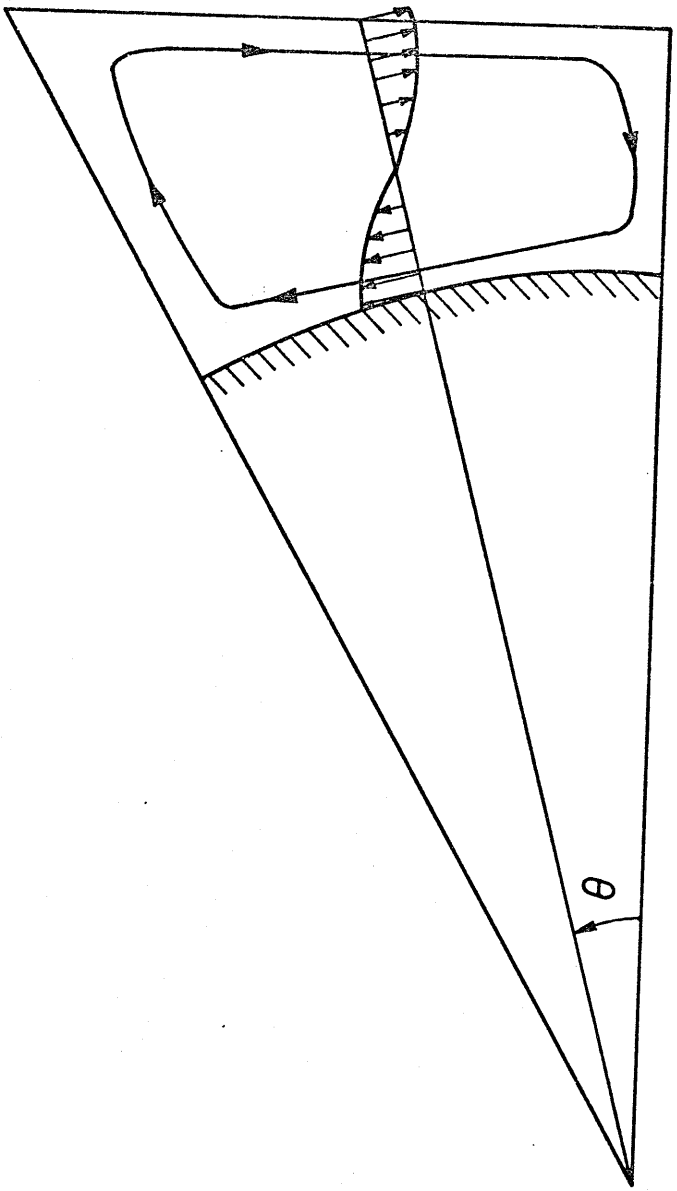

Fig. 2.5. Schematic Reprsentation of Secondary Flow Pattern Proposed By Eifler and Nijsing .

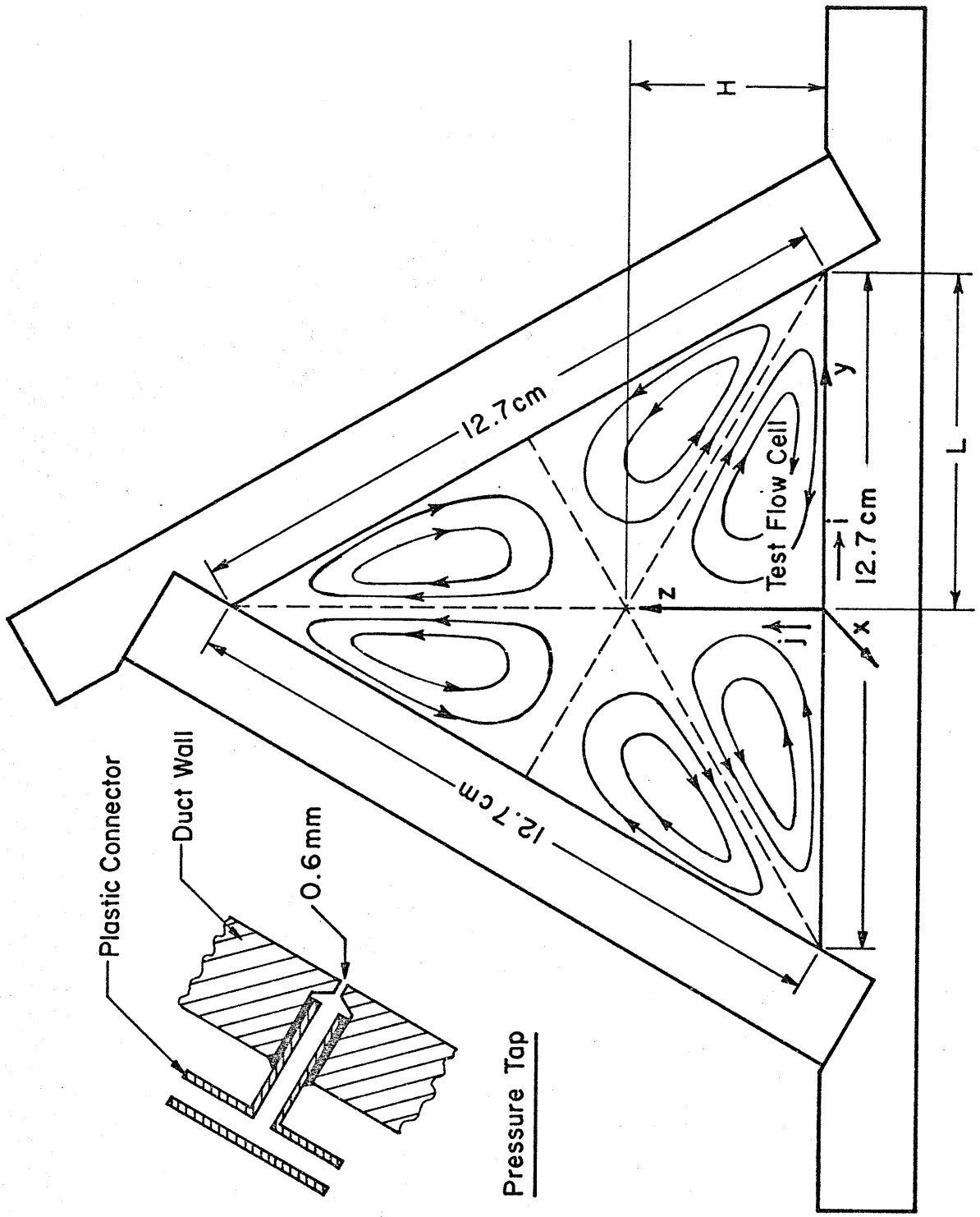

Fig.3.1. . Cross-Section of Equilateral Triangular Test Section.

1. Duct
2. Nozzle
3. Canvas Couplings
4. Damper
5. Fan Section
6. Silencer
7. Diffuser
8. Corner with Turning Vanes
9. Diffuser
10. Corner with Turning Vanes
11. Transition
12. Screen Section
13. Contraction Cone
14. Transition
15. Transition
16. Transition
17. Wooden Entrance Section
18. Plexiglass Test Section
19. Test Station

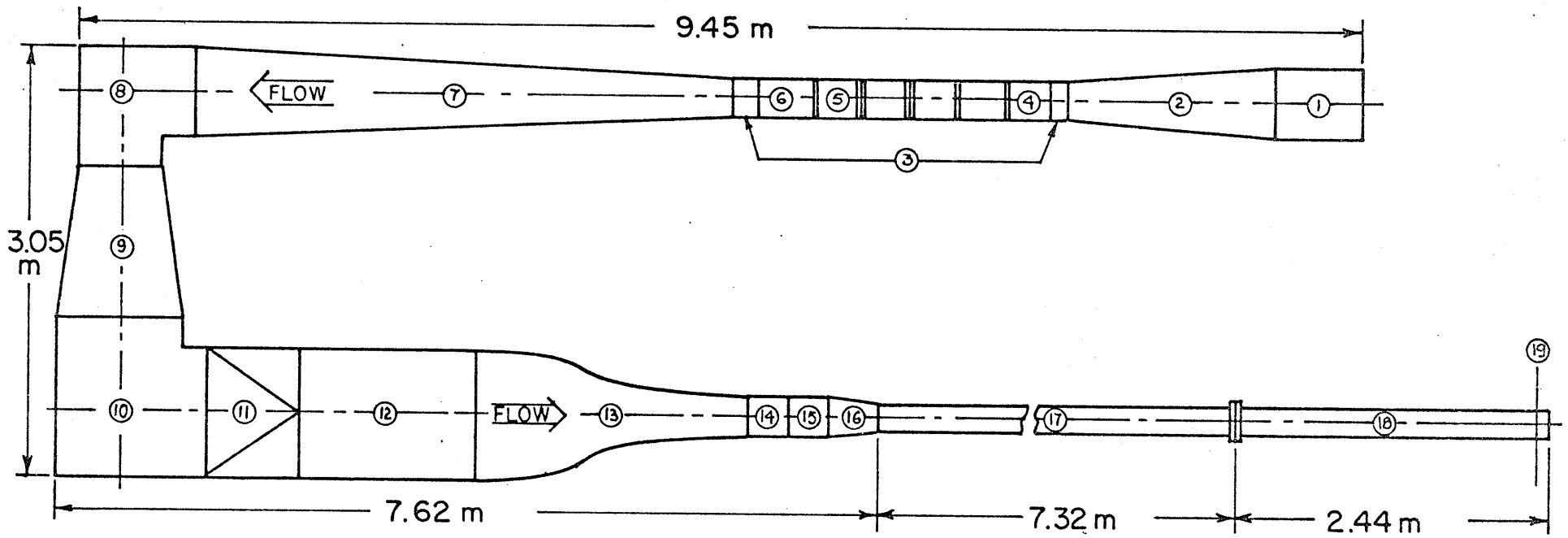

Fig. 4.1. Plan View of Wind Tunnel for Triangular Duct Turbulence Studies.

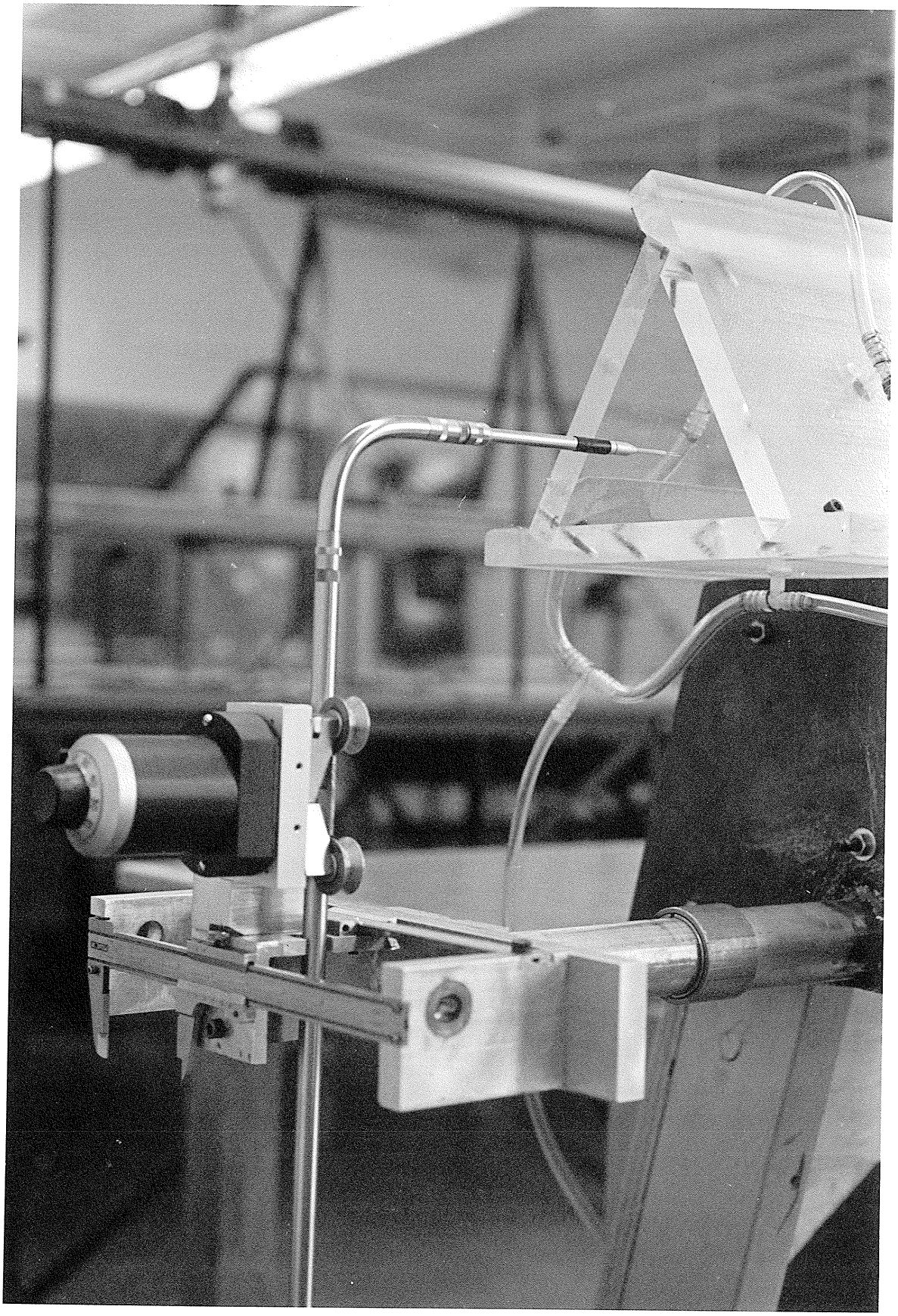

Figure 4.2. Traversing Mechanism

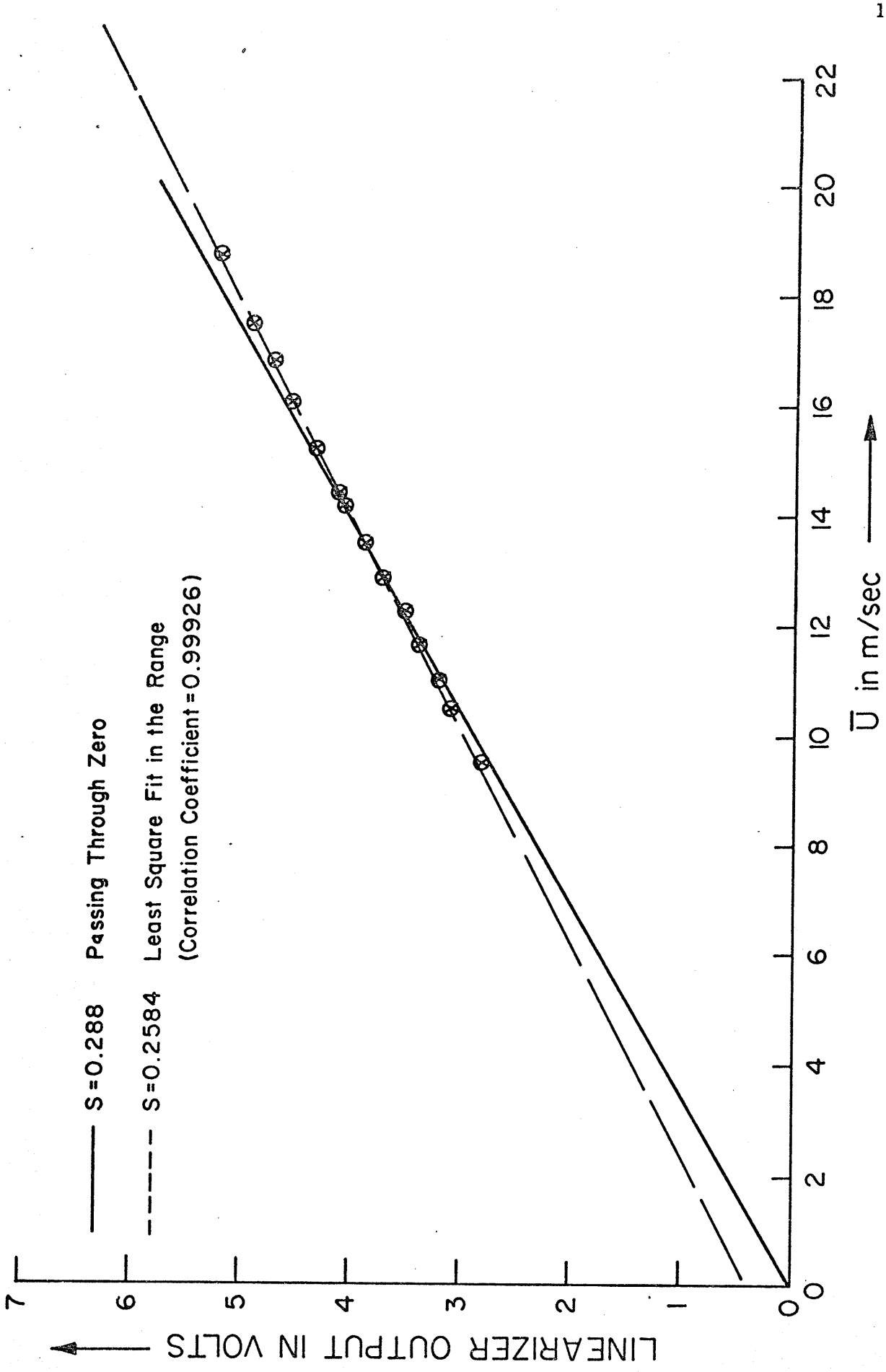

Fig. 4.3 Calibration of Slanting Single Wire Probe

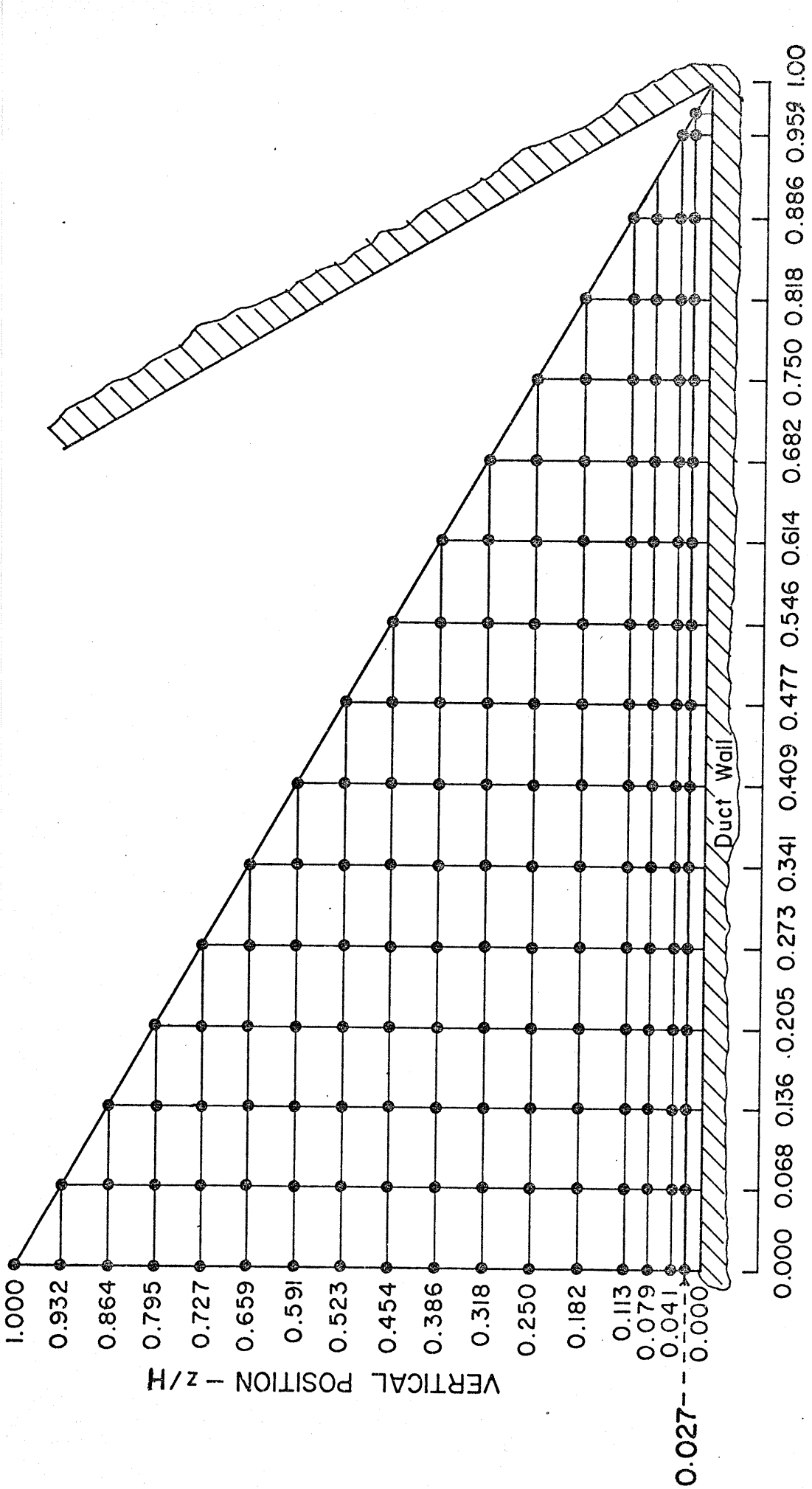

Fig. 5.1. Primary Flow Cell Sub-Division for Measurements.

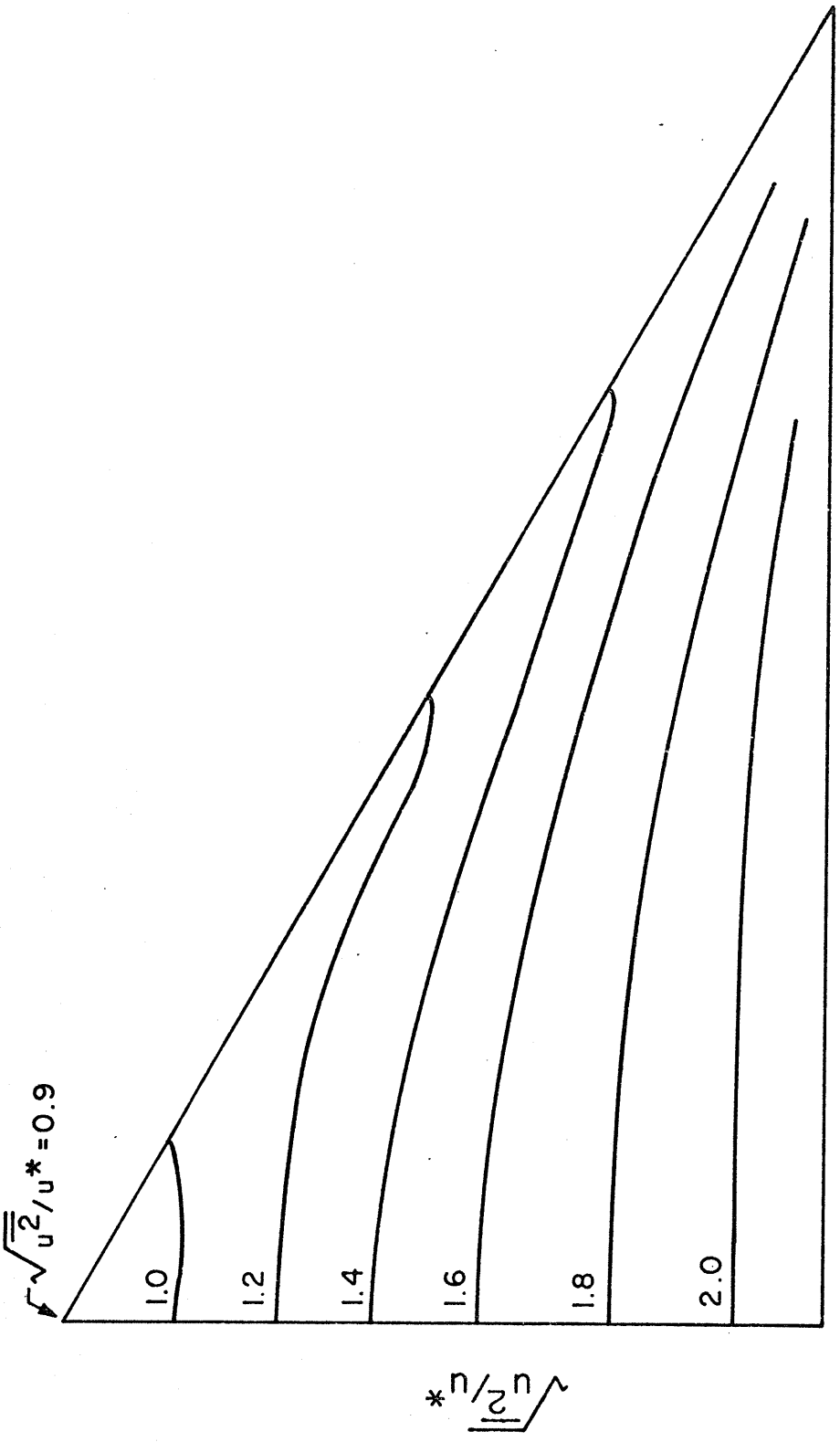

Fig.5.2.Contour Plot of $\sqrt{u^2}/u^*$ Distribution. Re = 53,000.

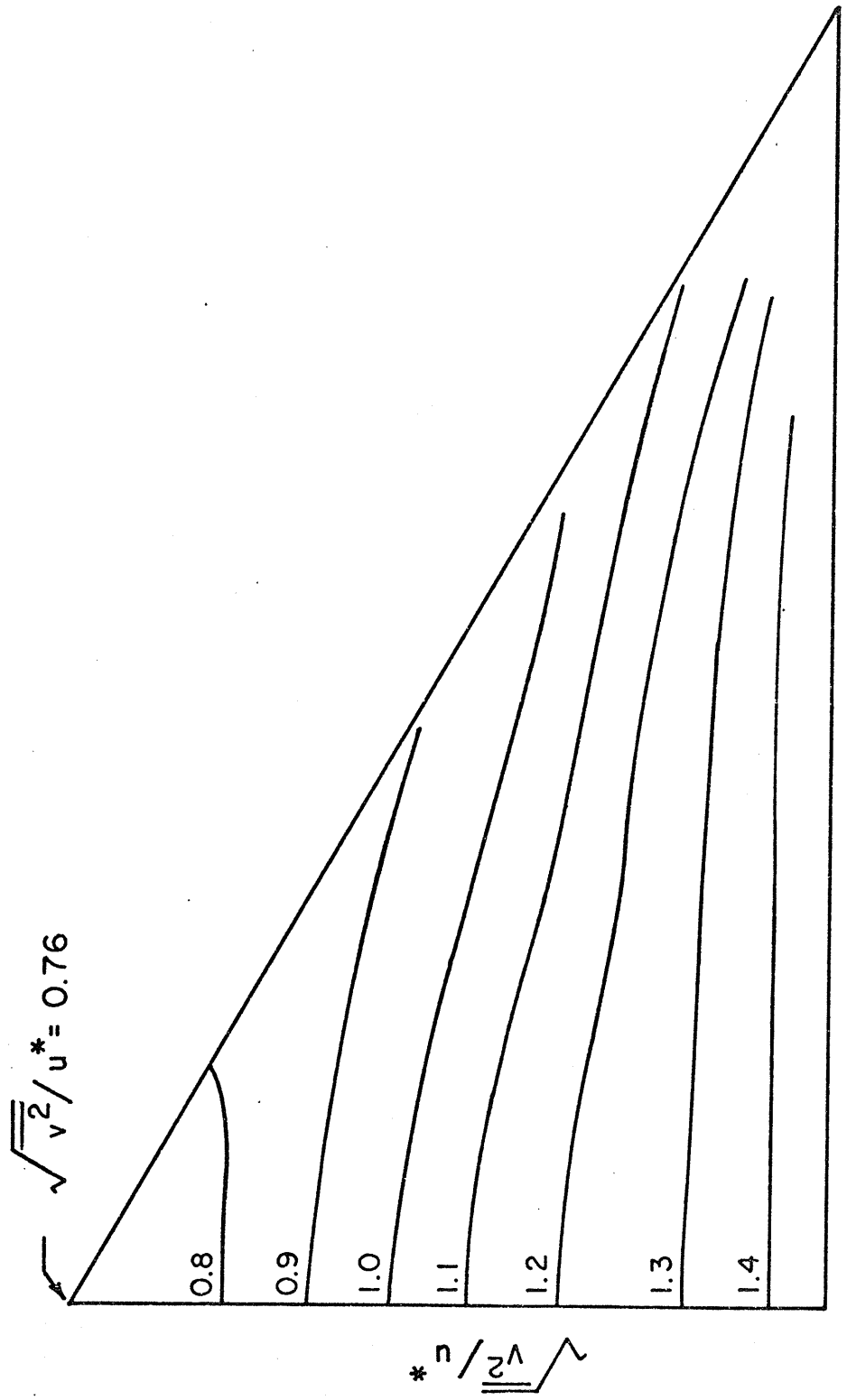

Fig.5.3. Contour Plot of $\sqrt{\overline{v^2}}/u^*$ Distribution , Re = 53,000.

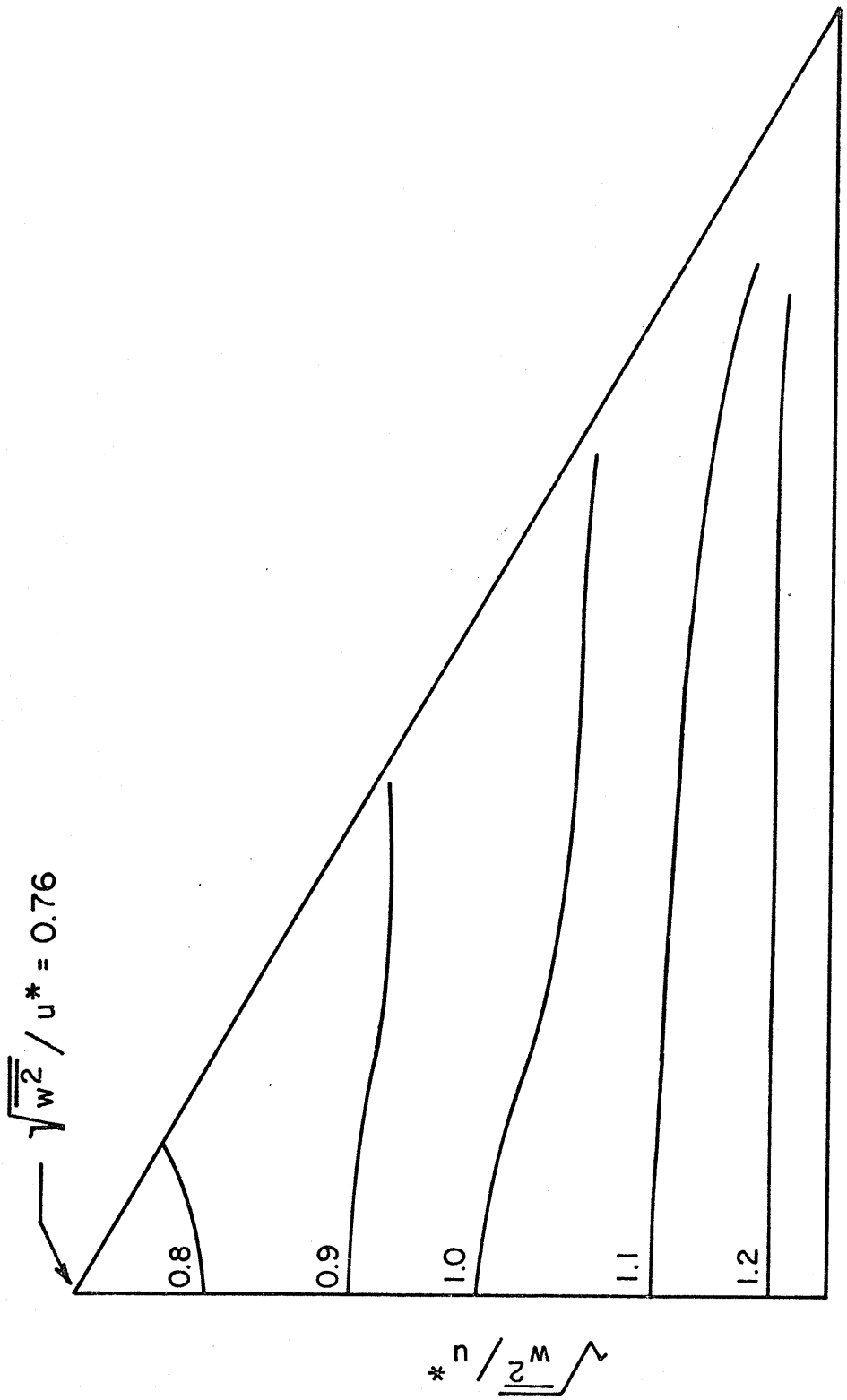

Fig.5.4. Contour Plot of $\sqrt{\overline{w^2}}/u^*$ Distribution. Re = 53,000

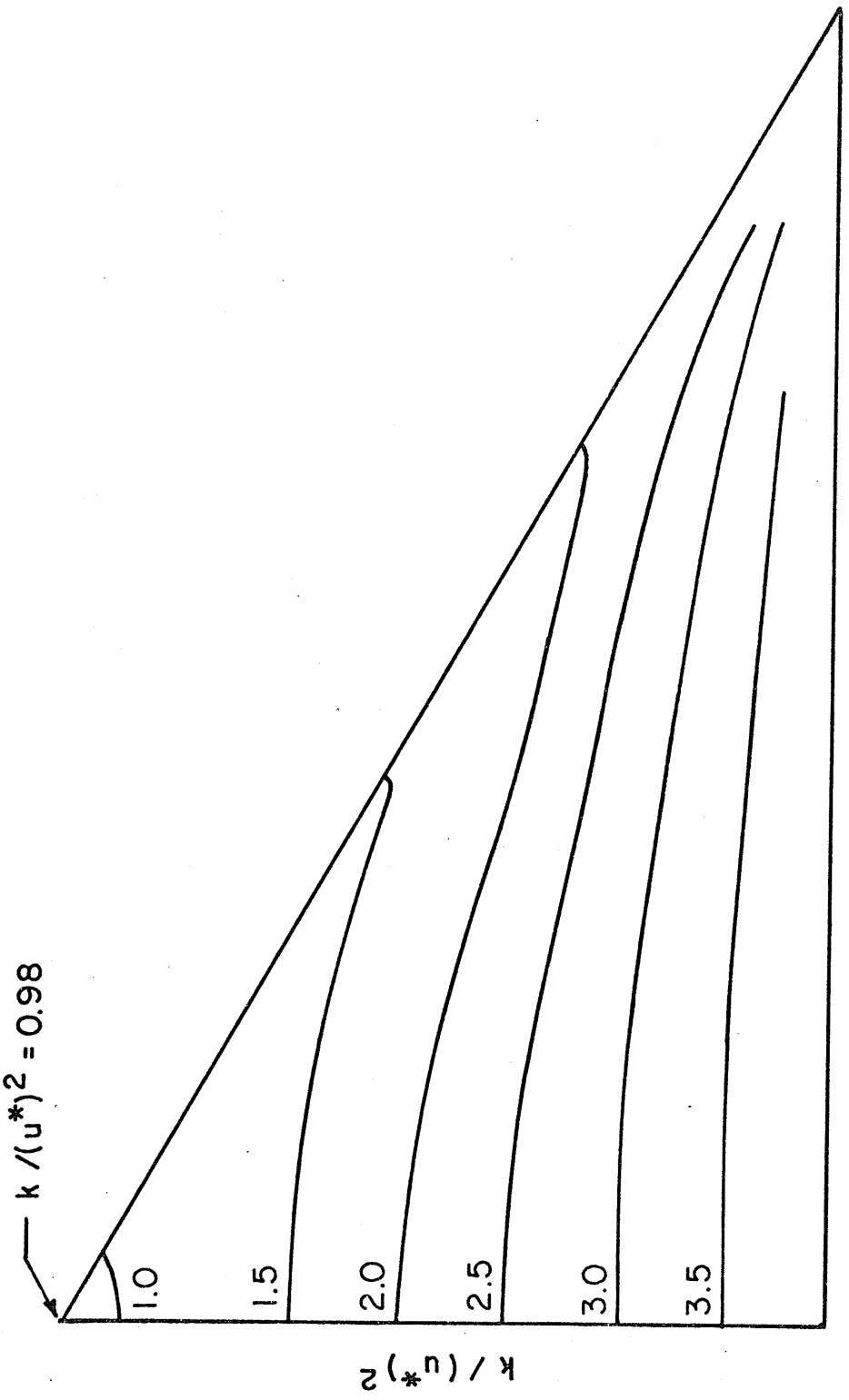

Fig,5.5. Contour Plot $k/(u^*)^2$ Distribution. Re = 53,000

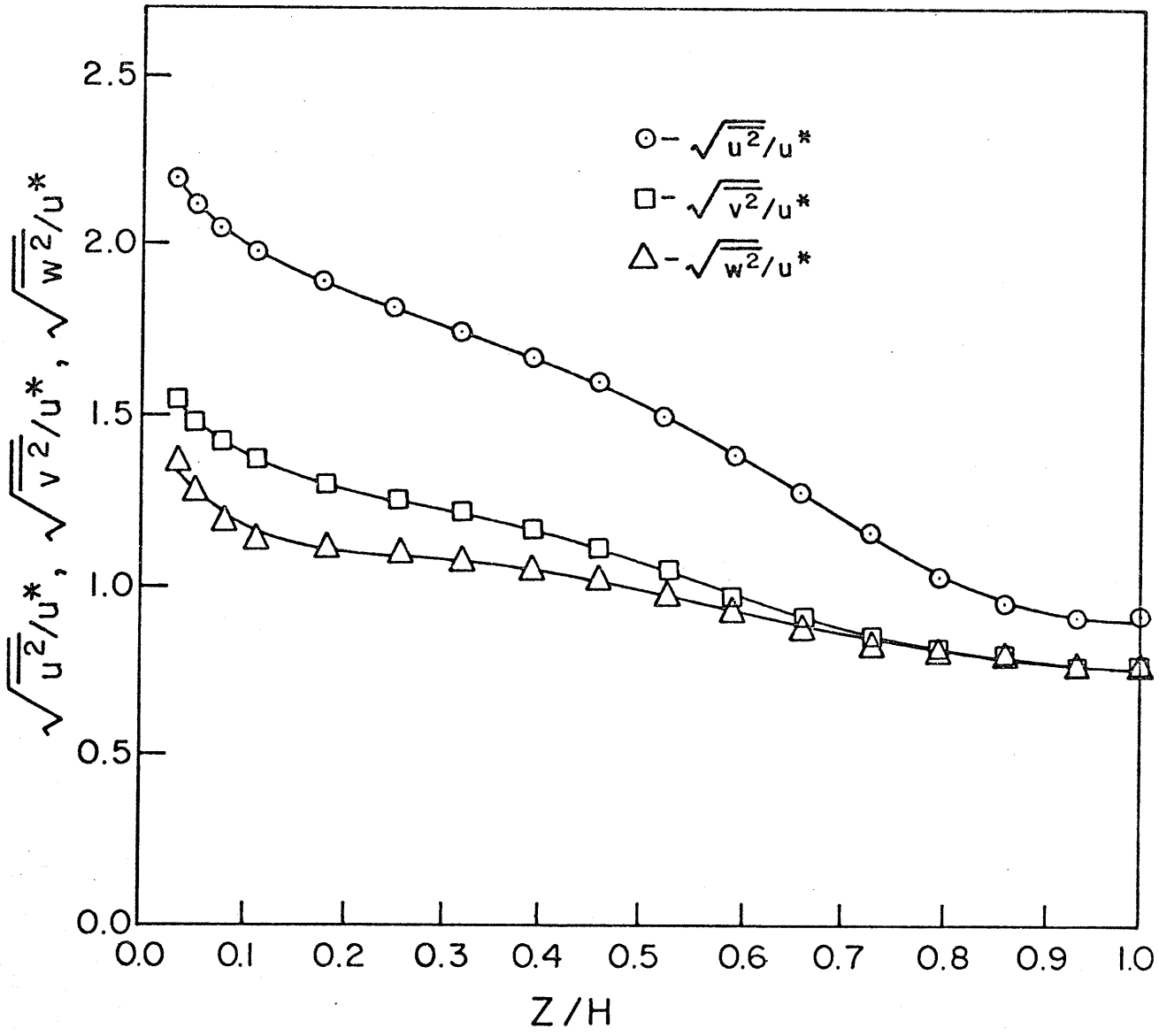

Fig.5.6. .Turbulence Intensities along Midwall Bisector. Re = 53,000.

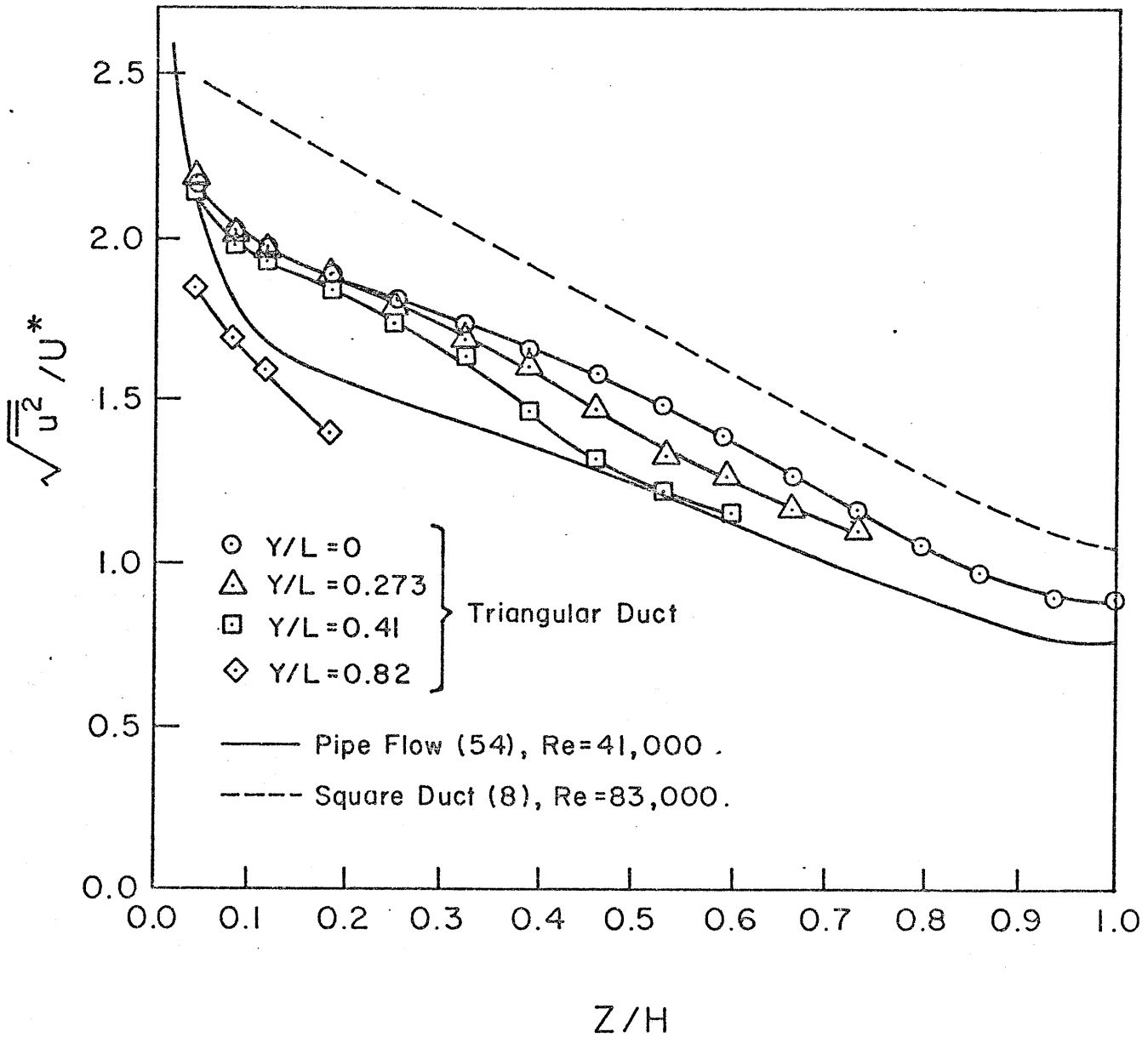

Fig. 5.7. Distribution of $\sqrt{u^2}/U^*$ Normal to Wall , Re = 53,000 .

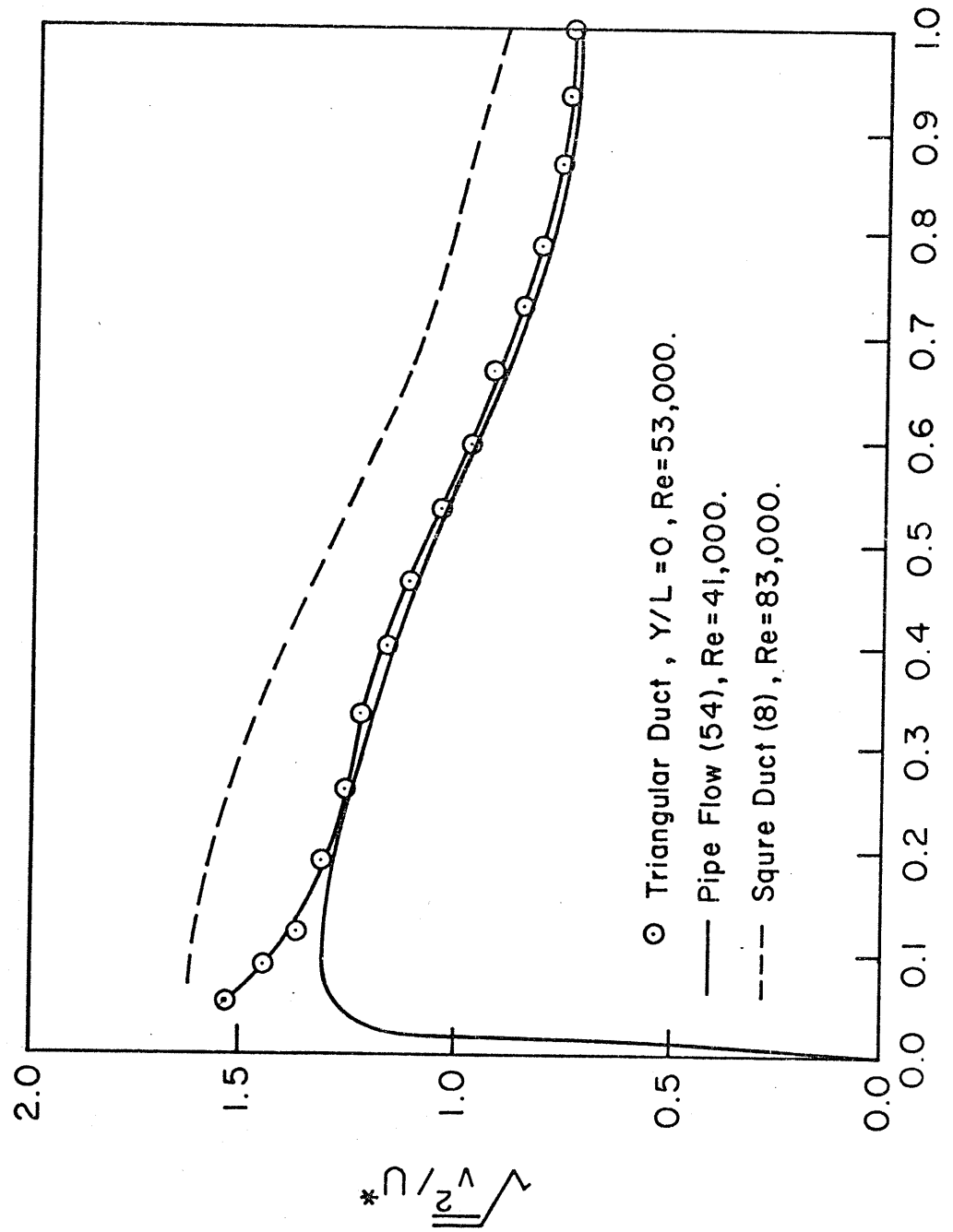

Fig. 5.8. Distribution of $\sqrt{v^2}/U^*$ Normal to Wall , Re=53,000 .

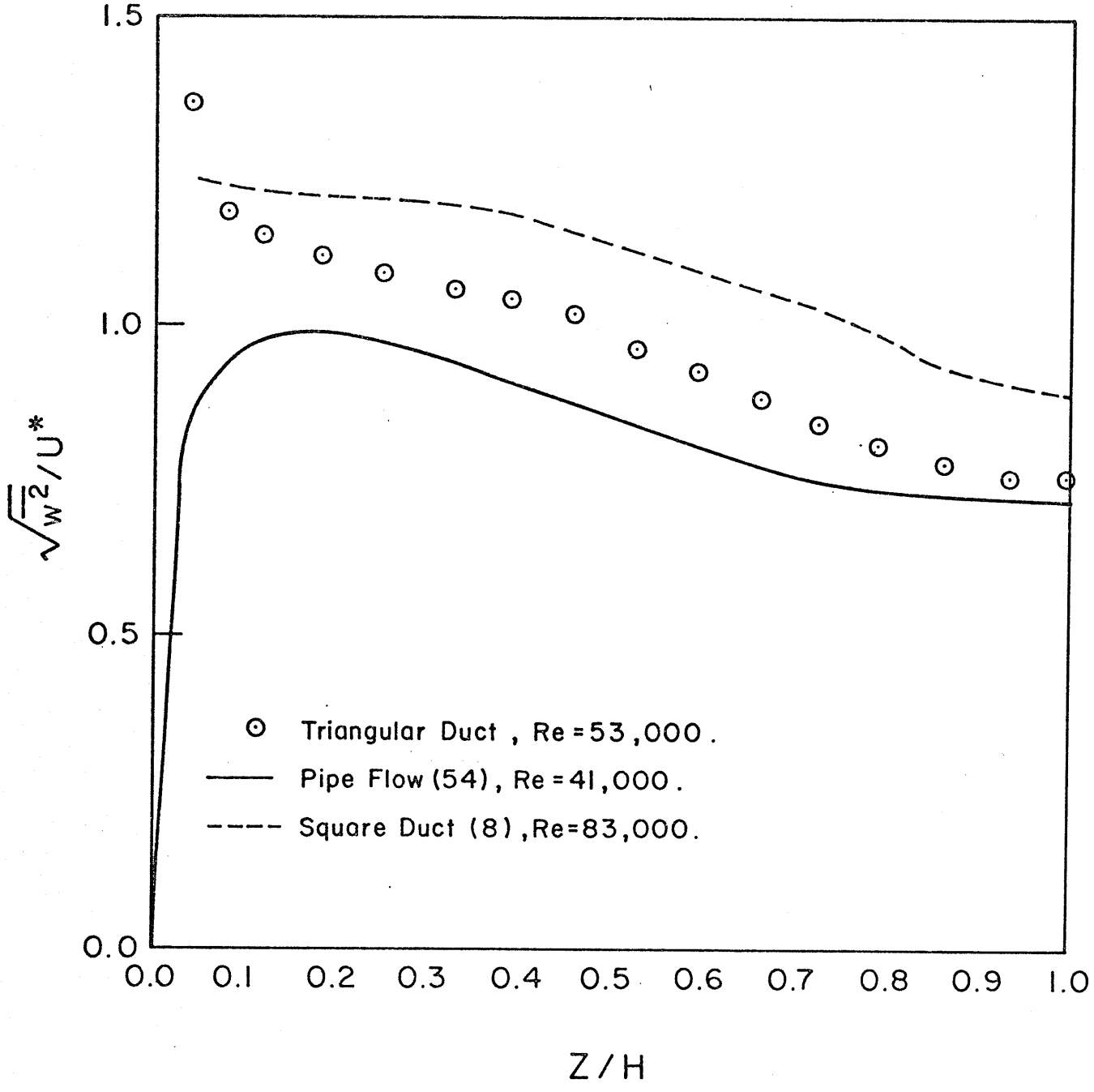

Fig. 5.9. Distribution of $\sqrt{\overline{w^2}}/U^*$ Normal to Wall, Re = 53,000.

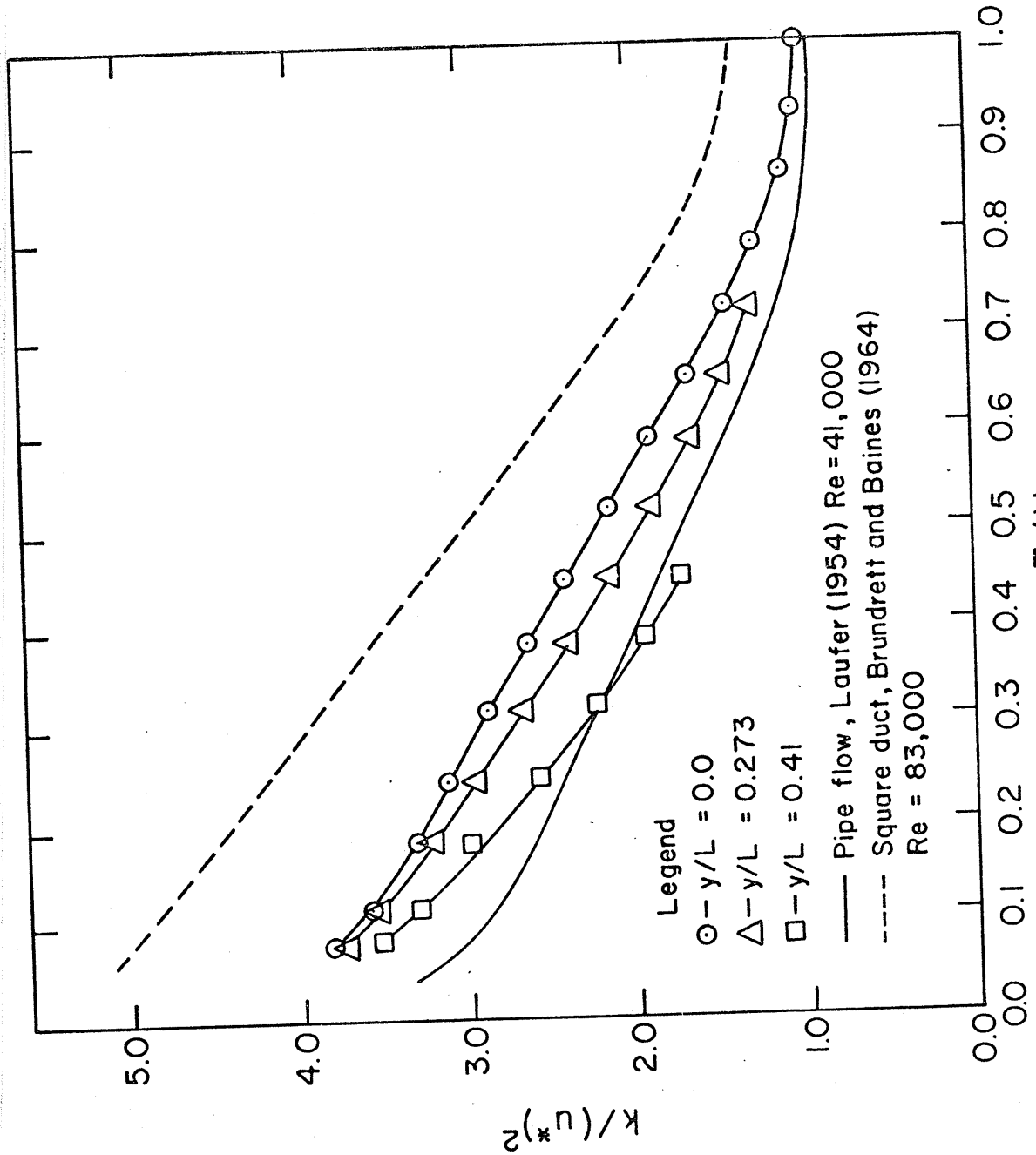

Fig. 5.10. Distribution of $k/(u^*)^2$ Normal to Wall. Re = 53,000.

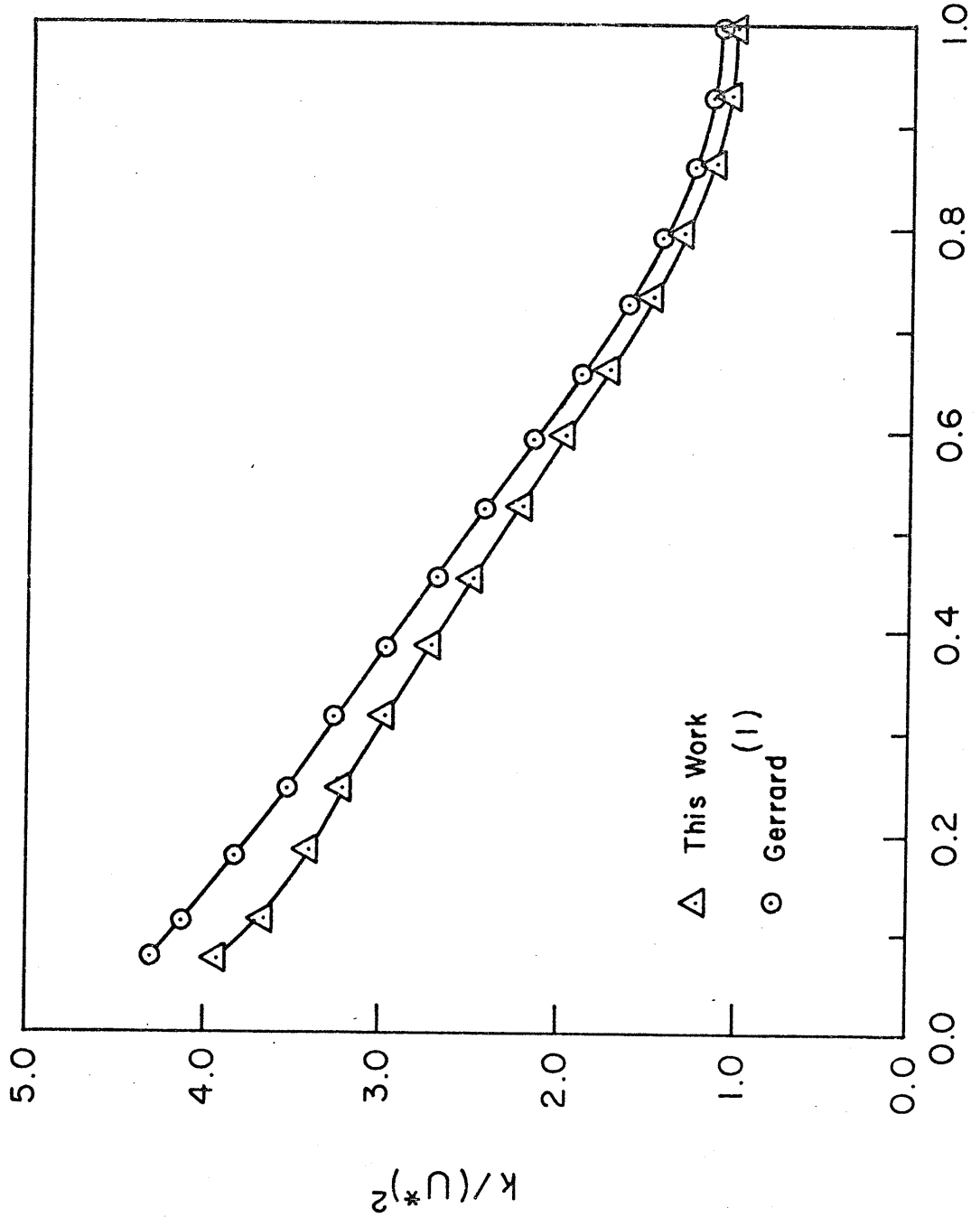

Fig.5.11. Comparison of Measured $k/(U^*)^2$ Normal to Wall with Previous Work, y/L=0.0, Re=53,000.

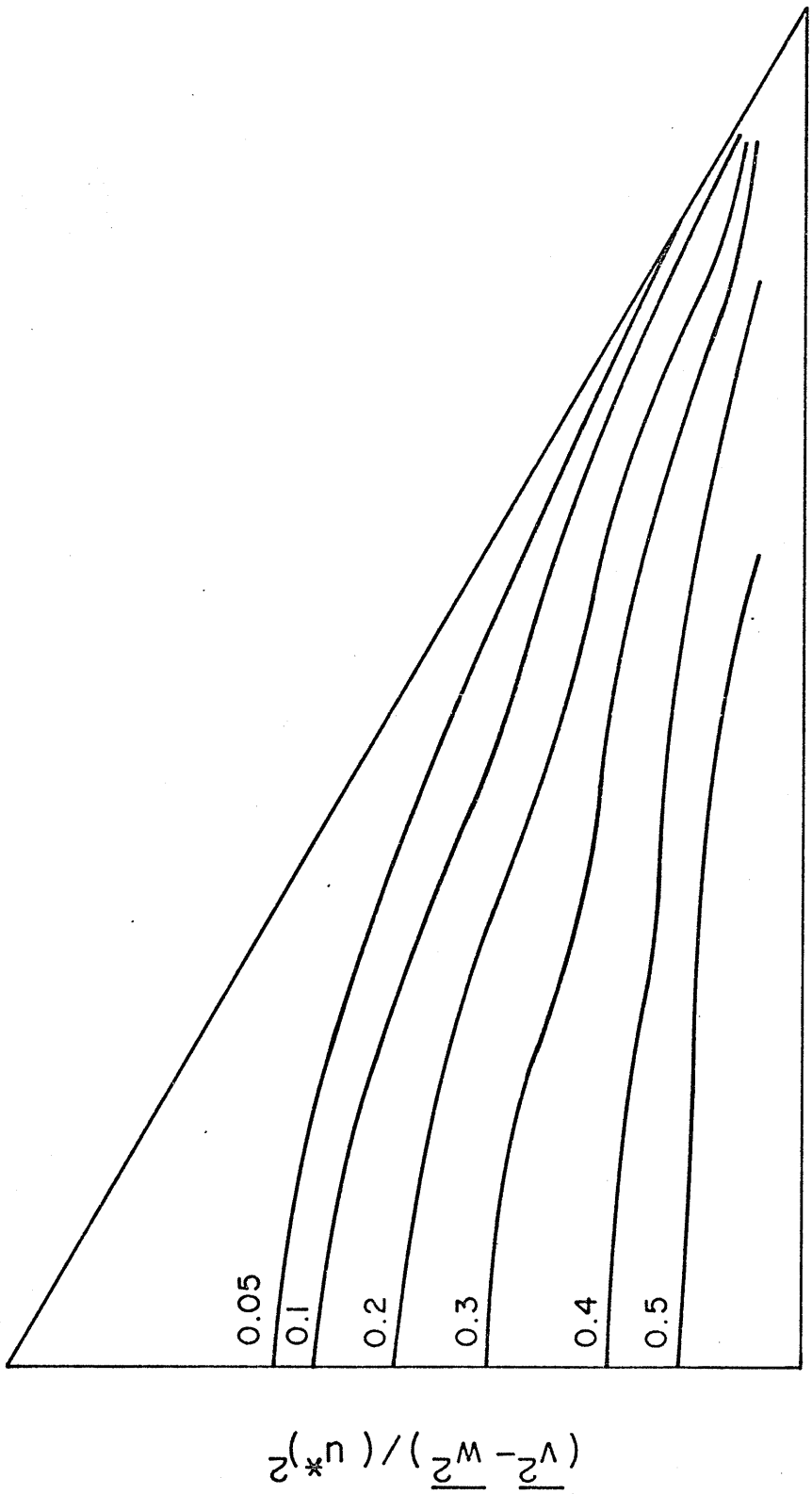

Fig.5.12 .Contour Plot of $(\overline{v^2} - \overline{w^2})/(u^*)^2$ Distribution . Re = 53,000.

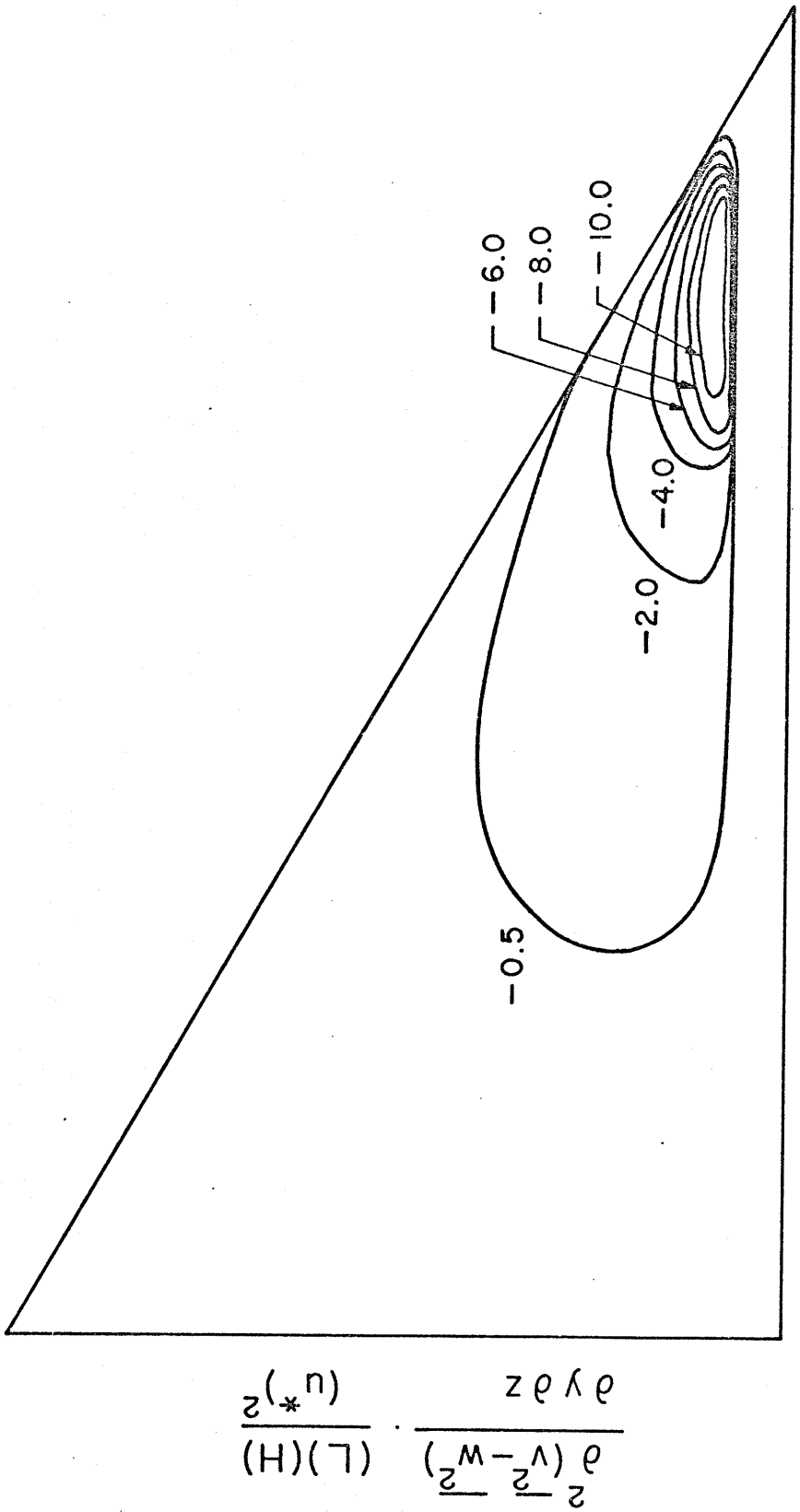

Fig.5.13. . Vorticity Production Contours Based on Normal Stresses. Re=53,000

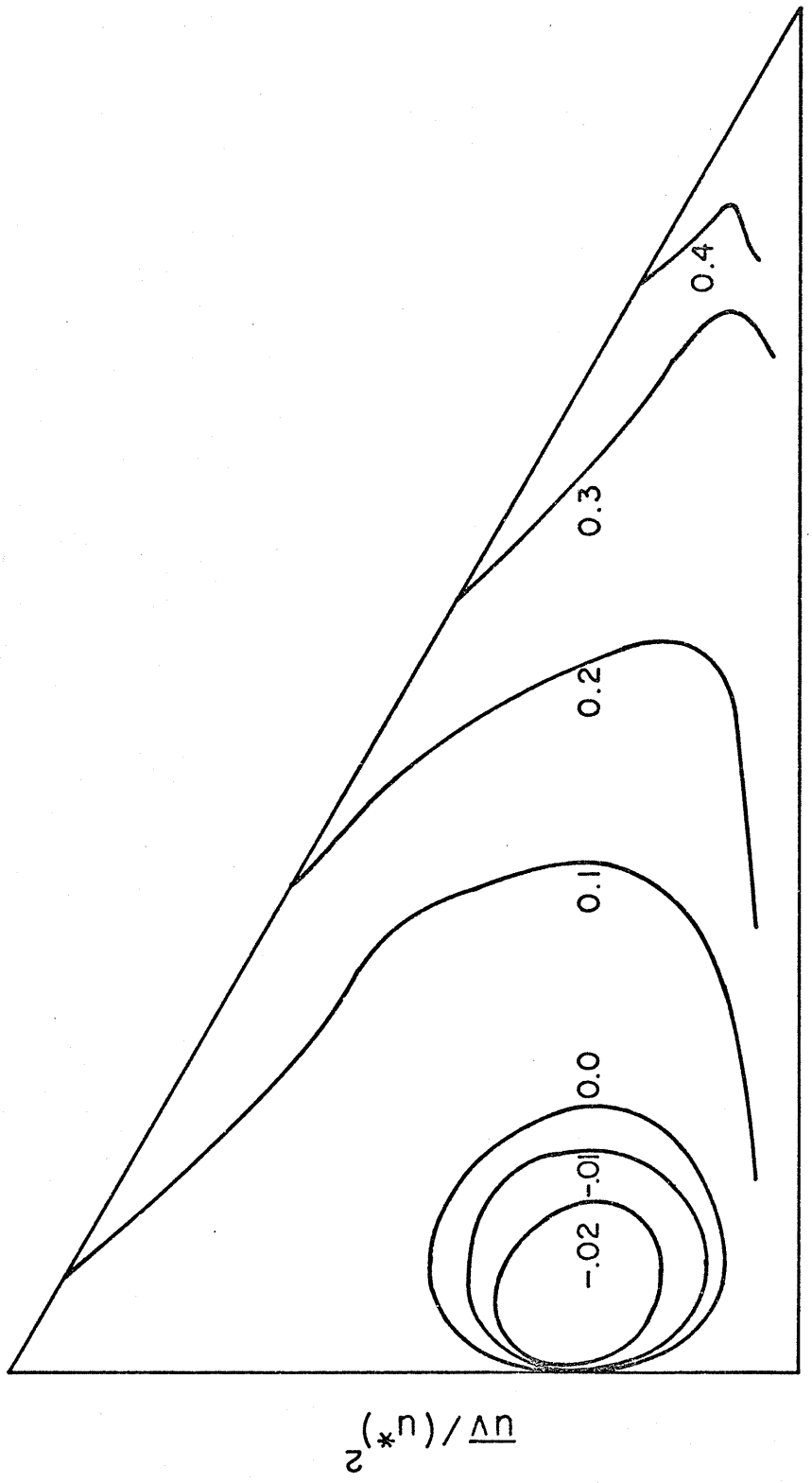

Fig.5.14. Contour Plot of $\overline{uv}/(u^*)^2$ Distribution. Re = 53,000

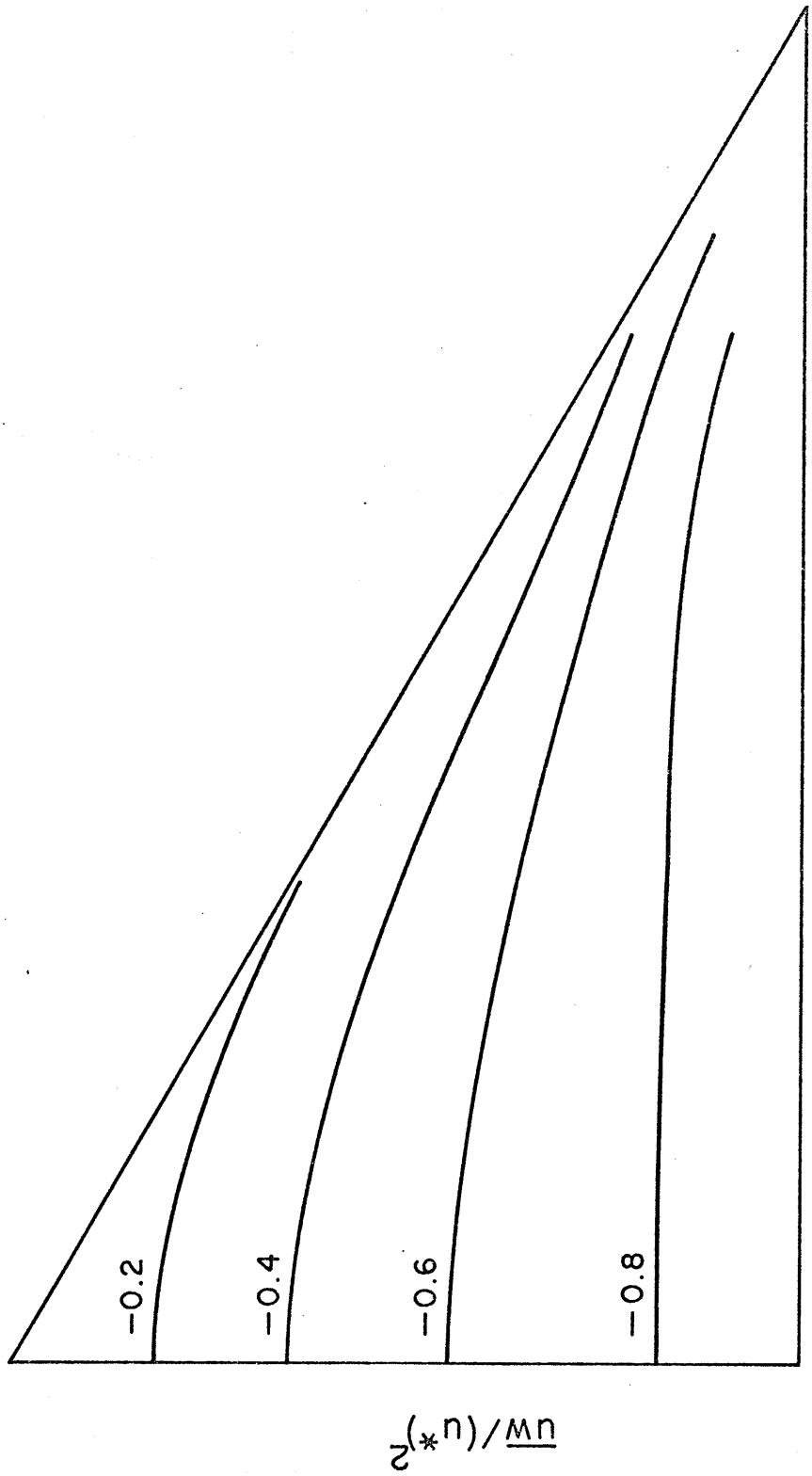

Fig.5.15.. Contour Plot of $\overline{uw}/(u^*)^2$ Distribution . Re = 53,000.

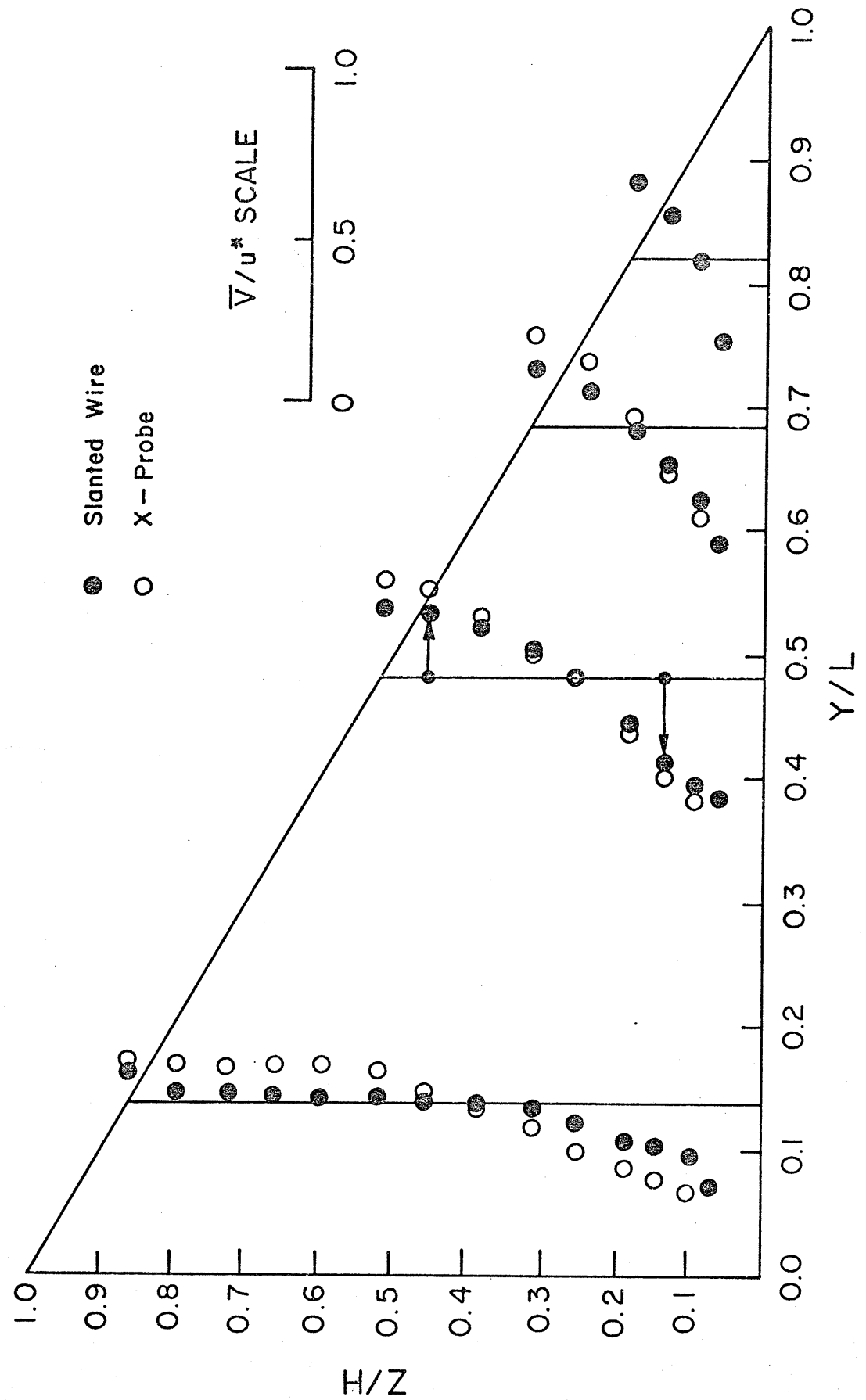

Fig.5.16.. Comparison of Measured $\overline{V}$ by X – Probe and Slanted Wire Probe at Different Vertical Planes, Re. = 53,000.

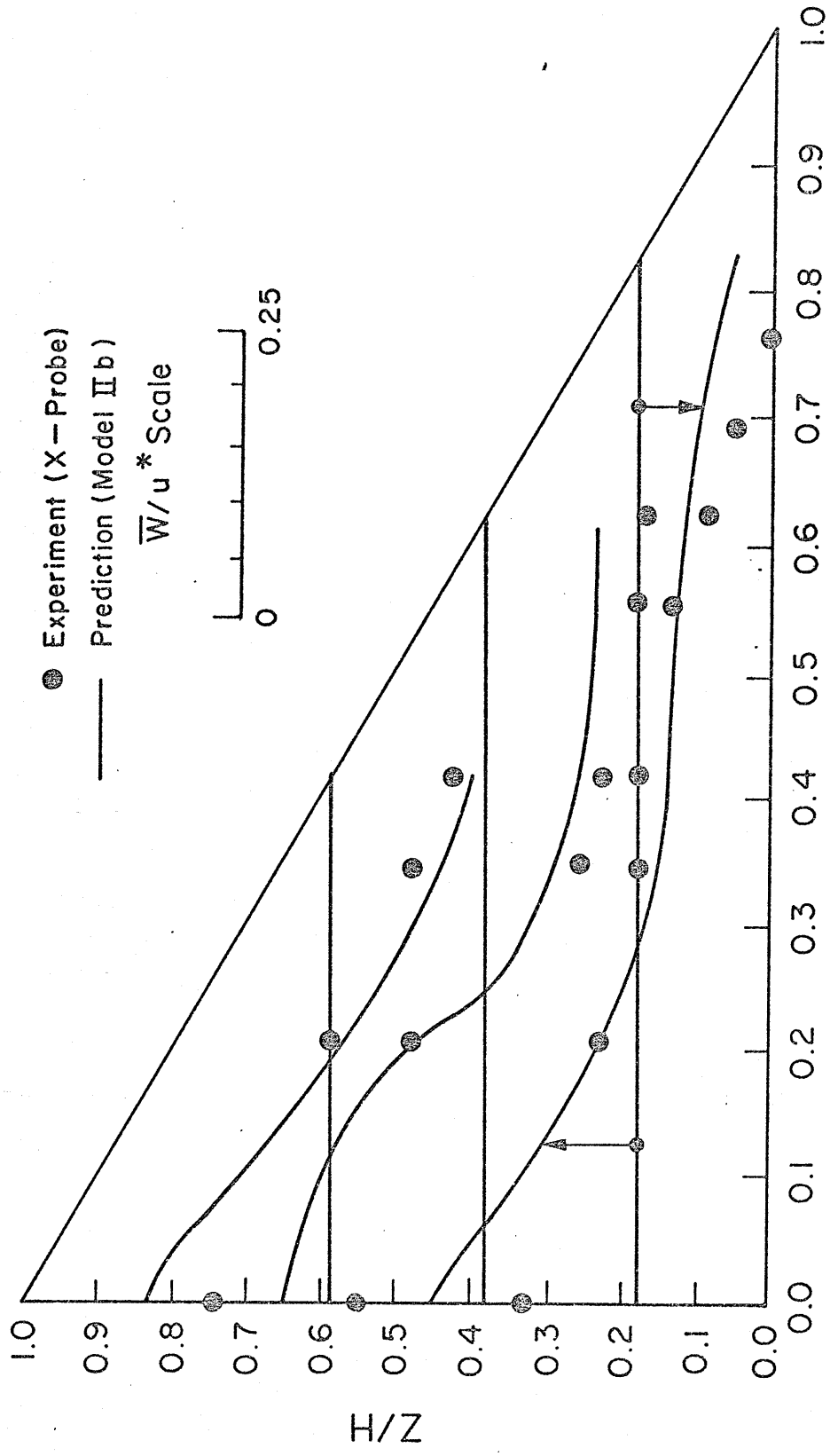

Fig.5.17. Measured and Predicted (Model IIb) $\overline{W}$ Distributions at Different Horizontal Planes. Re=53,000.

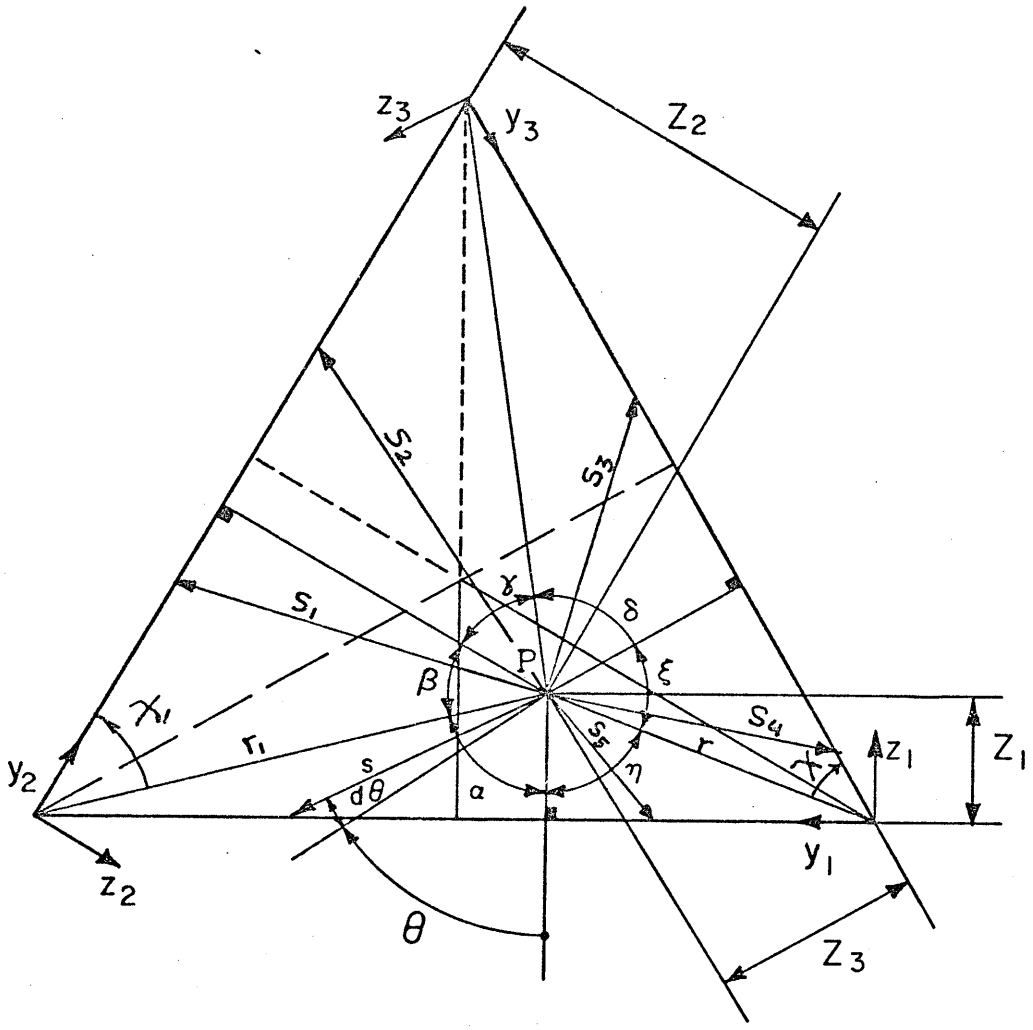

Fig.6.1. Notation for Buleev length scale calculation.

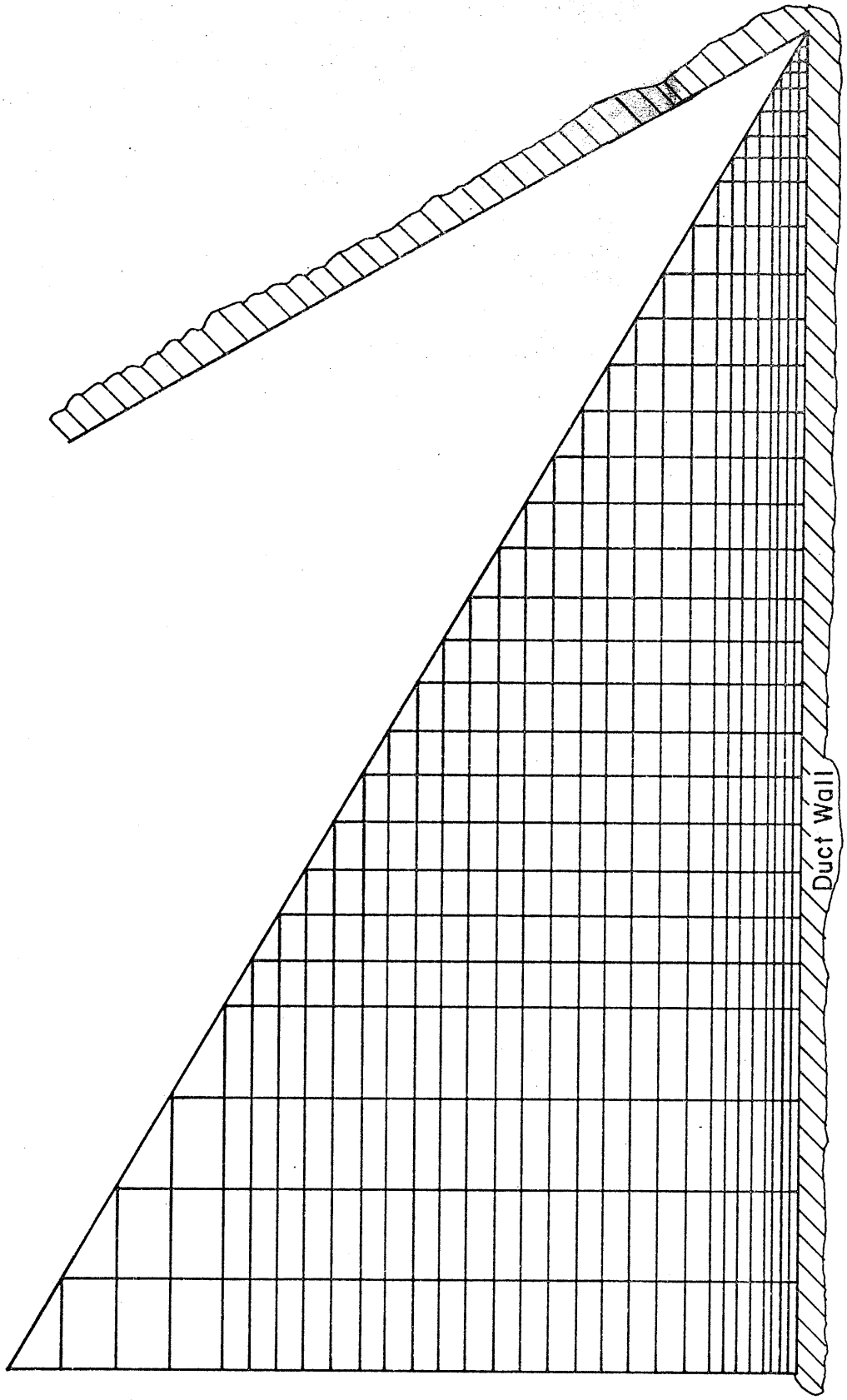

Fig. 7.1 Finite Difference Grid for Numerical Prediction (TABLE 2).

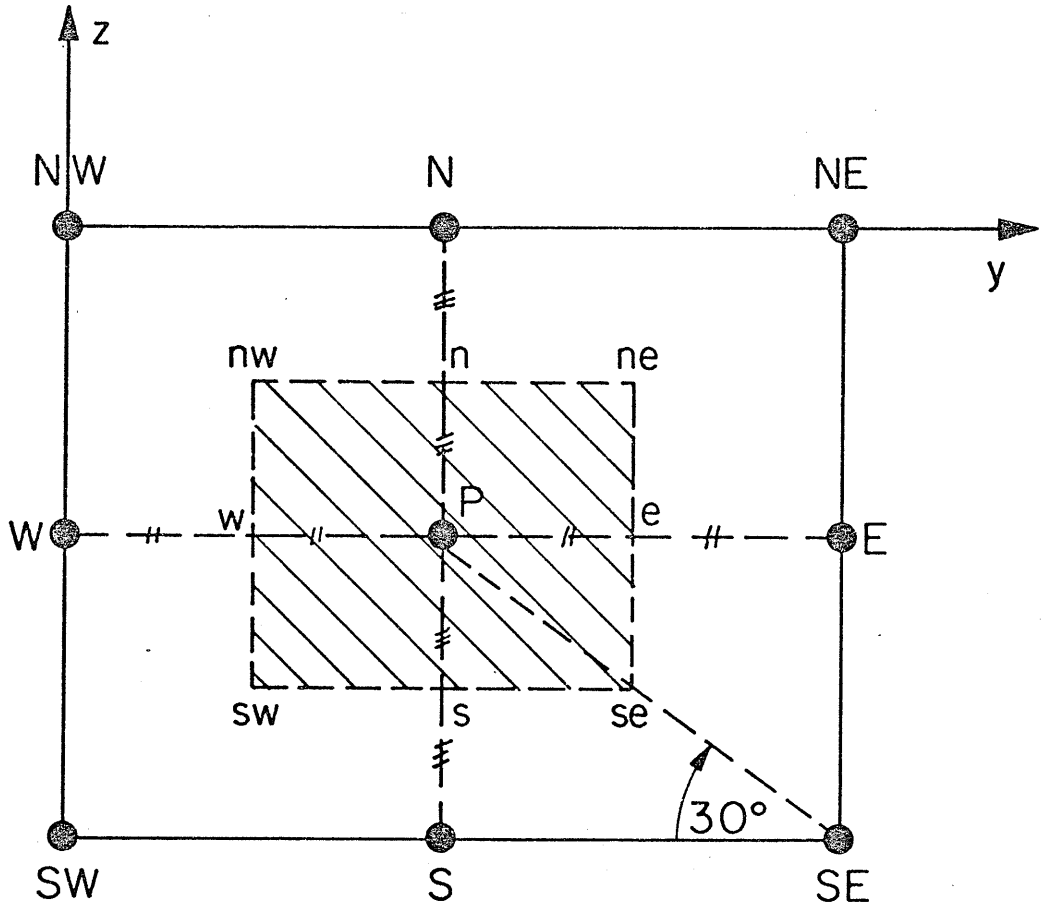

Fig. 7.2. Portion of the Finite Difference Grid and the Area of Integration .

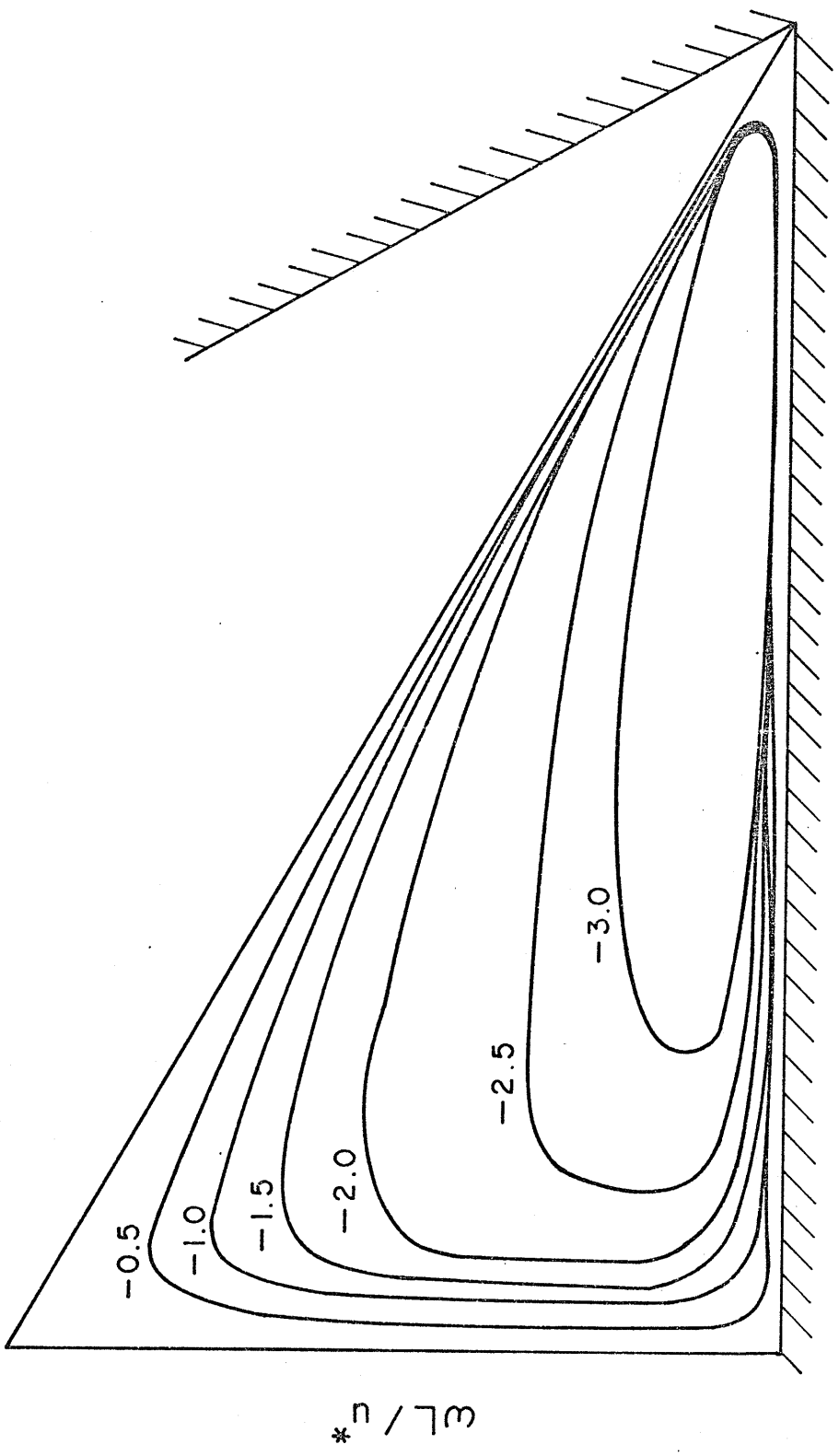

Fig. 8.1. Predicted Dimensionless Vorticity Distribution, Model IIb. Re = 53,000.

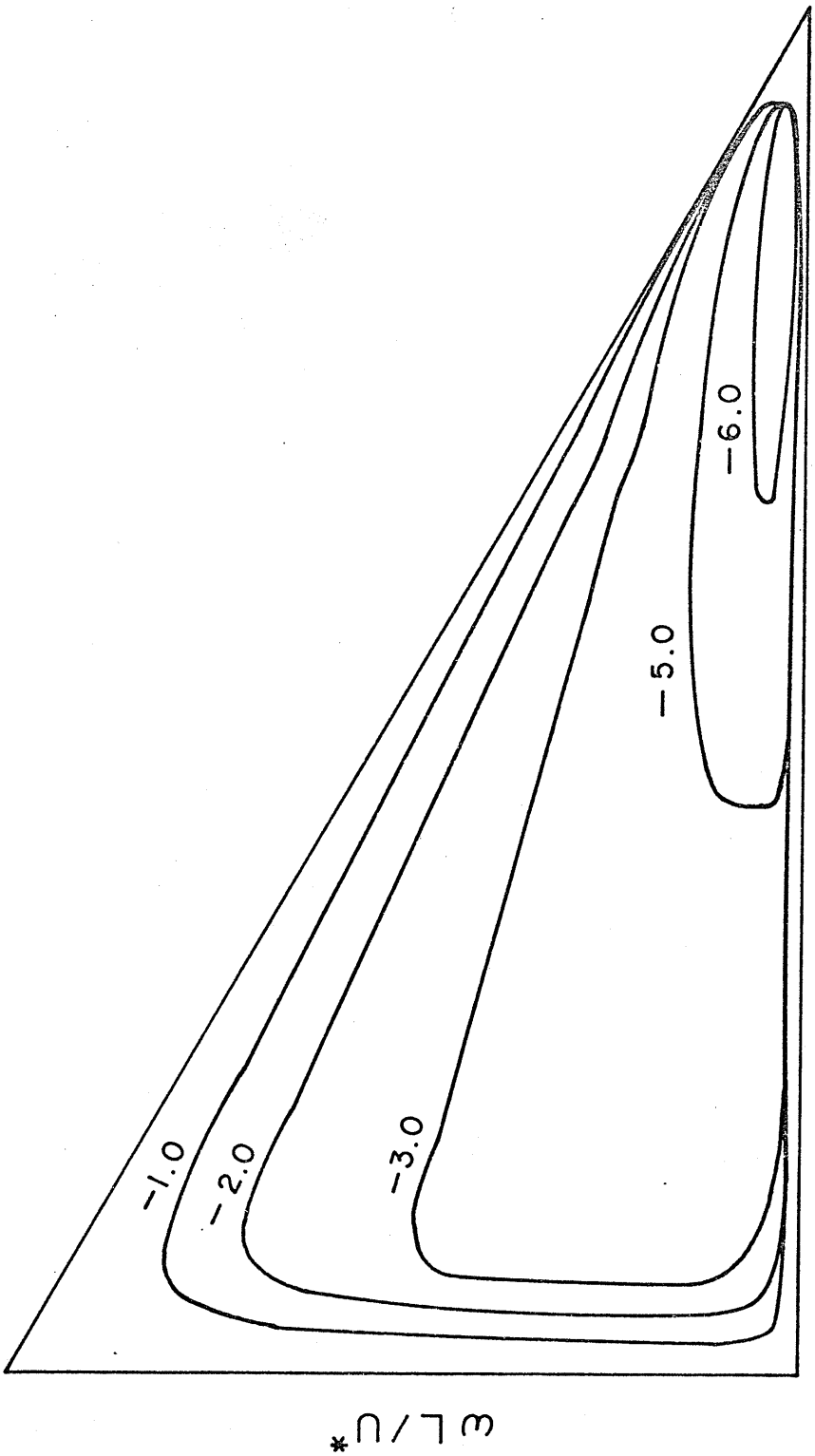

Fig. 8.2. Predicted Dimensionless Vorticity Distribution, Model IIb, Re = 107,300.

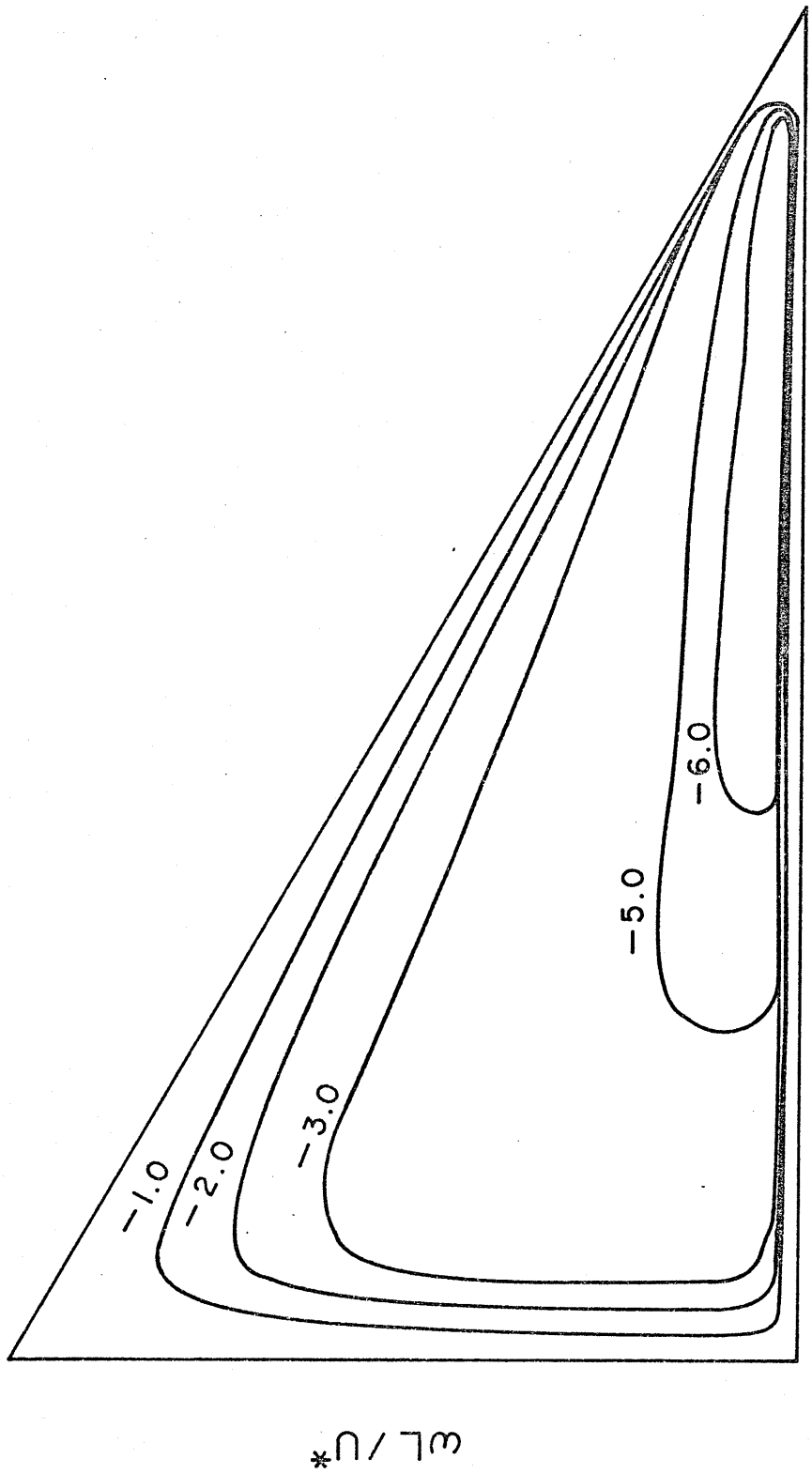

Fig. 8.3. Predicted Dimensionles Vorticity Distribution , Re = 150,000.

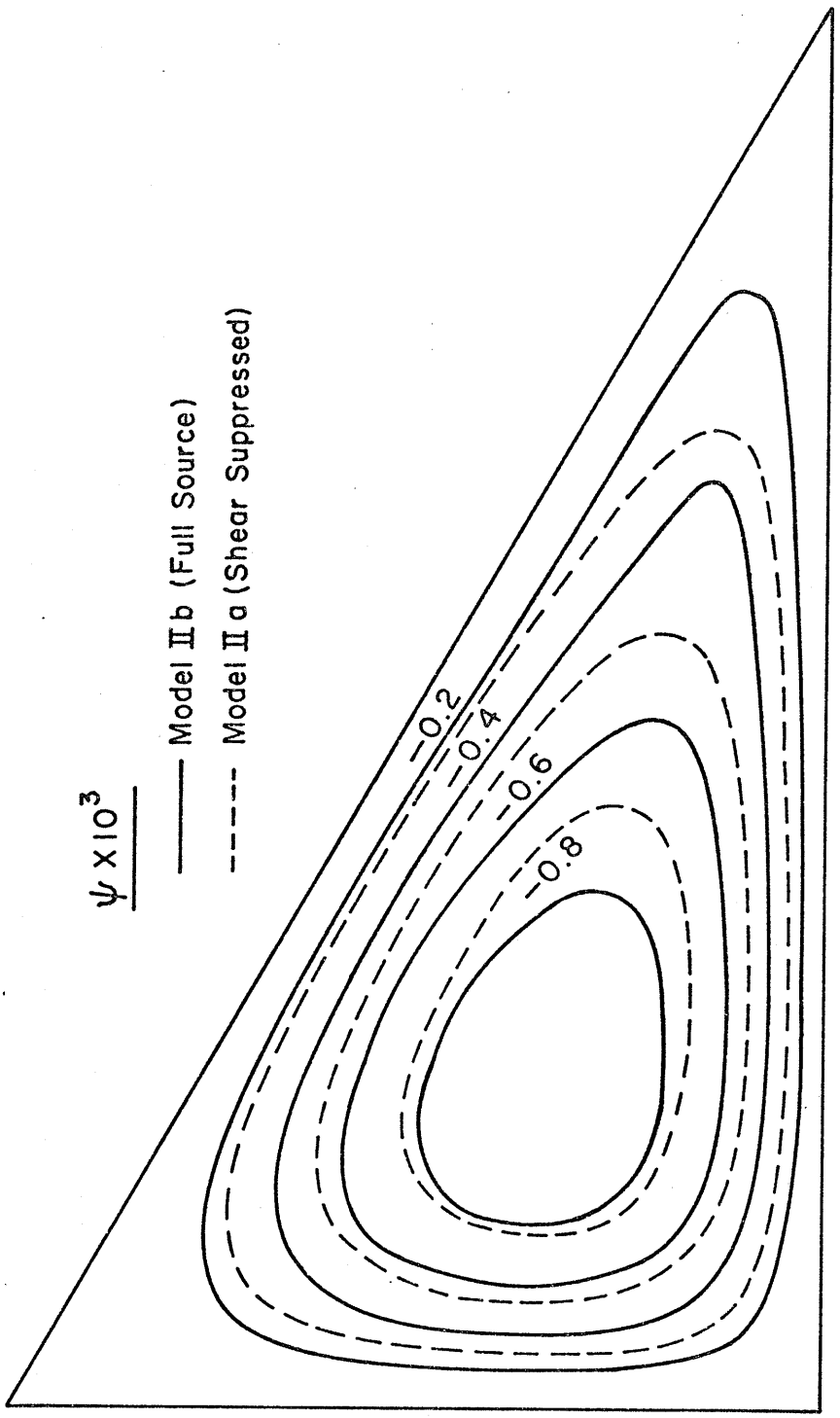

Fig.8.4. Contour Plots of Predicted Stream Function Distribution. Re = 53,000.

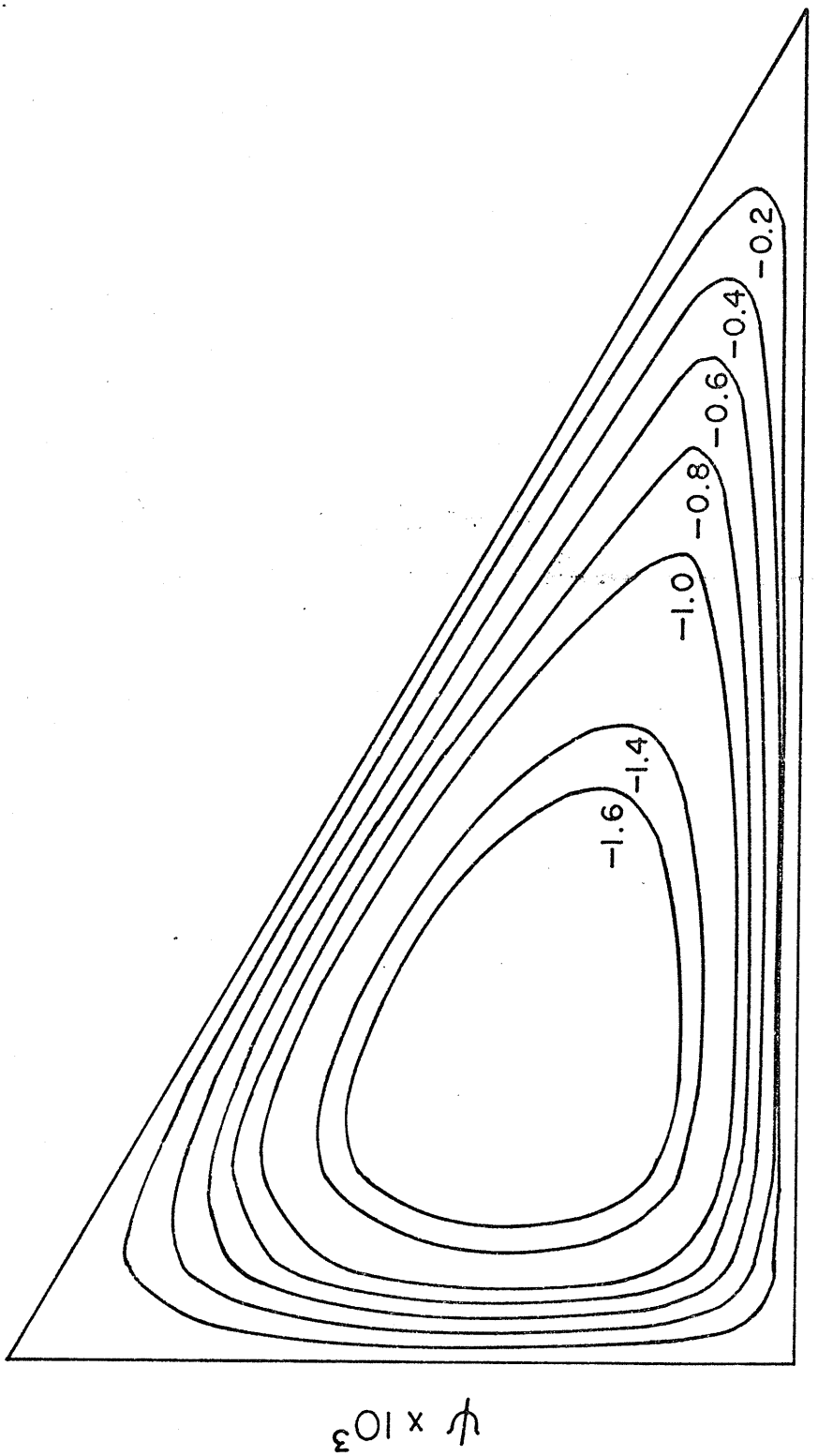

Fig. 8.5. Contour Plots of Predicted Stream Function Distribution, Model IIb, Re=107,300.

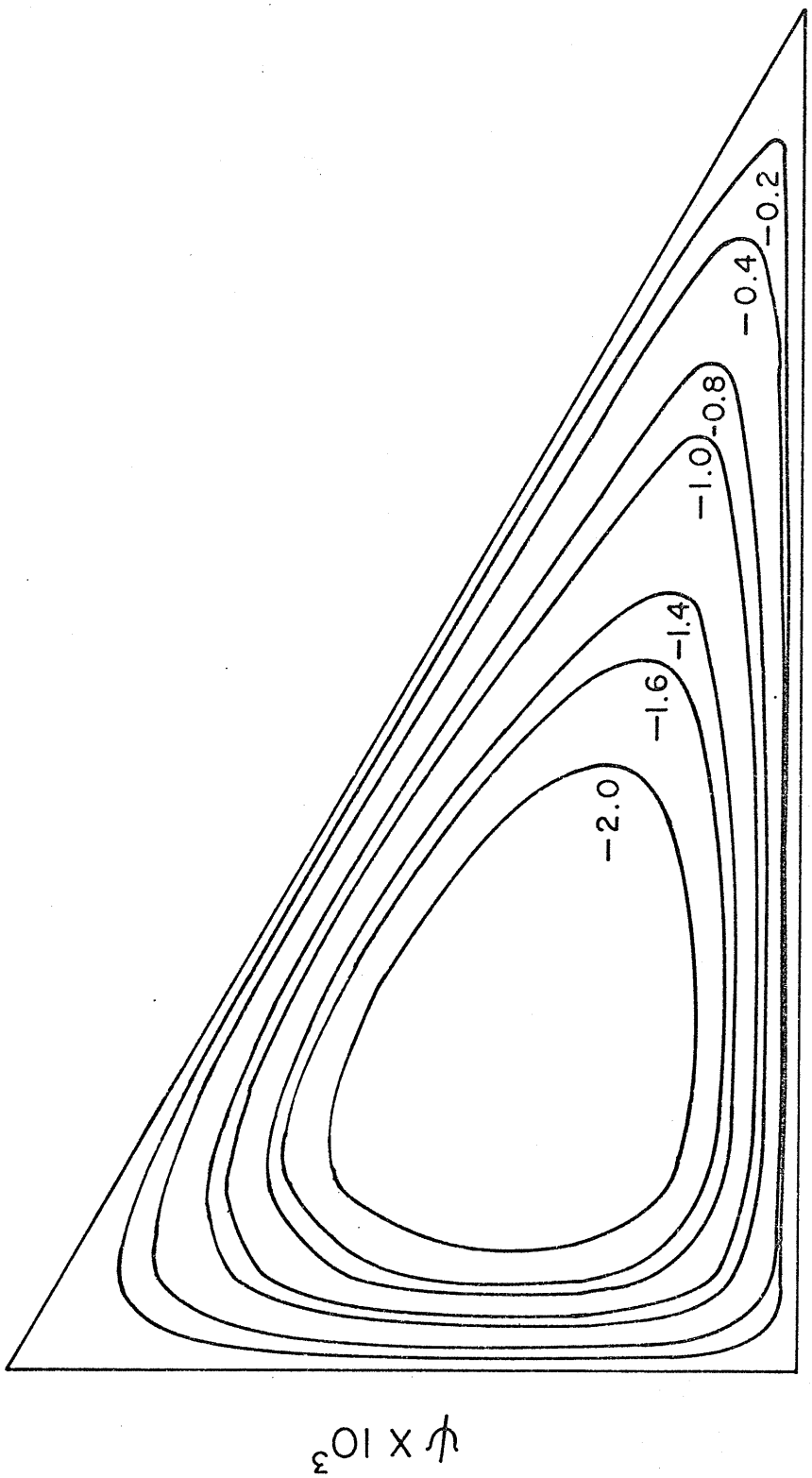

Fig.8.6. Contour Plots of Predicted Stream Function Distribution, Model II b, Re = 150,000.

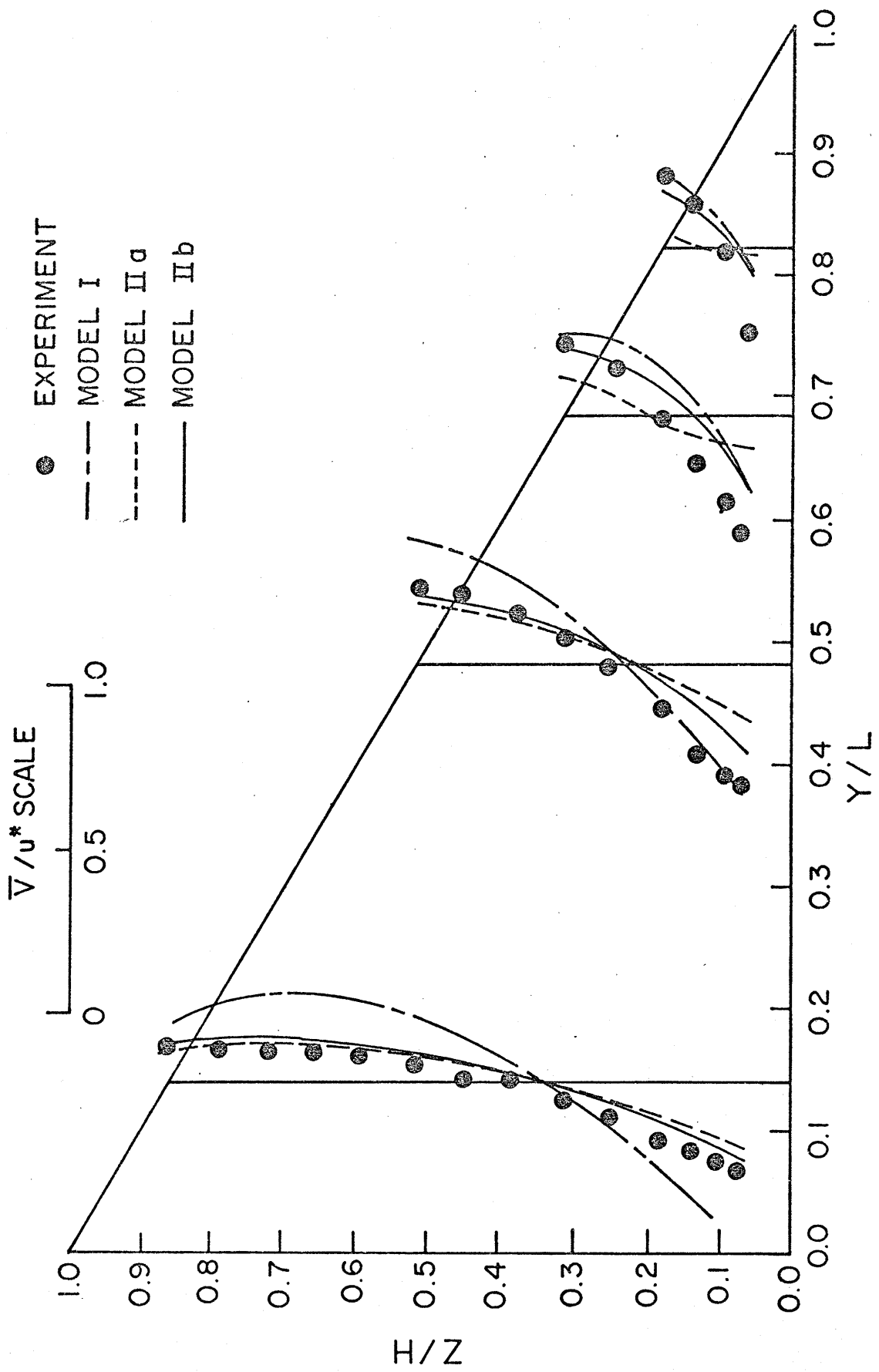

Fig. 8.7. Comparison of Predicted and Measured $\overline{V}$ Results. Re. = 53,000.

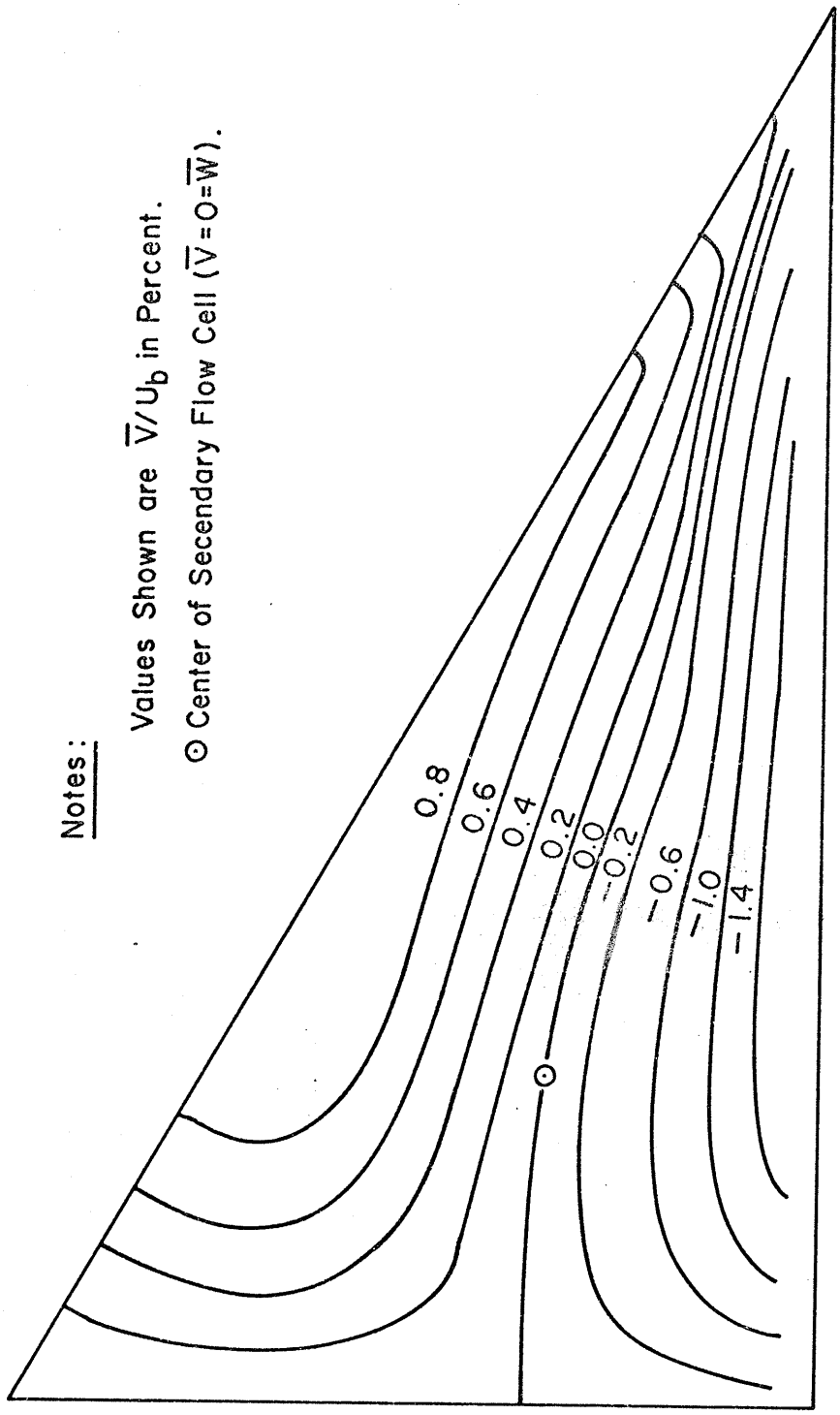

Fig.8.8. Contour Plots of $\overline{V}$ Predicted by Model II b . Re=53,000

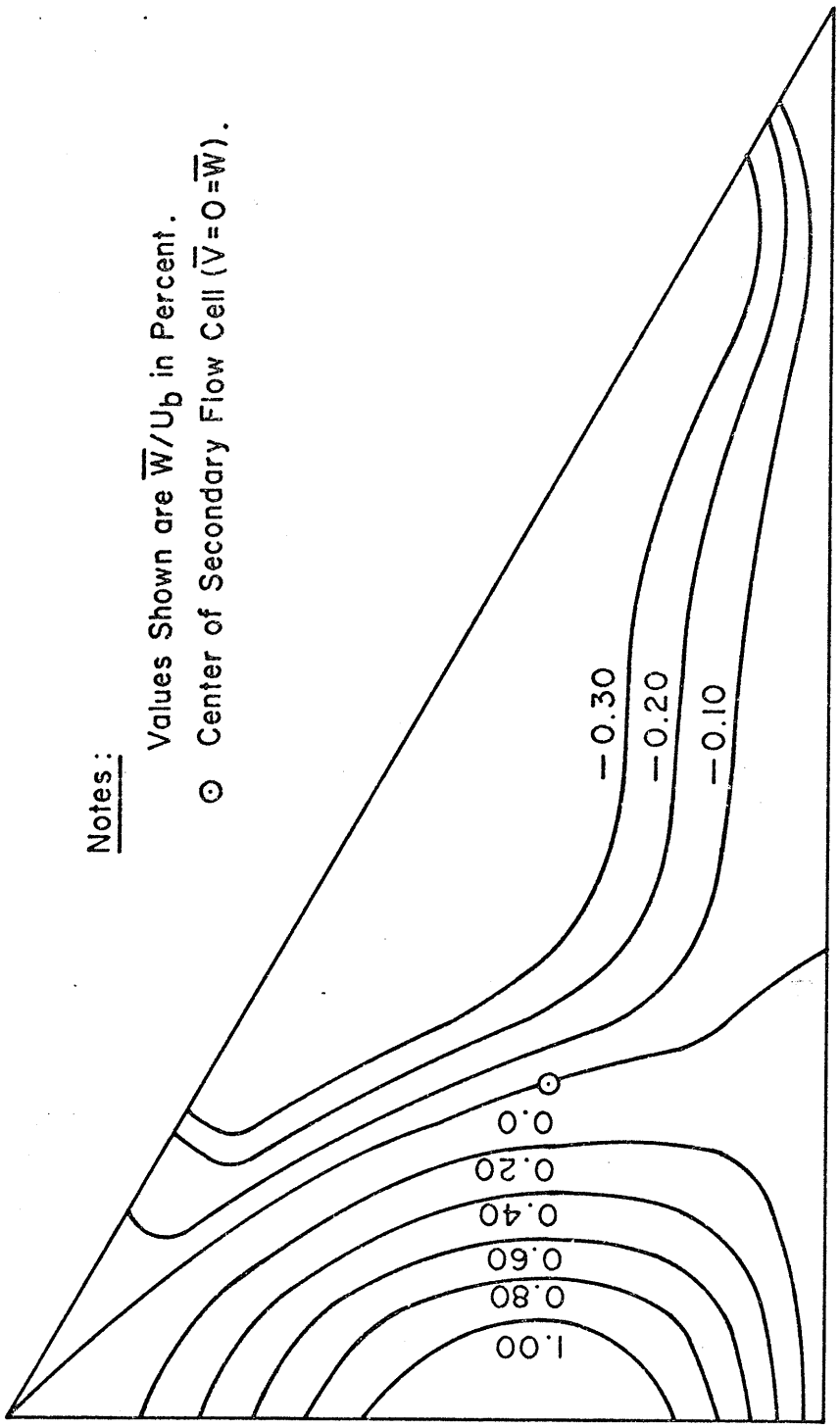

Fig.8.9. Contour Plots of $\overline{W}$ Predicted by Model II b. Re=53,000.

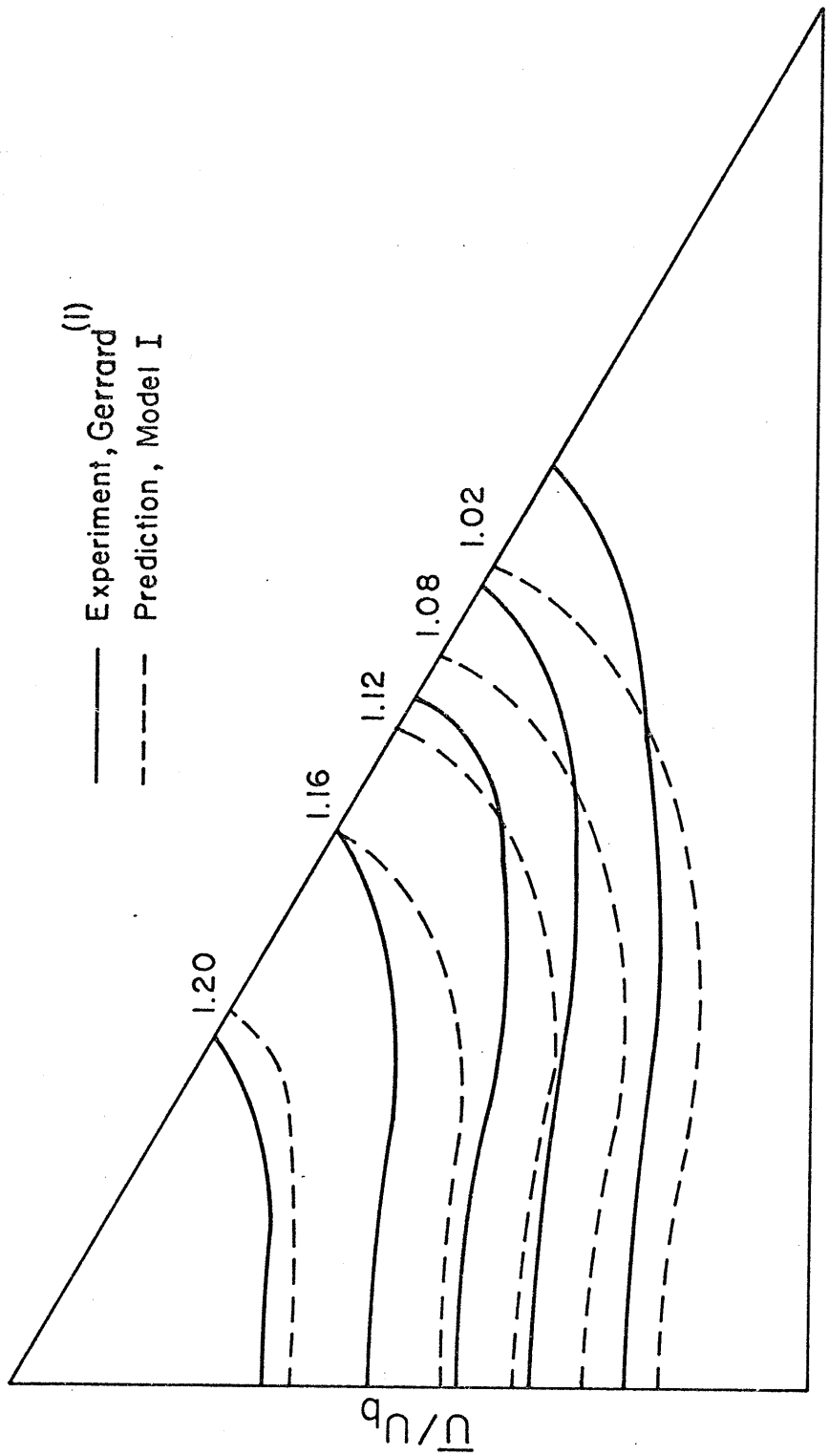

Fig.8.10.Comparison of Predicted (Model I) and Measured $\bar{U}$ Results , Re=53,000

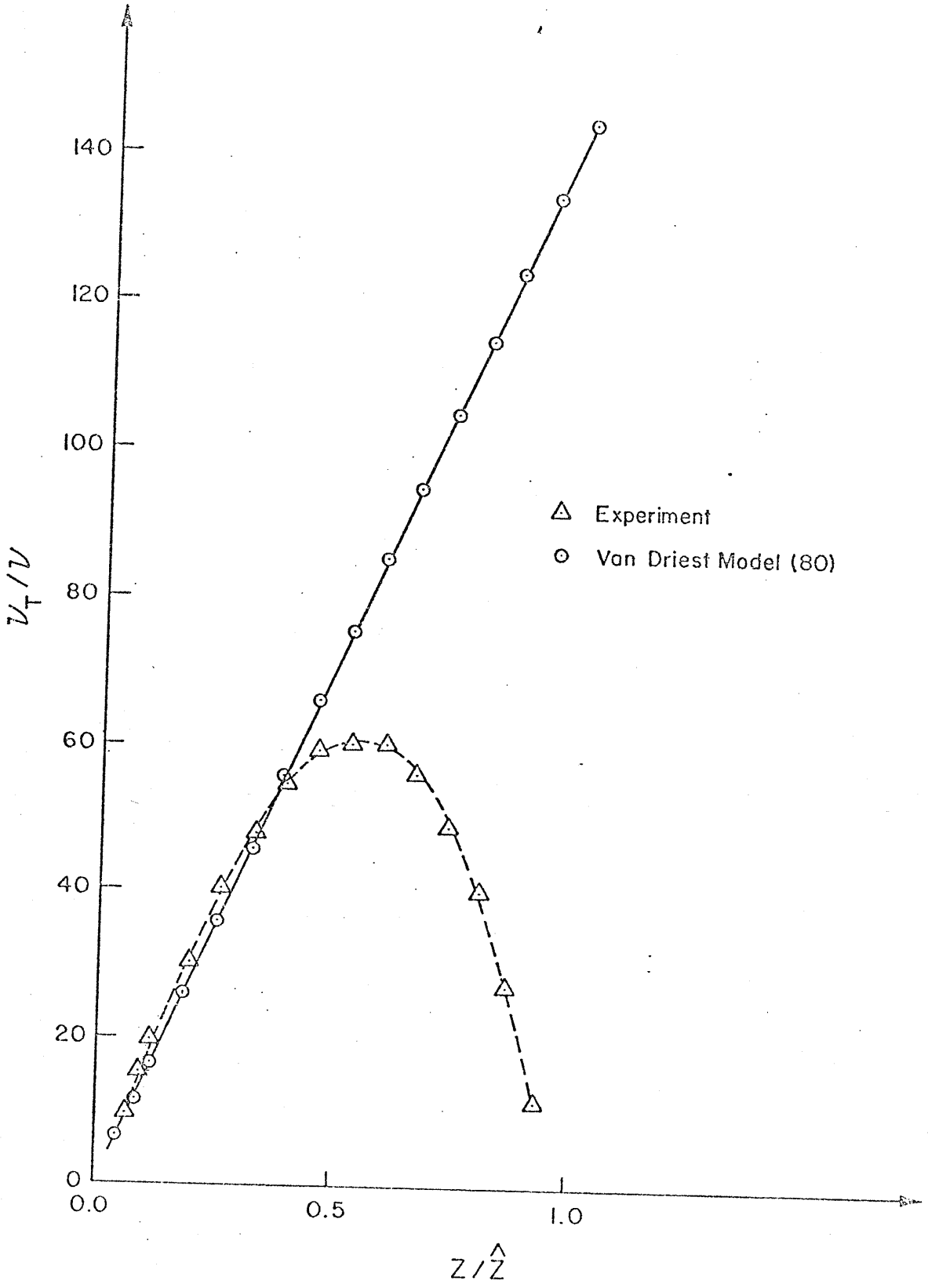

Fig. 8.11. Comparison of Van Driest Eddy Viscosity Model with Experimental Values, $y/L=0$, $Re=53,000$.

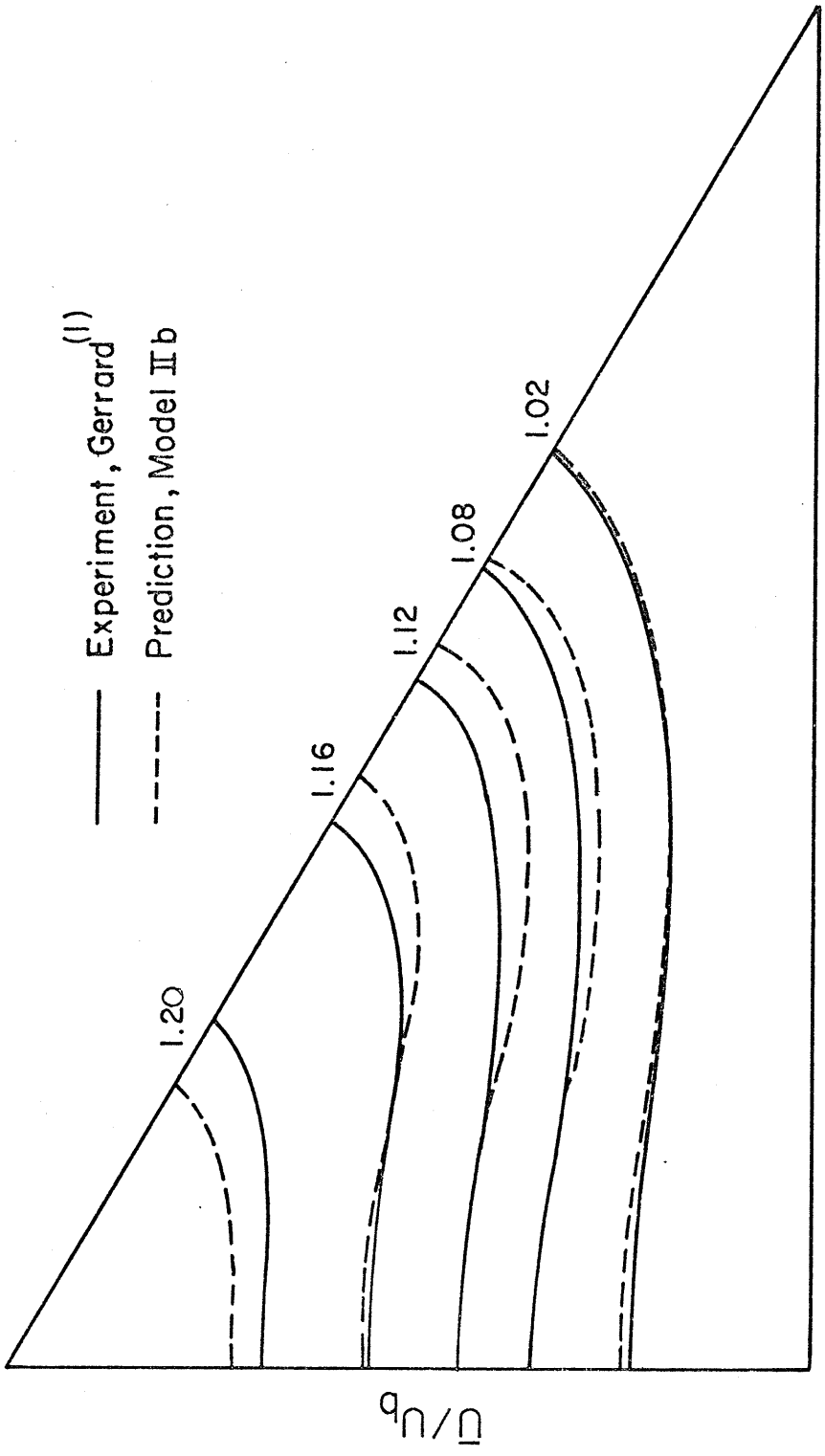

Fig. 8.12. Comparison of Predicted (Model IIb) and Measured $\bar{U}$ Results. Re = 53,000.

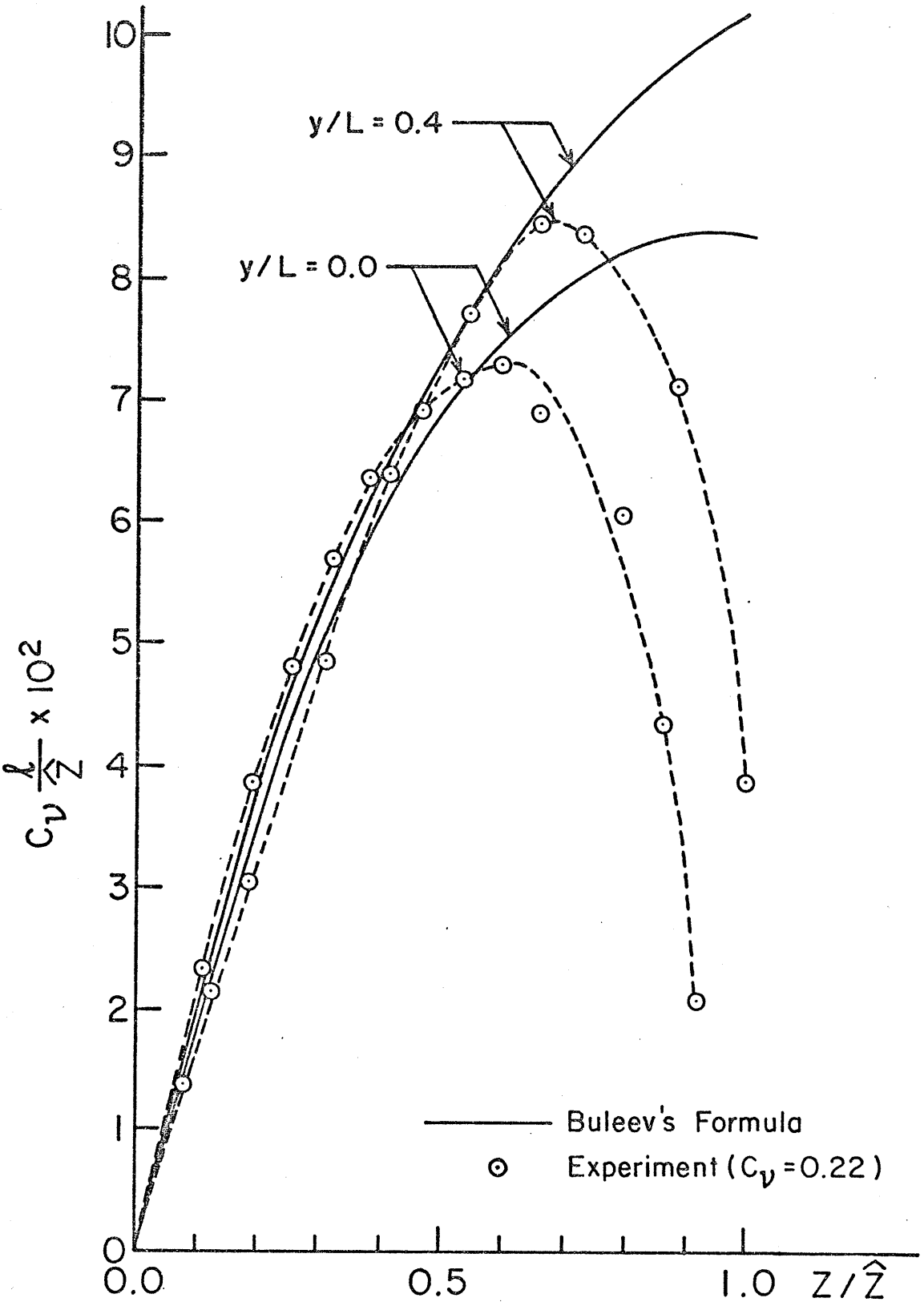

Fig.8.13. Comparison of Buleev's Length Scale with Experimental Values . Re = 53,000.

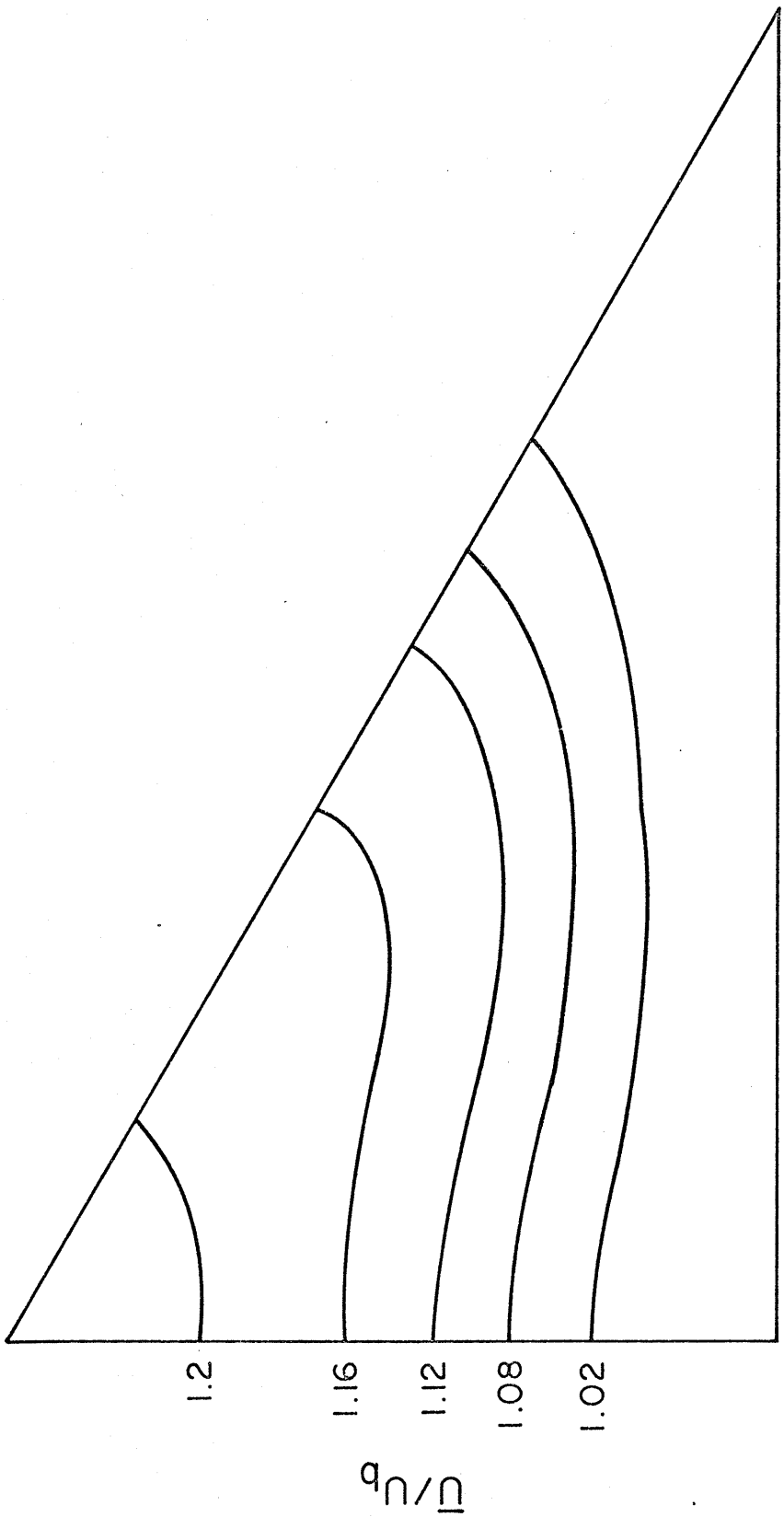

Fig. 8.14. Predicted Mean Axial Velocity Distribution, Model II b, Re=107,300.

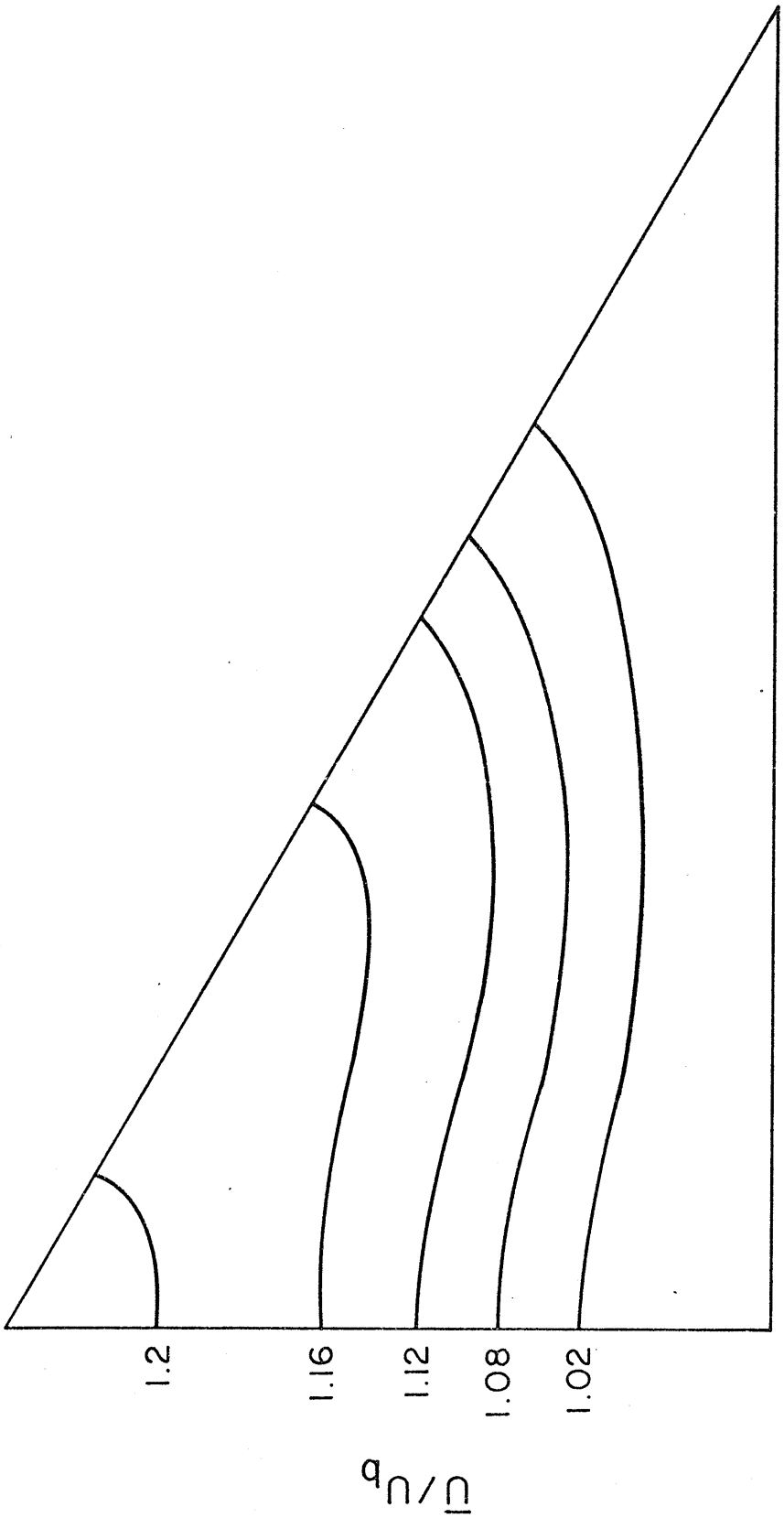

Fig. 8.15. Predicted Mean Axial Velocity Distribution, Model II b, Re = 150,000.

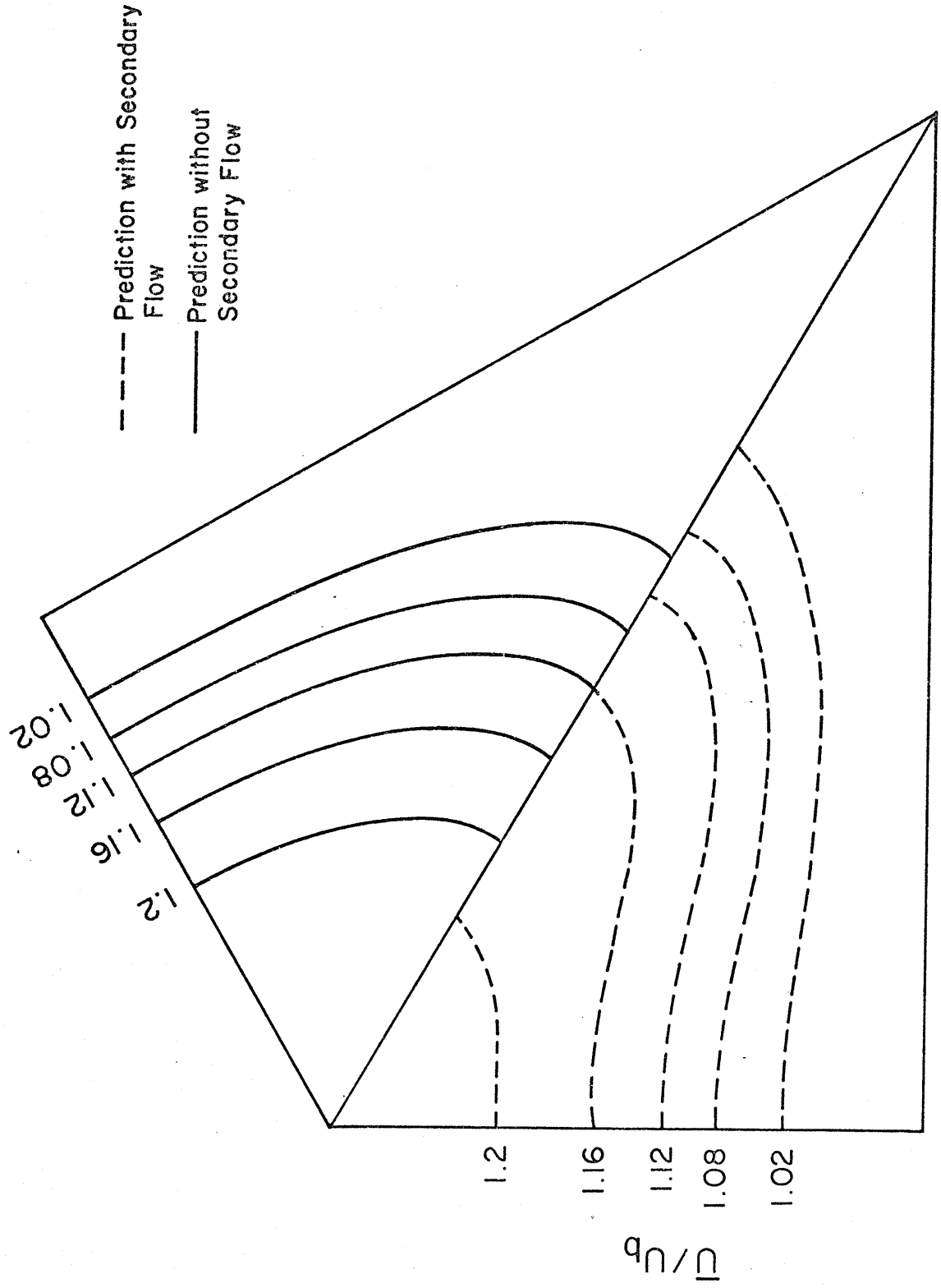

Fig. 8.16. Comparison of Predicted (Model II b) $\bar{U}$ Results with and without Secondary Flow, Re = 53,000.

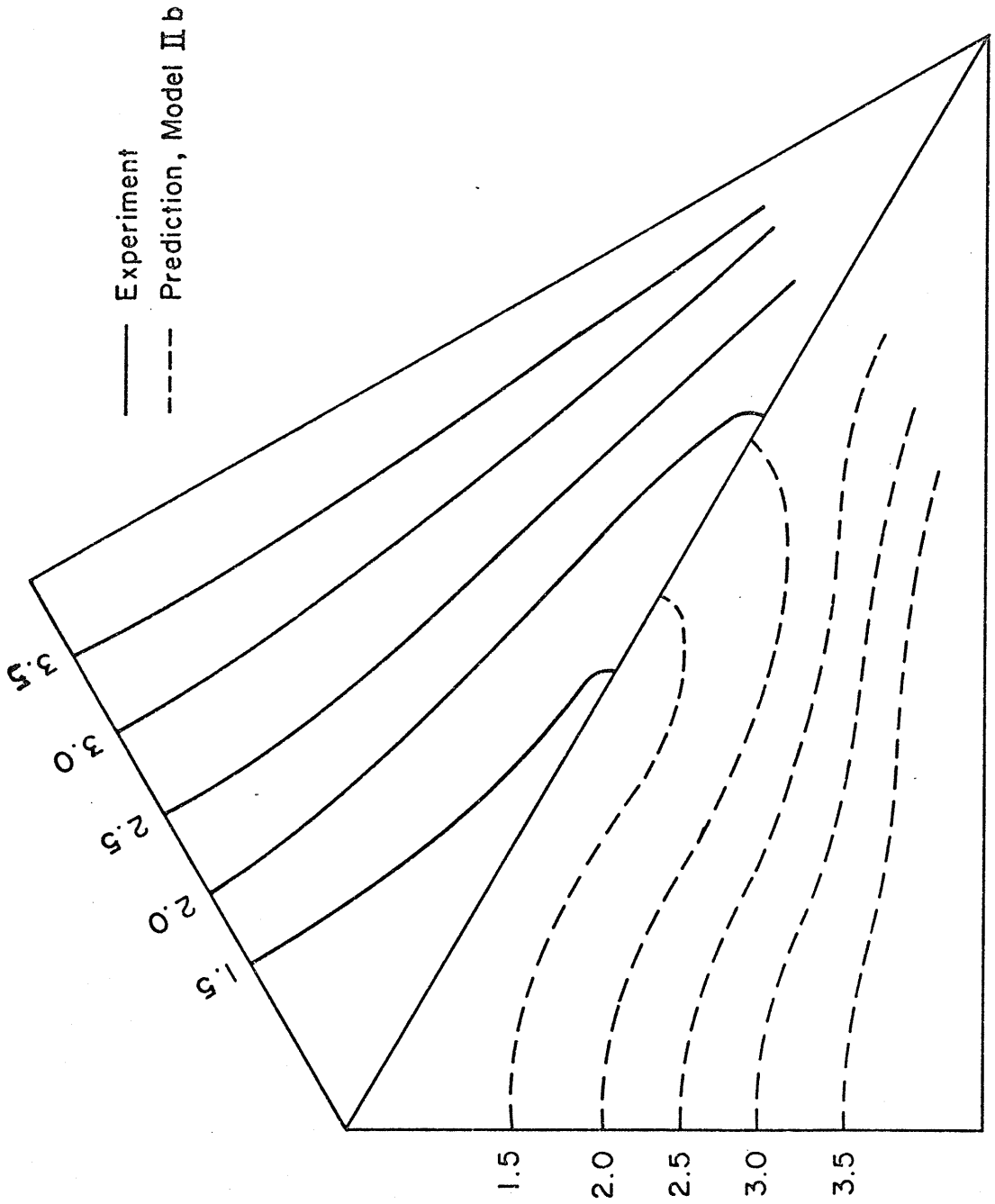

Fig.8.17. . Comparison of Predicted (Model IIb) and Measured k . Re=53,000.

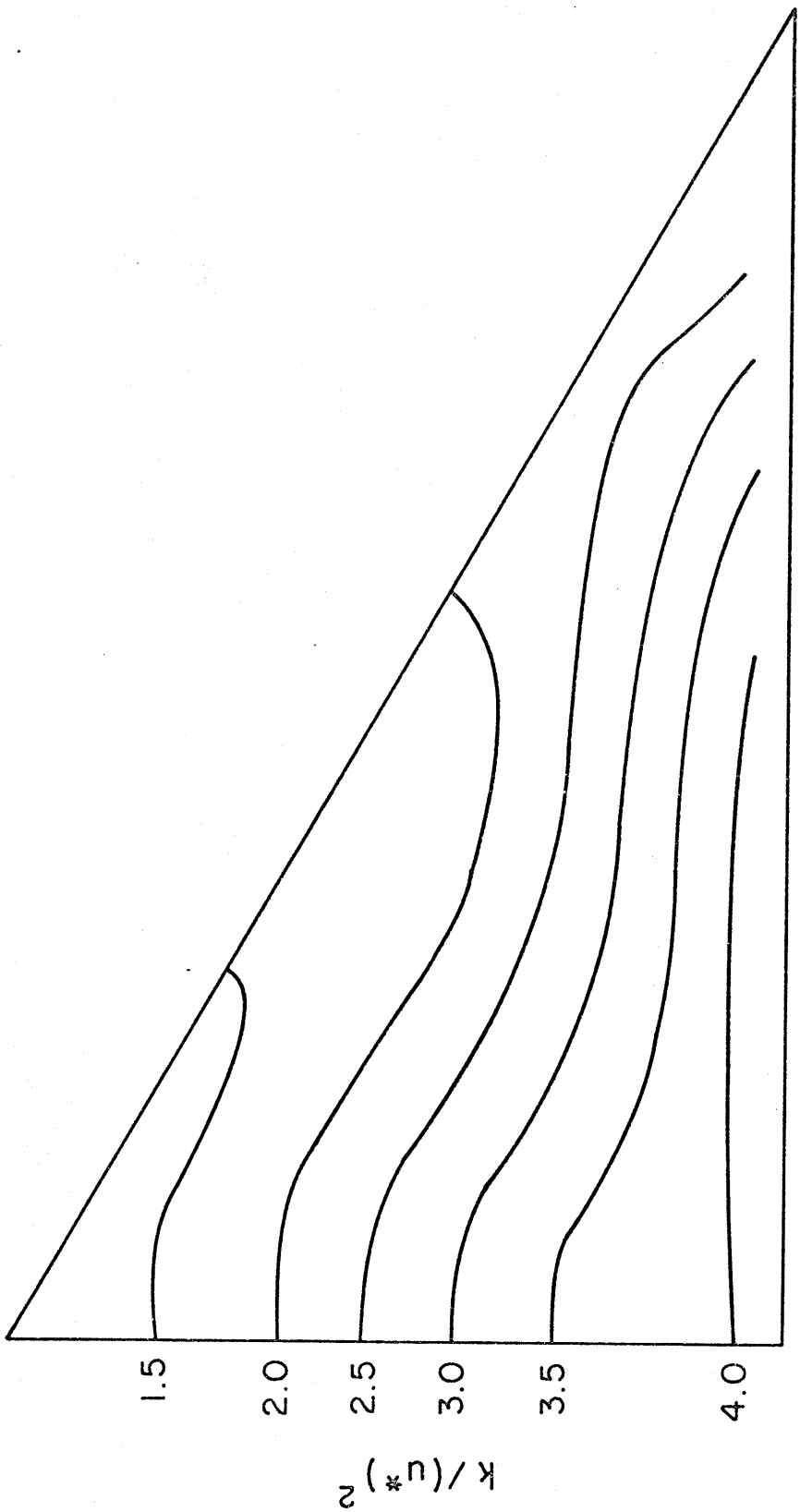

Fig. 8.18. Predicted k Distribution , Model IIb , Re = 107 , 300

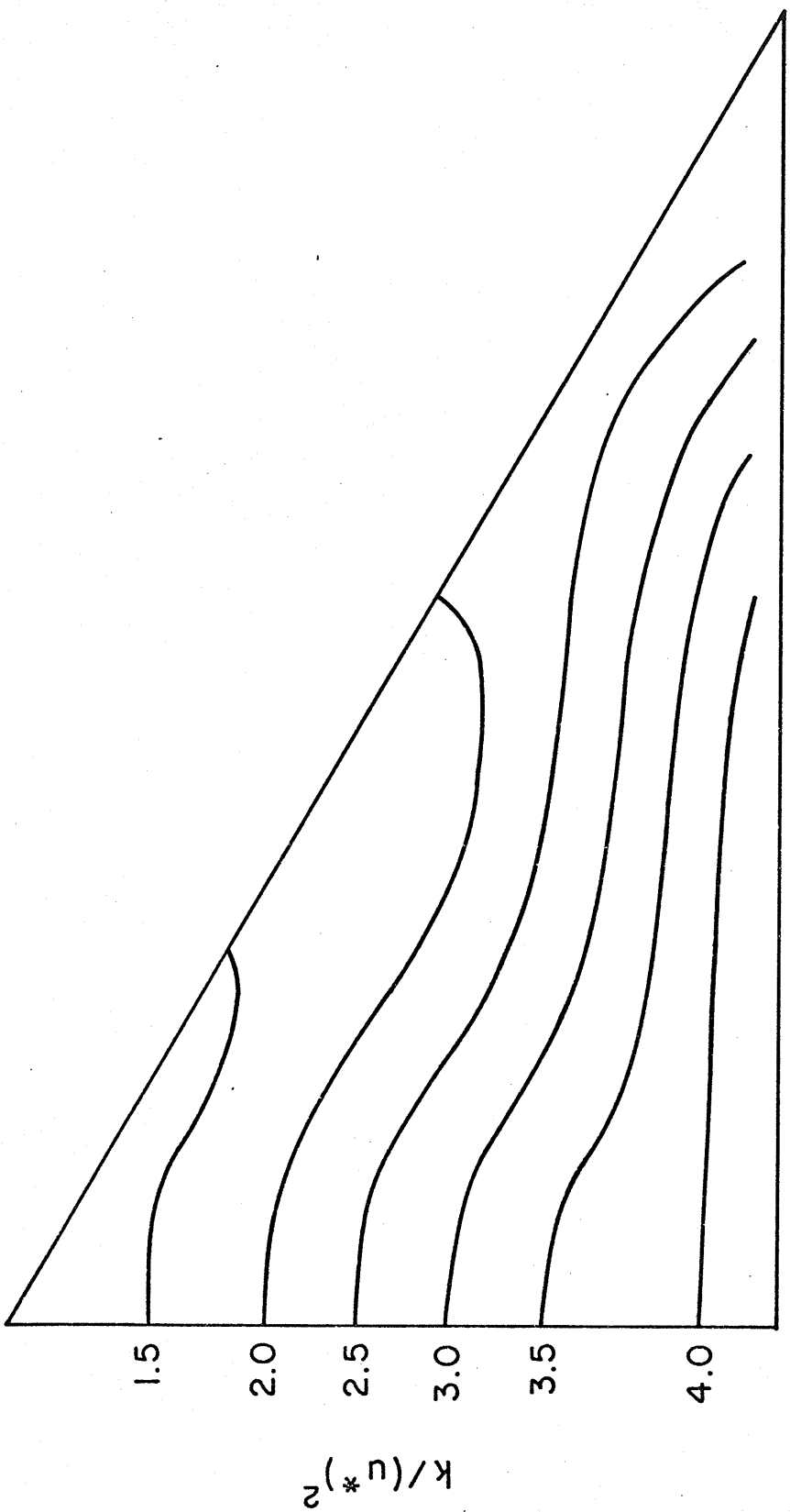

Fig.8.19. Predicted k Distribution, Model IIb, Re=150,000

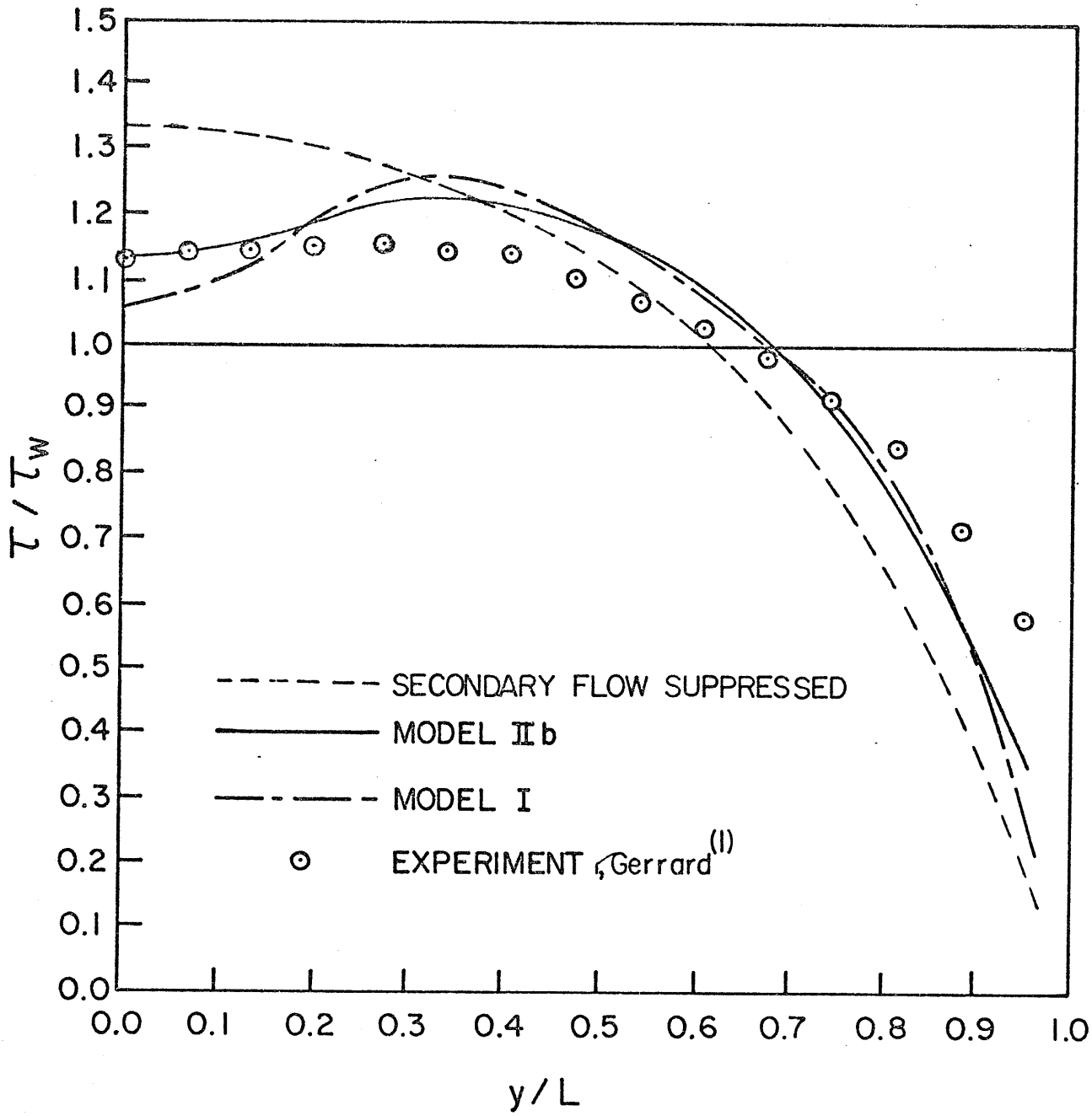

Fig.8.20 Comparison of Measured and Predicted Wall Shear Stress Distributions . Re = 53,000.

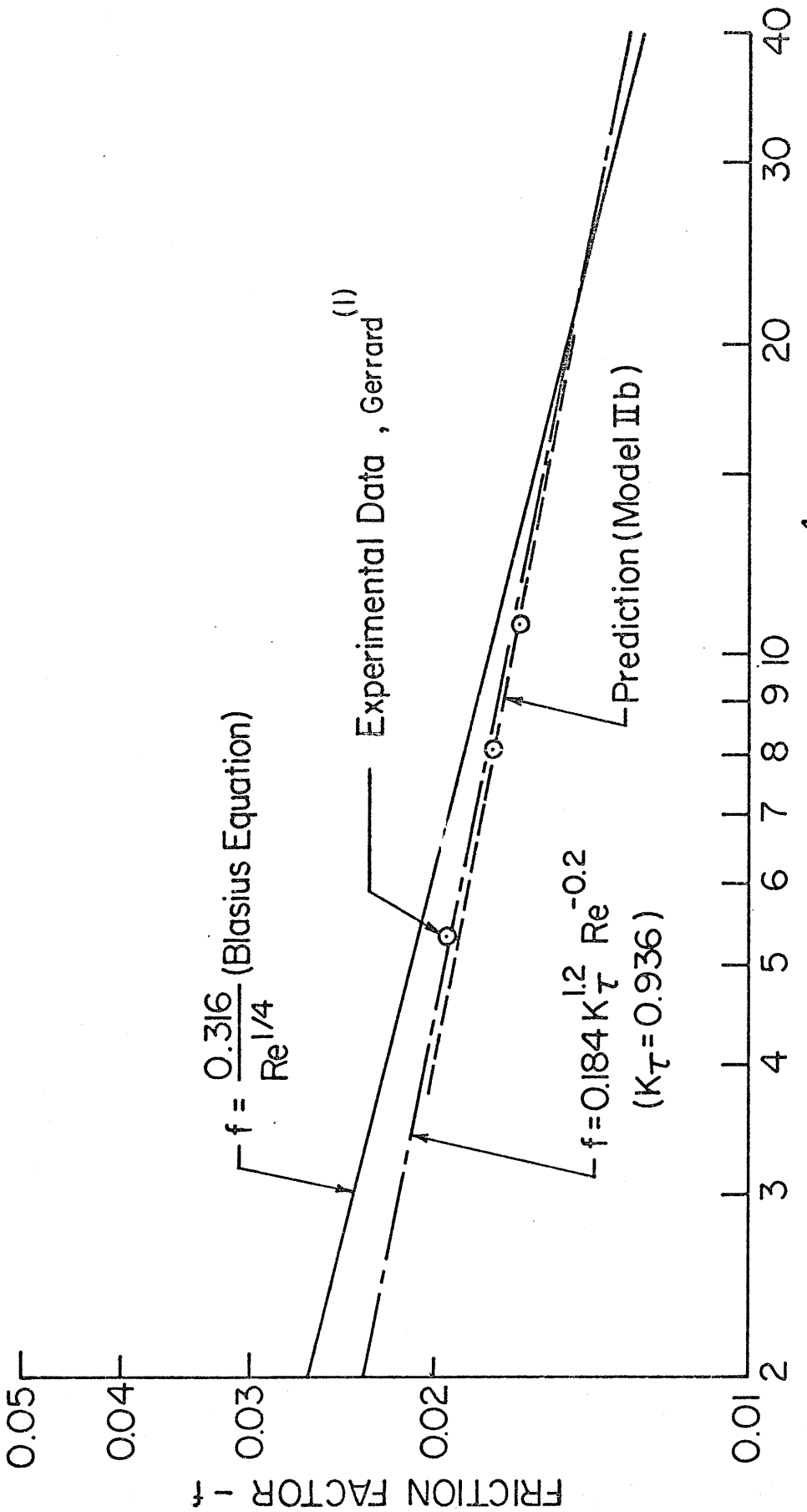

Fig.8.21. Friction Factor vs. Reynolds Number in Equilateral Triangular Duct.

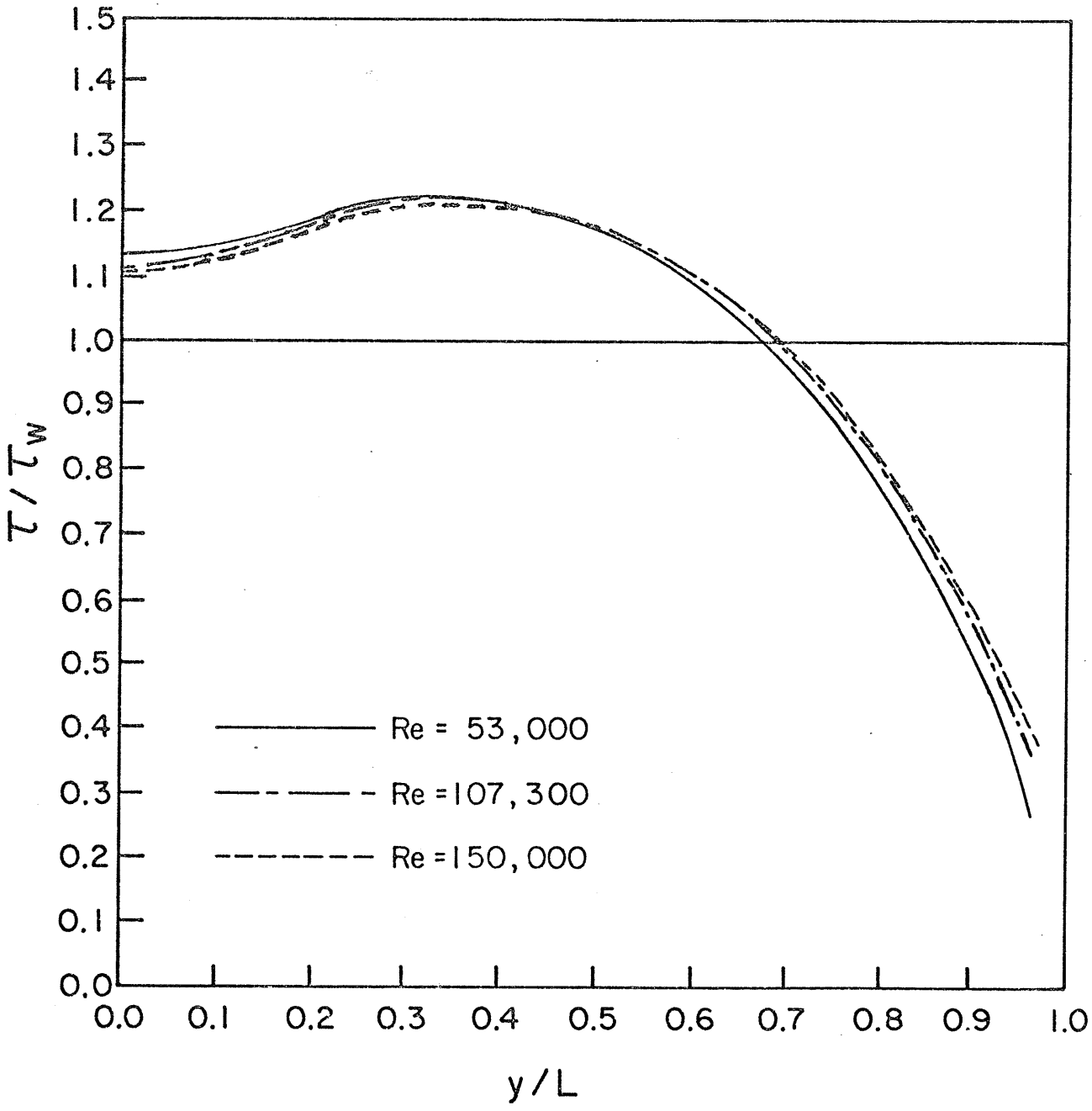

Fig. 8.22. Comparison of Predicted Wall Shear Stress (Model IIb) at different Reynolds Numbers.

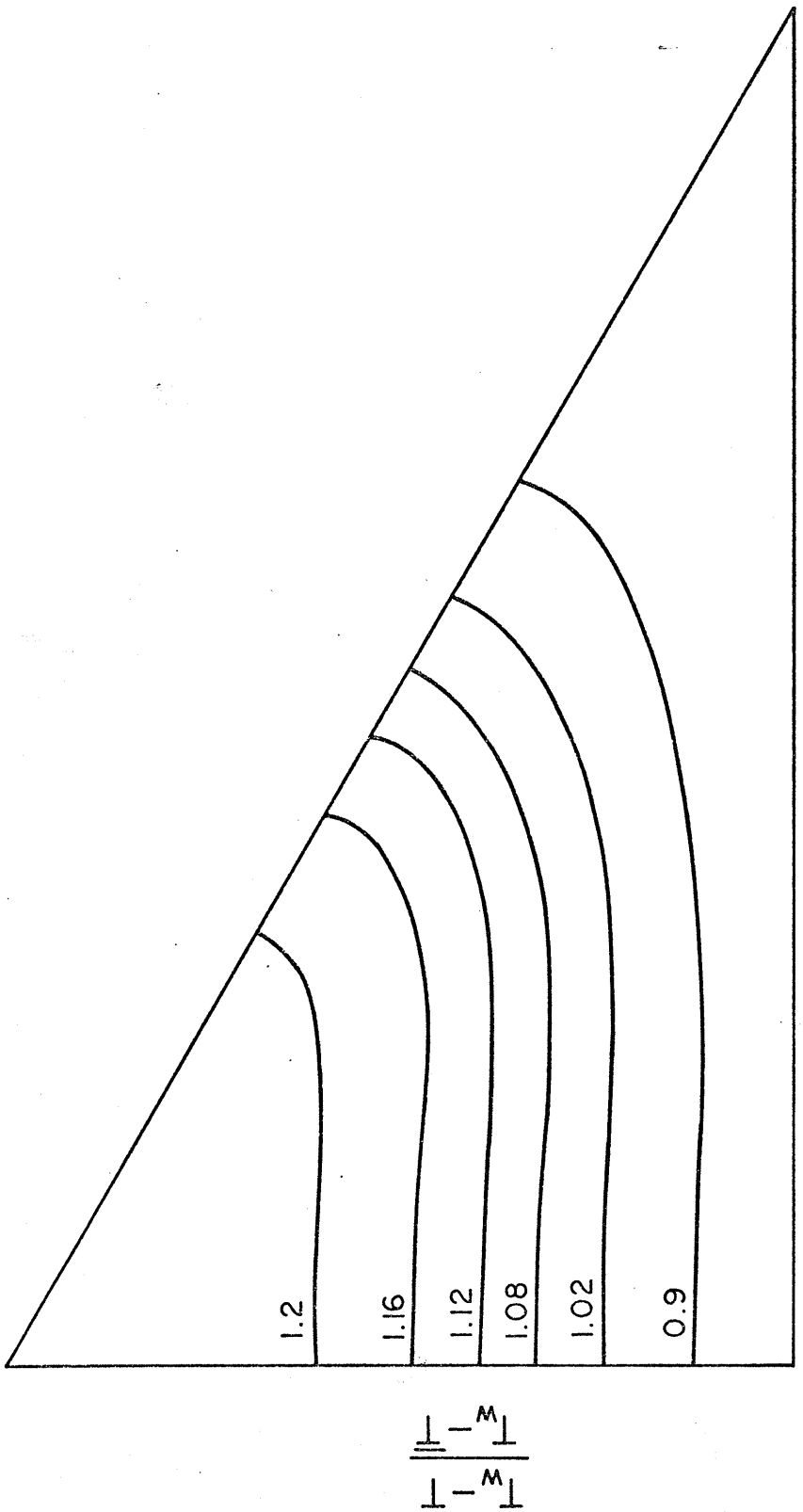

Fig.8.23. Contour Plot of Dimensionless Temperature Distribution. Re = 53,000.

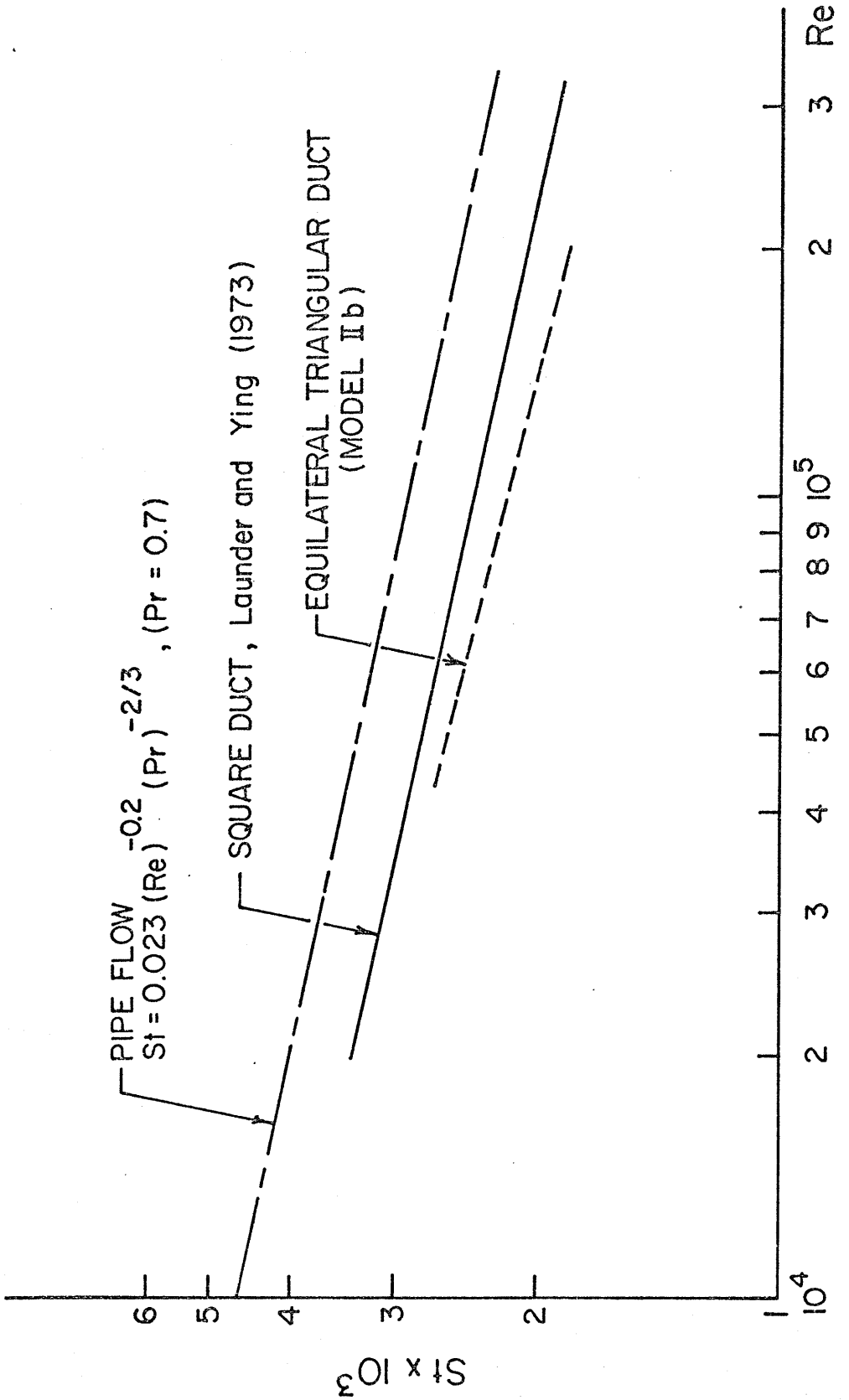

Fig.8.24. Stanton Number Dependence on Reynolds Number.

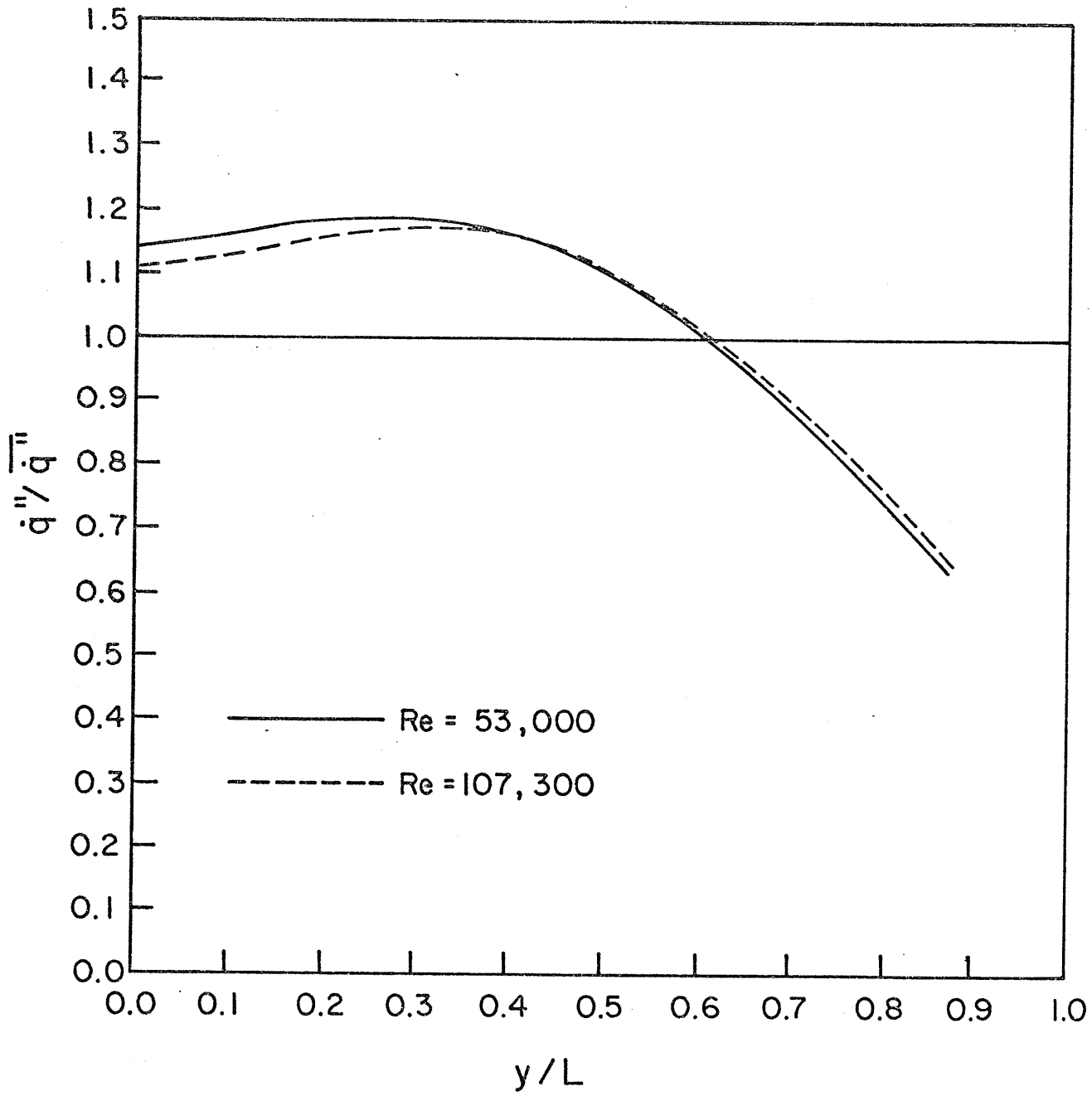

Fig.8.25. Predicted (Model II b) Local Heat Flux Distribution at Two Reynolds Numbers.

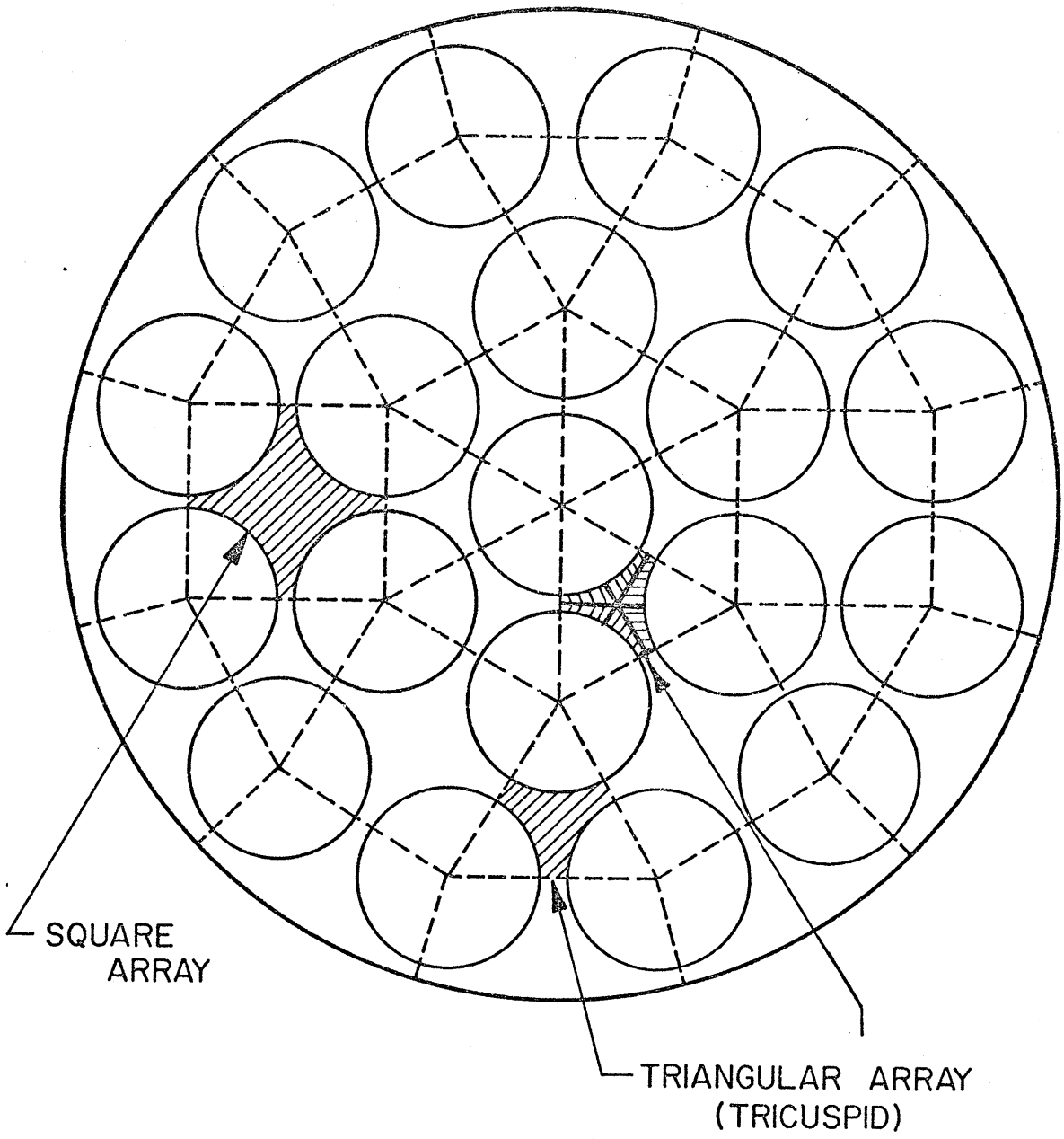

FIG.9.1. CROSS-SECTION of TYPICAL NINETEEN ELEMENT FUEL BUNDLE.

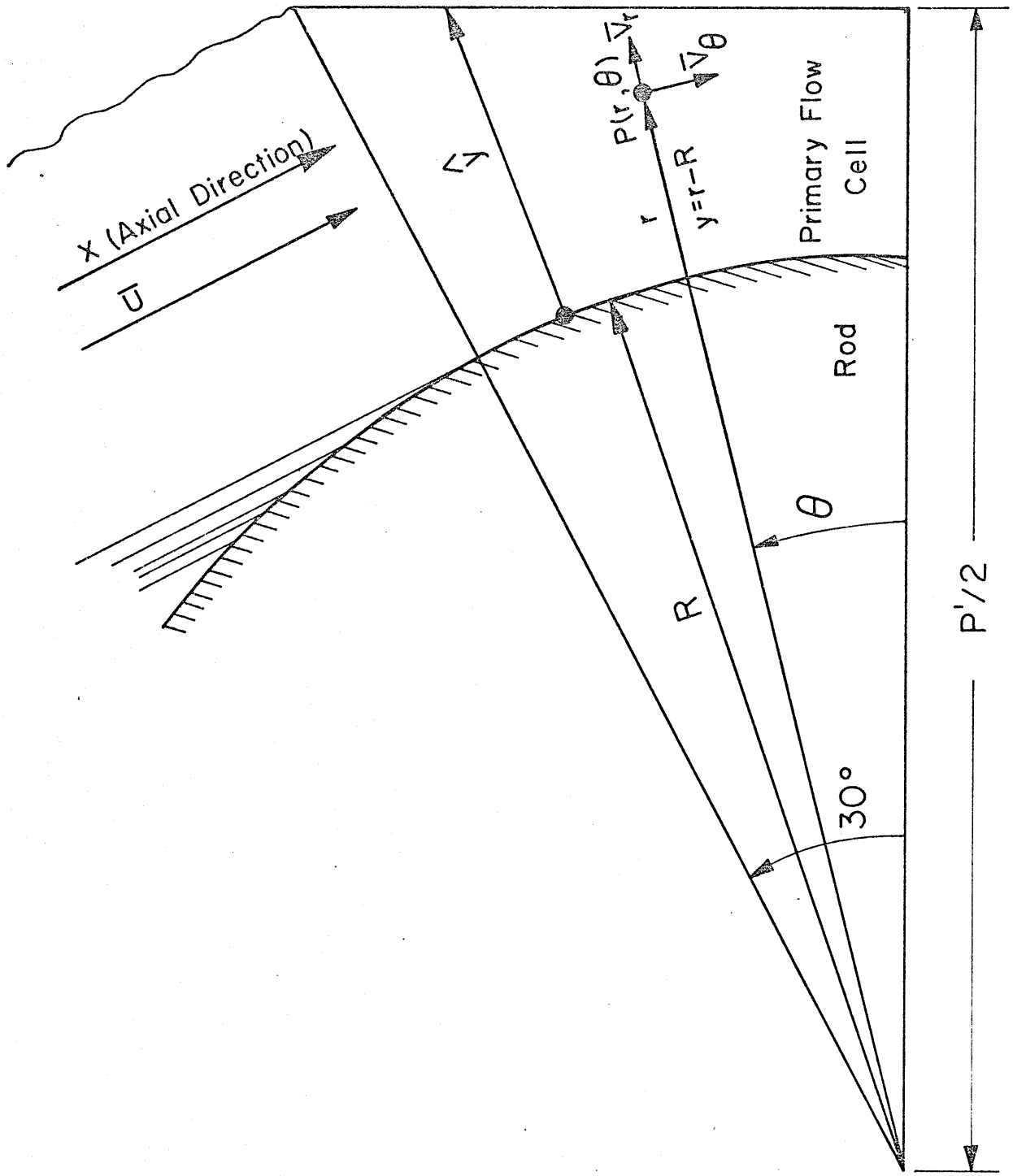

Fig. 9.2. Cylindrical Coordinate System and Velocity Directions.

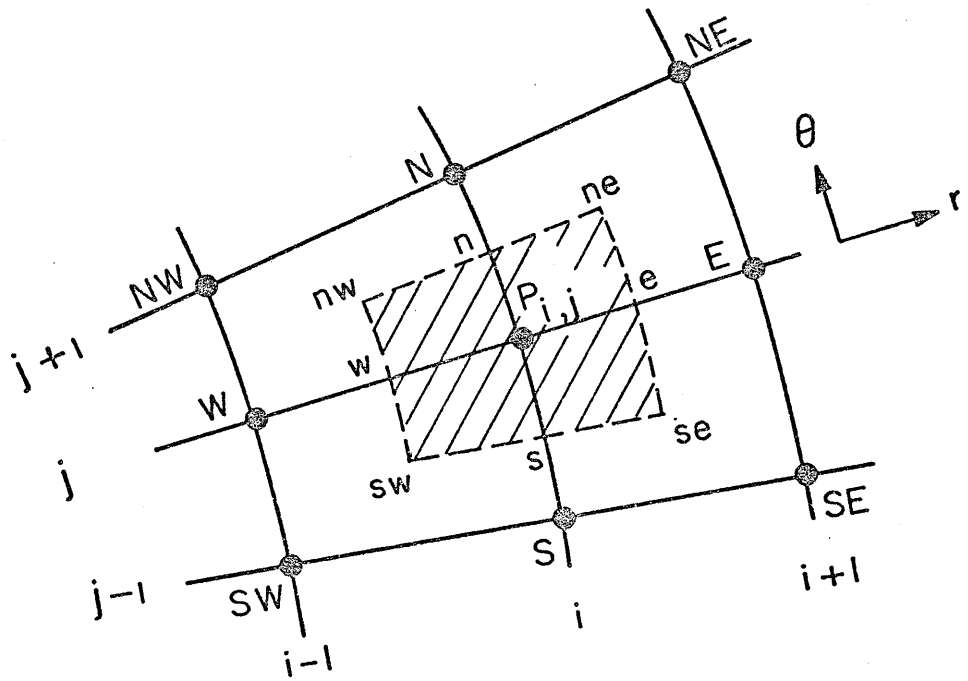

Fig. II. 1. Part of the Finite Difference Grid for Numerical Integration .

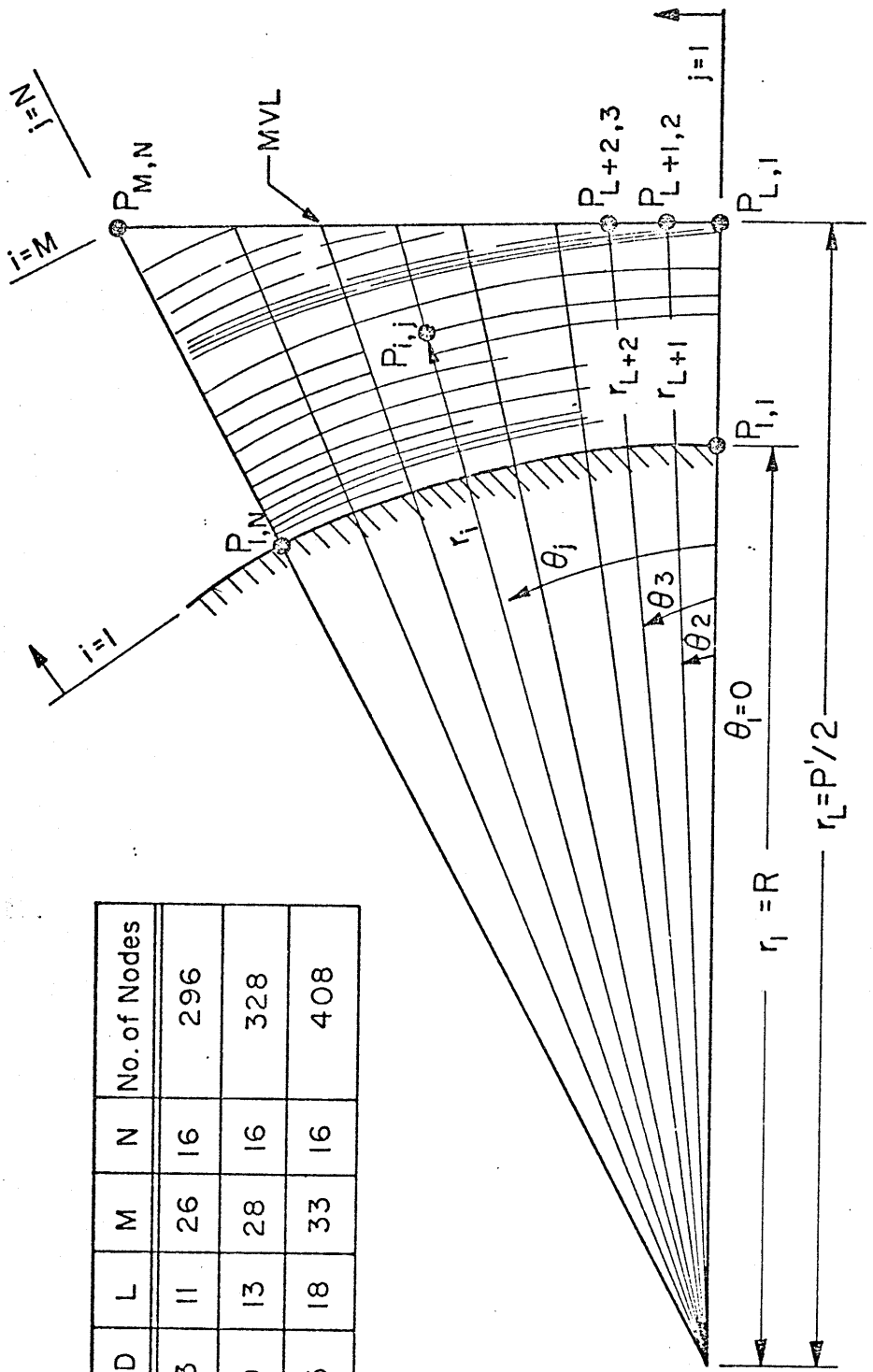

P'/D	L	M	N	No. of Nodes
1.123	11	26	16	296
1.20	13	28	16	328
1.35	18	33	16	408

Fig. II.2. Grid Notations for The Computar Program.

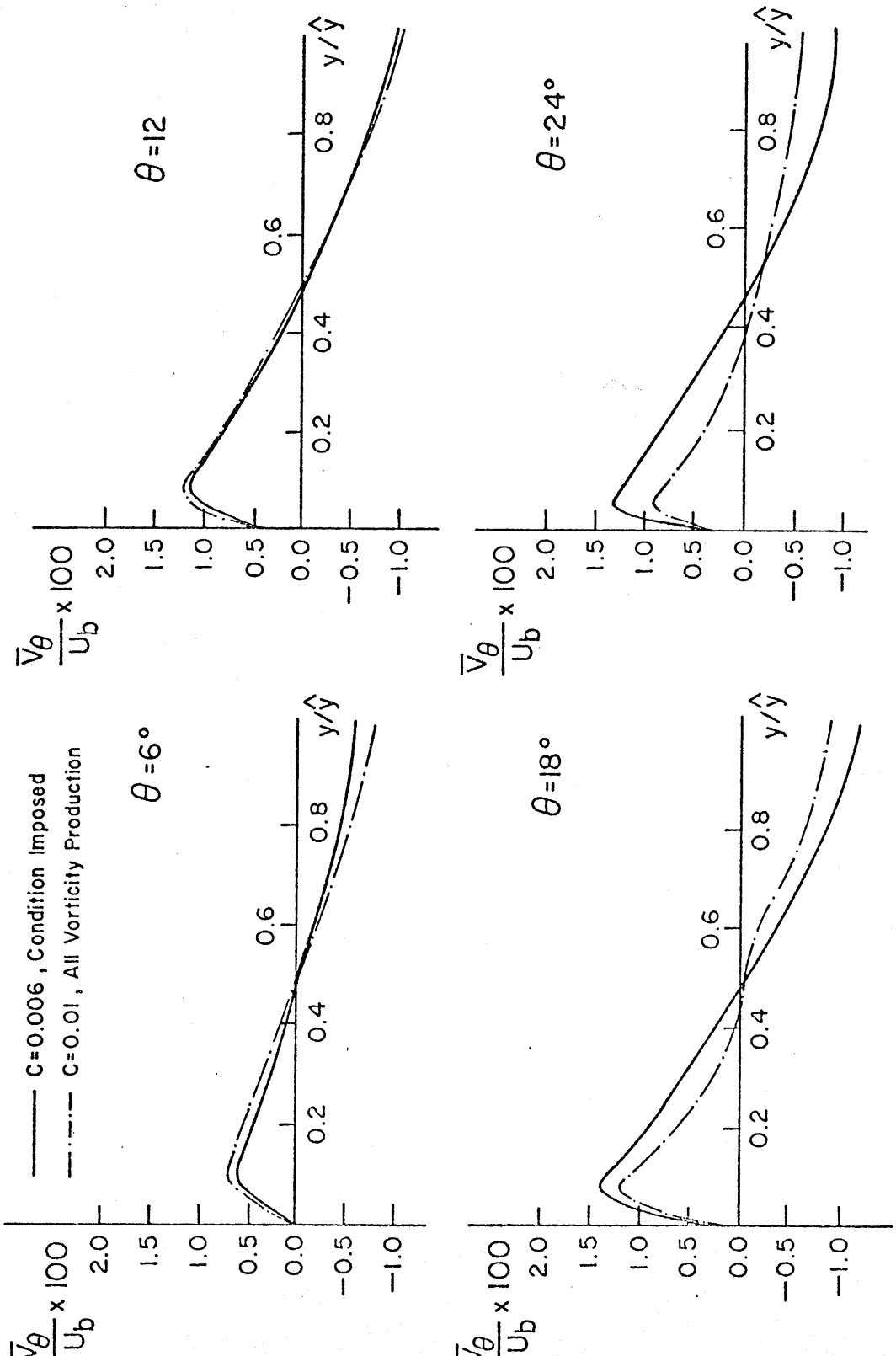

Fig.12.1. Predicted Secondary Velocity Component $\bar{V}_\theta$, Re=27,000, P'/D=1.123.

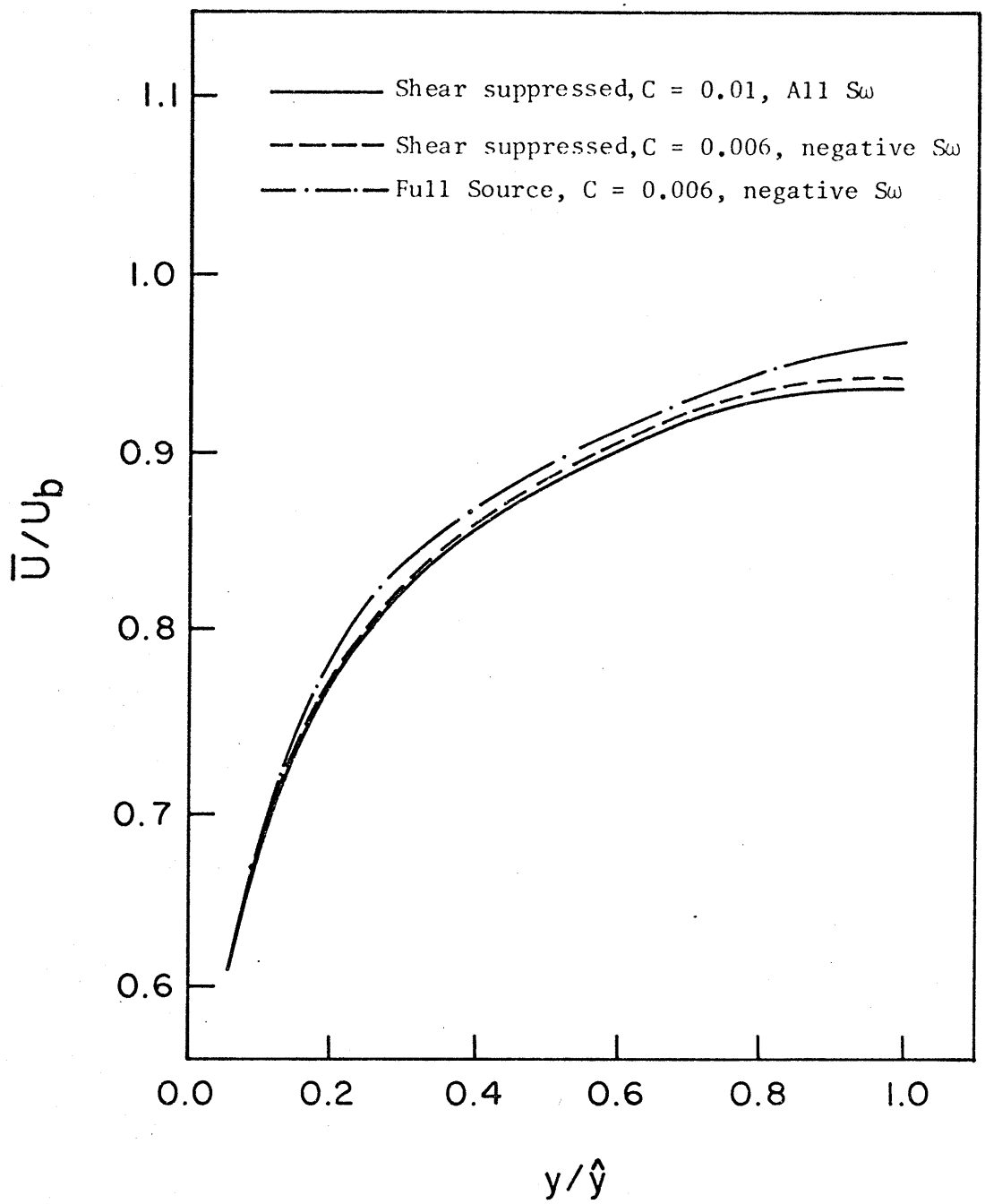

Fig.12.2 Predicted $\bar{U}$ Distribution with Different Vorticity Source Terms, $P'/D=1.123$, $Re=27{,}000$, $\theta=0°$

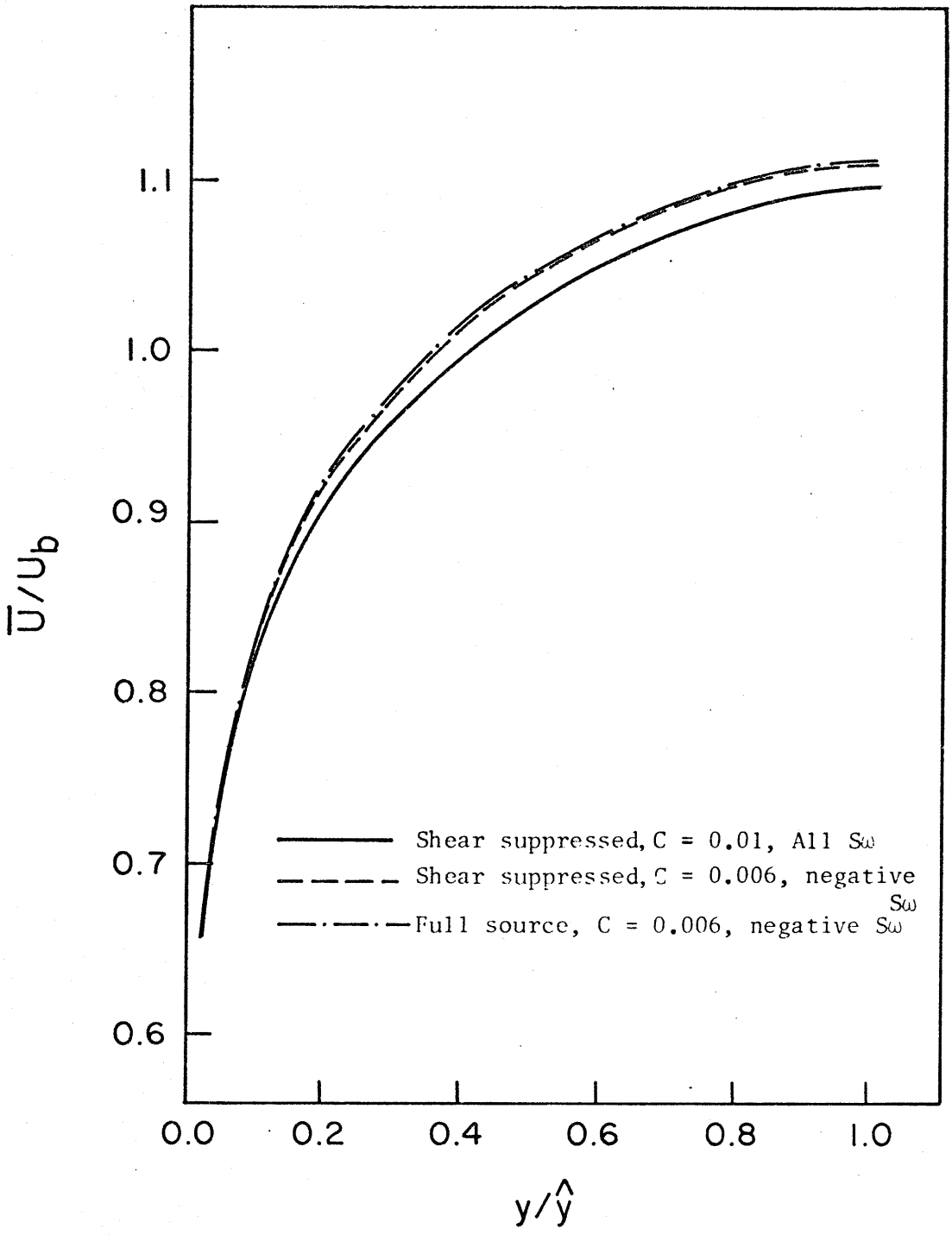

Fig. 12.3. Predicted $\bar{U}$ Distribution with Different Vorticity Source Terms, P'/D=1.123, Re=27,000, θ=15°.

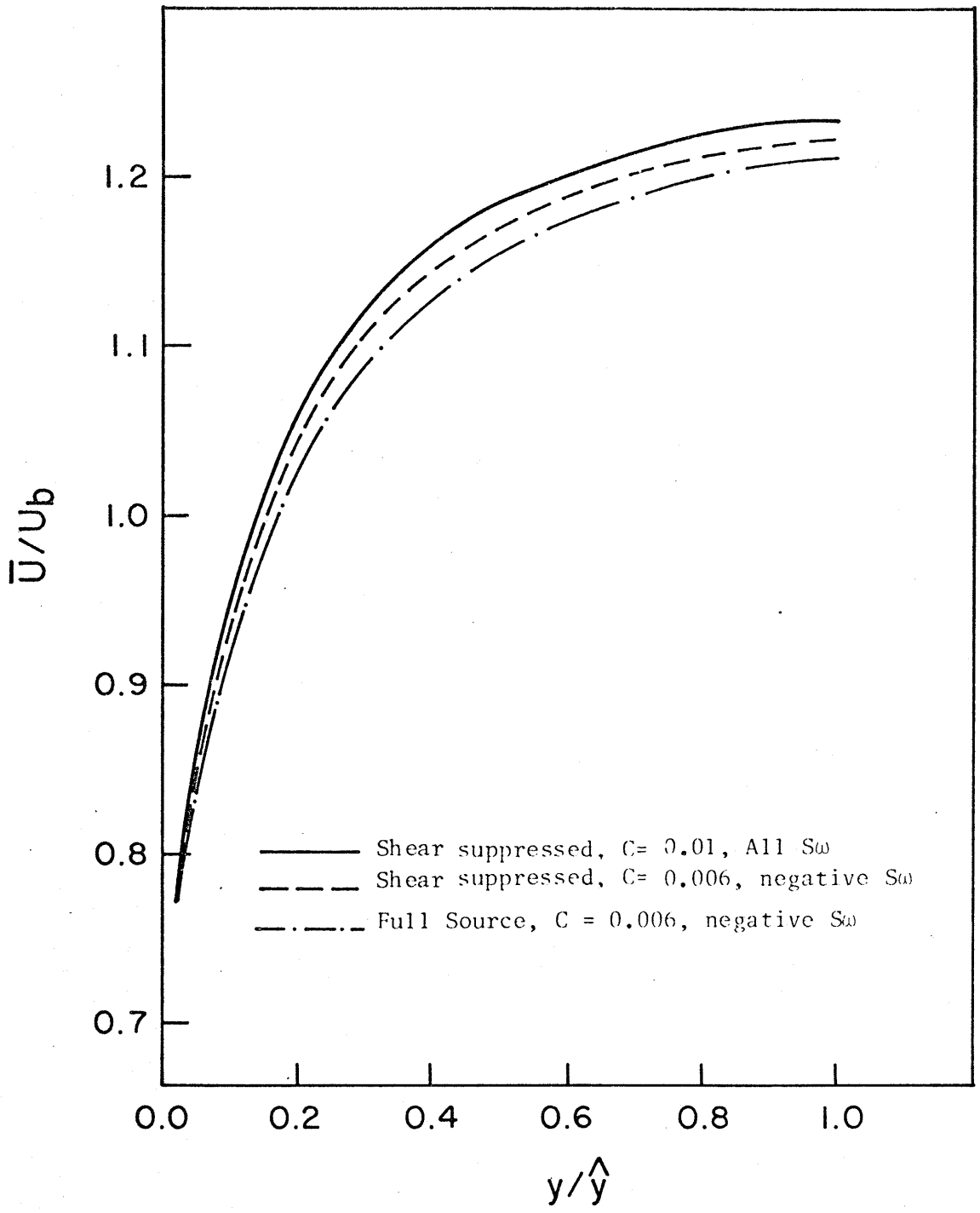

Fig. 12.4. Predicted $\bar{U}$ Distribution with Different Vorticity Source Terms, $P'/D=1.123$, $Re=27,000$, $\theta=30°$.

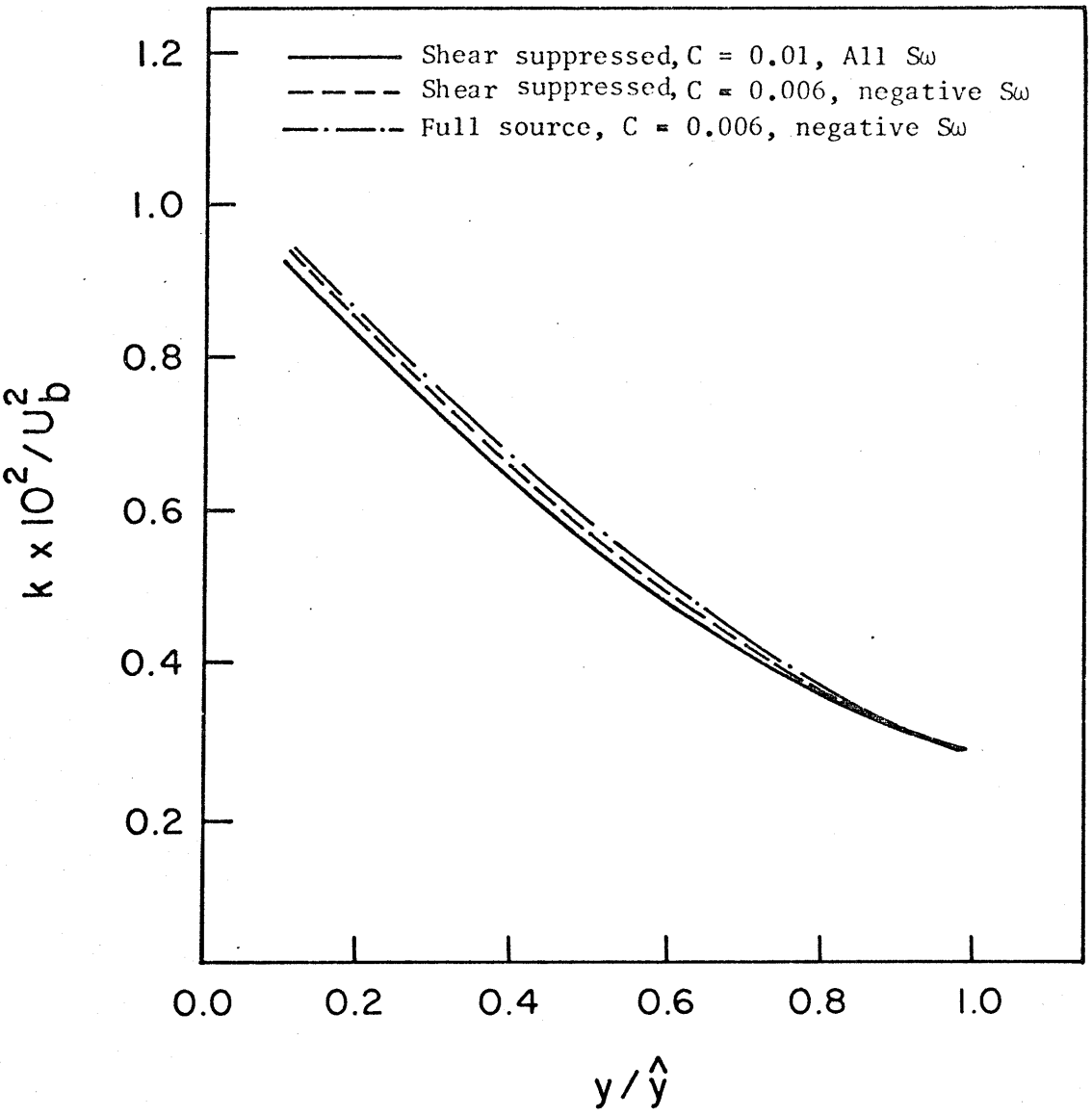

Fig. 12.5. Predicted k Distribution with Different Vorticity Source Terms, $P'/D = 1.123$, $Re = 27,000$, $\theta = 0°$.

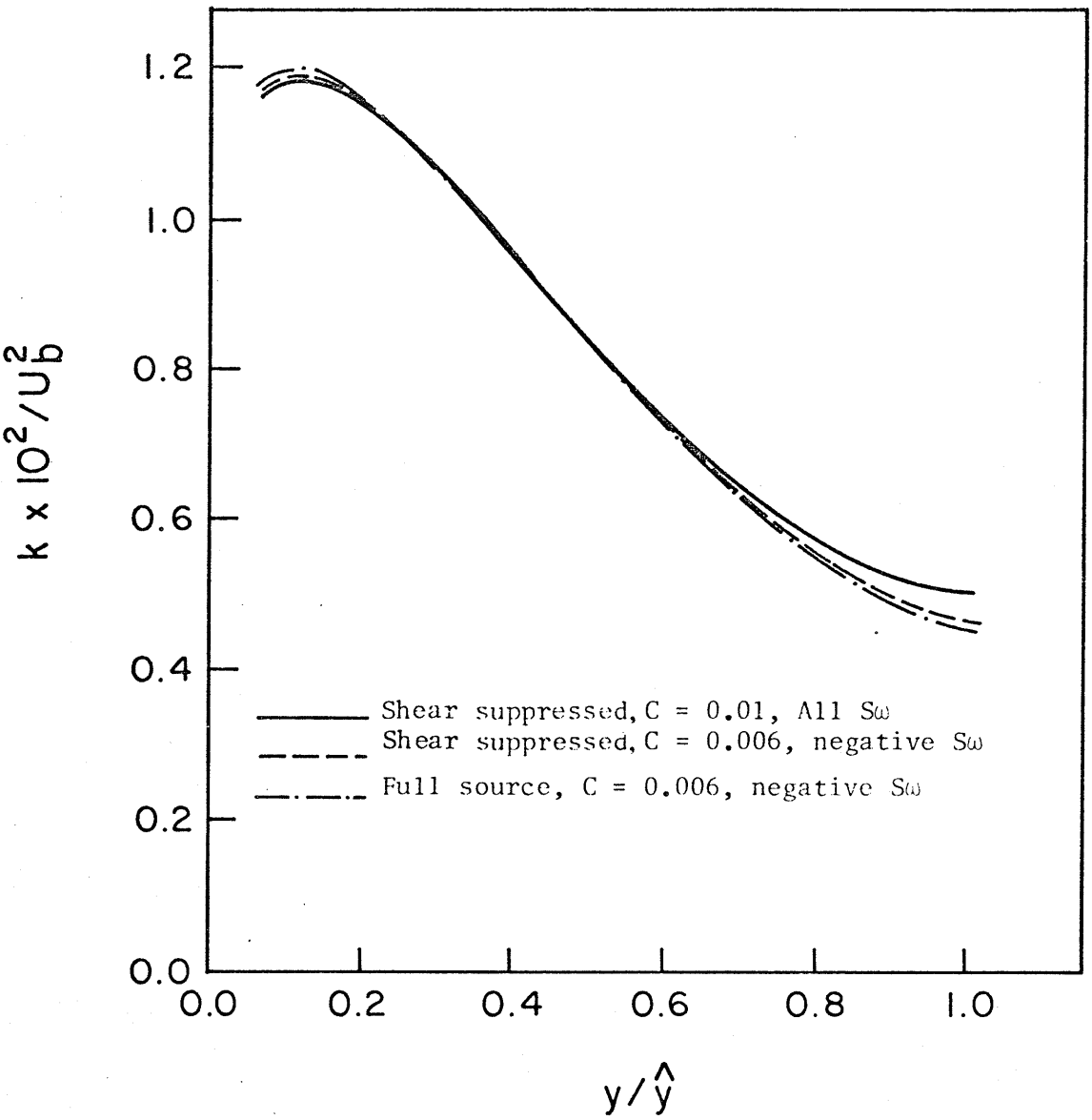

Fig. 12.6. Predicted k Distribution with Different Vorticity Source Terms, P'/D=1.123, Re=27,000, θ=15°.

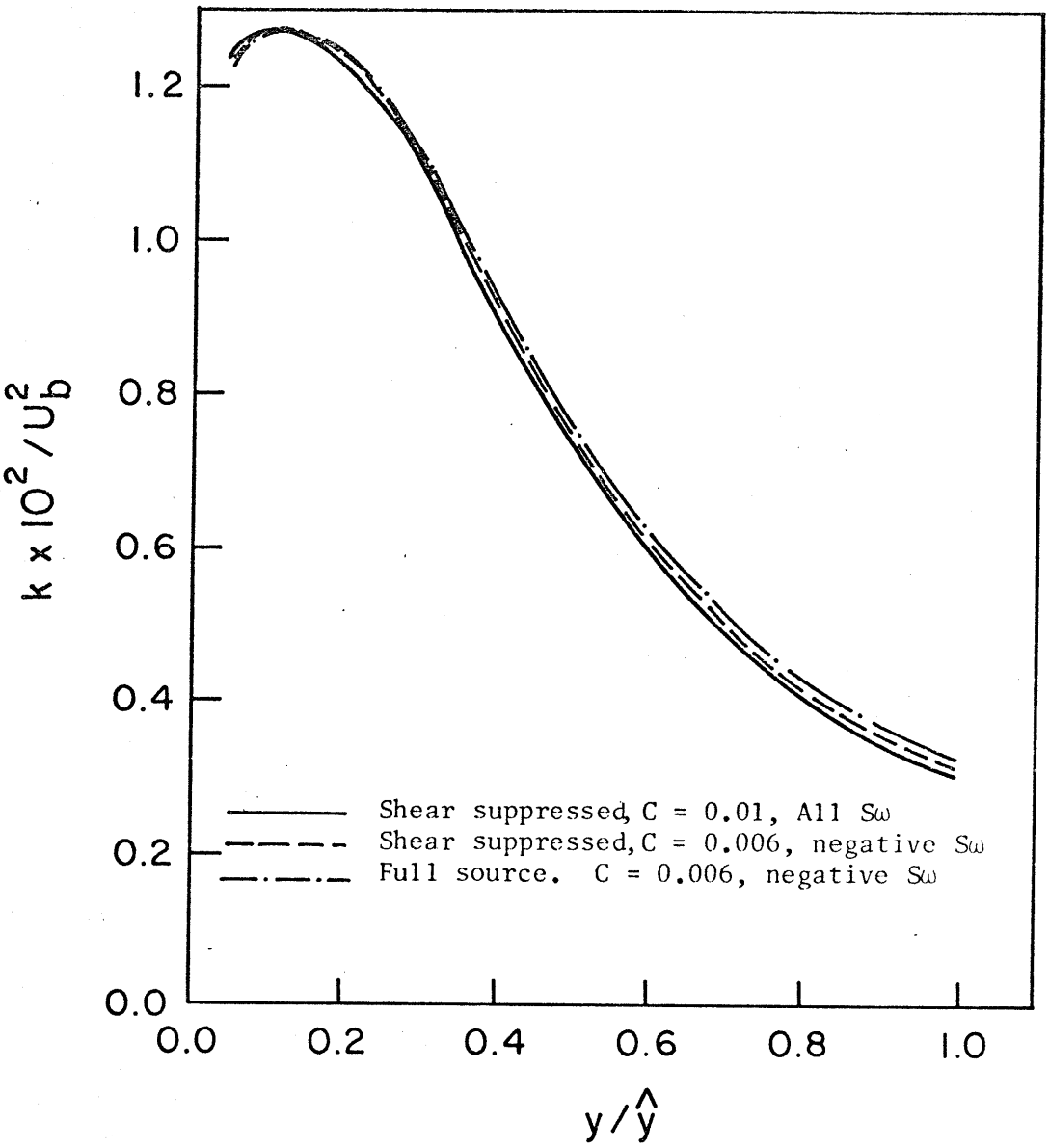

Fig. 12.7. Predicted k Distribution with Different Vorticity Source Terms, $P'/D = 1.123$, $Re = 27{,}000$, $\theta = 30°$.

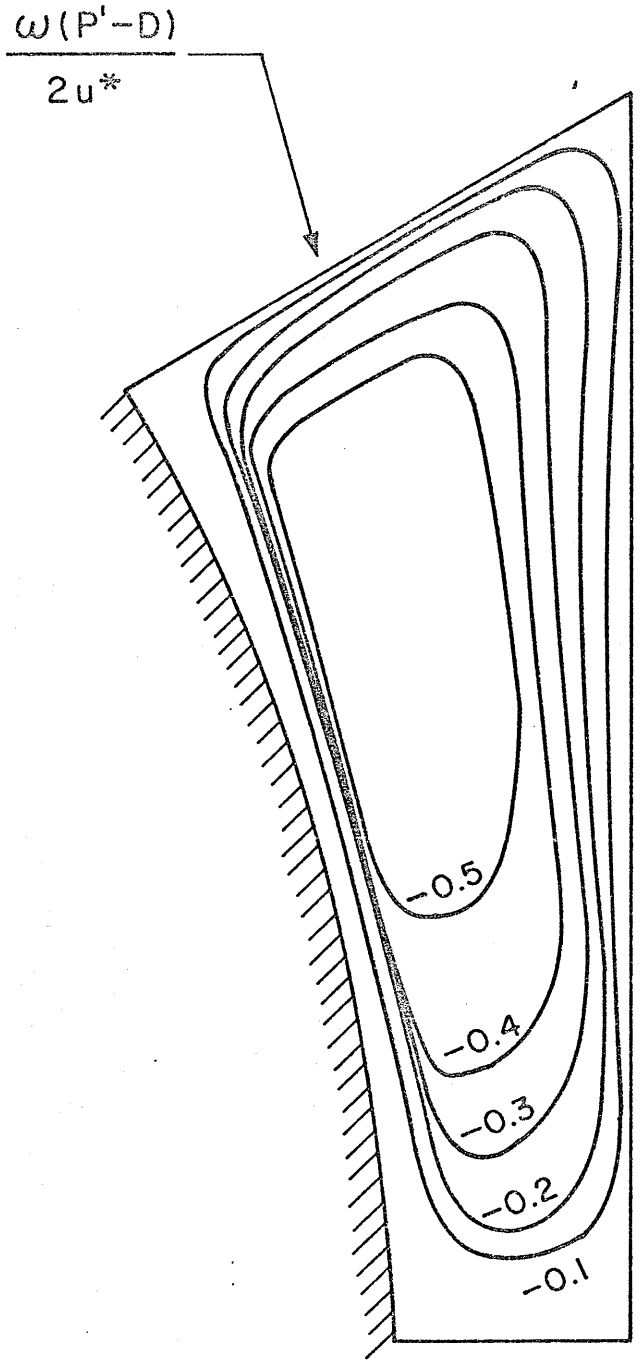

Fig. 12.8. Predicted Dimensionless Vorticity Distribution , Re=27,000 , P'/D=1.123

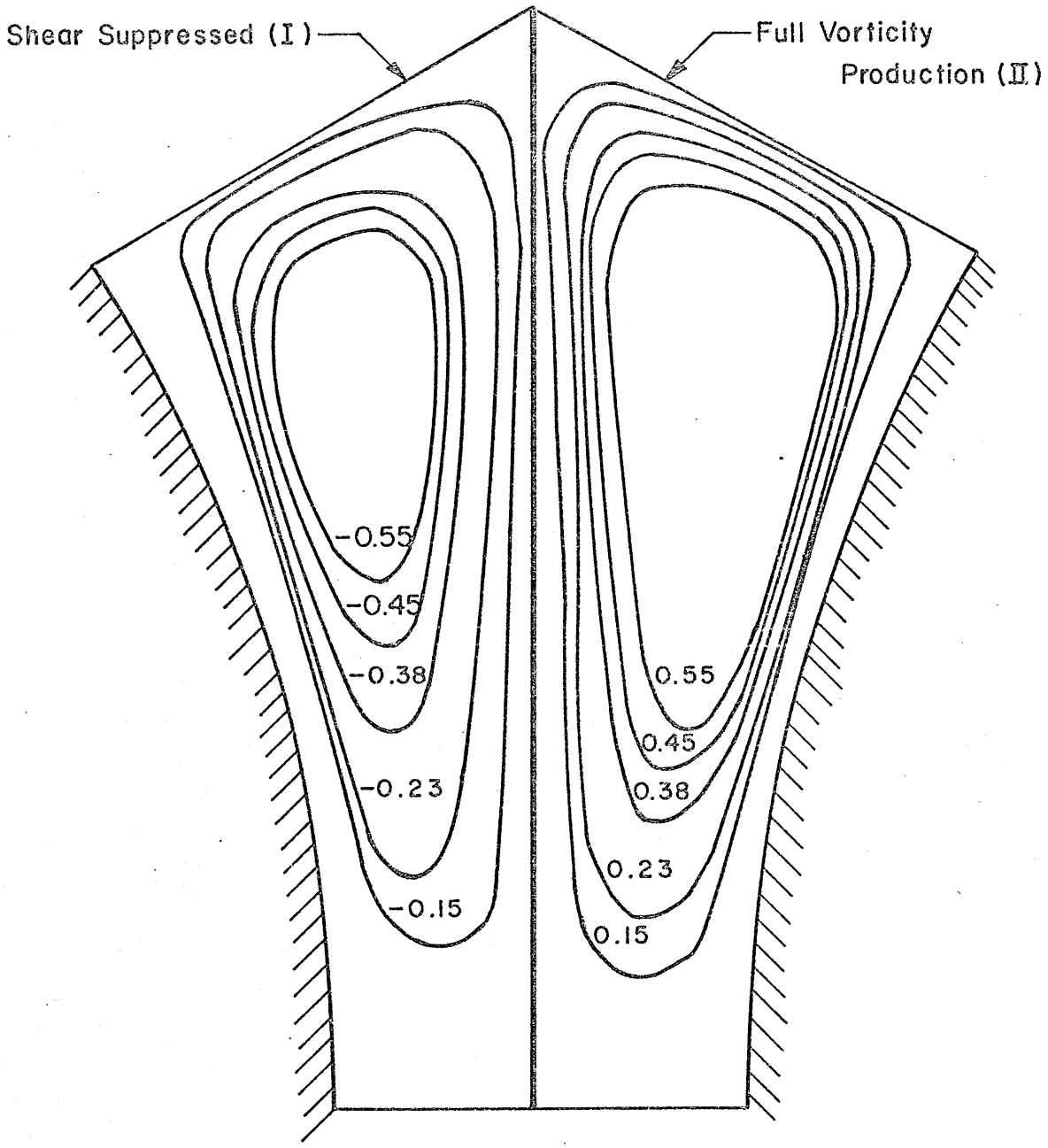

Note: Value Plotted are $\psi/(\psi_{MAX})_I$ where $(\psi_{MAX})_I$=0.02

Fig.12.9. Contour Plots of Predicted Stream Function Distribution, Re=27,000, P'/D=1.123.

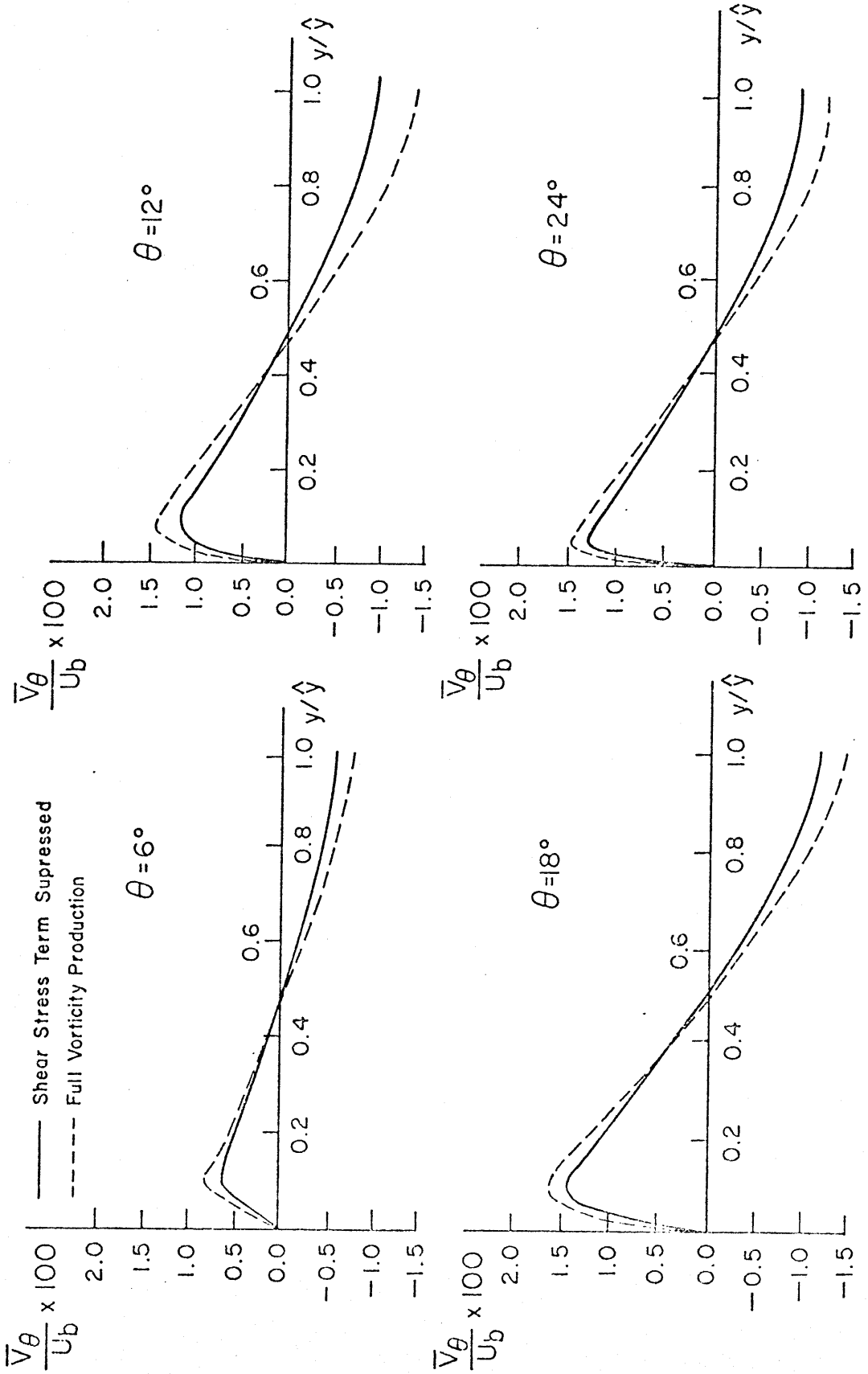

Fig. 12.10. Predicted Secondary Velocity Component $\overline{V}_\theta$, Re=27,000, P'/D=1.123.

Values Shown are $\overline{V}_\theta / U_b$ in Percent.

⊙ Center of Secondary Flow Cell

($\overline{V}_\theta = 0 = \overline{V}_r$)

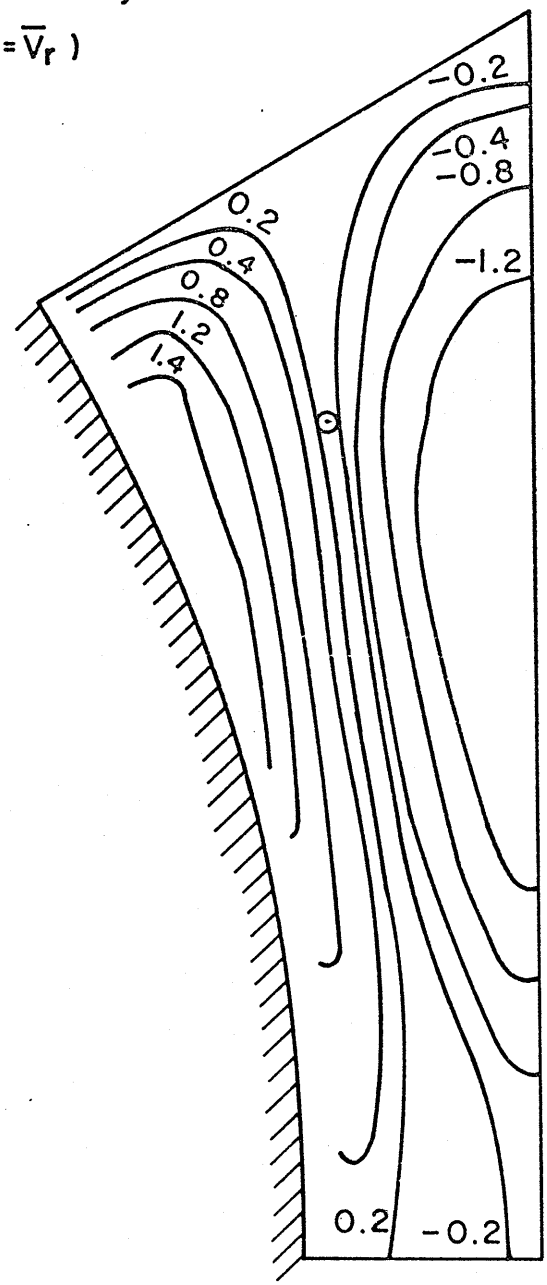

Fig. 12.11. Contour Plots of Predicted $\overline{V}_\theta$, Re = 27,000, P'/D = 1.123.

Values Shown are $\overline{V}_r / U_b$ Percent .

⊙ Center of Secondary Flow Cell ($\overline{V}_r = 0 = \overline{V}_\theta$)

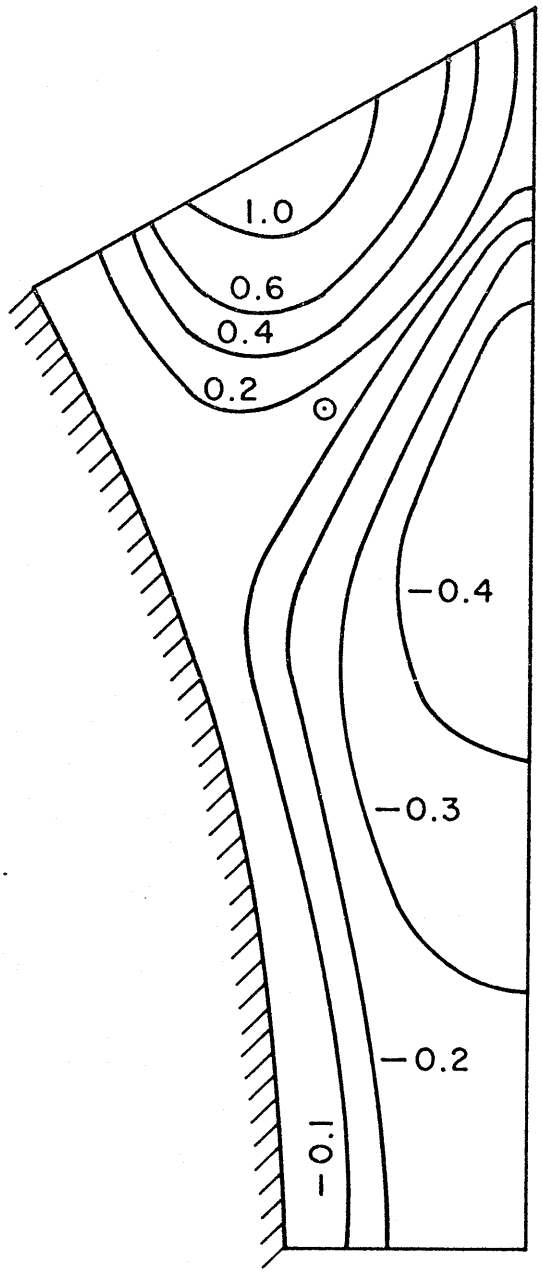

Fig. 12.12 . Contour Plots of Predicted $\overline{V}_r$, Re=27,000 , P'/D = 1.123 .

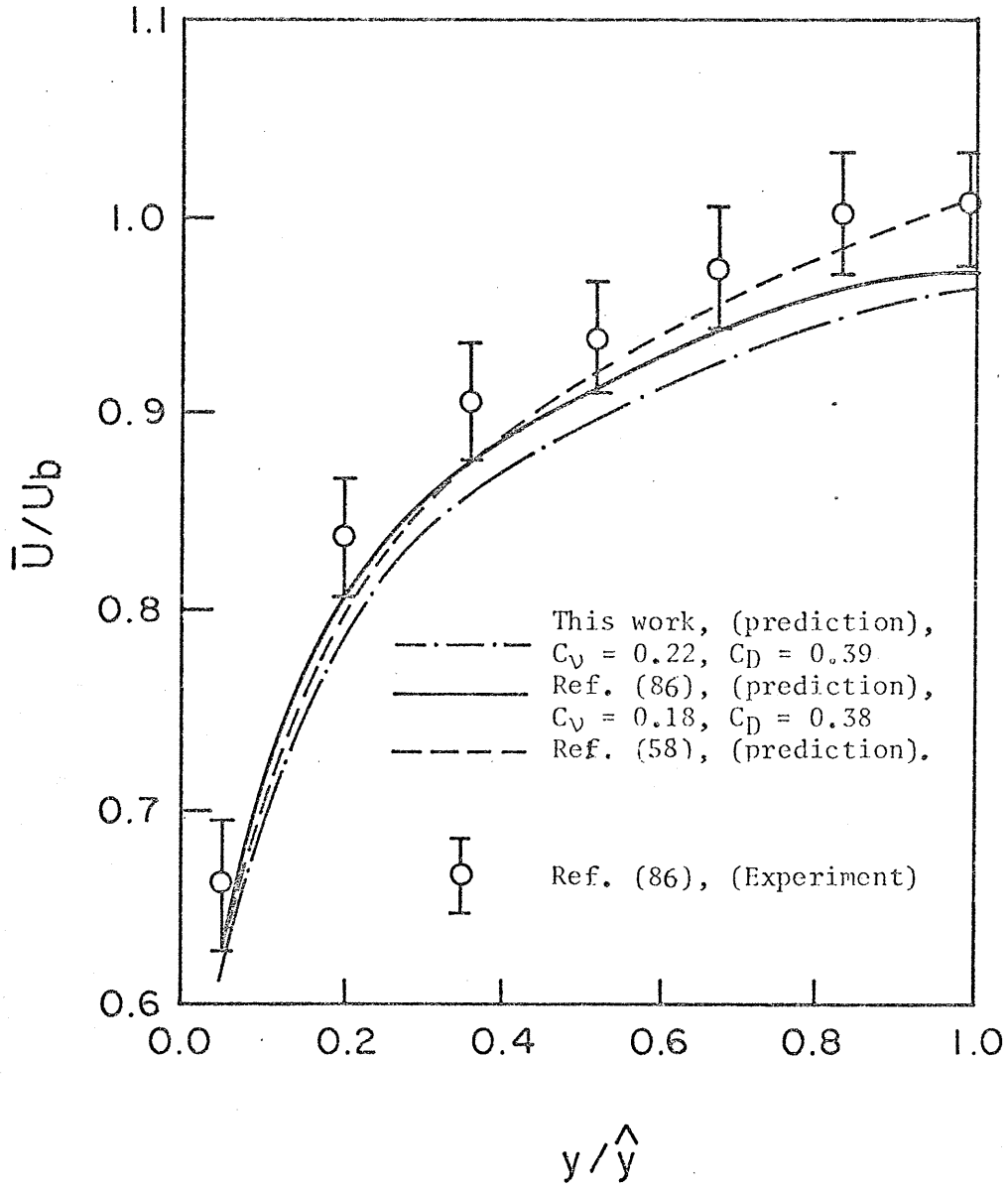

Fig. 12.13. Comparison of Predicted $\bar{U}$ with Previous Work, θ=0°, Re=27,000, P'/D=1.123.

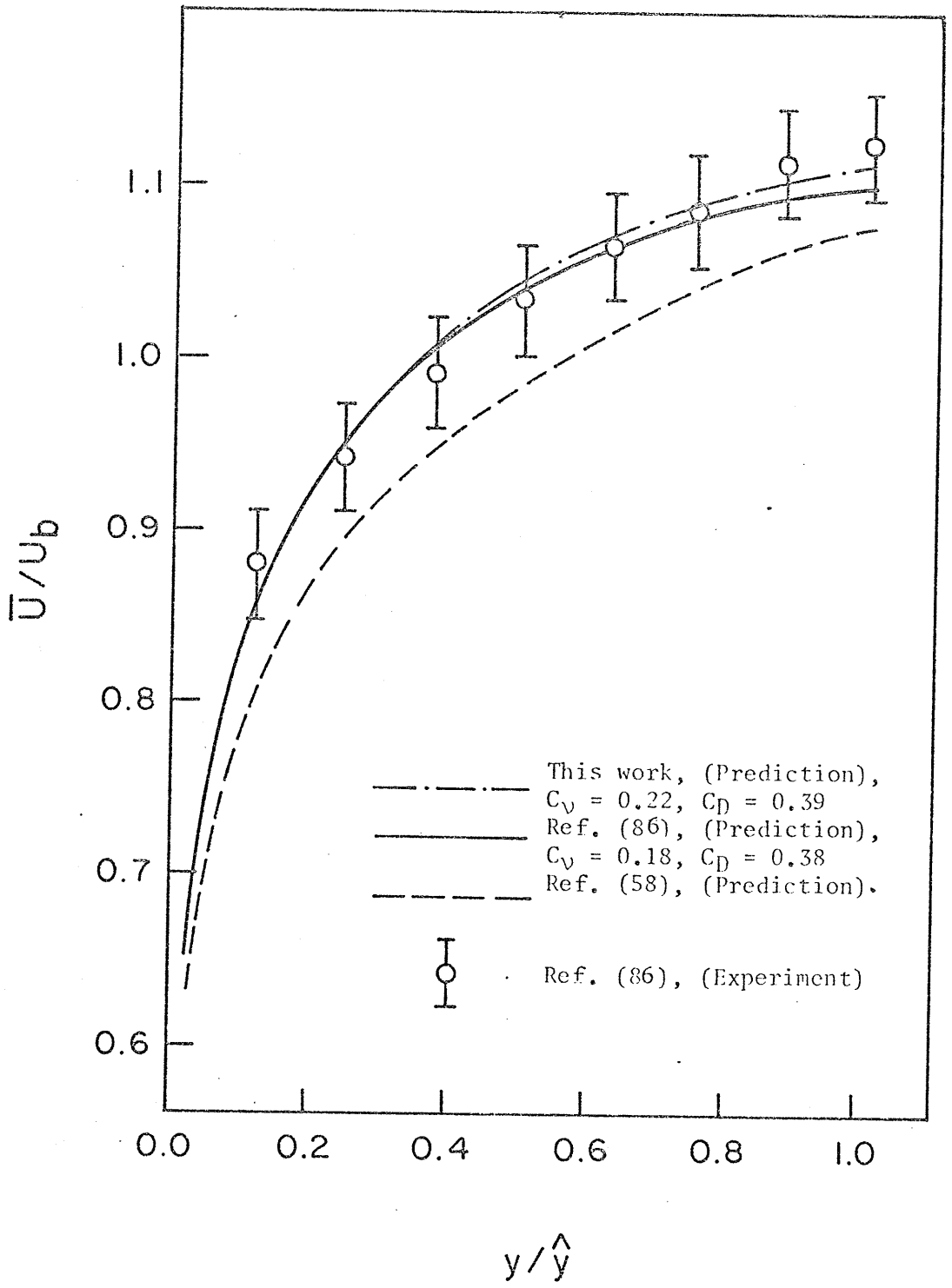

Fig. 12.14. Comparison of Predicted $\bar{U}$ with Previous Work
θ=15°, Re=27,000, P'/D=1.123.

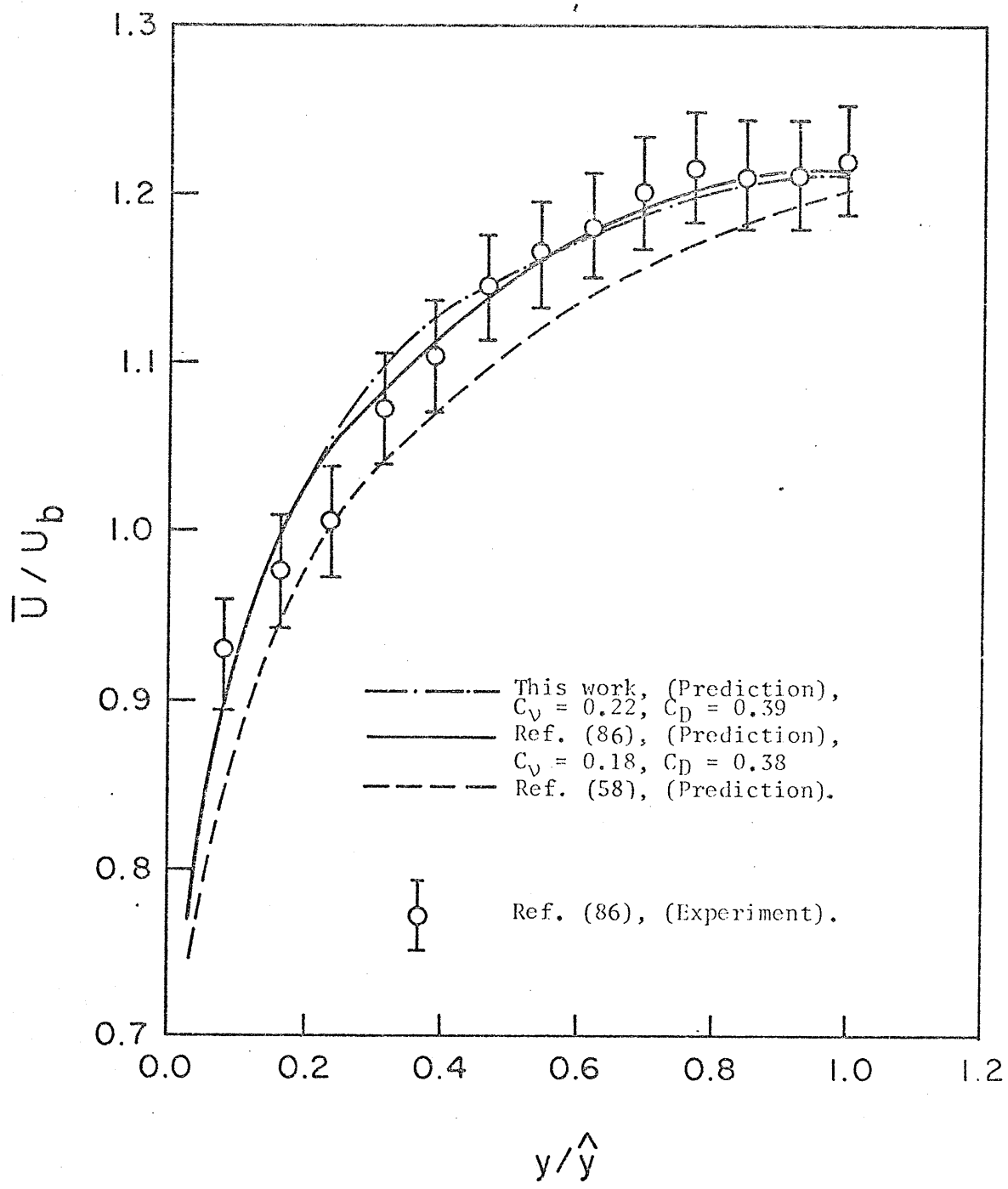

Fig.12.15 . Comparison of Predicted $\bar{U}$ with Previous Work , θ=30°, Re=27,000 , P'/D=1.123 .

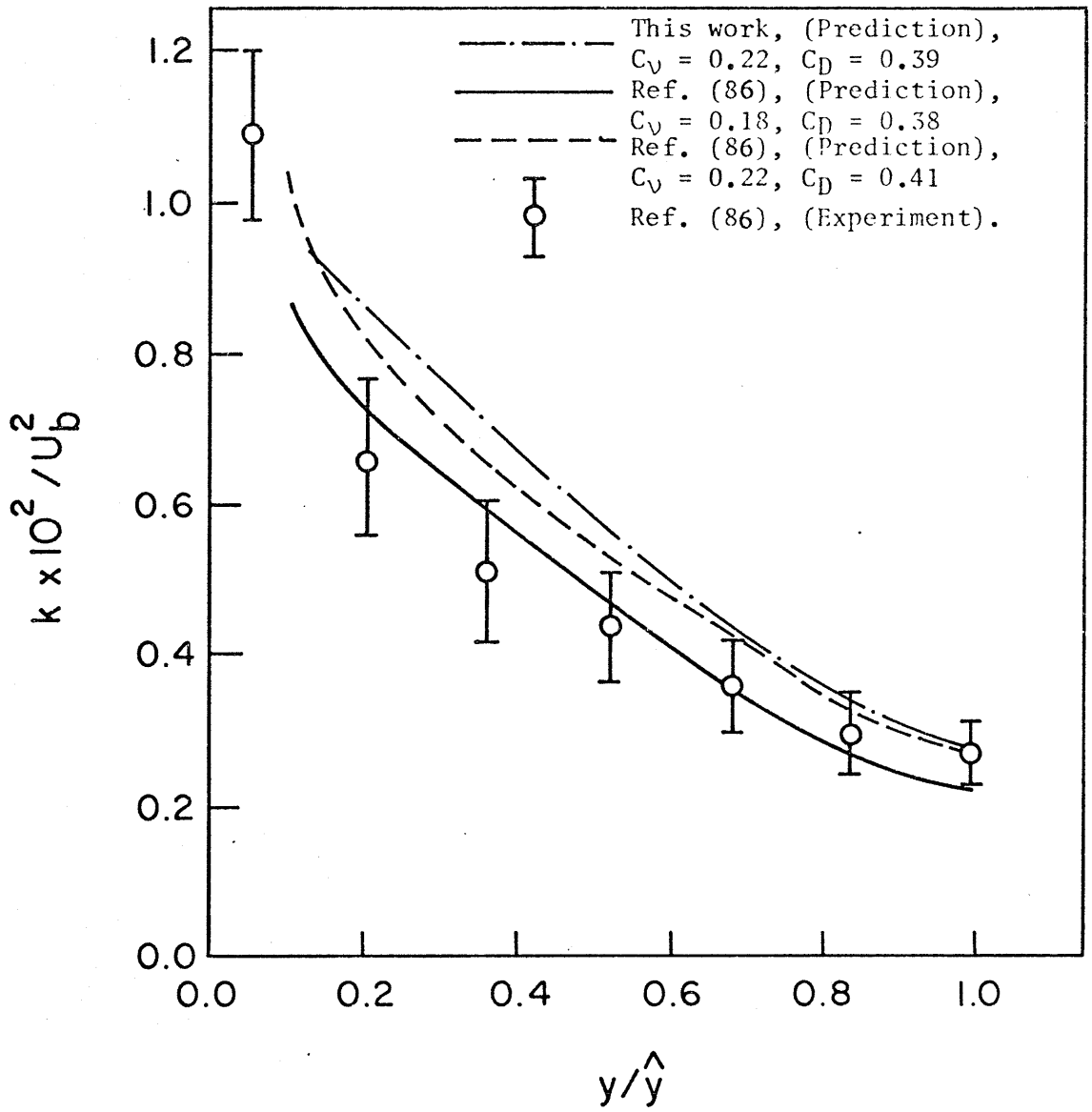

Fig.12.16. Comparison of Predicted k with Previous Work, θ=0°. Re=27,000, P'/D=1.123.

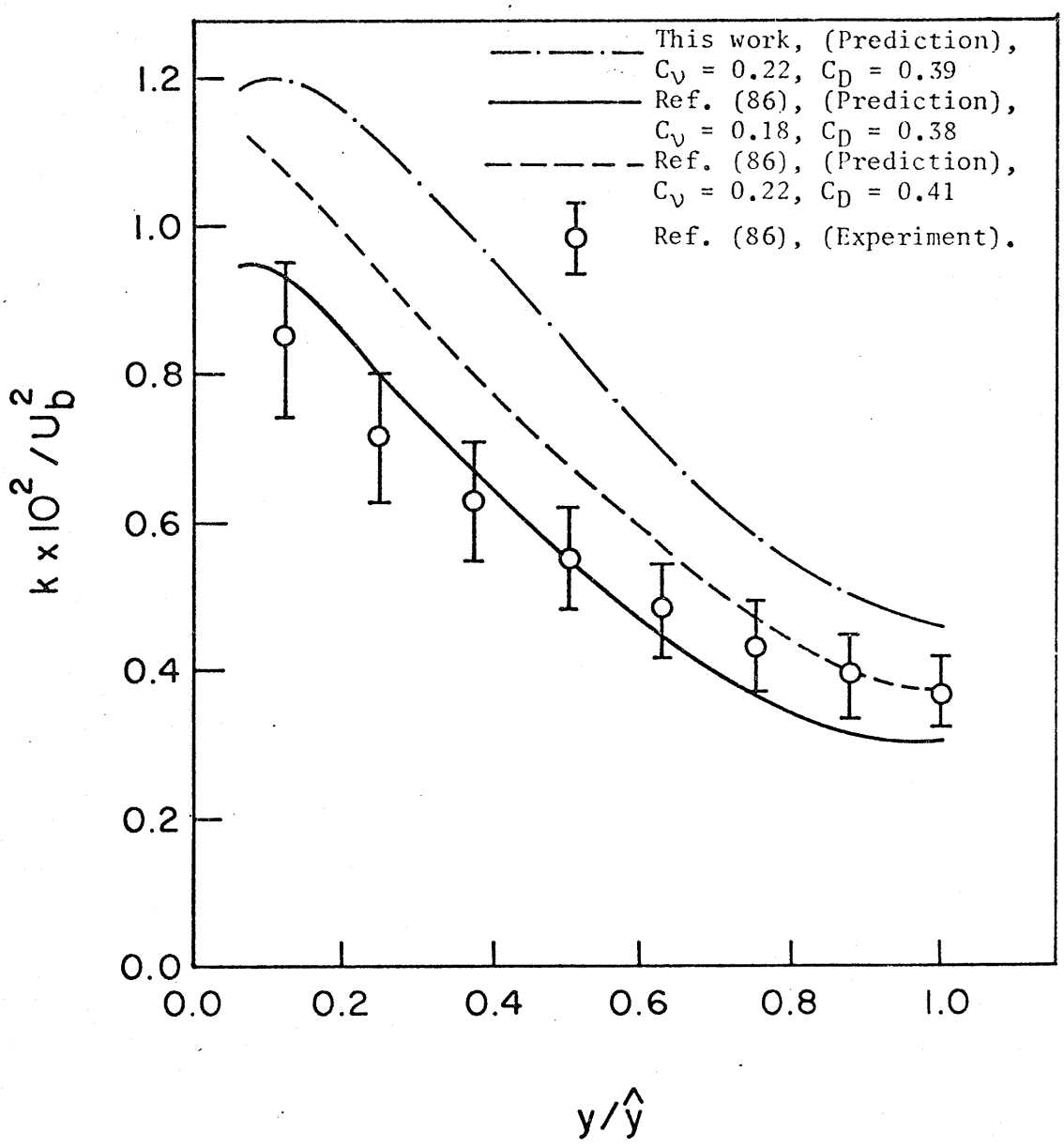

Fig. 12.17. Comparison of Predicted k with Previous Work, θ=15°. Re=27,000, P'/D=1.123.

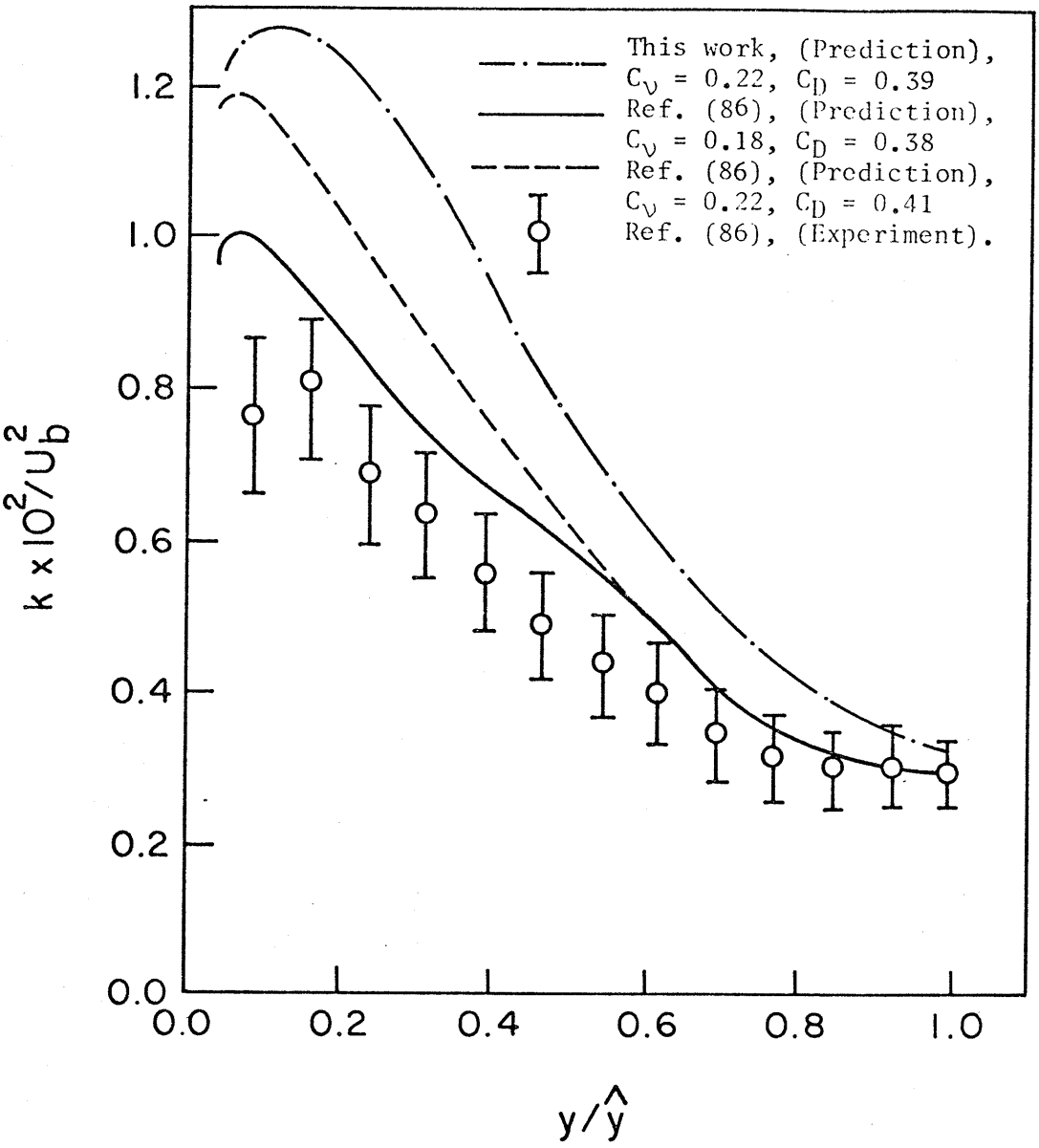

Fig. 12.18. Comparison of Predicted k with Previous Work, θ=30°
Re=27,000, P'/D=1.123 .

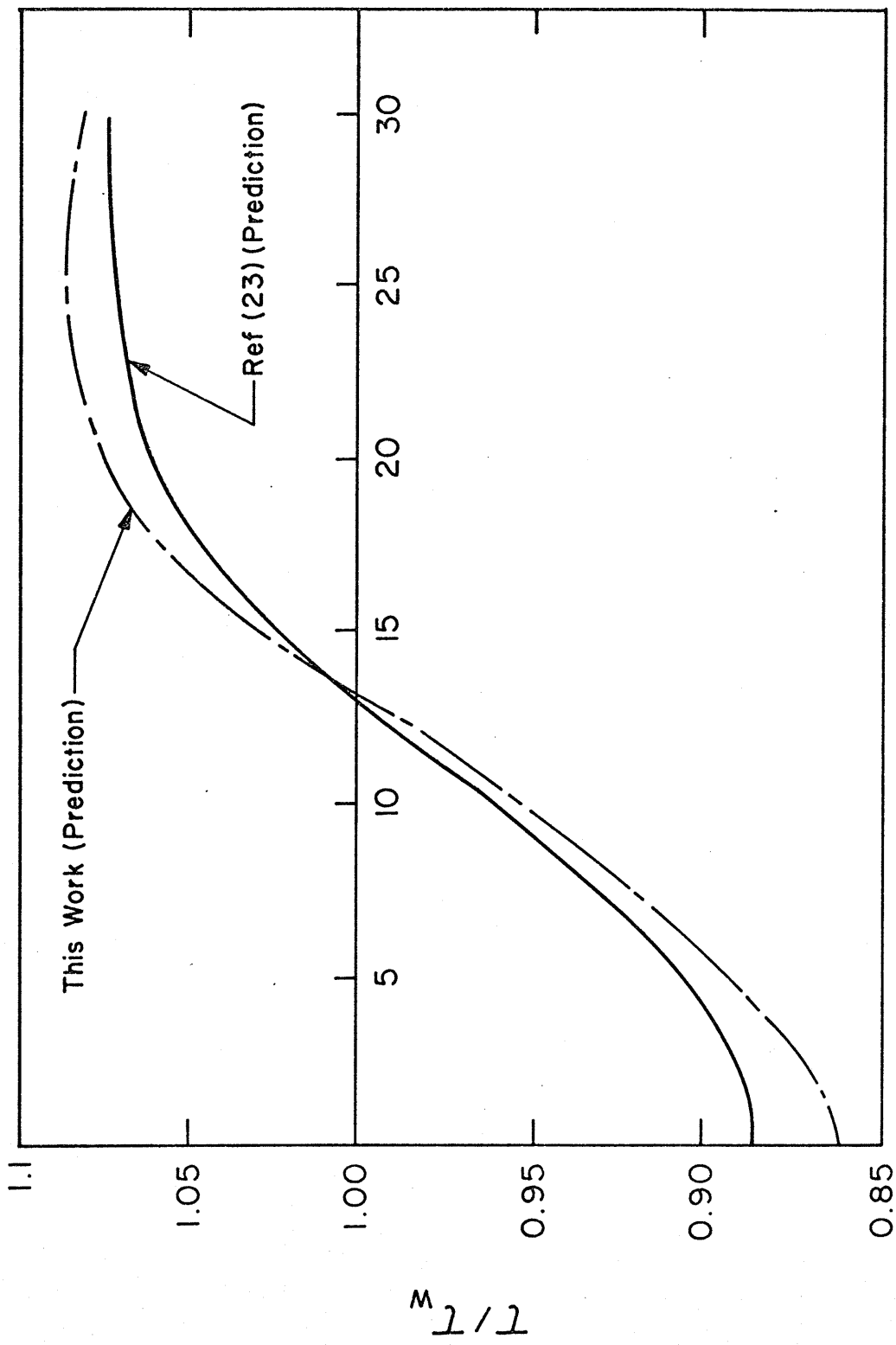

Fig. 12.19. Predicted Wall Shear Stress, Re = 27,000, P'/D = 1.123.

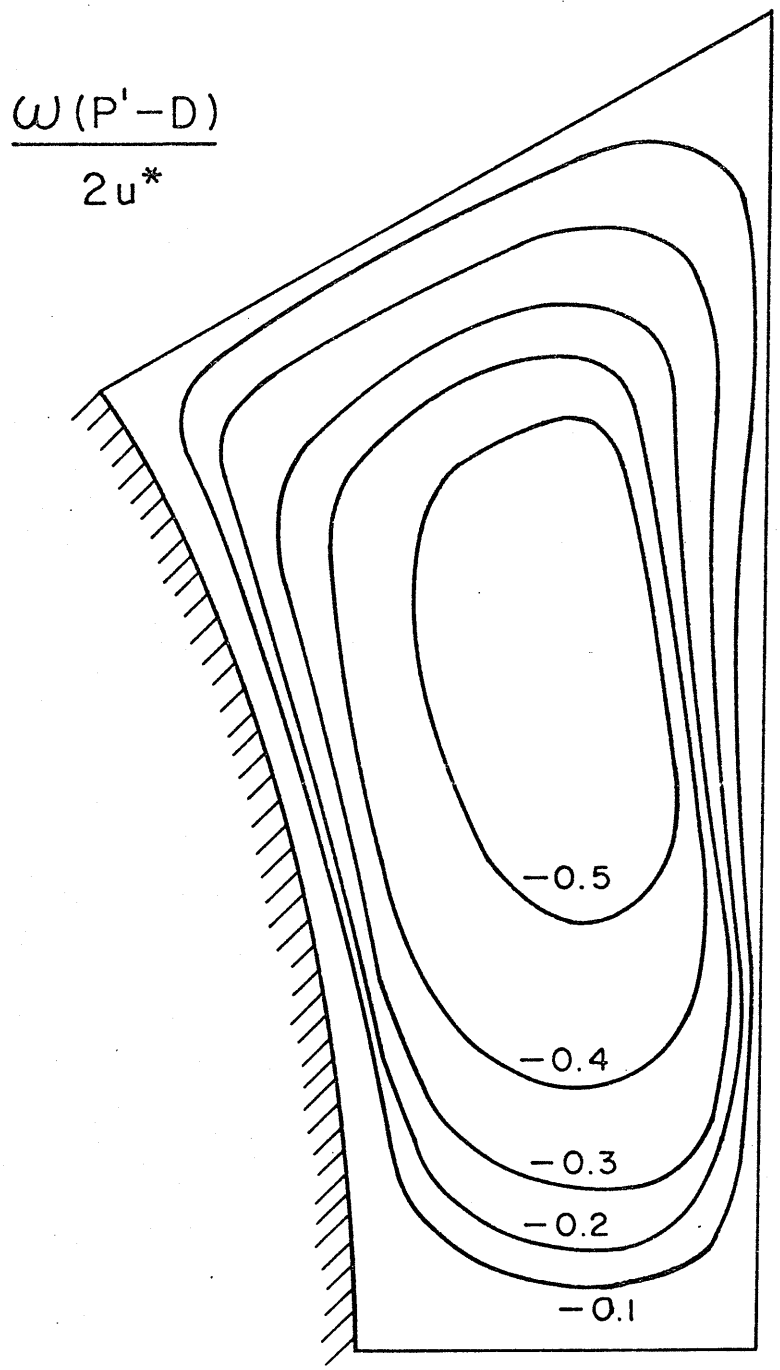

Fig. 12.20. Predicted Dimensionless Vorticity Distribution, Re=49,100, P'/D=1.2.

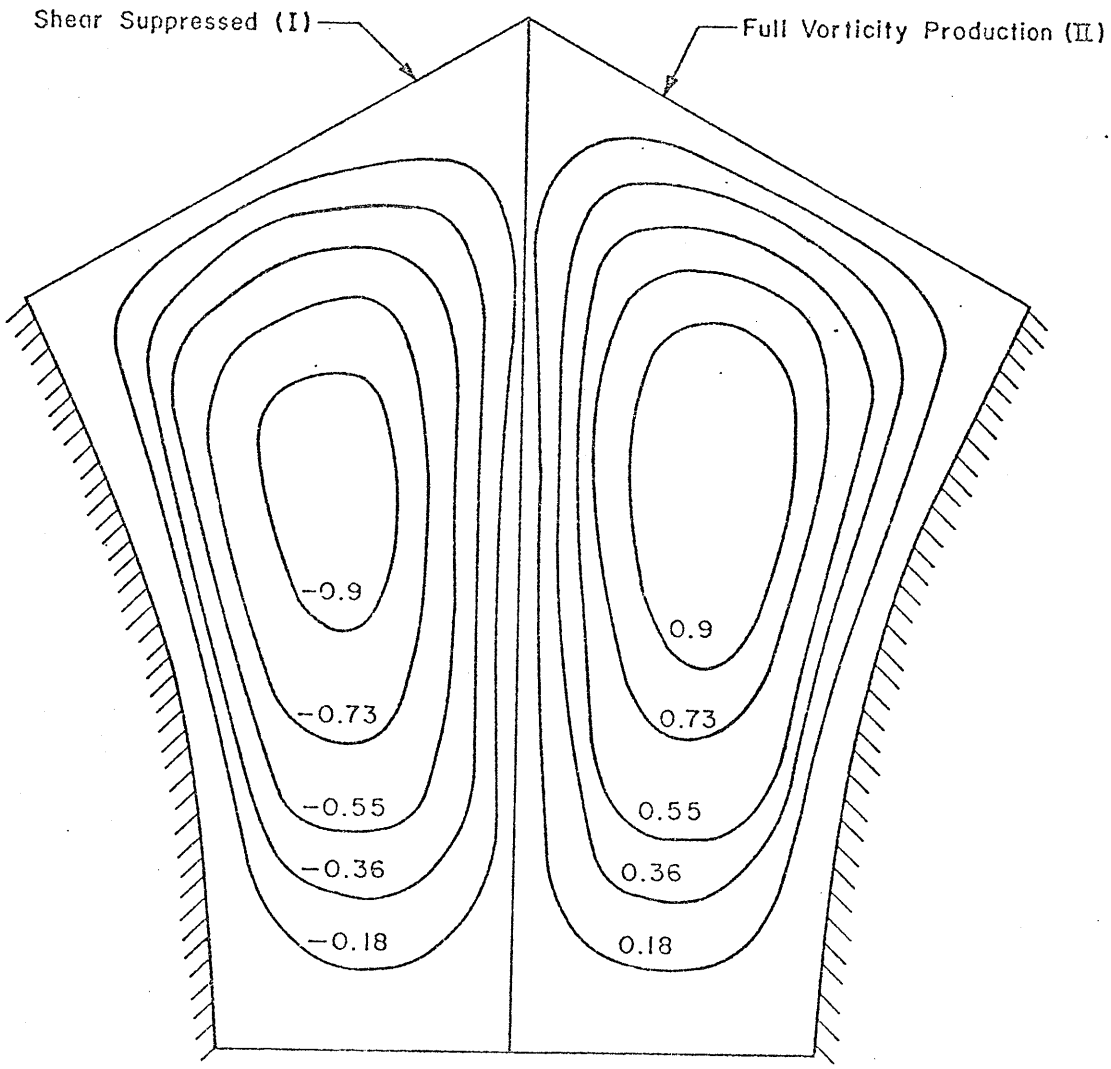

Note: Values Plotted are $\psi/(\psi_{MAX.})_I$ where $(\psi_{MAX.})_I = 0.014$

Fig. 12.21: Contour Plots of Predicted Stream Function Distribution, Re=49,100, P'/D=1.2.

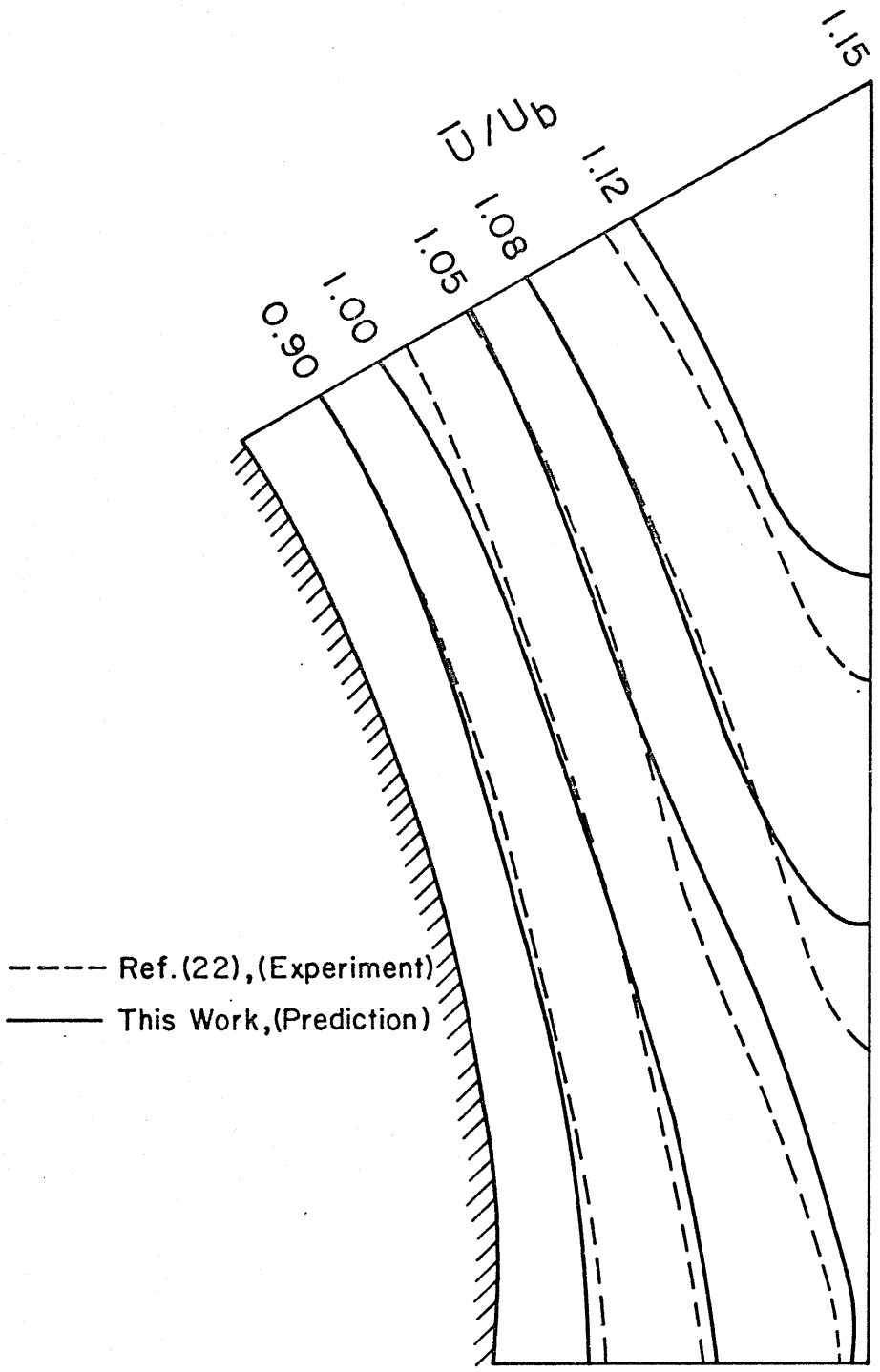

Fig. 12.22. Comparison of Predicted $\bar{U}$ Contours with Experimental Work, Re = 49,100, P'/D = 1.2.

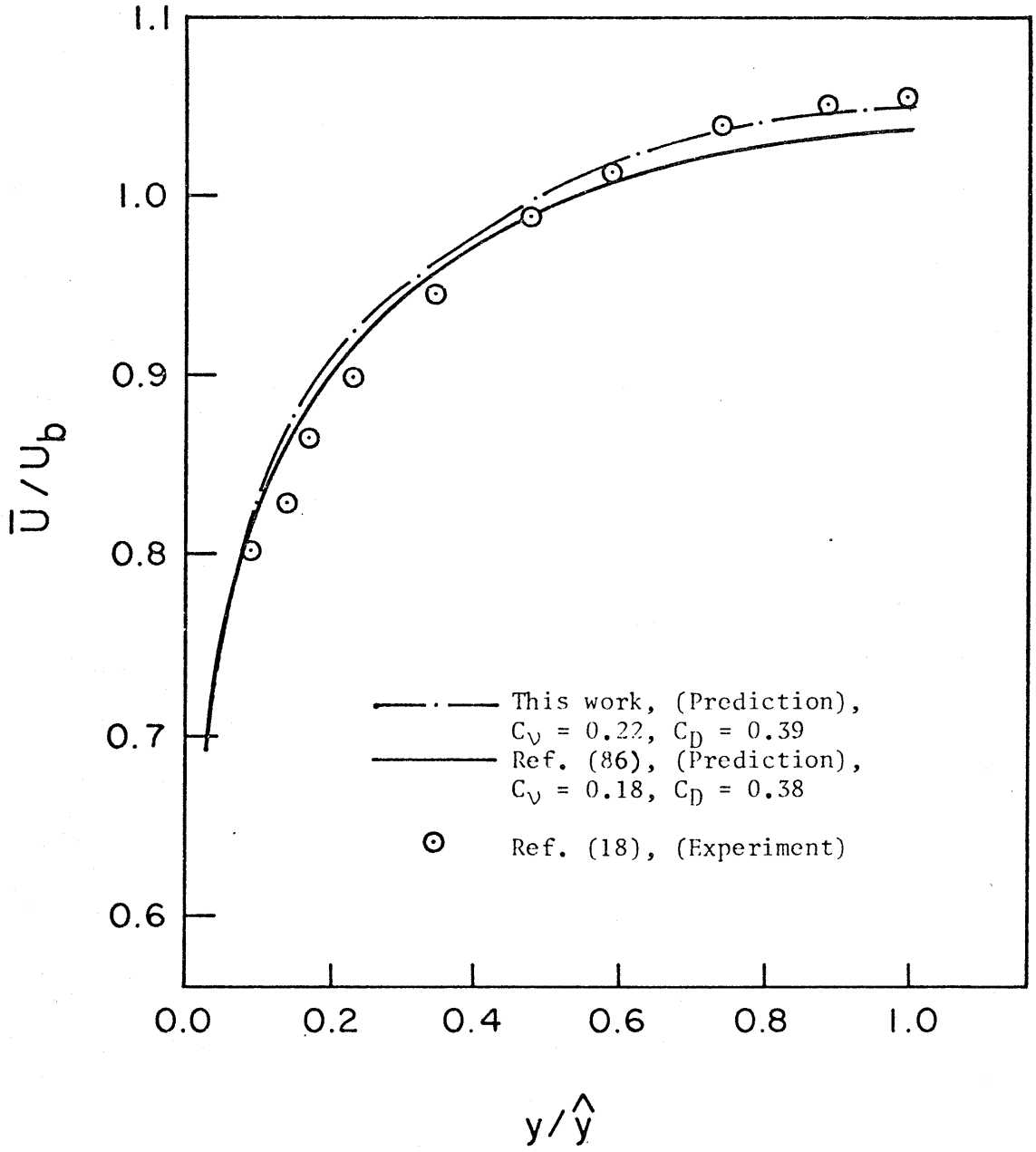

Fig. 12. 23 . Comparison of Predicted $\bar{U}$ with Previous Work , θ=0°, Re=149,000 , P'/D=1.217.

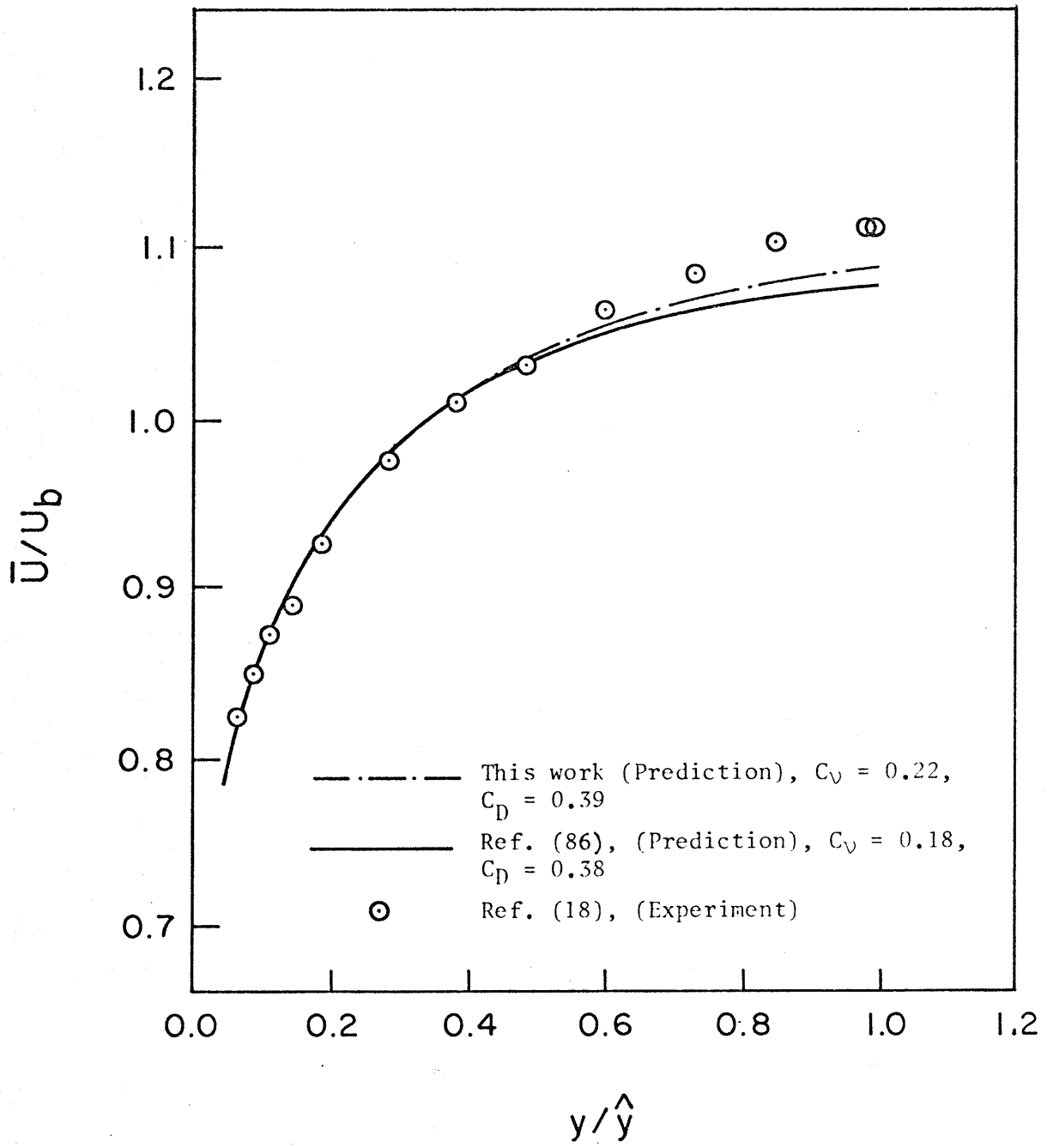

Fig. 12.24. Comparison of Predicted $\bar{U}$ with Previous Work, θ=15°, Re=149,000, P'/D=1.217.

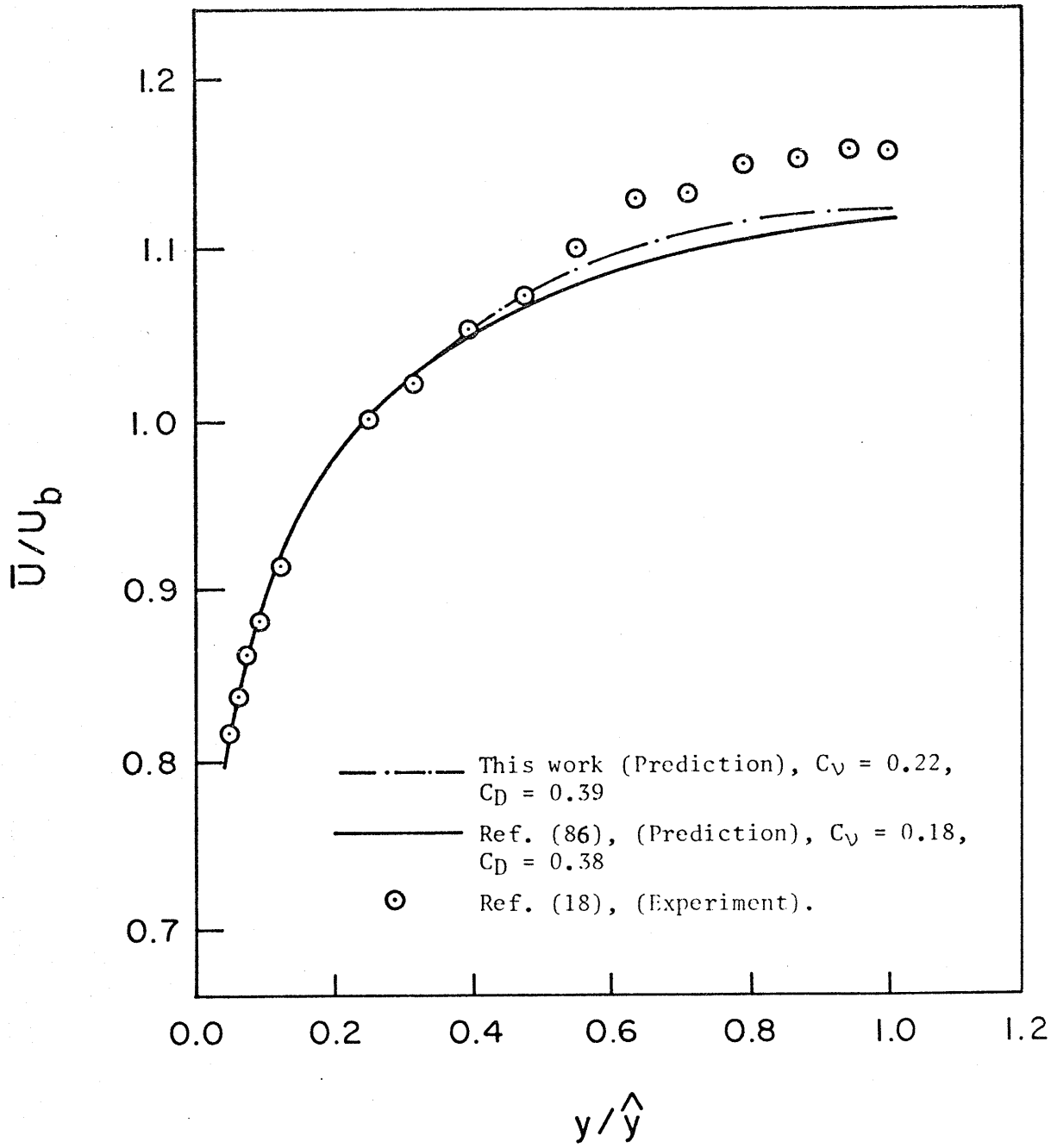

Fig. 12.25. Comparison of Predicted $\bar{U}$ with Previous Work, θ=30°, Re=149,000, P'/D=1.217.

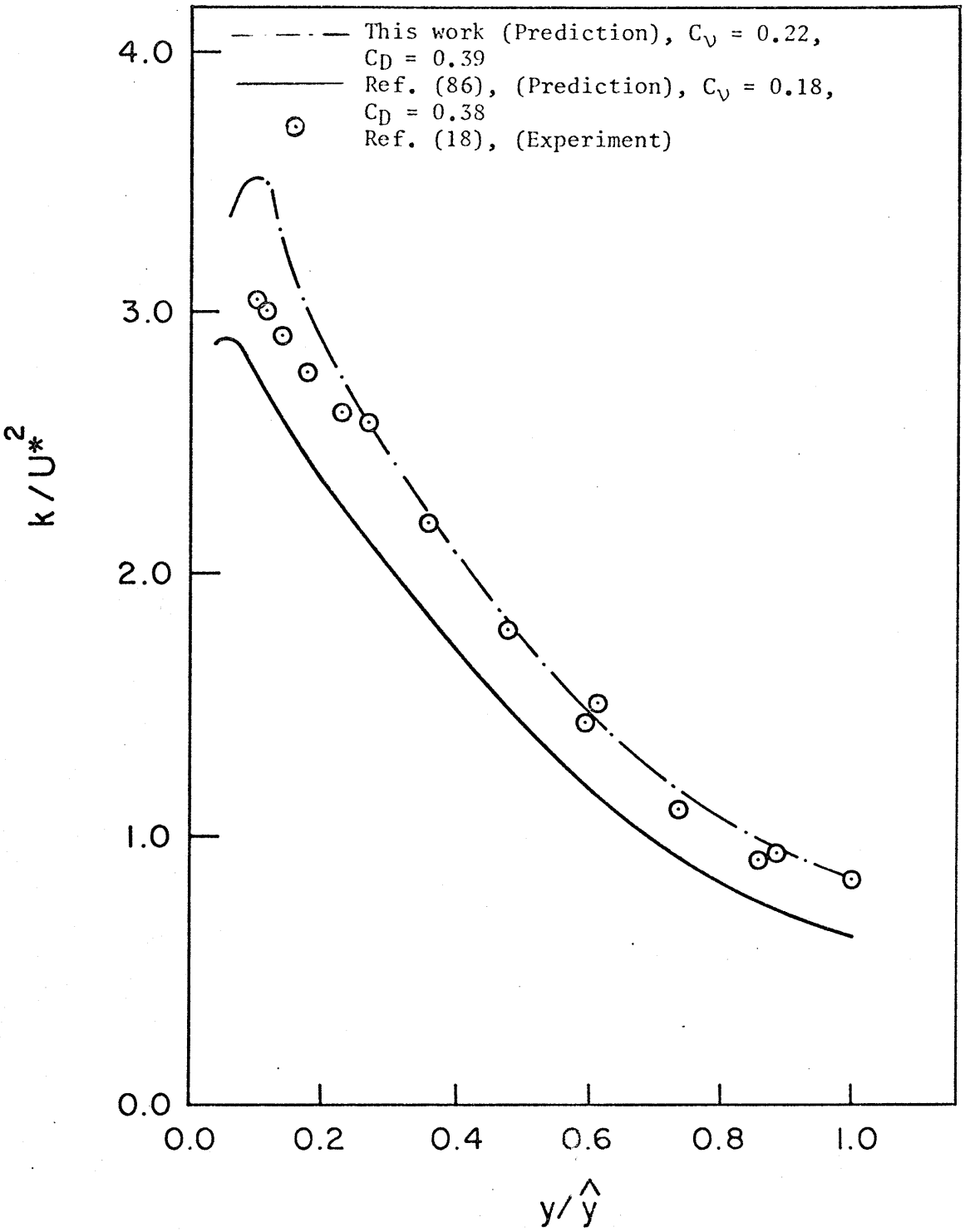

Fig. 12.26. Comparison of Predicted k with Previous Work, θ=0°, Re=149,000, P'/D=1.217.

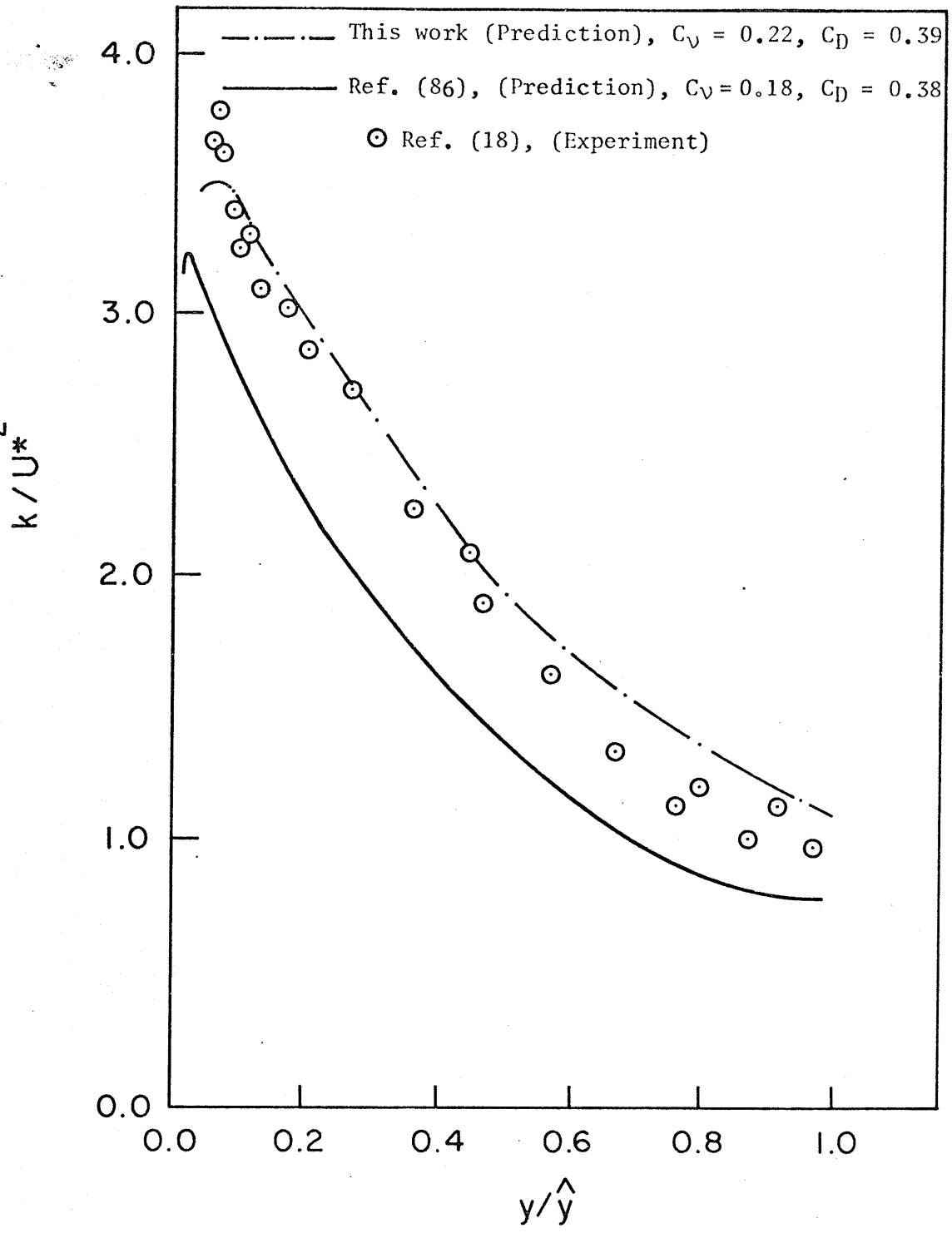

Fig.12.27. Comparison of Predicted k with Previous Work, θ=18°, Re=149,000, P'/D=1.217.

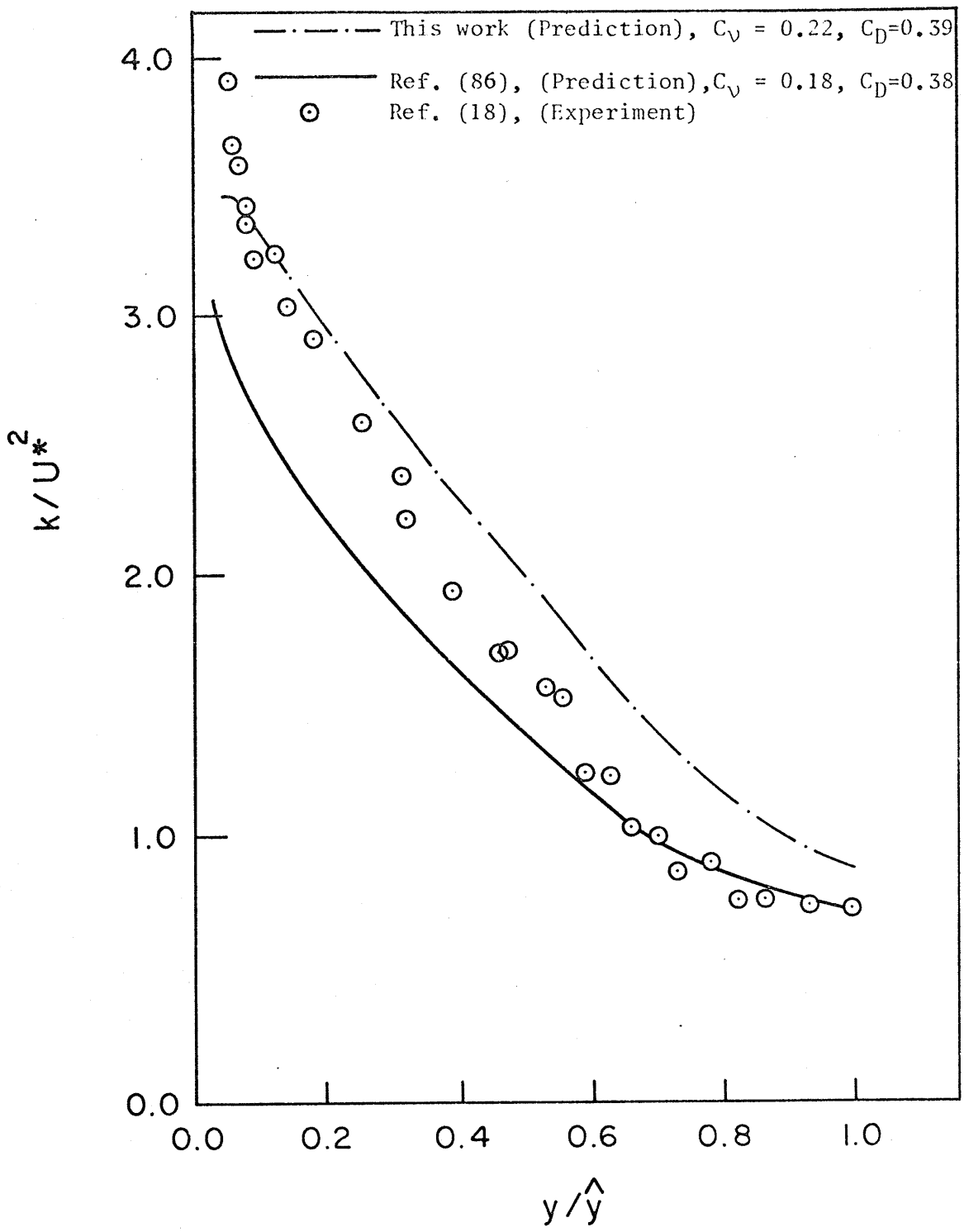

Fig.12.28. Comparison of Predicted k with Previous Work, θ=30°, Re=149,000, P'/D=1.217.

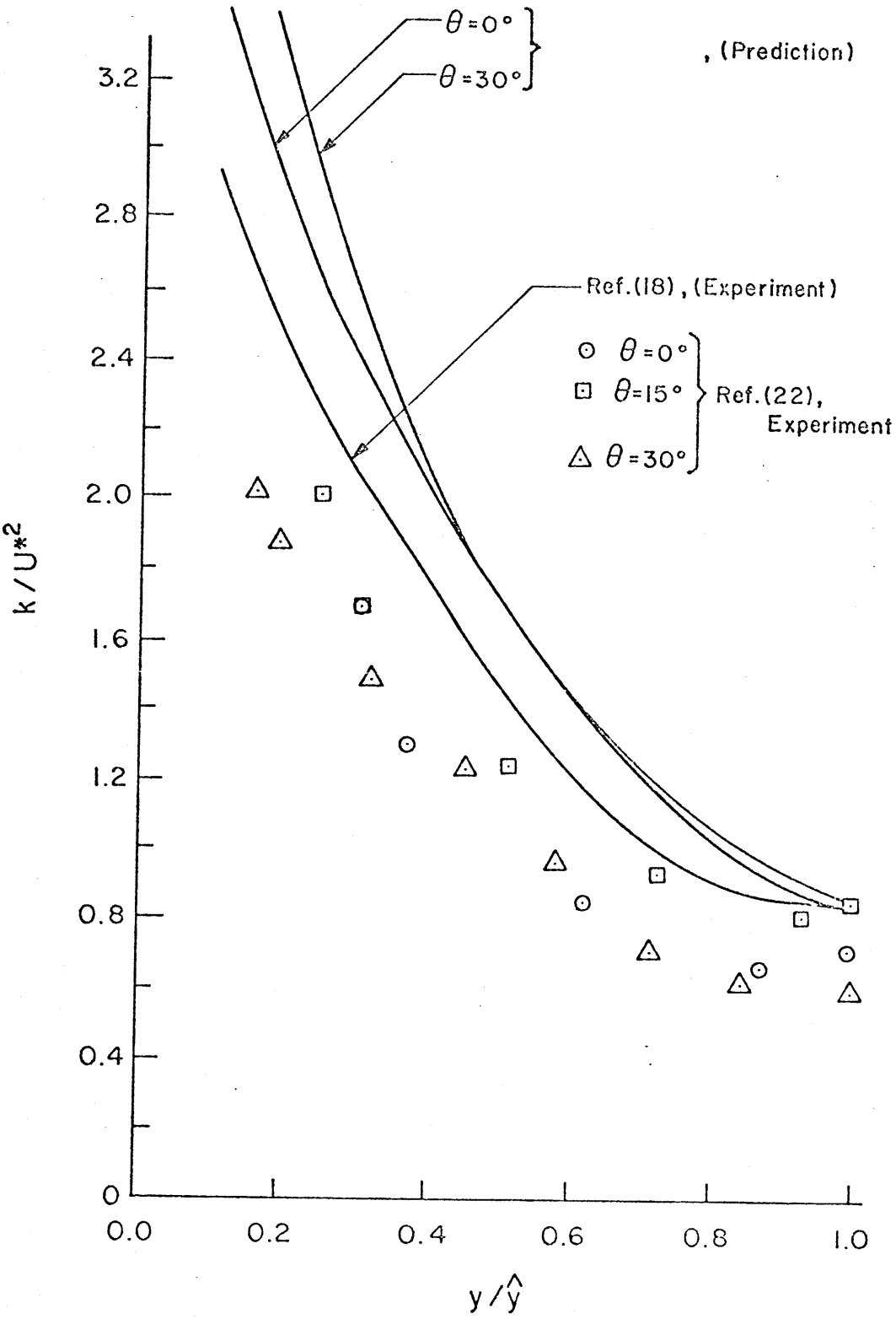

Fig.12.29. Comparison of Predicted k with Experimental Work, Re=49,100 , P'/D=1.2

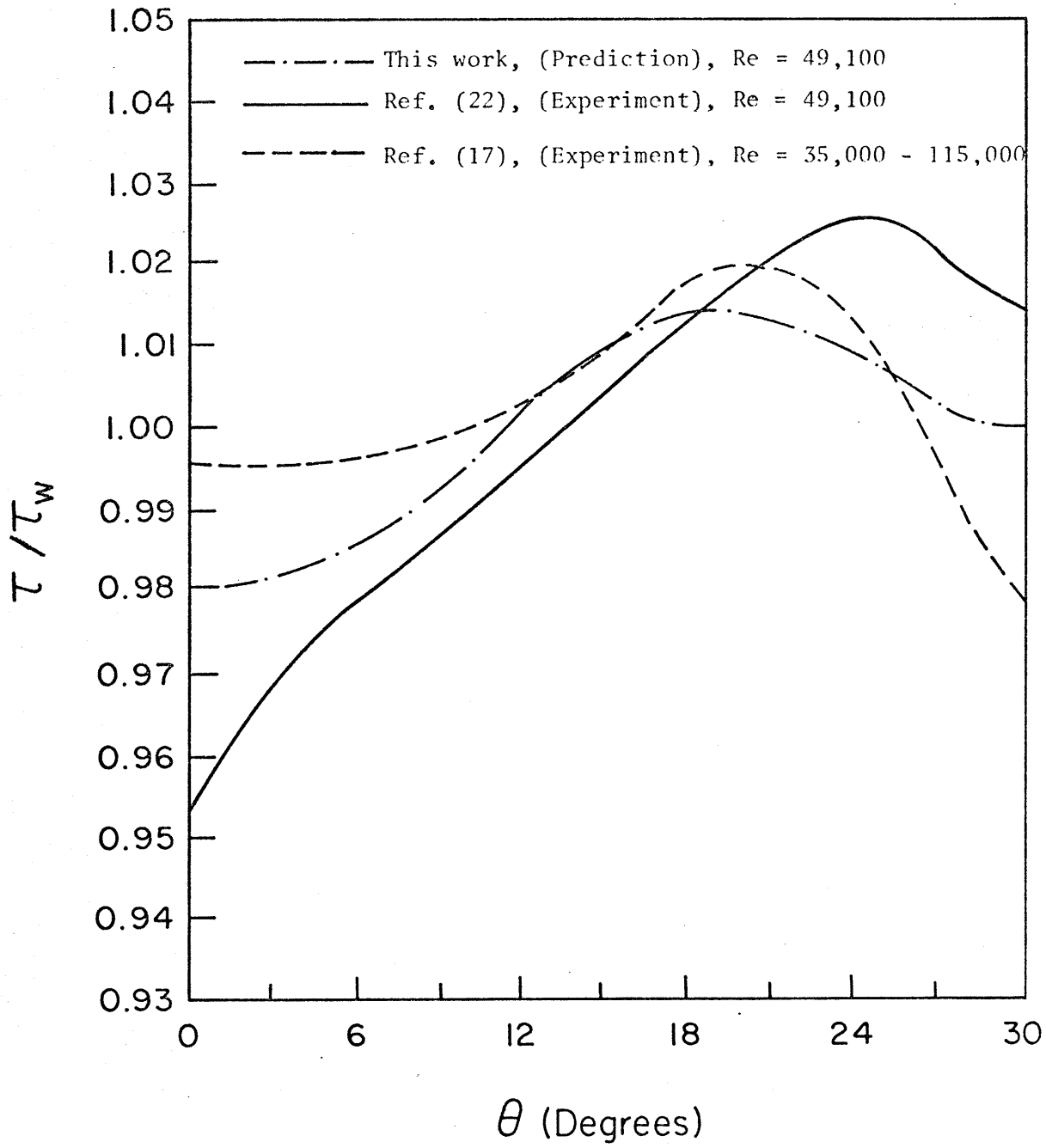

Fig. 12.30. Comparison of Predicted τ Distribution with Experimental Work, $P'/D = 1.2$.

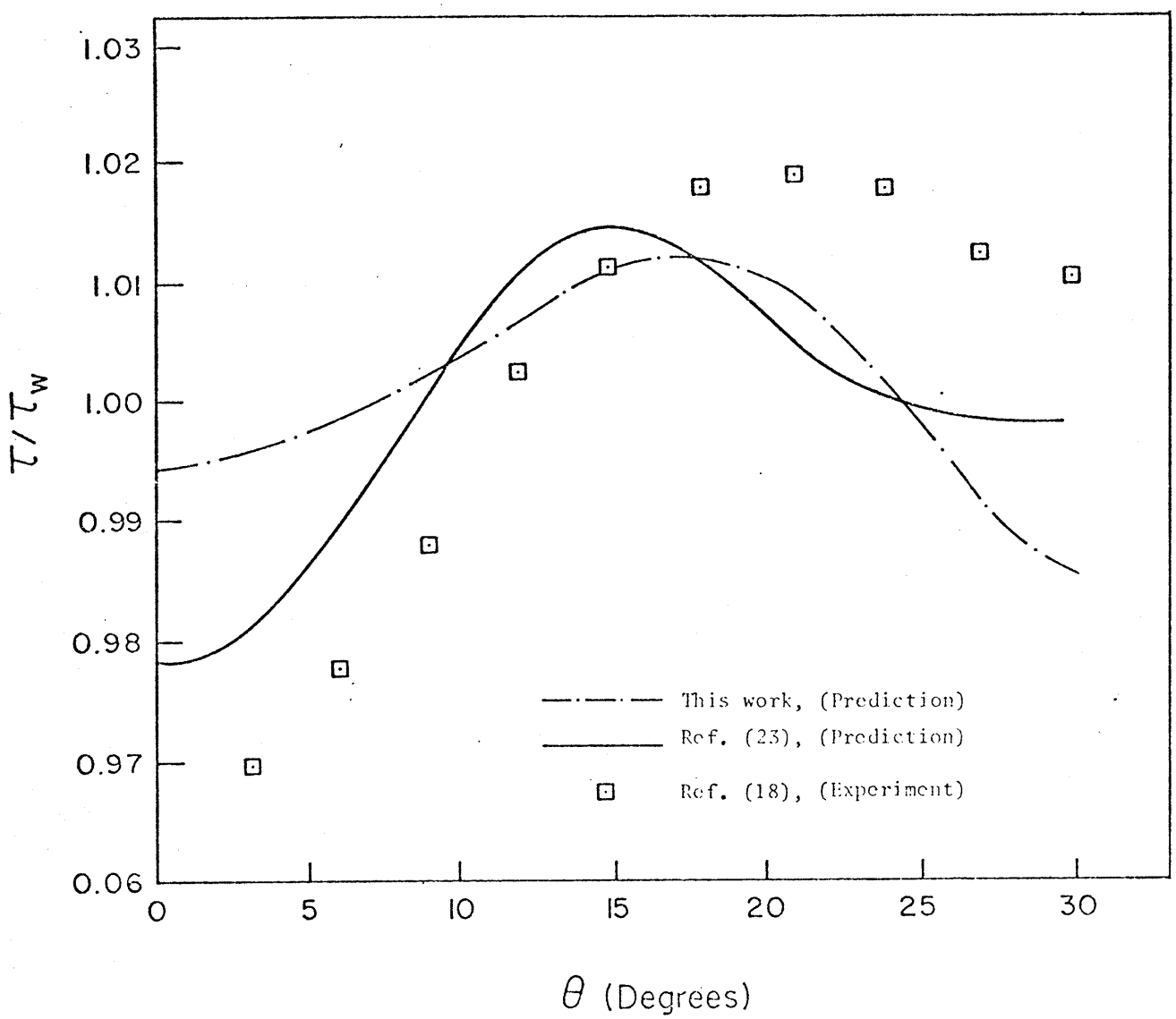

Fig. 12.31. Comparison of Predicted τ Distribution with Previous Work, Re=270,000, P'/D=1.217.

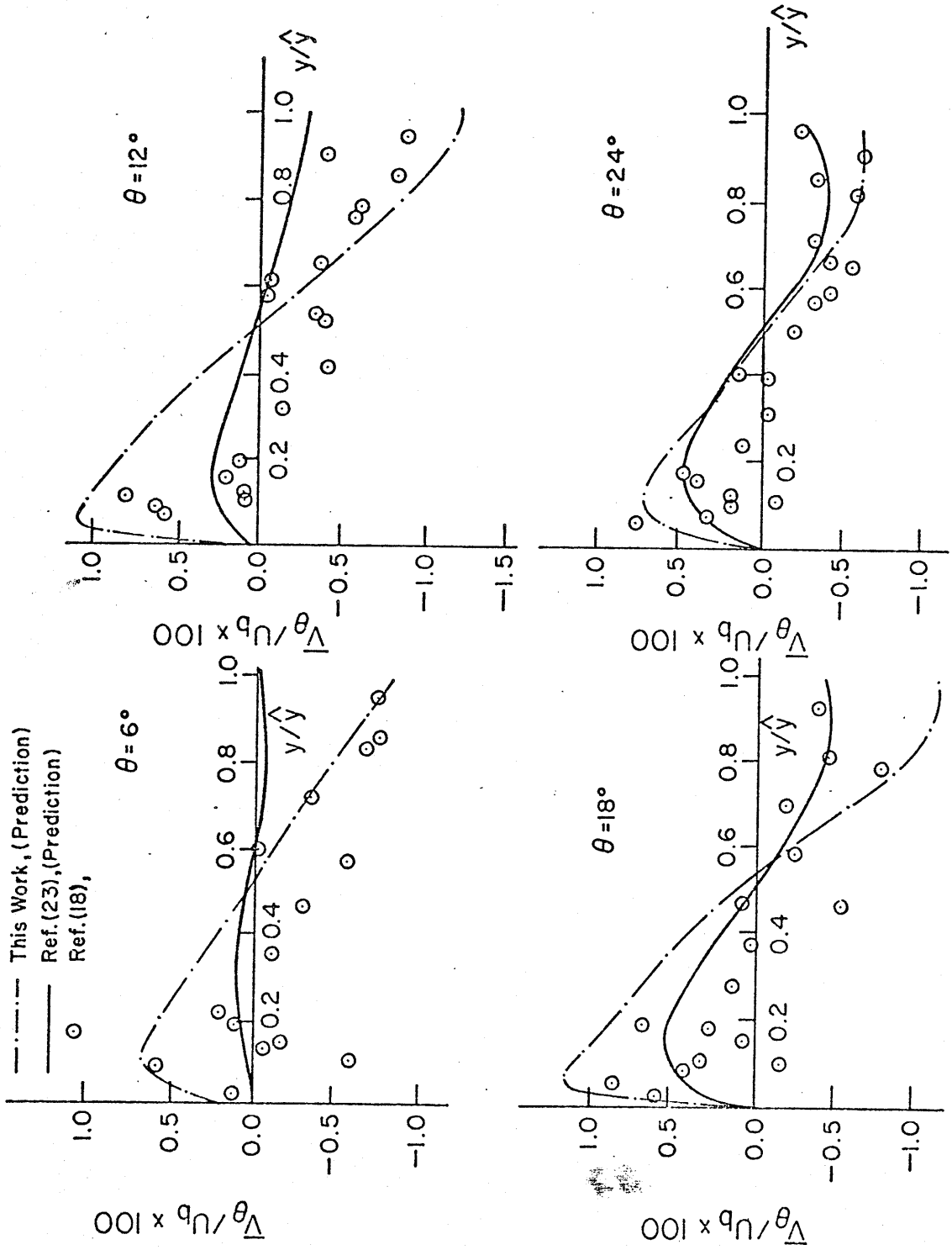

Fig. 12.32. Comparison of Predicted Secondary Velocity Component $\overline{V}_\theta$ with Previous Work, Re=149,000, P'/D=1.217.

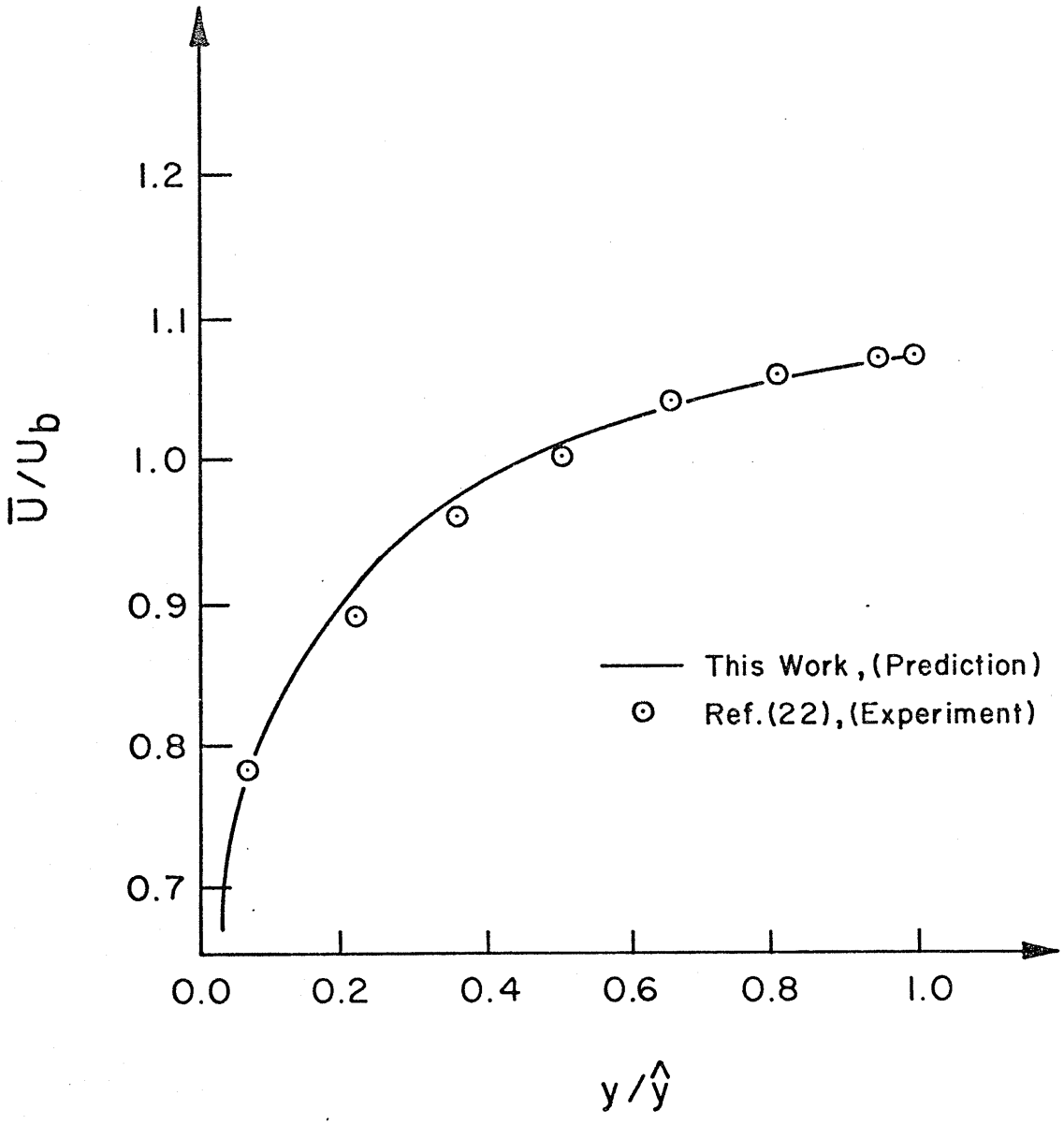

Fig.12.33. Comparison of Predicted $\bar{U}$ with Experiment, $\theta = 0°$, Re = 48,130 and $P'/D = 1.35$.

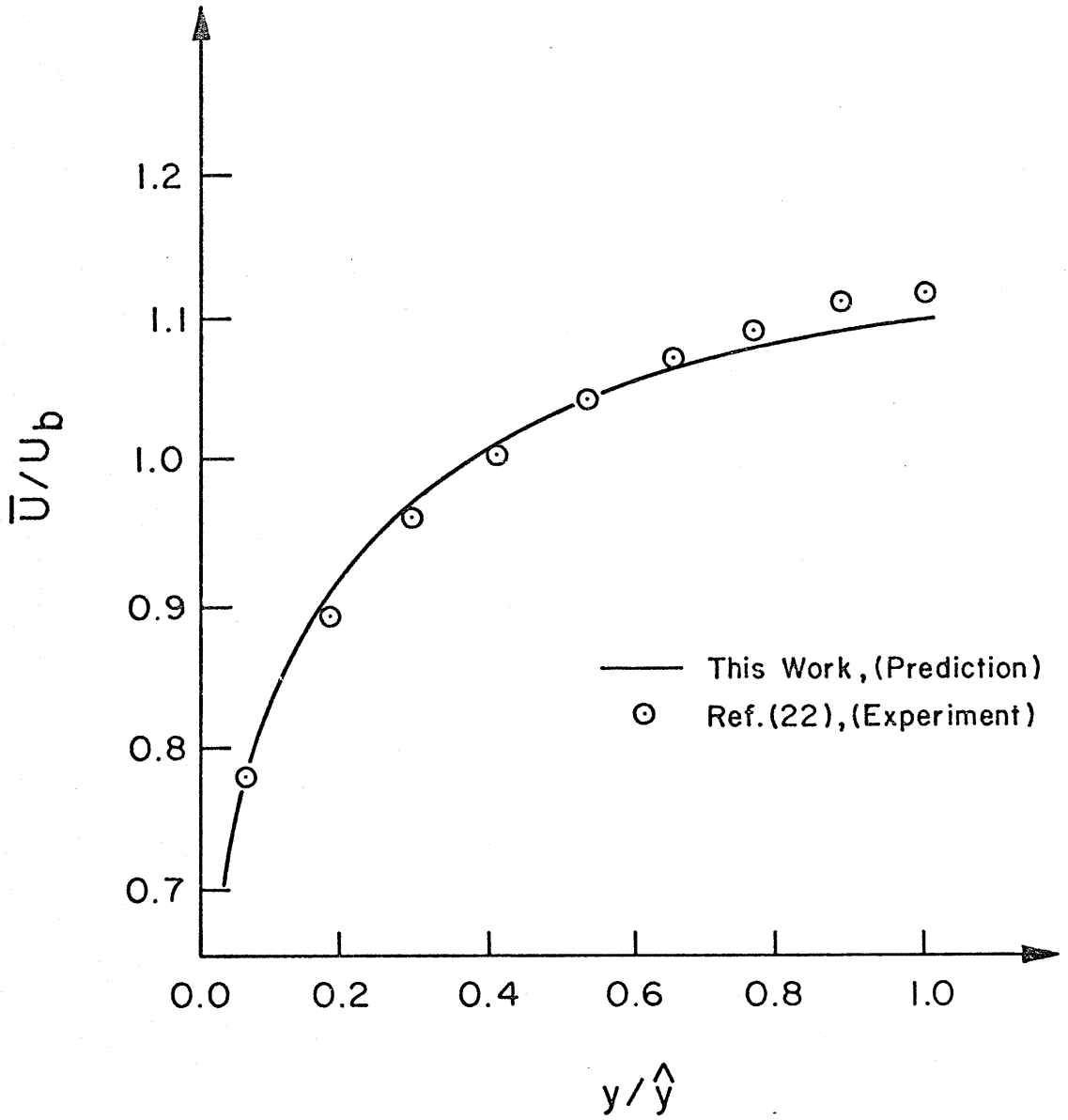

Fig. 12.34. Comparison of Predicted $\bar{U}$ with Experiment, $\theta = 18°$, Re = 48,130 and $P'/D = 1.35$.

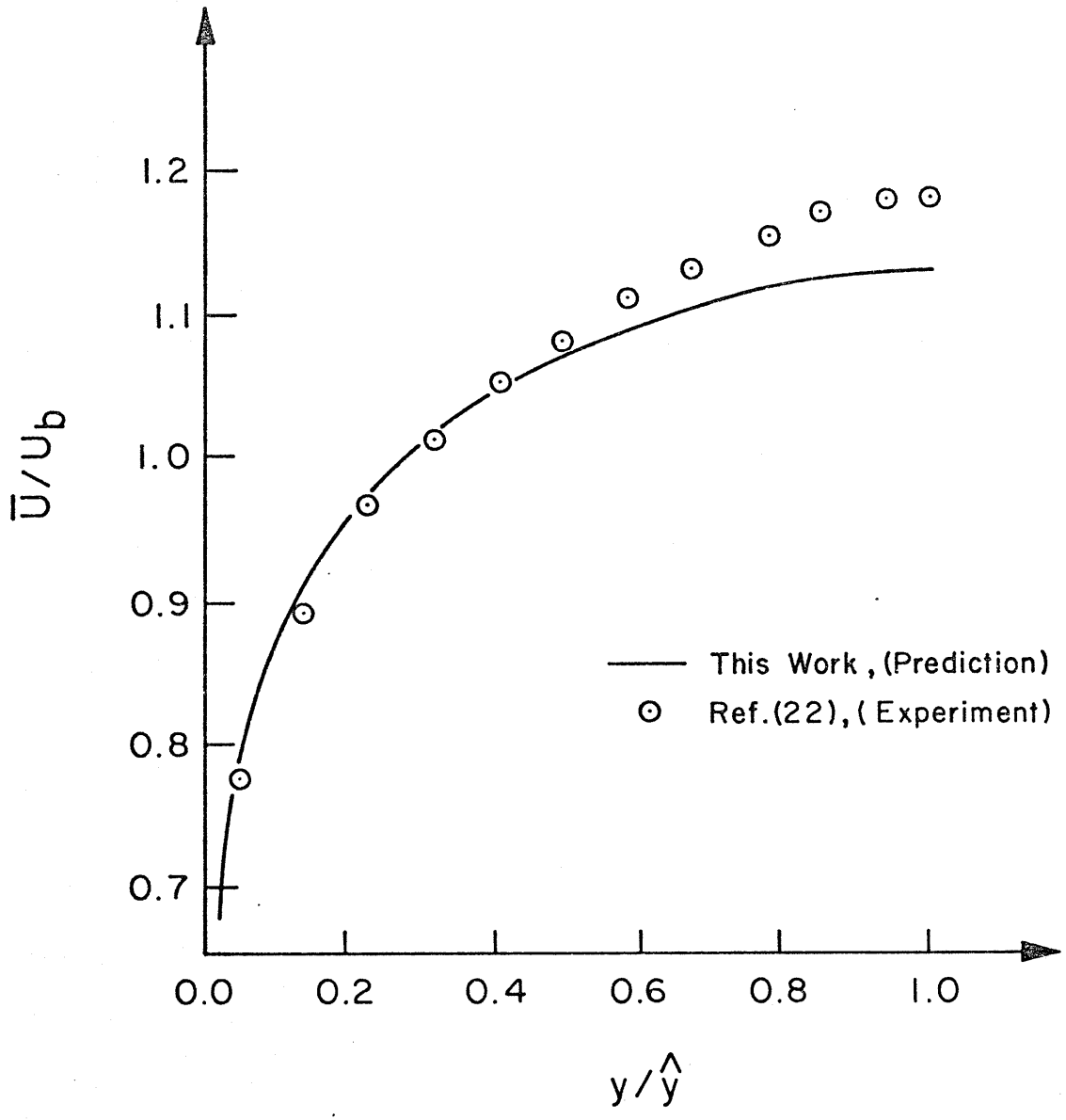

Fig. 12.35. Comparison of Predicted $\bar{U}$ with Experiment, $\theta = 30°$, Re = 48,130 and $P'/D = 1.35$.

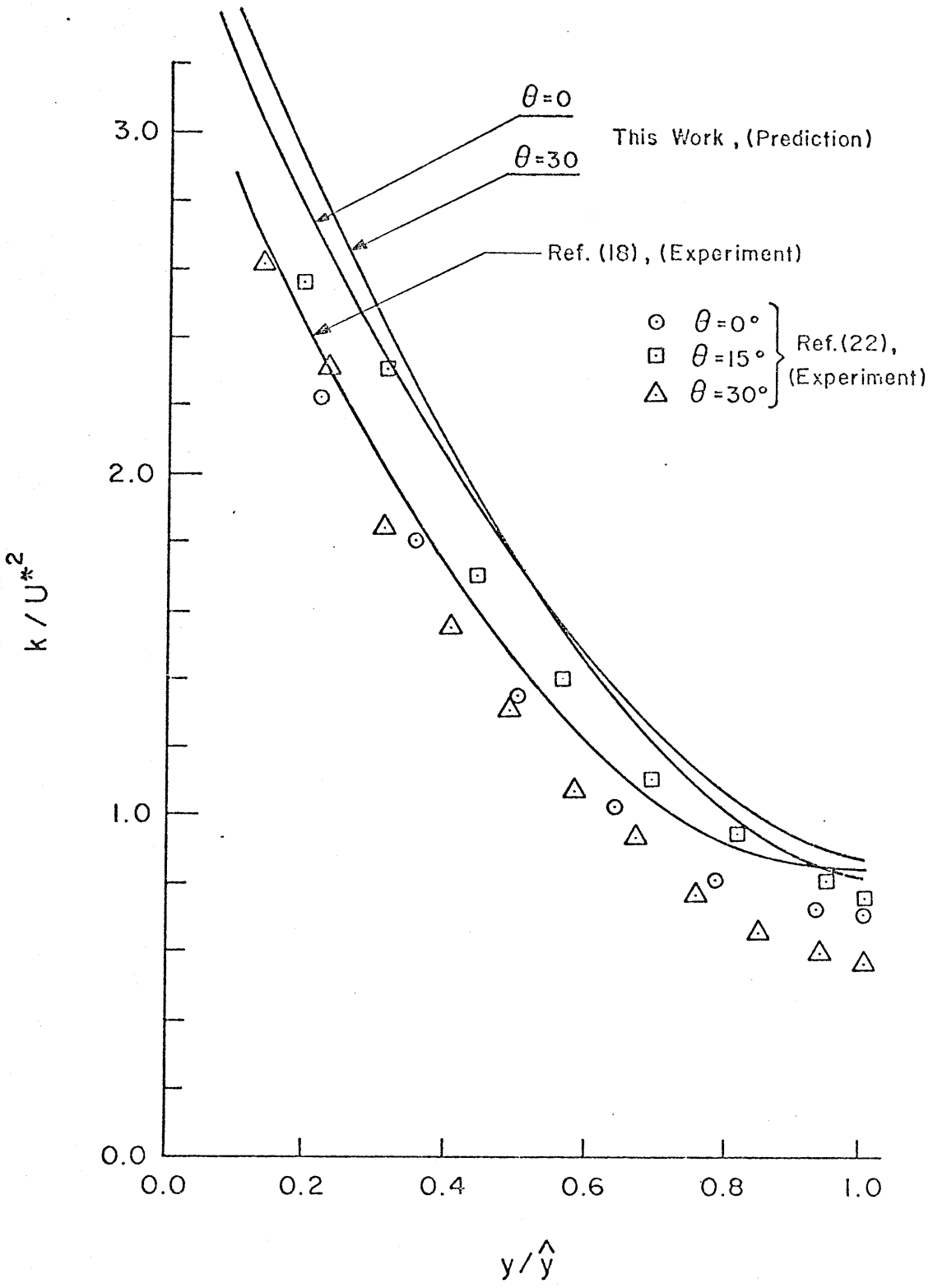

Fig. 12.36. Comparison of Predicted k with Experimental Work, Re=48,130 , P'/D=1.35.

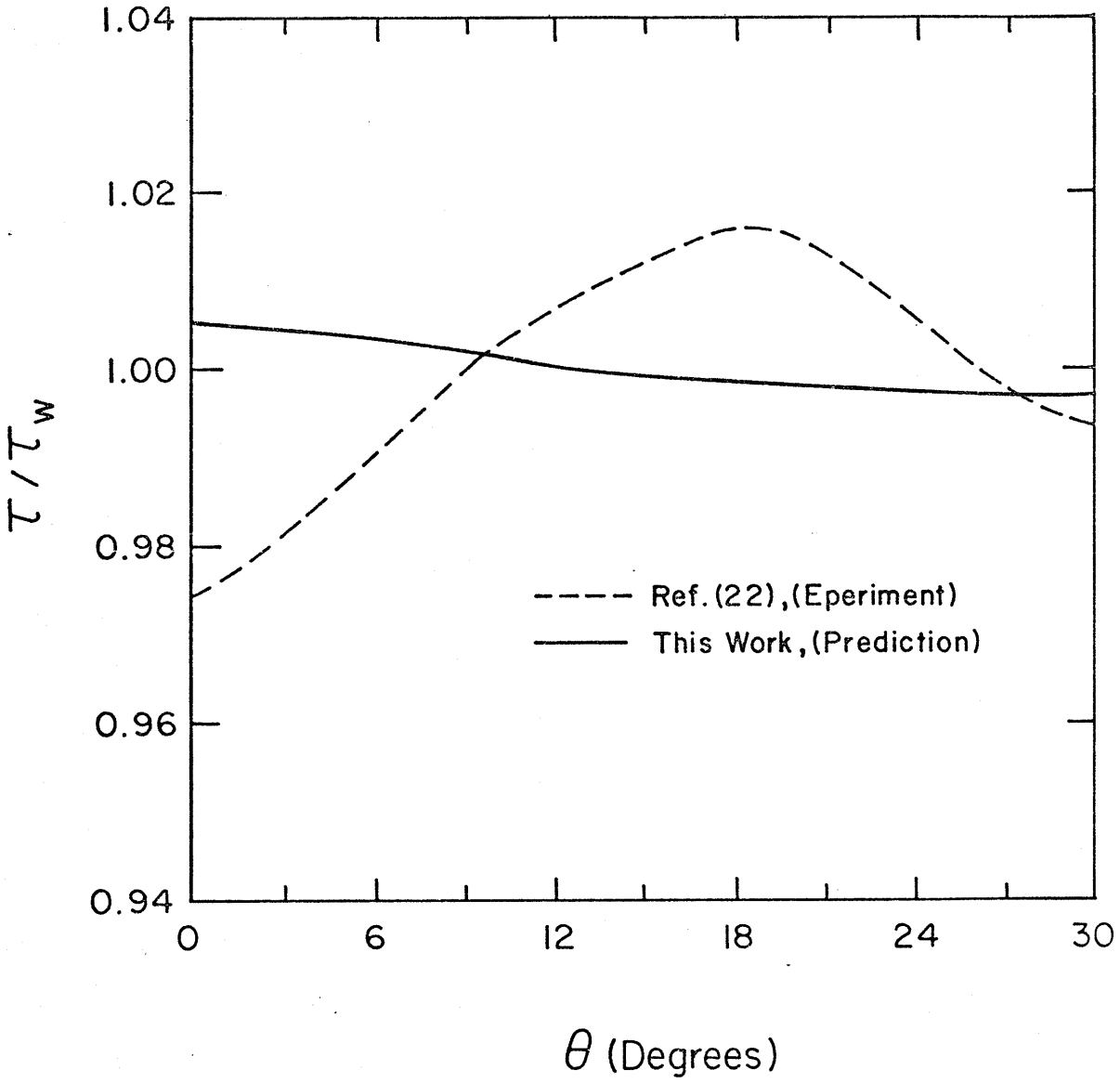

Fig. 12.37 . Local Wall Shear Stress Distribution , Re = 48,300 , P'/D = 1.35 .

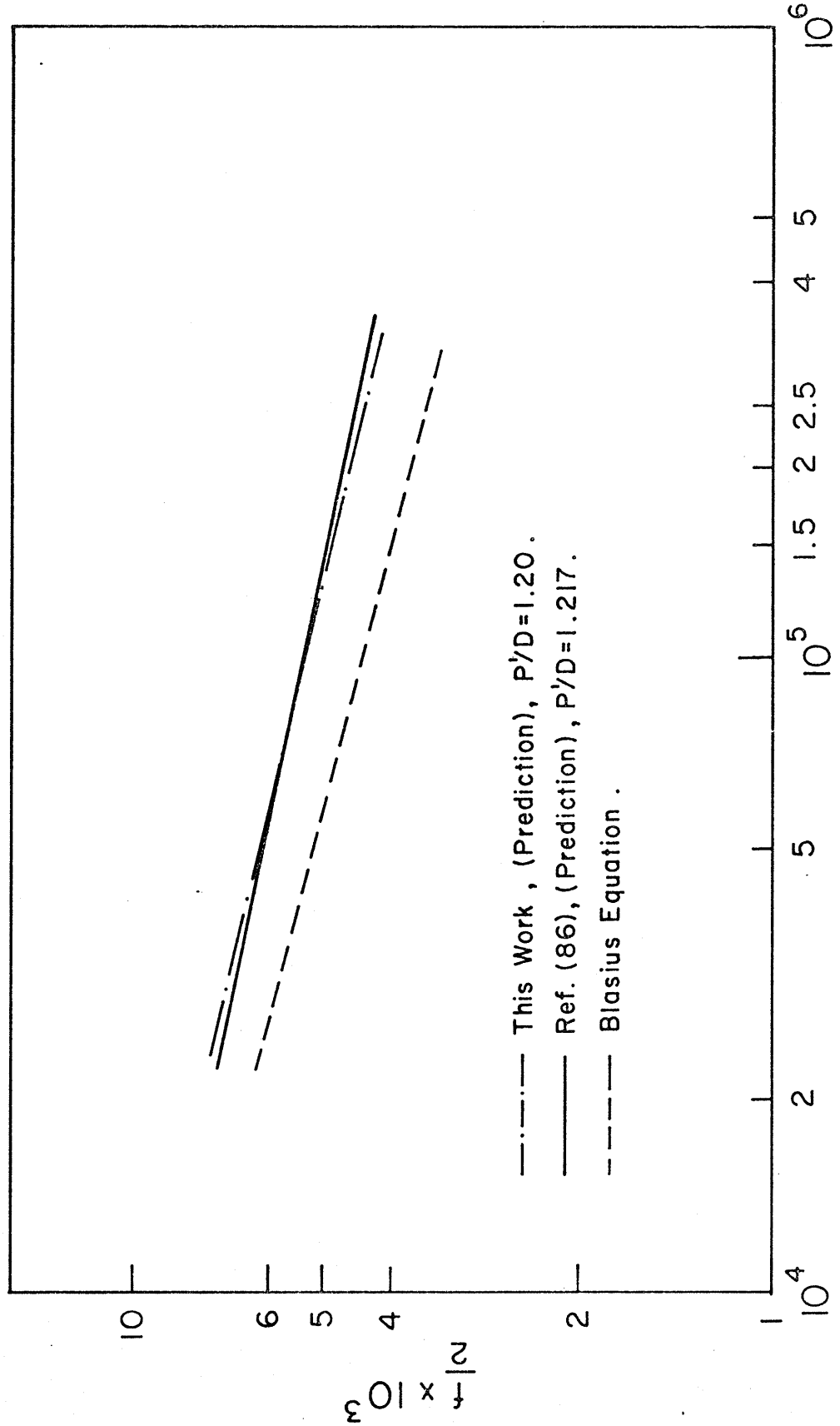

Fig.12.38. Friction Factor Dependence on Reynolds Number .

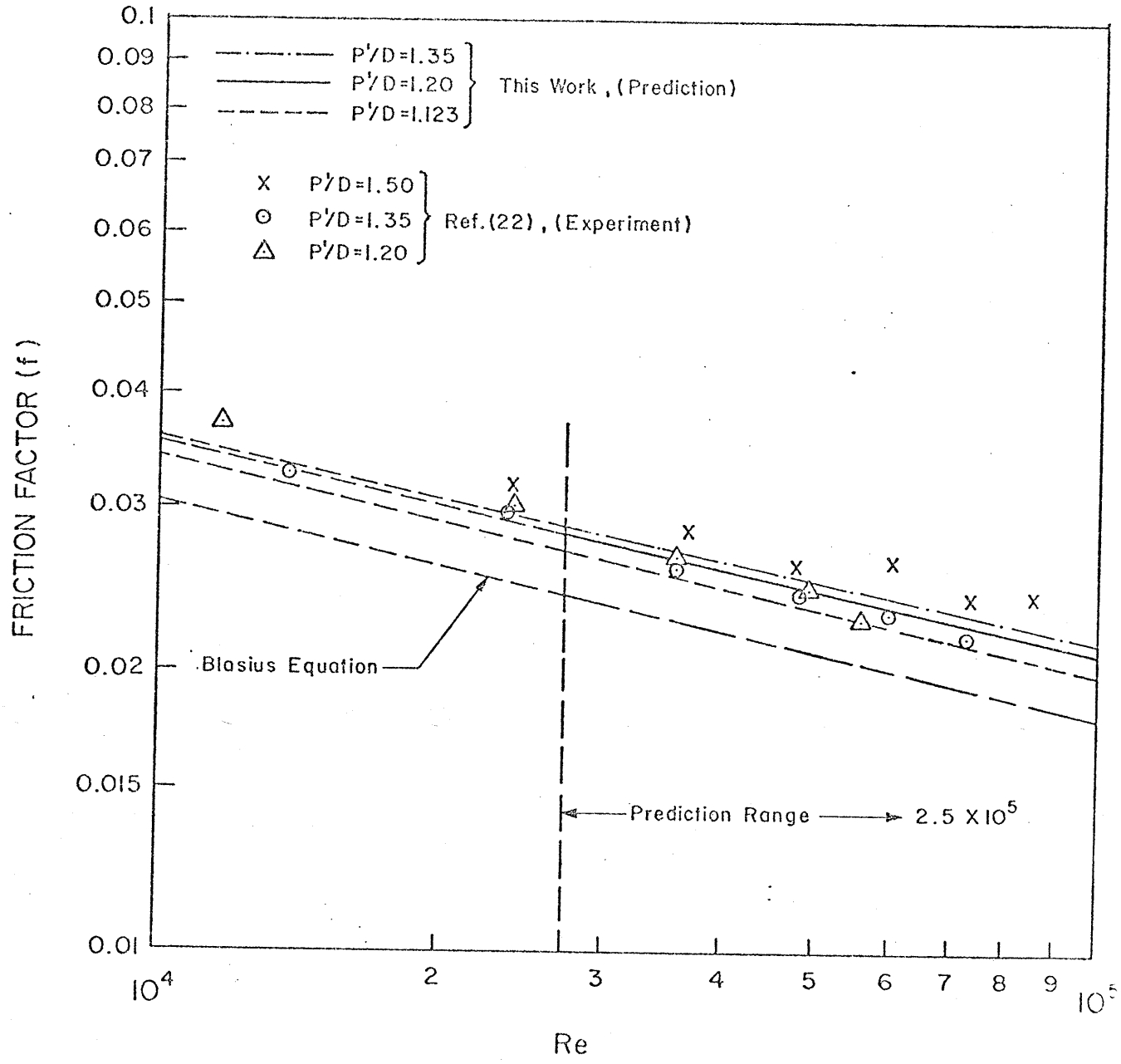

Fig. 12.39 . Effect of Reynolds Number on Friction Factor for Differnt P'/D Ratio .

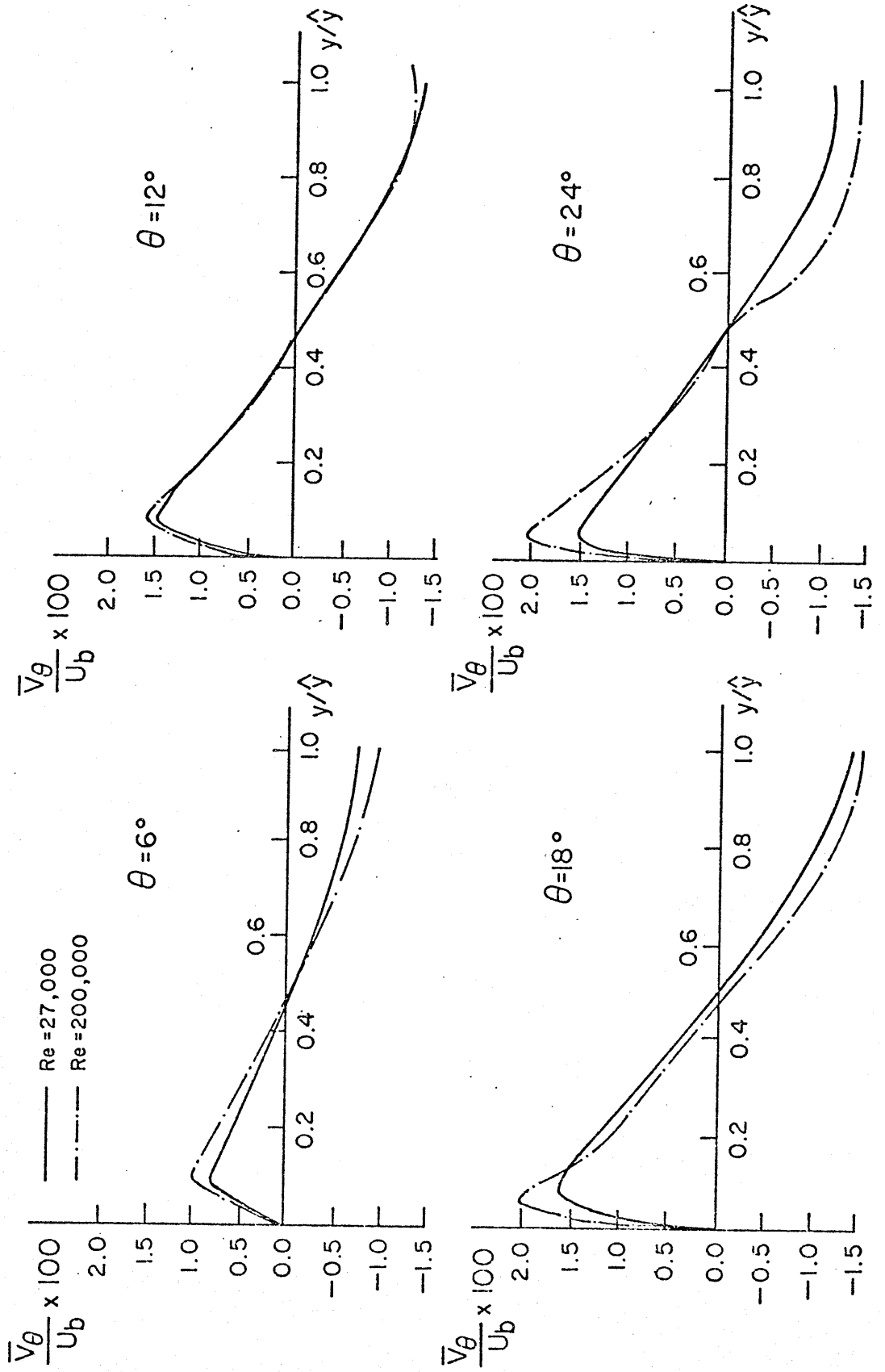

Figure 12.40: Effect of Reynolds Number on the Secondary Velocity Component $\bar{V}_\theta$, P'/D = 1.123

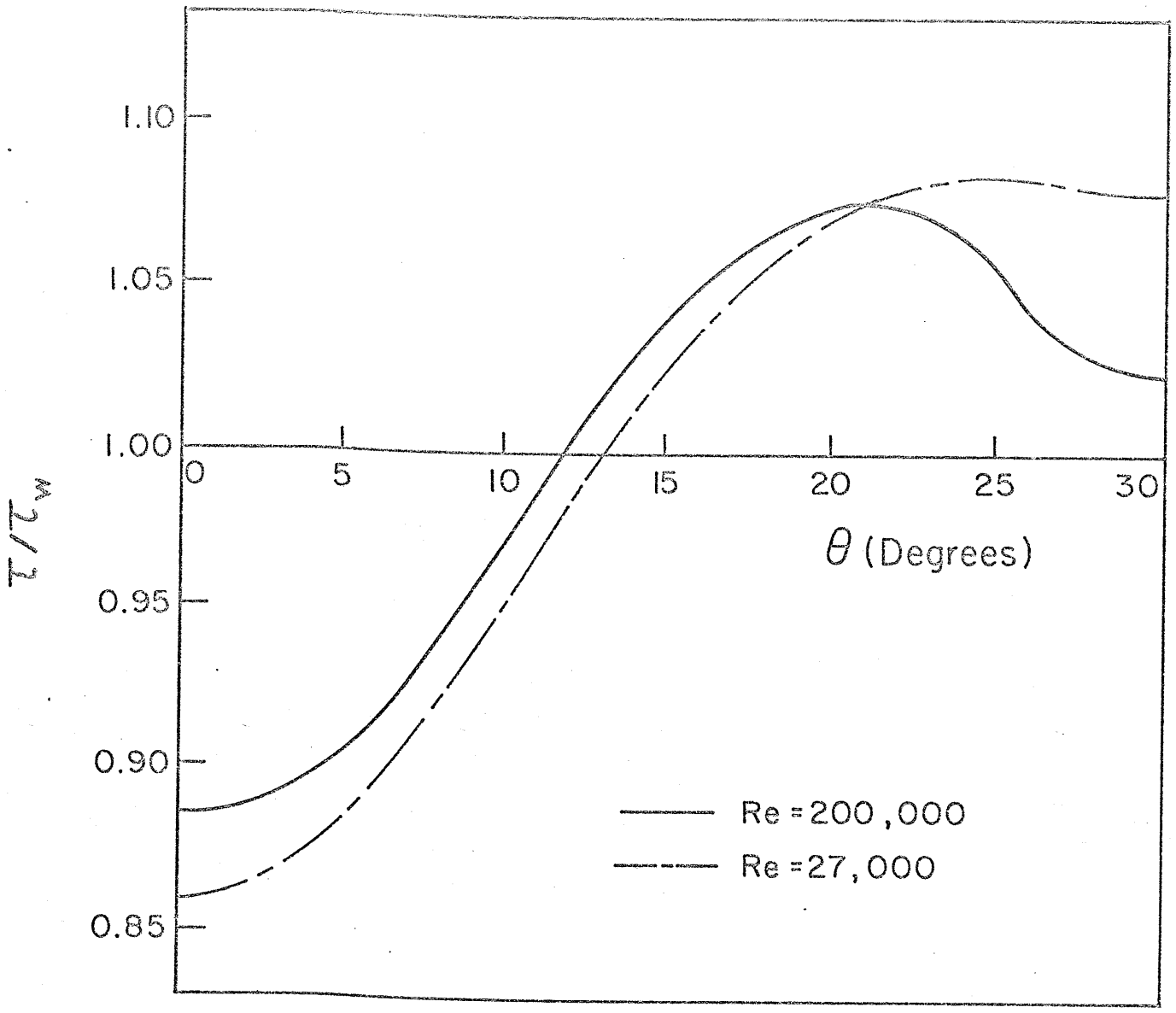

Fig. 12.41. Effect of Reynolds Number on Local Wall Shear Stress Distribution, P/D = 1.123.

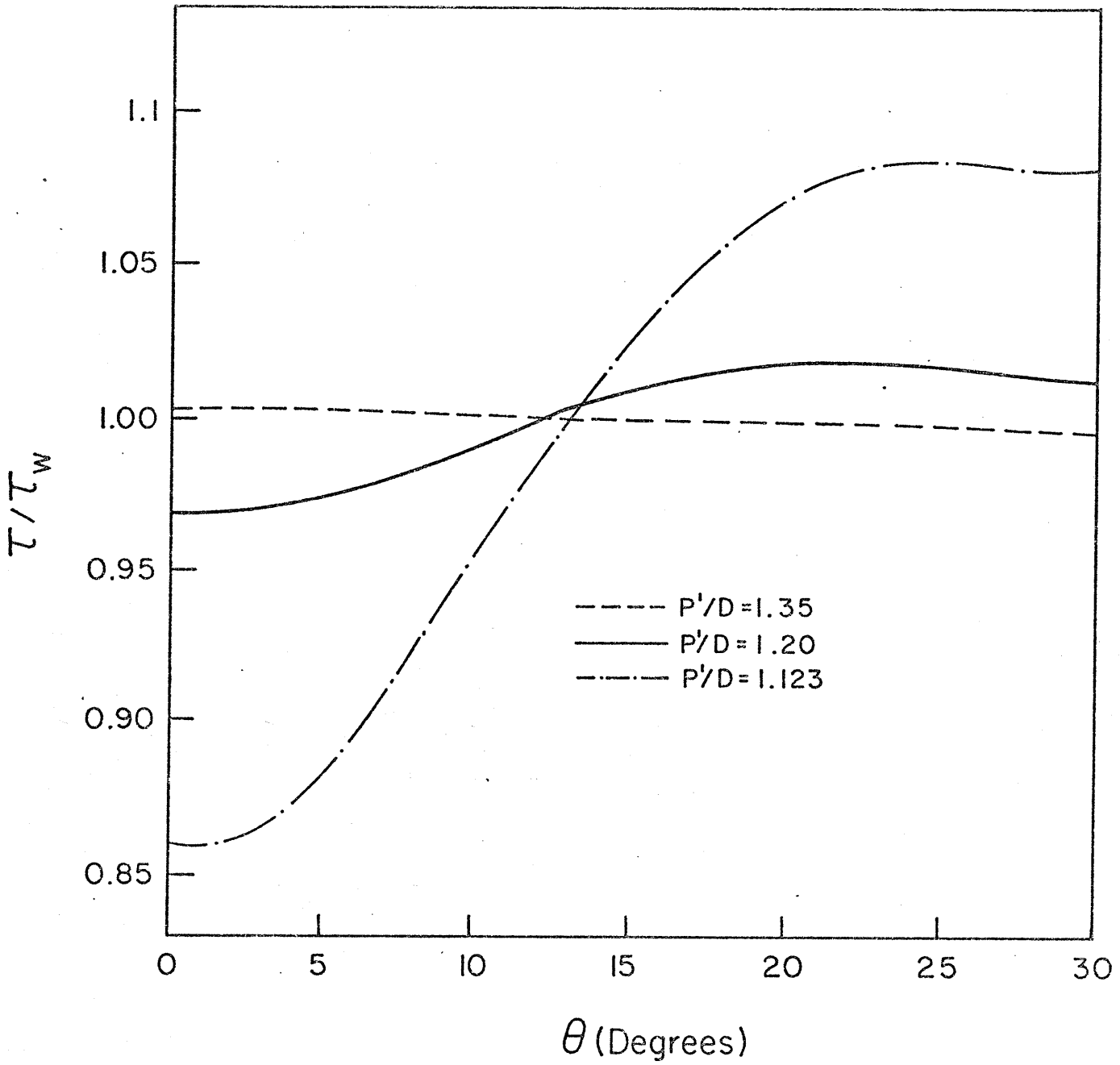

Fig. 12.42. Effect of P'/D Ratio on Local Wall Shear Stress Distribution, Re = 27,000 .

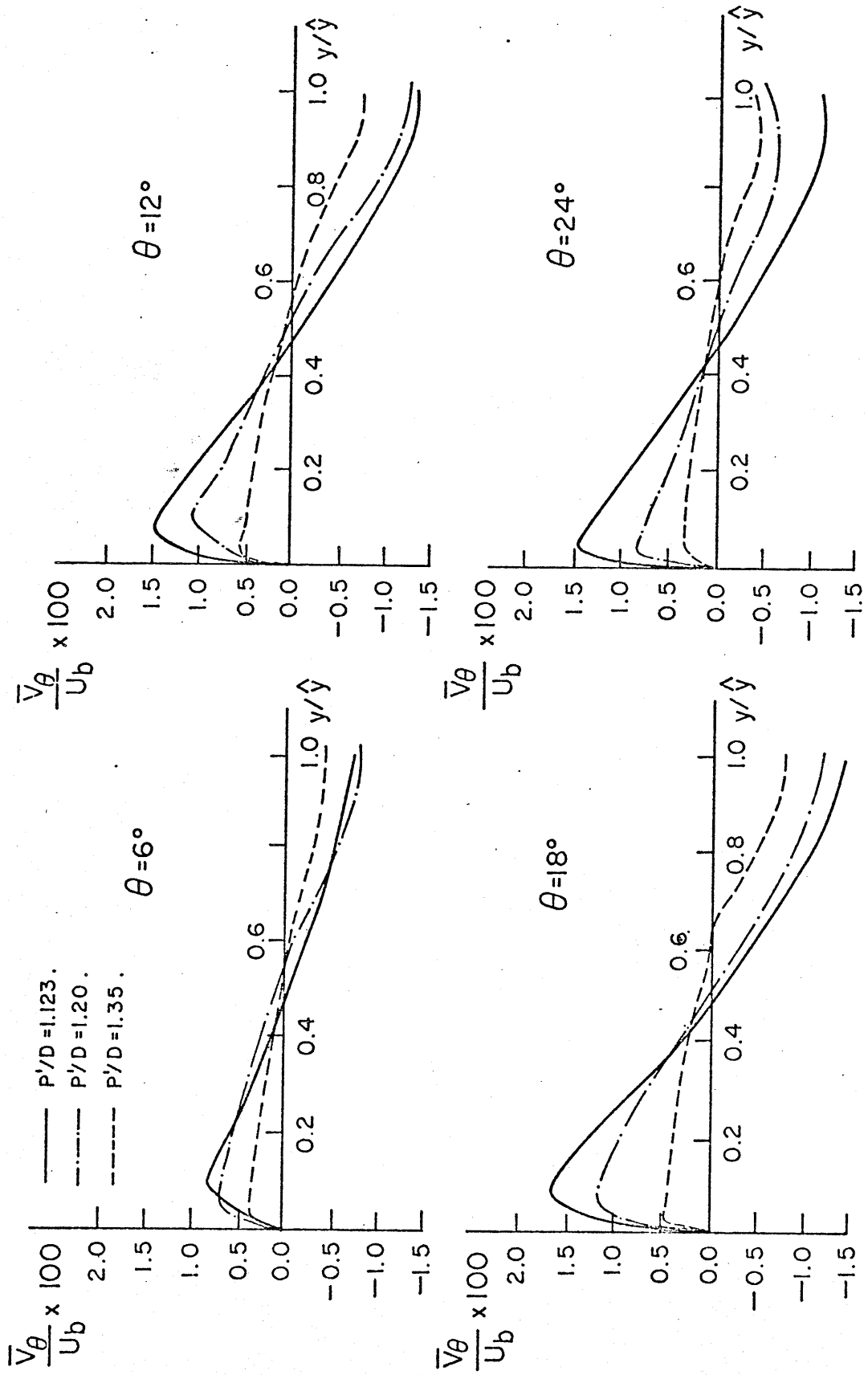

Fig.12.43. Effect of P'/D Ratio on The Secondary Velocity Component $\bar{V}_\theta$, Re= 27,000.

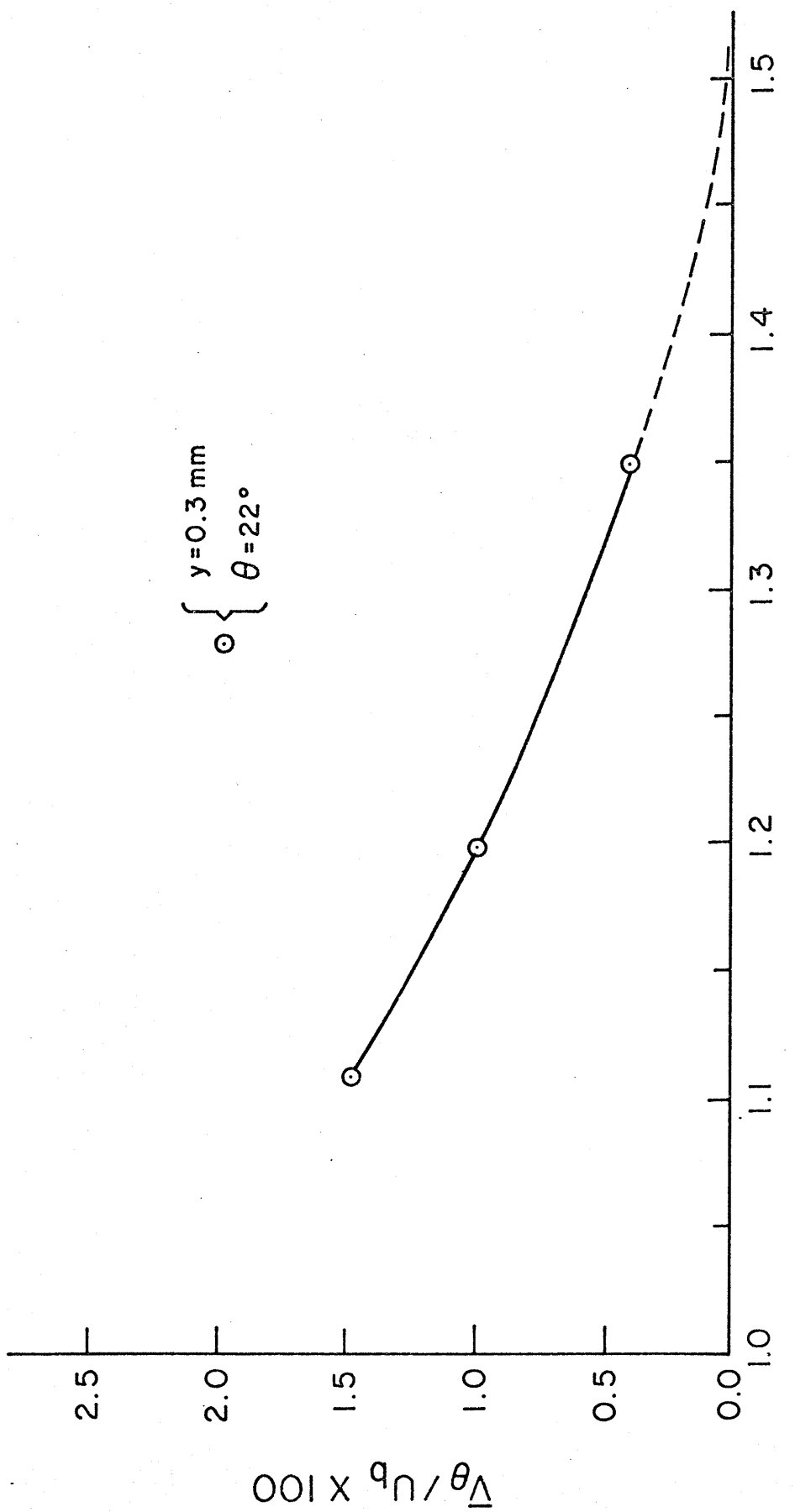

Fig.12.44. Predicted Secondary Velocity Component $\overline{V}_\theta$ at a Fixed Point for Different P'/D Ratios, Re=27,000.